IMPERIAL COLLEGE LONDON

DOCTORAL THESIS

Thermo-Hydro-Mechanical Coupling within a Geomechanical Multiphase Model Framework with special reference to Fractured Rock Masses in the Vicinity of a Geological Disposal Facility for Radioactive Waste

Clément JOULIN

Supervisors:

Dr. John-Paul LATHAM,

Dr. Jiansheng XIANG

and Professor Christopher PAIN

A thesis submitted in fulfilment of the requirements

for the degree of Doctor of Philosophy

in the

Applied Modelling & Computation Group (AMCG)

Department of Earth Science and Engineering

May 2019

Abstract

Thermo-Hydro-Mechanical Coupling within a Geomechanical Multiphase Model Framework with special reference to Fractured Rock Masses in the Vicinity of a Geological Disposal Facility for Radioactive Waste

A novel numerical approach for the modelling of Thermo-Hydro-Mechanical (THM) processes in the vicinity of a Geological Disposal Facility (GDF) for the long-term storage of radioactive waste is presented. This work is based on a dual numerical code framework with a multiphase flow solver for thermo-hydraulic processes and a geo-mechanical solver for mechanical processes in fractured and fracturing rock masses. The method has a unique continuum-discontinuum configuration that allows each of the THM processes to be represented with the most suited formulation, thus improving the accuracy and complexity of the simulations. Thermal processes are implemented within the geo-mechanical solver using both an explicit and an implicit approach, the latter allowing the modelling of temperature over large time scales, an important feature in the context of geological disposal. Moreover, a novel thermal contact approach is presented to investigate the heat transfer between contacting solids and its application to heat transfer across fractures is discussed. Furthermore, a thermo-mechanical coupling formulation is derived in the geo-mechanical solver, enabling thermal expansion and thermally induced fracturing. Then, the THM coupling is finalised using a conservative projection method that enables information exchange between superimposed numerical meshes e.g. heat transfer between the thermo-hydraulic and the thermo-mechanical solvers. Both applications in porous media and with laminar flow are explored. Finally, the THM dual framework is applied to the modelling of thermal spalling occurring in the excavation walls of a deposition hole in a GDF. The potential of the method to offer new predictive capabilities and insights on unexplained experimental observations is demonstrated by considering the concurrence over time of THM factors influencing spalling, especially multi-phase flow in the continuum and explicitly represented fractures in the discontinuum.

Declaration of Authorship

I, Clément JOULIN, declare that this thesis titled, 'Thermo-Hydro-Mechanical Coupling within a Geomechanical Multiphase Model Framework with special reference to Fractured Rock Masses in the Vicinity of a Geological Disposal Facility for Radioactive Waste' and the work presented in it are my own. I confirm that:

- This work was done wholly while in candidature for a research degree at this University.
- Where any part of this thesis has previously been submitted for a degree or any other qualification at this University or any other institution, this has been clearly stated.
- Where I have consulted the published work of others, this is always clearly attributed.
- Where I have quoted from the work of others, the source is always given. With the exception of such quotations, this thesis is entirely my own work.

Signed: Clement Joulin

Date: 30/05/2019

Acknowledgements

When I moved from Paris to London to start this PhD adventure, I could not have imagined how much I would have changed by the end of it. It has taken four years to complete the work and there have been many times during that period where I have wished that I could finish the research faster to move on to greener pastures. But over the years I grew to like the PhD life and embrace the independence which came with it, the only thing I had to worry about was the research and as a result this gave me both time and freedom for my hobbies, dreams, family, friends and partner. Although I was yearning for something different, in the end it did not stop me from enjoying my present situation. As I move on from academia, I can look back with no regrets.

The most important aspiration I have for this work is that it will be useful to others; I hope that my research will be of value and provide a foundation to those interested in the subject. I have worked very hard to make this thesis as complete and detailed as possible. There are many people that have made this possible and I feel very grateful that I have had them during this journey.

I would like to start with my parents who always supported my decisions and who provided the environment and the education that allowed me to be successful at school and to be able to complete a PhD, I know my luck and I am grateful to them.

Next, I want to thank my supervisors, Jason for his ongoing and irreplaceable technical support, availability and friendliness. JP for the overall supervision of my PhD and his understanding and support when times were difficult. Chris for his challenging development requests for which I had to surpass myself. I also wish to thank all of my PhD mates that were in the same boat and with which sharing and laughing was essential; Indi, Larry, Lluis, Pablo, Ado and last but not least, Thomas, a spiritual brother with whom I have so much in common, you made this whole experience a lot nicer.

I also want to mention my Ju Jitsu family, all Senseis and Ukes, in particular, Elena, Lewis, Sébastien, Shaan, Leo, all Whitechapel Jitsu club, especially Emeka and Chix, my last and most inspiring mentor. Thoughts as well to the Crewdson house and to all the people that I have met while living there; Cheikh, Elenora, Ana and my man Jono - my late night LoL companion, a great man. The struggle is real on the path to stable freelancing - but it's always worth it.

I would also like to thank my friends and fellow practitioners in the Buddhist Society and Byokusuma Sangha; Karuna, Nitima, Edward, Pratistha, Rajesh, Alex and many more. You have shown tremendous support and kindness, thank you.

Finally, I want to mention the most important person I have met during the past four years, my partner Daisy. You have been the greatest source of support, especially during the writing of the thesis when I would write all day and you would be the only person I would talk to. Your advice, proofreading, joyfulness, care and attention are very precious to me and I intend to keep it around!

Contents

List of Figures

List of Tables

Abbreviations

General

LLW	**L**ow **L**evel **W**aste
ILW	**I**ntermediate **L**evel **W**aste
HLW	**H**igh **L**evel **W**aste
LLWR	**L**ow **L**evel **W**aste **R**epository
GDF	**G**eological **D**isposal **F**acility
URL	**U**nderground **R**esearch **L**aboratory
ASPE	**Ä**spö **P**illar **S**tability **E**xperiment
BRIE	**B**entonite-**R**ock **I**nteraction **E**xperiment

Organisations

AMCG	**A**pplied **M**odelling and **C**omputation **G**roup
BEIS	**D**epartment for **B**usiness, **E**nergy & **I**ndustrial **S**trategy
CoRWM	**Co**mmittee on **R**adioactive **W**aste **M**anagement
DECC	**D**epartment of **E**nergy and **C**limate **C**hange
DECOVALEX	**DE**velopment of **CO**upled models and their **VAL**idation against **EX**periments
DTi	**D**epartment of **T**rade and **i**ndustry
IAEA	**I**nternational **A**tomic **E**nergy **A**gency
NAMRC	**N**uclear **A**dvanced **M**anufacturing **R**esearch **C**entre
NAO	**N**ational **A**udit **O**ffice
NDA	**N**uclear **D**ecomissioning **A**gency
SKB	Swedish Nuclear Fuel and Waste Management Company

UNFCCC	**U**nited **N**ations **F**ramework **C**onvention on **C**limate **C**hange
WNA	**W**orld **N**uclear **A**ssociation

Numerical Methods

FEM	**F**inite **E**lement **M**ethod
FDM	**F**inite **D**ifference **M**ethod
FVM	**F**inite **V**olume **M**ethod
BEM	**B**oundary **E**lement **M**ethod
DEM	**D**iscrete **E**lement **M**ethod
DDA	**D**iscontinous **D**eformation **A**nalysis
FEMDEM	**F**inite-**D**iscrete **E**lement **M**ethod
PETSc	**P**ortable, **E**xtensible **T**oolkit for **S**cientific **C**omputing

À mes Parents…

Chapter 1

Introduction

1.1 Nuclear Legacy

There are at present about 450 operational nuclear reactors in 31 countries, with the majority located in Europe and North America (IAEA, 2017). In 2018, Nuclear power accounts for 11% of the world's electricity production (WNA, 2018). At the 21st Conference of Parties in 2015 (COP21), 180 states and the European Union accounting for more than 87% of global greenhouse gas emissions ratified the Paris Agreement, committing to keep "a global temperature rise this century well below 2 degrees Celsius above pre-industrial levels and to pursue efforts to limit the temperature increase even further to 1.5 degrees Celsius" (UNFCCC, 2016) .

Energy production in the UK accounts for nearly 30% of the carbon dioxide emissions with 34% for the transport sector, 18% from business and 17% from the residential sector (BEIS, 2018a). Since 1990, emissions from energy generation have been reduced by more than half, predominantly as a result of the increasing presence of low carbon energy alternatives in the energy mix (BEIS, 2018a). However, currently half of the UK's energy production still relies on fossil fuels (coal and gas, BEIS 2018a). In order for the UK to meet the targets laid out in the Paris Agreements and in the UK legislation (BEIS, 2017), the efforts to support renewable energies (solar, wind, tidal, geothermal, hydro and bio energy) or nuclear energy must be pursued.

There are currently 15 operating nuclear reactors generating 21 % of the UK's electricity supply (WNA, 2018), however all but one of the reactors are due to retire in 2030 (NAMRC, 2015). In 2006, the UK government policy towards nuclear power shifted, recognising that this energy source has a role in reducing emissions and in maintaining the energy mix (DTi, 2006). For the first time in two decades, this commitment has led the UK to undergo a period of new nuclear build, with Hinkley Point C scheduled for operation in 2025 (NAO, 2017). The UK government has also put forward policies to support the next generation of small and advanced nuclear reactors (BEIS, 2018b). The UK government intends for a geological waste disposal facility (GDF) to host both waste generated from nuclear new build and legacy waste (WNA, 2018).

1.2 Radioactive Waste

Most of the UK radioactive waste is accumulated as the result of research and development activities on nuclear power, alongside operational waste arising from energy production and military related programmes. Radioactive wastes are classified by their radiation and heat generation levels which impacts on the method by which they must be managed. The classification in the UK is as follows (NDA and BEIS, 2017):

- **Low Level Waste (LLW)** contains the lowest level of radioactivity, up to 4 Giga Becquerel (GBq) per tonne of alpha activity or up to 12 GBq per tonne of beta or gamma activity. Most of the LLW is accumulated as the result of exploitation or decommissioning operations of nuclear facilities i.e. as materials that have become contaminated through exposure to radioactive radiation. In the UK, LLW accounts for about 75% of the current total radioactive waste volume (NDA, 2017a).
- **Intermediate Level Waste (ILW)** exceeds the upper boundaries of the LLW radioactivity level but does not generate a significant amount of heat. ILW is composed of nuclear reactor components and sludges from the treatment of radioactive liquid effluents. In the UK, ILW accounts for about 23% of the current total radioactive waste volume (NDA, 2017a).
- **High Level Waste (HLW)** generates significant amounts of heat due to its high radioactivity level. HLW represents less than 2% of all radioactive waste

in volume but accounts of over 90% of the radioactivity (NDA, 2017a). HLW is mainly composed of spent reactor fuel that is no longer efficient for generating electricity and typically arises in the liquid form.

It is important to note that based on the current classification, the longevity of the waste is not taken into account. Depending on their exact composition, radioactive waste materials can remain highly radioactive and potentially harmful to humans and the environment for up to hundreds of thousands of years .

At present, the volume of radioactive waste totals to approximately $132,000\ m^3$ (NDA, 2017a). However, the majority of the waste to be accounted for remains part of existing facilities and will arise after the shut-down and decommissioning of the existing nuclear power plants. The total volume forecast by year 2125 amounts to $4,770,000\ m^3$ (NDA, 2017a) with approximately 90% of LLW, 10% of ILW and 0.03% of HLW (NDA and BEIS, 2017).

1.3 Waste Management

The waste being harmful to Humans and the Environment, providing a long term solution for the management of those wastes safely and at acceptable costs is a major challenge for the nuclear industry. Currently in the UK, materials termed as LLW are cut, compacted or incinerated to reduce their volume for disposal (DECC, 2010). They are then grouted within metal containers and stored in above or near-surface facilities known as Low Level Waste Repositories (LLWR, DECC, 2010).

For disposal, ILW may also need treatment such as super-compacting, cutting or drying. ILW is placed and cemented in stainless steel containers, typically 500 litres drums or $3\ m^3$ boxes that will be kept in an interim storage facility until long-term disposal is available (NDA, 2017b).

HLW is melted with crushed glass and poured into 150 litres stainless steel canisters. This vitrification process ensures the waste is in a stable form for interim storage in air-cooled facilities for at least 50 years, allowing the waste to cool down and for a large part of its radioactivity to decay before permanent disposal (NDA, 2015).

For the long term management of ILW and HLW, the only concept to have gained international consensus and scientific support is the deep geological disposal. Long term storage of radioactive waste in a Geological Disposal Facility (GDF) is the solution adopted in a majority of nuclear countries, including Belgium, France, Finland, Germany, Japan, Sweden, Switzerland and the US.

1.4 The Generic Design of the GDF

The Swedish Nuclear Fuel and Waste Management Company (SKB, The Svensk Karnbranslehantering AB) has established a standard system for the geological waste disposal of radioactive waste. This includes three facilities: a central interim storage, an encapsulation plant for the packaging of the waste, and an underground repository.

The underground facility comprises of a system of vaults for the disposal of ILW, where several individual containers will be stored together (Figure 1.1).

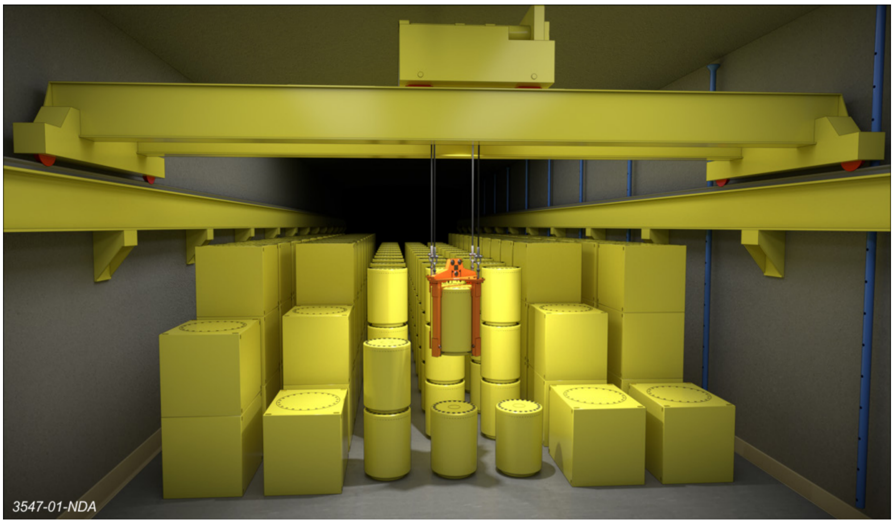

Figure 1.1: Disposal of ILW 500 litres drums and 3 meter cube boxes in an underground vault of a GDF (NDA, 2016).

Because of their heat generation, high level waste will be disposed in arrays of engineered tunnels (DECC, 2014), see Figures 1.2 and 1.4. To ensure their long term storage, the Swedish System defines a multi-barrier concept known as KBS-3 (Nuclear Fuel Safety - 3 barriers), see Figure 1.3. The KBS-3 comprises of two engineered and one natural barrier (SKB, 2010c):

- The canister (Figure 1.3b), encapsulates the vitrified HLW which is organised in arrays of cladding tubes (Figure 1.3a) to diffuse heat effectively. A cast iron insert protects the canister from mechanical stress and an outer copper envelope prevents corrosion.
- The buffer (Figure 1.3), made of bentonite, a clay based material which surrounds the canister. The buffer swells in the presence of water to provide a mechanical support pressure onto the walls of the deposition hole, allowing the excavation to withstand the in-situ and thermal stress. The role of the buffer is to delay any eventual radionuclide release from the canister.
- The host rock. The surrounding rock formation prevents radionuclide release upwards into the biosphere and also provides a stable chemical and mechanical environment for the engineered barrier. Hence the rock formation must be of low permeability as well as seismically inactive.

All excavated volumes (deposition holes, service and transport tunnels) will be backfilled to restore the mechanical equilibrium and continuity of the disrupted rock and to ensure they do not promote groundwater flow (NDA, 2016).

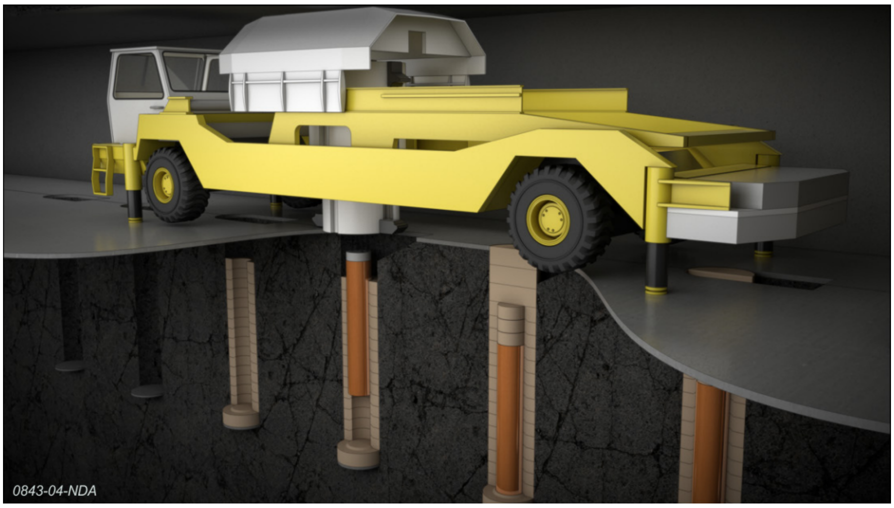

FIGURE 1.2: Deposition of HLW canisters in a GDF (NDA, 2016).

The facility must be built at great depths to be protected from significant climate or landform changes at the surface and to be protected from earthquakes as the magnitude of the seismic waves decreases with depth. Additionally, the waste must remain significantly below the aquifers to avoid potential water contamination and its transportation into the biosphere (NDA, 2016).

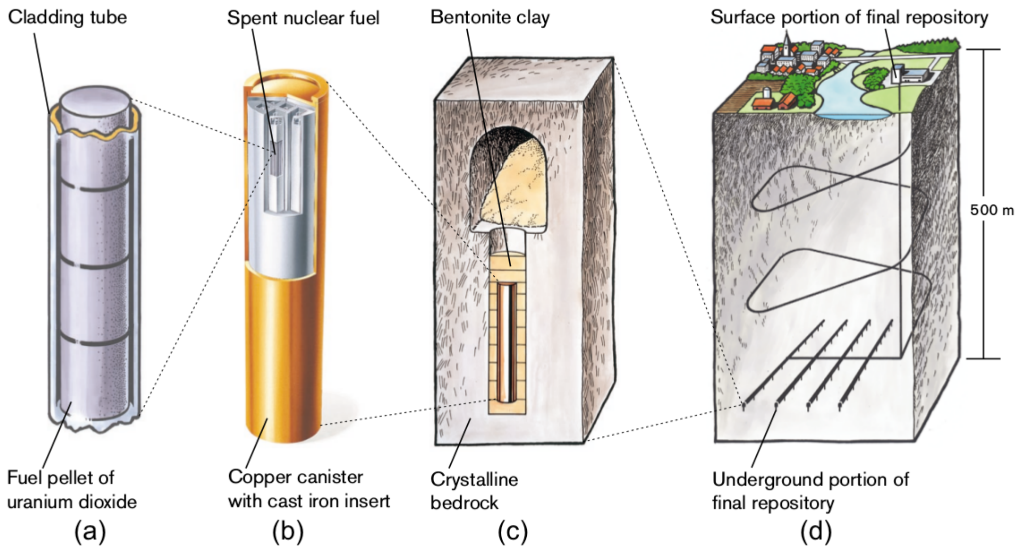

FIGURE 1.3: The multi-barrier system of the KBS-3 (SKB, 2000).

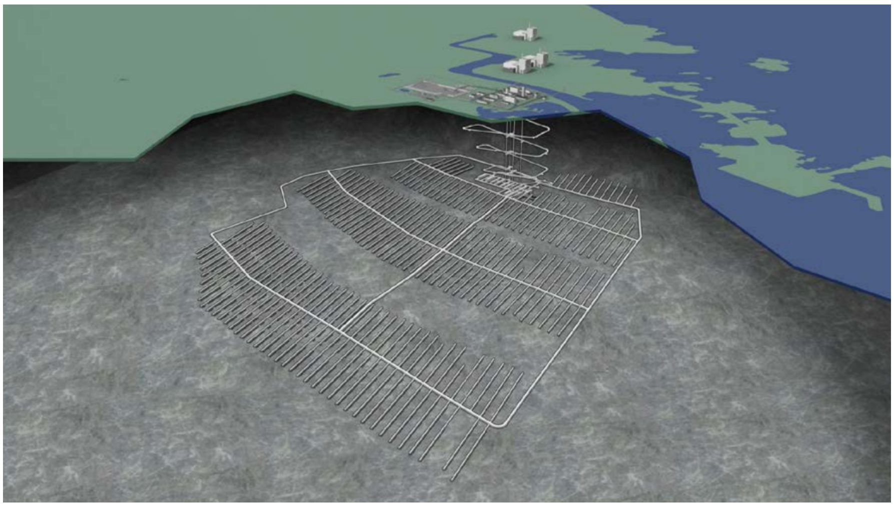

FIGURE 1.4: Aerial schematic view of the Forsmark repository in Söderviken, Sweden (SKB, 2018).

As highlighted by a White Paper from the UK Department of Energy and Climate Change (DECC, 2014), a repository must be located at a depth between 200 and 1,000 meters, the exact depth depending on the specificity of the site. There are three defined types of rock formation that may host a GDF, for each of them an appropriate depth is recommended (NDA, 2016):

(i) high strength crystalline rock: $\sim 650m$

(ii) low strength argillaceous sedimentary rock $\sim 500m$

(iii) evaporite or salt rock $\sim 650m$

As the chosen depth of the facility increases, the number of options available for access, construction, operation and closure of the repository will reduce. At greater depths, the in-situ stress in the rock mass is more important which increases the likelihood for irreversible changes to occur and to permanently lower the insulating quality of the engineered and natural barrier. As a result, designing the facility to meet the safety requirements becomes challenging and costs will be impacted.

1.5 Thermo-Hydro-Mechanical Processes

The term "coupled processes" means that processes are interdependent and that a change occurring in one of them impacts directly and indirectly the others (Tsang, 1987). Thermo-Hydro-Mechanical and Chemical coupled processes (THMC) are acknowledged by the international waste management community to have a significant long-term impact on the three-barrier system and are widely recognized to be of critical importance on post-closure safety of GDFs (Manepally et al., 2011, Stephansson et al., 2004, Tsang et al., 2004). It is the study of coupled processes that led to the threefold classification of host rocks due to the similarities in their THMC properties, namely crystalline, argillaceous, and salt rocks.

THMC coupled process became of importance in the 1980s (Noorishad et al., 1984, Tsang, 1987) with the first compilations of knowledge on the subject coinciding with early radioactive waste disposal programs (Manteufel et al., 1993). As the present does not explore chemical interactions, only thermo-hydro-mechanical processes will be considered.

1.6 Thesis Overview

1.6.1 PhD Scope & Research Objectives

Over the last three decades, a considerable number of experiments were conducted to understand the THM coupled behaviour of fractured rocks (Stephansson et al., 2004, Tsang et al., 2005). Small scale experiments were conducted in traditional rock mechanics laboratories whilst large scale experiments providing a more realistic insight into processes happening in a repository were conducted in Underground Research Laboratories (URL). Long term full scale experiments have been conducted in URL for up to 18 years (Fernández et al., 2018). However, repositories must contain the waste safely for at least several thousand years (RWM, 2016) and predicting with certitude the long-term coupled behaviour of the rock mass is experimentally impractical.

Natural analogues may complement experiments. These are phenomena that occurred in the environment with conditions and time scales similar to some of the key processes in radioactive waste storage (Miller, 2000). For example, the natural fission reactor of Oklo, Gabon within which self sustained nuclear chain reactions occurred for a few hundred thousand of years with the fission products contained within the rock formation for 2 billion of years (Gauthier-Lafaye et al., 1996). The examination of natural analogues can provide important insights in the long term coupled THMC behaviours but their number is limited.

In contrast, numerical methods have proven to be robust predictive tools offering approximations of the evolution of physical processes. The contribution of such methods is increasing and so is the size and complexity of the problems faced. Thus accurate, cost-effective and multi-physics numerical methods are in high demand, especially for the modelling of THM coupled processes.

The principal aim of the present research is to build up knowledge and capability in modelling thermo-hydro-mechanical processes that occur in fractured rock masses in the vicinity of a geological disposal facility for radioactive waste in the UK. The research is performed within the AMCG (Applied Modelling and Computation Group) at Imperial College London.

Within the AMCG two advanced technologies are available: i) a thermo-hydraulic solver ‘Fluidity’ for multiphase fluid dynamics and the branch ‘IC-FERST’ for multiphase flow in porous media ii) a geomechanical solver ‘Solidity’ for the mechanics of deformation and fracturing of rock masses. Note that in this thesis, the thermo-hydraulic solver and its branch IC-FERST will be referred as ‘Fluidity’.

For the modelling of THM coupled processes as well as for many other applications, numerical methods are divided within three categories, continuum, discontinuum and hybrid methods. Continuum methods model domains as un-interrupted, the contours of a fracture for instance would not be explicitly represented visually or structurally. Instead equivalent properties approximating the discontinuous behaviour of the fracture are introduced locally in the continuum. On the contrary, discontinuum methods represent explicitly the discontinuities with their sizes, shapes, boundaries and behaviours. The choice between continuum or discontinuum representation largely depends upon the size and configuration of the problem considered. Both methods have their own advantages and inconveniences which are related to either the accuracy and complexity in the physical processes or to the computational efficiency. Hybrid methods combine continuum and discontinuum but do not aim to overcome the limitations of each but rather to offer the best representation for each of the thermal, hydrological and mechanical processes. This results in enhanced accuracy and complexity in the physics but at a higher computational cost.

Fluidity is a continuum method and Solidity can use either a continuum, discontinuum or hybrid method. In the past decade, there have been several research efforts in the AMCG to produce a hybrid method with Fluidity and Solidity (Viré et al. 2012-2015, Lei 2016, Yang et al. 2016 and Obeysekara et al. 2018). The Fluidity-Solidity hybrid approach, also referred as ‘fluid-solid coupling’, consists of a dual framework within which the two numerical codes run in a sequence and communicate at specific time intervals to exchange information relevant to the coupled processes. The past numerical research developments and those which continued simultaneously with this research work led to mature capabilities able to tackle fluid-solid coupling for deformation, fracturing and fluid flow in porous media (Obeysekara, 2018).

However, until now, only the coupled hydro-mechanical behaviour of fluids and solids was considered. The present research work intends to extend the coupled capabilities of the Fluidity-Solidity hybrid method to thermo-hydro-mechanical coupling. This addition will improve the accuracy when modelling un-saturated porous and fractured rock masses, including predictions of flow, stress and fracturing, thereby contributing towards safer repository designs.

The specific objectives of the research work are the following:

1. Implement and validate a heat conduction solver for Solidity
2. Derive, implement and validate a thermo-mechanical coupling formulation for the finite strain theory of Solidity (Xiang et al., 2009a)
3. Perform and validate thermally induced fracturing in Solidity
4. Derive, implement and validate a fluid-solid thermal coupling formulation for the Fluidity-Solidity dual framework
5. Improve the Fluidity-Solidity framework for the modelling of THM coupled processes in the context of radioactive waste repository, this involves:
    - THM coupling in porous media
    - THM coupling in fractured rock
    - THM induced fracturing
    - THM coupling with multiphase flow
    - THM modelling over large time scales
6. Apply the Fluidity-Solidity framework to a realistic GDF performance scenario

1.6.2 Contributions of the Thesis

The contributions of the present research work are summarised as follows:

1. Implementation and validation of an explicit heat conduction model within Solidity.
2. Implementation and validation of an implicit heat conduction model with a solver handling matrix system of equations within the explicit Solidity framework

3. Derivation, implementation and validation of a novel contact heat transfer formulation for Solidity. The heat transfer between contacting bodies is solved explicitly or implicitly, the latter achieved by integrating contact heat transfer interaction terms in the matrix system
4. Derivation, implementation and validation of a thermo-mechanical coupling formulation for the finite strain theory in Solidity
5. Validation of three-dimensional thermal fracturing within the FEMDEM method
6. Derivation, implementation and validation of a novel immersed shell-body method for fluid-solid coupling of heat transfer within the Fluidity-Solidity framework
7. Application of the THM coupled capabilities of the Fluidity-Solidity dual framework to the thermal spalling problem.

1.6.3 Thesis Structure

This research work is organised so that the geological waste disposal concept and the importance of coupled processes are introduced in the first chapter in order to justify the choices made in numerical developments throughout the thesis. In the second chapter, the numerical methods employed commercially and in the scientific literature for the modelling of coupled THM processes in the context of geological waste disposal of radioactive waste are reviewed. The advantages and limitations of the Fluidity-Solidity dual framework are discussed and the range of applications suited for the method is highlighted. Development work undertaken on the dual framework is then presented sequentially, each chapter for each key technology building up towards the modelling of coupled THM processes.

Chapter 3 introduces the formulation of a heat conduction model for Solidity with explicit and implicit solvers. Further, a novel thermal contact model to capture heat transfer between contacting solid bodies is presented and its potential for THM coupled applications is discussed. In Chapter 4, a thermo-mechanical coupling formulation for the finite strain theory of Solidity is derived and validated against analytical solution and experimental results. Additionally, several test cases of thermally induced fracturing in three dimensions are performed. Then, the following Chapter 5 finalises the THM coupled approach by putting forward the details, implementation and validation of a novel numerical method to couple heat transfer between the thermo-hydraulic and the thermo-mechanical solvers of the Fluidity-Solidity architecture. Then, the THM coupled approach is applied to the thermal spalling problem in Chapter 6. The investigation aims to demonstrate the potential of the method to provide insight on recent experimental findings whilst improving understanding and predictive capabilities of thermal spalling. At last, the conclusions of the thesis as well as recommendations for further work are presented on Chapter 7.

Chapter 2

Literature Review : Modelling of THM Coupled Processes in the Vicinity of a GDF

Numerical methods are a preferred choice for predicting the behaviour of coupled THM processes, the technologies and methods for improving their accuracy have received a considerable amount of attention in the literature (Jing, 2003, Jing et al., 1993, Manteufel et al., 1993, Noorishad et al., 1984, Stephansson et al., 2004). Coupled processes in geo-systems involve multiple classes of physical and chemical processes into complex configurations. They often result in non-linear behaviours that require specifically developed numerical methods as it is not sufficient to model each process separately. THM processes are of utmost importance for GDF performance assessment, along with chemical processes they determine the long-term behaviour of the three-barriers system (Manepally et al., 2011, Stephansson et al., 2004, Tsang et al., 2004). Thus THM coupled numerical tools are in high demand to support the safety case of GDFs for regulatory approval.

For the past four decades, several international projects led the research on advanced numerical methods for THM modelling such as the ongoing DECOVALEX project (since 1992, decovalex.org), the Yucca Mountain repository project (Manteufel et al., 1993) or the EU-funded THERESA project (THERESA, 2009). They brought together technologies from both the research and private sector in an effort to understand and predict the processes at play, establish a consensus in the results and build up expertise in the modelling procedure. In this literature review, an overview of the main THM coupled processes likely to take place in the buffer and surrounding rock formation of a GDF is given first. Then, a comparative analysis is performed for the most advanced softwares and codes of each category of numerical methods ever employed for THM coupled modelling in the context of radioactive waste repositories. Finally, the numerical framework employed in this research is detailed and the novelty compared to the other existing numerical methods is discussed.

2.1 Coupled THM processes in the vicinity of a GDF

There are in total 6 different THM coupling relations to potentially be taken into account (Manepally et al., 2011):

1. Thermal ➞ Hydrological (T➞H)
2. Hydrological ➞ Thermal (H➞T)
3. Hydrological ➞ Mechanical (H➞M)
4. Mechanical ➞ Hydrological (M➞H)
5. Thermal ➞ Mechanical (T➞M)
6. Mechanical ➞ Thermal (M➞T)

Due to of the extensive number of coupled processes, it is important that their relevance and magnitude for the specific problem studied is understood for the sake of the computational efficiency of the numerical tool.

Of the above mentioned process some may be weakly linked (Manepally et al., 2011) with a straight forward, computationally light implementation that may just modify the input parameters of a given process. For instance, liquids become lighter with rising temperatures (T➞H) thus the temperature may be weakly coupled with the fluid's density.

Other processes have to be strongly linked with a structural implementation in the code, they are often associated with a higher computational cost. For example, fluid flow is strongly coupled with temperature (H➞T) and as a result an additional term is required in the energy equation to model heat transport by convection (refer to equation 5.2).

Finally, for some processes a weak or a strong coupling can apply. This is the case for, hydro-mechanical interactions in fractures (see Section 2.1.4). The decision between the two depends on whether or not the accuracy of a strong coupling and the associated computational cost is necessary for the problem considered. Note that in the next section, the strength of the coupling link will be presented based on how it has been considered in the research.

Couplings may also be unidirectional or one-way coupled e.g. T➞M, as opposed to two-way coupled e.g. T➞M and M➞T (Tsang, 1991). One direction may be considered critical whereas the other may be negligible. For example, in radioactive waste storage related problems the change of temperature controls the thermal expansion and the associated change of stress in the rock mass (T➞M) whereas the modification of the thermal gradient due to mechanical deformation (M➞T) is negligible as overall displacements in the rock are relatively small and slow.

THM processes may be specific to i) non-generic engineered barriers configurations e.g. open-drift with above boiling temperatures (Birkholzer et al., 2005b), ii) certain rock types e.g. clay and iii) the repository phase e.g. glaciation period (Hökmark et al., 2010). This review aims to be generic and therefore is restricted to a) the heating-cooling phase of GDFs for HLW disposal, as this is when and where the THM coupled processes will prevail (see Sequence 3 on Figure 2.1 and Figure 2.2), b) crystalline rocks because their THM behaviour is fundamental and is also found in other rock types, c) with temperatures below boiling not to consider phase change and d) with the standard bentonite buffer. The THM coupled processes considered are summarised on Figure 2.3.

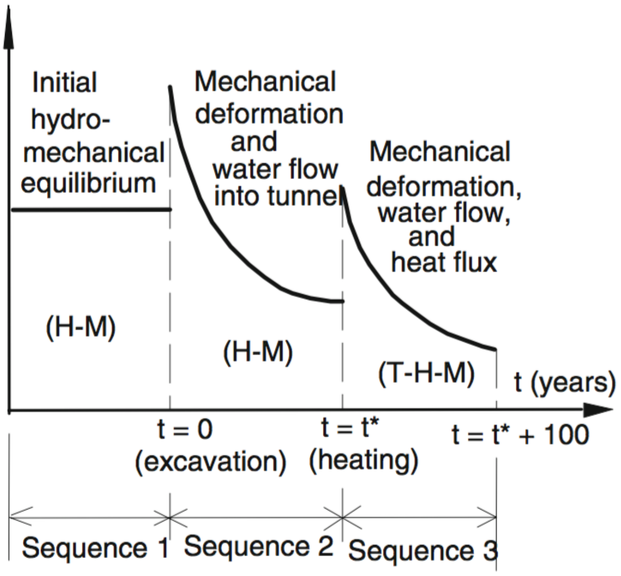

FIGURE 2.1: Different loading sequences in repository performance. Sequence 1: pre-excavation, sequence 2: post-excavation, sequence 3: post-closure heating (Tsang et al., 2009).

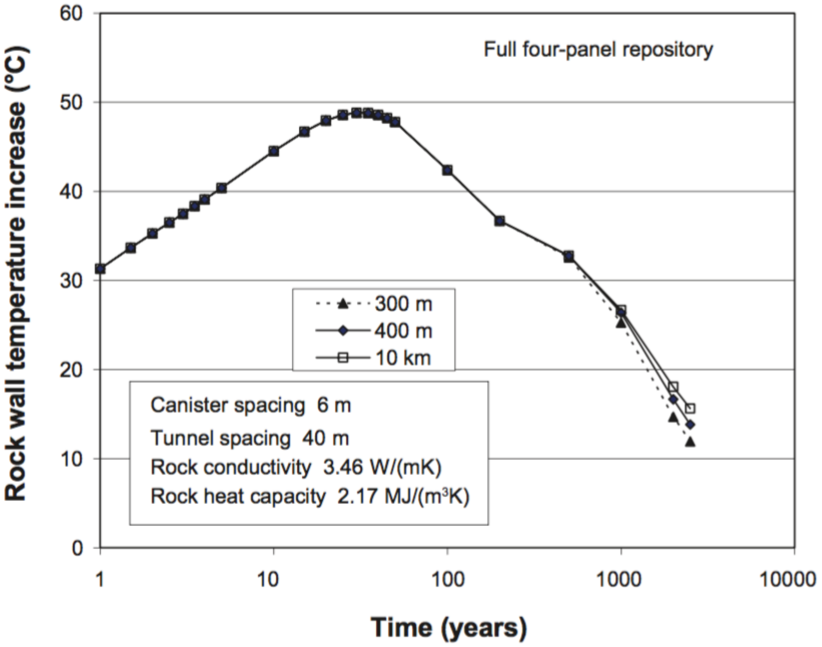

FIGURE 2.2: Rock wall temperature increase for three different repository depth assumptions: 300 m, 400 m and 10,000 m Hökmark et al. (2009).

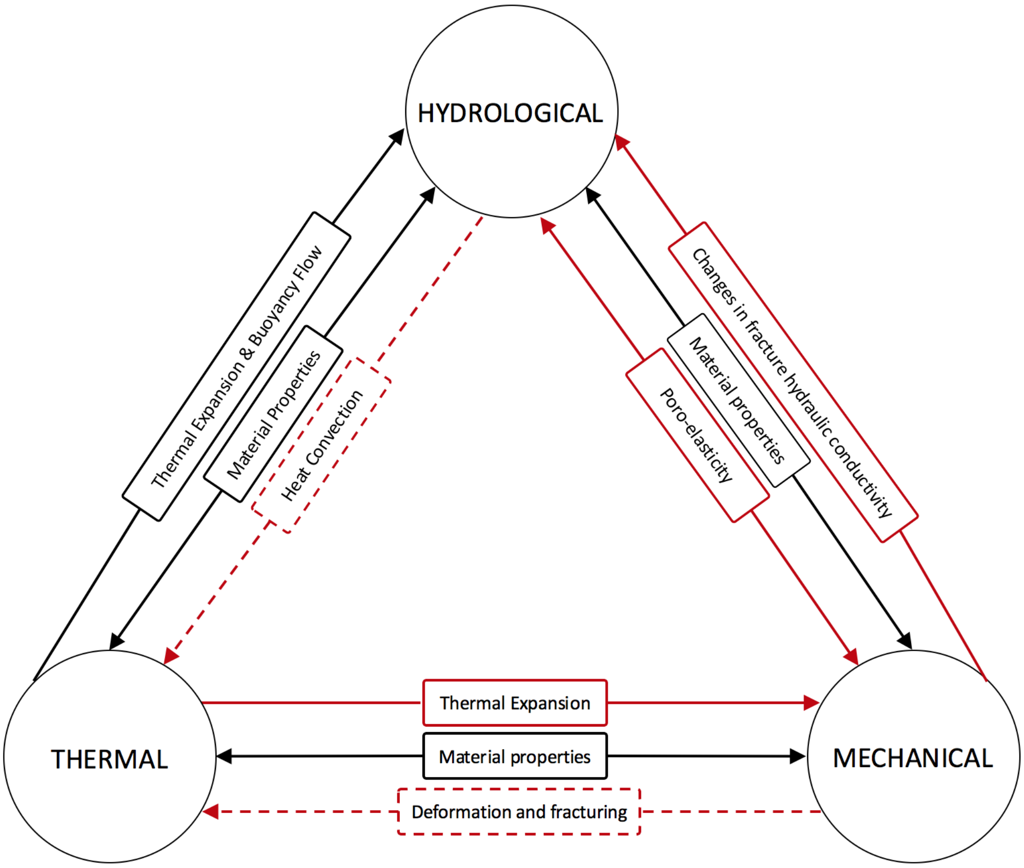

FIGURE 2.3: Diagram of the THM coupled processes considered in this work. Red lines indicate strongly coupled processes and black lines indicate weakly coupled processes. Solid lines indicate couplings of significance in waste repository applications and dashed lines are used for uncertain or of low impact coupled processes. Inspired from Manepally et al. (2011).

2.1.1 Thermal → Hydrological

Thermal expansion and buoyancy flow - Weak Coupling

The emplacement of HLW in a deposition hole of a GDF will generate significant amounts of heat. Heat will gradually transfer to the surrounding rock producing a radial thermal gradient around the deposition hole. The liquid contained in the pores and fractures of the rock will expand as fluids become lighter with increasing temperatures. This process is known as thermal expansion and is a weak coupling because it is achieved by introducing a temperature dependent density in the fluid equation (refer to equation 5.2).

Additionally, as a result of the thermal gradient, the expansion in the fluid will not be uniform and the resulting pressure gradients can induce flows. This process is known as buoyancy flow and will be a consequence of the T→H coupling. Wang and Tsang (1980) and Wang et al. (1981) studied porous media buoyancy flow in single fractures and found that the flow in fractures perturbs the natural buoyancy patterns in crystalline rocks when the fracture hydraulic conductivity is much greater than that of the rock matrix.

Material properties - Weak Coupling
Other fluid properties may also be temperature dependent such as the thermal expansion coefficient or the viscosity of the fluid.

2.1.2 Hydrological → Thermal

Heat convection - Strong Coupling
The hydrology of the domain is able to affect the temperature field when heat is transported via fluid flows, this process is known as heat convection. This is a strongly coupled process as an additional term must be added in the energy equation.

Fluid flow may be induced as a response to the deformation of the rock mass (forced convection, M→H) or induced by buoyancy flow (natural convection, T→H). Thus, heat convection will be the result of indirect couplings M→H→T or T→H→T. However, because of the large time scales in repository applications and due to the overall low permeability of the rock, the natural and forced convection are anticipated to have small implications. Thereby, heat transfer in the rock mass is thought to be dominated by heat conduction (Patrick, 1986, Wilder and Ramirez, 1991).

Material properties - Weak Coupling
The thermal properties of the porous matrix, i.e. heat conductivity and heat capacity are dependent on the saturation in pore water of the rock matrix (de Vries, 1975).

2.1.3 Hydrological → Mechanical

Material properties - Weak Coupling
Studies by Jacobsson and Bäckström (2005) and Feng et al. (2001) indicate that the presence of water reduces the uniaxial compressive strength of rocks. Moreover, Feucht and Logan (1990) observed, a reduction of the frictional strength with an increase of saturation for a sandstone. Similar conclusions were made in experimental and numerical

modelling work performed within the DECOVALEX-THMC project (Bäckström et al., 2008, Hudson et al., 2008). The alterations caused in the rock by interaction with pore water are happening at the microscopic level and can be taken into account by introducing a weak coupling between saturation level and mechanical properties.

Effective Stress - Strong Coupling

The fluid contained in fractures and within the pore space exerts a pressure on the rock matrix influencing its overall stress state. The pore fluid pressure influence on the rock matrix is known as the effective stress thanks to the works of Terzaghi (1925) and Biot (1941) who proposed the theory of consolidation or poro-elastic theory. The effective stress is the H➞M part of the poro-elasticity, it is strongly coupled because an additional term is necessary in the mechanical equation (Biot, 1941).

In large scale radioactive waste repository applications, the pressure is determined by gravity i.e. by the weight of the water column at a given depth. Because hydrostatic pressure is significantly smaller than the in-situ stress in the rock mass, the H➞M is often not considered of importance. Moreover, the fluctuations in the fluid pressure due to thermal expansion of the fluid are often ignored in the modelling (Birkholzer et al., 2005a,b, Koyama et al., 2013). When considered, such fluctuations in the fluid pressure are deemed to be of no consequences (Rutqvist et al., 2009b, 2001b).

Buffer Swelling - Strong or Weak Coupling

The hydration of the bentonite buffer causes it to swell, applying a compressive stress normal to the excavation walls. This will prevent the excavation from yielding under the in-situ and thermal stress. Local saturation levels and fluid pressures are critical for the bentonite swelling process and for the necessary support on the drift walls (Birkholzer et al., 2005a, Glamheden et al., 2010). If the bentonite material is represented in the modelling, swelling is specific to the THM properties of the material (Dueck and Nilsson, 2010) and the implementation of a strongly coupled constitutive model is necessary (Åkesson et al., 2010). If it is not represented and thus the deposition hole is left open, a weakly coupled boundary condition may be applied to emulate the bentonite support pressure, see Figure 2.4.

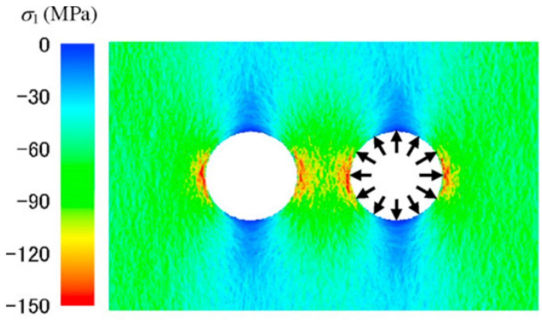

FIGURE 2.4: Maximal principal stress for an unsupported (left) and supported (right) deposition hole. The arrows represent the support pressure boundary condition. Simulation results from Koyama et al. (2013).

2.1.4 Mechanical → Hydrological

Mechanical processes have a direct impact on the hydrologic conditions by changing the configuration of the rock matrix within which the fluid flows. The stress level influences the porosity of the rock matrix and the aperture of fractures. A change in the rock matrix void space correspond to a change in volume of the fluid domain, inducing pressure gradients, fluid flow and changes in the hydraulic conductivity and storativity of the matrix.

M→H in the pores - Strong coupling

Mechanical compression of a porous matrix can lead to a reduction of the pore space, squeezing the interstitial fluid. This compression will change the fluid pressure and induce flows, given that the fluid is considered compressible. This coupling is the M→H part of poro-elasticity (Biot, 1941) and requires a strong coupling link. This is because the mechanical stress must be coupled with the Darcy equation for flow in porous media (Obeysekara, 2018).

M→H in fractures - Strong coupling

Fractures are thought to be the main medium of fluid flow because host rocks are selected to be of relatively low porosity. The coupled hydro-mechanical behaviours of single fractures will be dependent on (Olsson and Barton, 2001, Tsang, 1991):

- aperture – the distance between two fracture walls,
- roughness of the fracture walls,

- mechanical contact area - where stresses may be transferred,
- matedness - how geometrically conforming the fracture walls are,
- spatial correlation - the variation of fracture aperture along the fracture plane,
- tortuosity - the bending of the stream lines over fracture asperities and contact points,
- channelling - fluid flow through preferred pathways inside a fracture of variable aperture,
- stiffness - mechanical properties of the fractures and its response to shear and normal stresses.

Increasing the stress normal to a fracture plane will reduce its aperture while increasing the stress in the horizon of the plane will induce shearing of the fracture. Shearing increases the hydraulic aperture of fractures because it reduces the initial matedness of the rough fracture walls and allows for more fluid to flow. Fracture network properties such as connectivity and orientation of the fractures (Lei, 2016) must also be considered as sets of fractures affecting the tortuosity of flow patterns will be encountered in radioactive waste repository applications. In numerical methods, to assess the impact of fractures on the hydraulic conditions, complex strongly coupled models with explicit representation of fractures can be employed. Alternatively, weakly coupled models approximate the behaviour of a fracture by changing the hydraulic properties of the computational grid element containing the fracture (see Section 2.2).

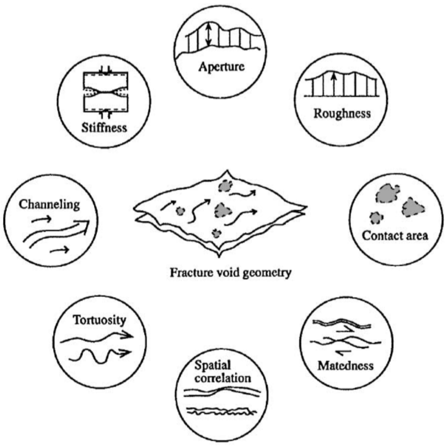

FIGURE 2.5: Mechanical and hydraulic properties of single fractures (Olsson and Barton, 2001).

2.1.5 Thermal → Mechanical

Thermal expansion - Strong coupling

In repository applications, the major heat driven process is the thermal expansion of the rock. Thermal expansion is a strongly coupled process because it requires the mechanical equations to be modified. A typical granite has a coefficient of thermal expansion of 8×10^{-6} $/°C$, for a temperature rise of a $50°C$ a 0.015% of volume change is induced (see Chapter 4). Although a ground surface uplift of up to a few tens of centimetres is expected above the GDF (Hökmark et al., 2010, Wheeler et al., 2015), large thermal stresses will be localised near the deposition holes, as shown on Figure 2.6. This is because significant thermal gradients will only be found within a few tens of meters from the heat source (Hökmark et al., 2010), Figure 2.7.

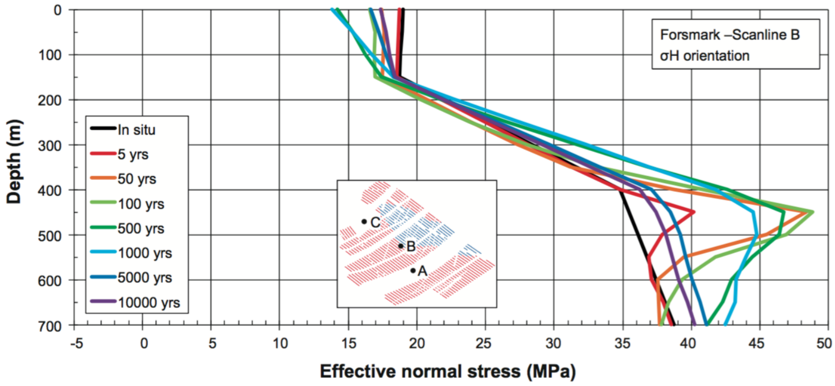

Figure 2.6: Effective normal stress as a function of depth, repository depth is $460m$ (Hökmark et al., 2010).

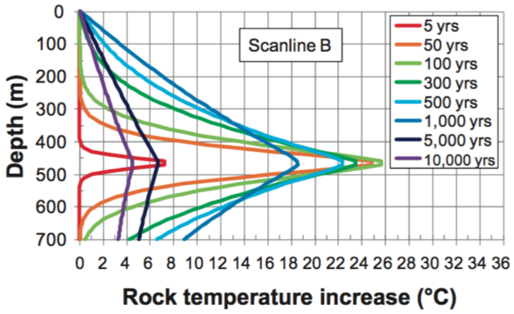

Figure 2.7: Temperature increase as a function of depth, repository depth is $460m$, Hökmark et al. (2010).

In the vicinity of a deposition hole, thermal stresses will influence the porosity of the media and the fracture apertures. For an horizontal deposition hole, the generated horizontal thermal stress is expected to close up vertical fractures and thus to reduce the overall hydraulic transmissivity of the rock (Birkholzer et al., 2005b, Rutqvist et al., 2009b, Rutqvist and Tsang, 2003).

It is important to highlight that directly above the repository structure, due to heating a large zone of shearing (Figure 2.8) is to be expected together with a reduction of the normal stress (Hökmark et al., 2010, Jing et al., 1993, Min et al., 2005) because the rock is more confined laterally than vertically, as shown on Figure 2.9a. The stress ratio (the ratio of vertical stress to horizontal stress) is inherently lower for shallower depths, hence even where the thermal gradient is relatively small, the potential for shearing may not be negligible.

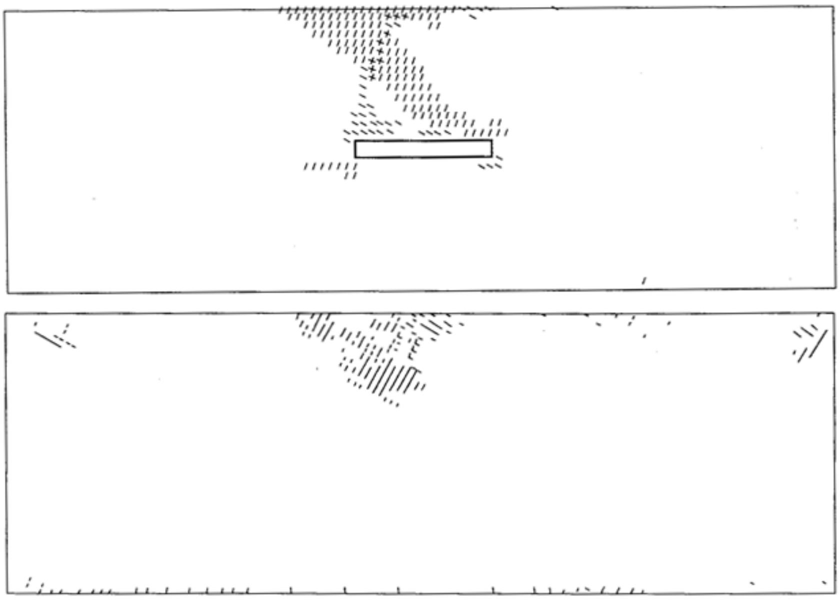

Figure 2.8: Predicted fractured (top) and sheared zone (bottom). The figure represents numerical results of a 2D vertical slice model of a 500x60m repository region at 500m depth (Jing et al., 1993).

Moreover, for shallow depths Hökmark et al. (2010) predicted significant hydraulic transmissivity changes from a factor of 1.5 to 2.5 (Figures 2.9b and 2.9c) depending on the inclination and the location of the considered fractures, this effect being driven by the loss of compression in certain zones, such as shallow regions above the repository (Figure 2.10) or regions not directly above the repository (Figure 2.11).

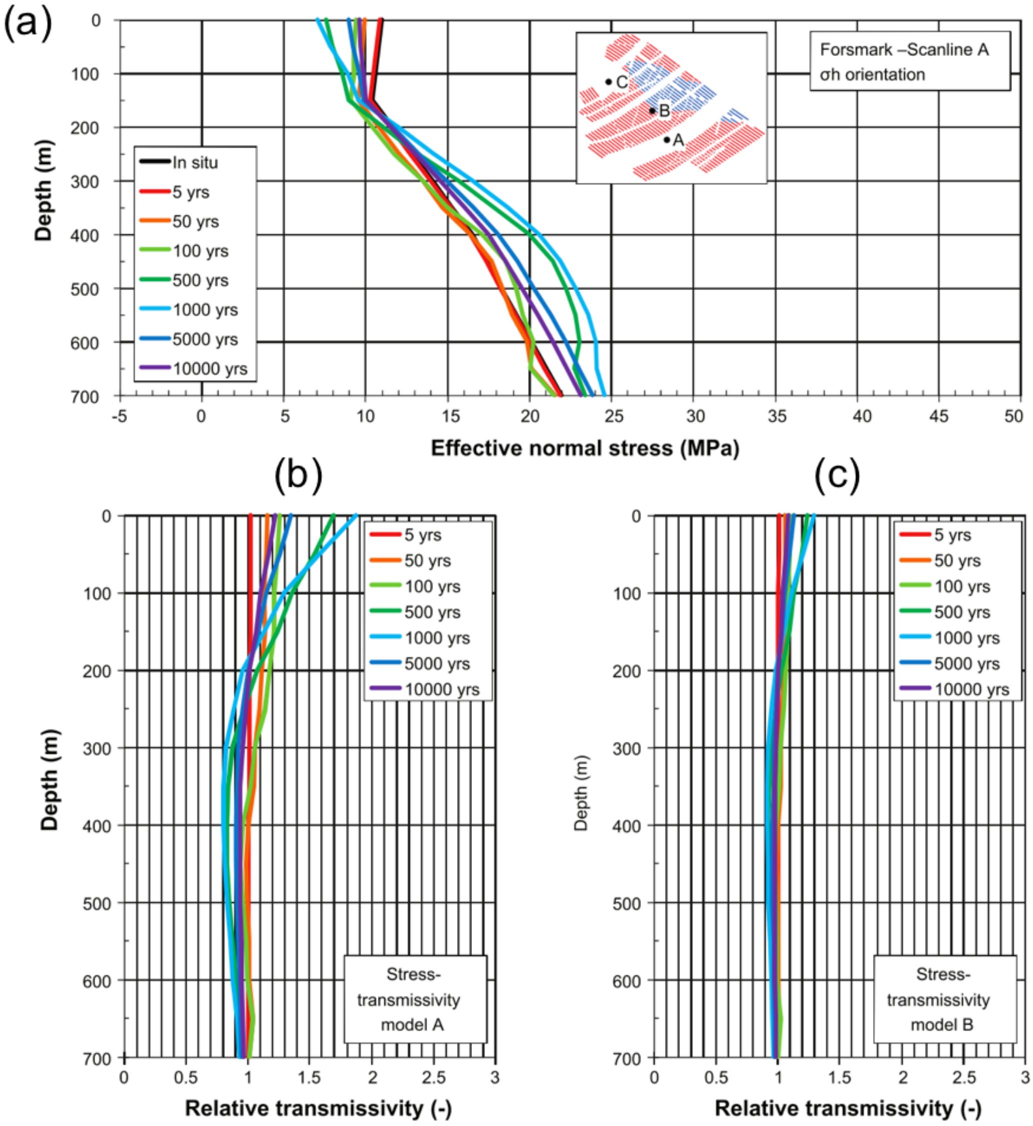

FIGURE 2.9: Effective normal stress as a function of depth (Hökmark et al., 2010).

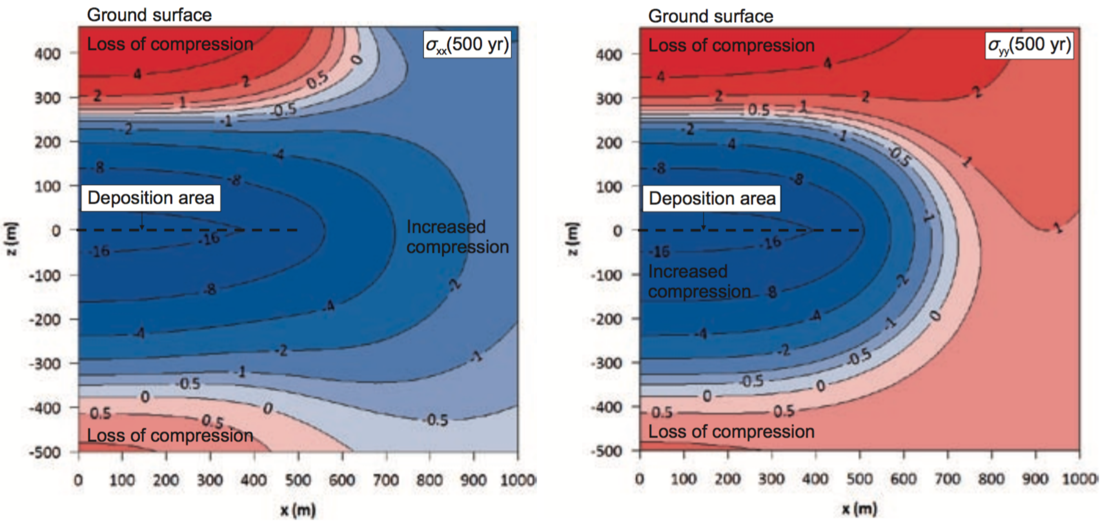

FIGURE 2.10: Thermally induced horizontal stress after 500 years, contours in MPa (Hökmark et al., 2010).

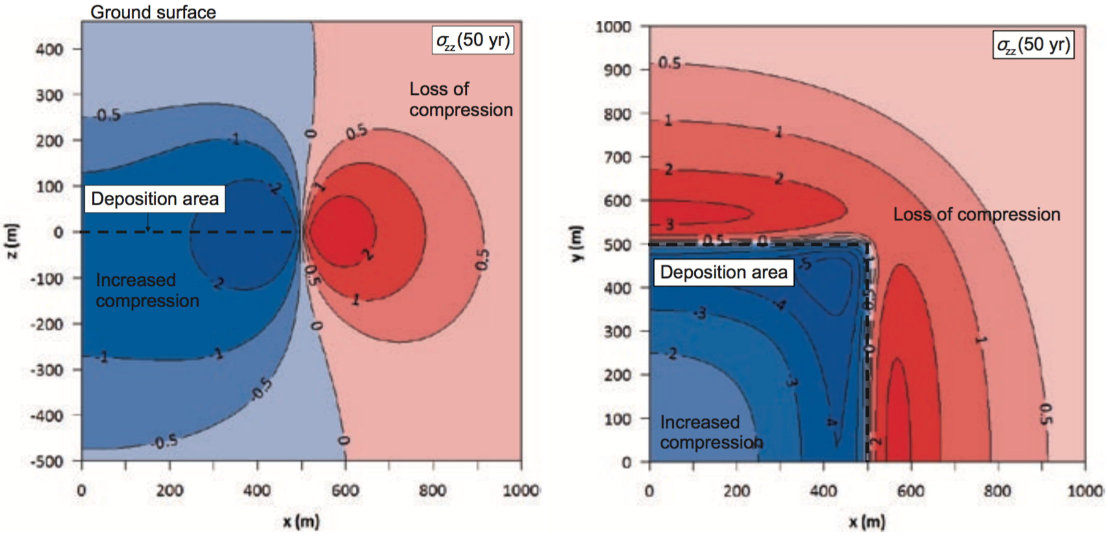

FIGURE 2.11: Thermally induced vertical stress after 50 years, contours in MPa (Hökmark et al., 2010).

Material properties - Weak coupling

Heat influences the thermal properties of the rock (thermal expansion coefficient, heat conductivity and capacity) and its mechanical properties such as the Young's modulus.

2.1.6 Mechanical → Thermal

Deformations in the rock mass - Strong coupling

Large deformations of the rock can modify the temperature field but because the displacements are relatively small and slow, this coupling is largely negligible. It is also worth mentioning that open fractures may act as heat resistances in dry conditions. However, experimental results by Lin et al. (1991) concluded their effect to be insignificant. The implementation of such M→T coupling will be complex as it involves changes in the equations and possibly in the formulation to introduce discontinuities.

Material properties - Weak coupling

Large strain in the rock mass may influence the heat transfer and strain dependent thermal properties may be introduced.

2.2 State of the Art THM modelling

THM processes are based on three main laws of physics that are well established in fluid and solid mechanics: Hooke's law of elasticity of solids, Darcy's law for fluid flow in porous media and Fourier's law of conduction heat transfer.

In numerical modelling the above laws are translated into partial differential equations (PDEs). When the THM processes are coupled, the equations become inter-dependent as each equation takes into account contributions from the others.

The first coupled THM numerical models were available in the early 1980's (Noorishad et al., 1984), models have since seen tremendous evolution in terms of accuracy, sophistication of the coupled processes, model size and number of spatial dimensions. To achieve complete THM coupled modelling of the multi-barrier system a number of key capabilities are shortlisted:

Three-dimensional modelling: using all three dimensions enables the modelling of sophisticated configurations such as with several arrays of deposition holes, revealing processes happening at different scales. It also allows to capture complex THM interactions such as flow patterns in connected fracture networks.

Multiphase flow: the consideration of gaseous and liquid phases flowing in the rock mass and buffer is important for the assessment of radionuclide migration and determinates the bentonite buffer re-saturation time (Dessirier et al., 2017, Glamheden et al., 2010), warrant of the mechanical stability of the deposition hole.

Heterogeneity modelling: rock masses have complex and non-uniform properties that may differ by orders of magnitude. If such heterogeneities are known, it is important that they are taken into account in the modelling input.

Multi-material modelling: to capture the THM behaviour of the multi-barrier system, all materials, i.e. canister, buffer and host rock must be represented. Each of them having their own THM properties and boundary conditions.

Implicit solvers: such solving methods produce results with no time steps restriction, they are said to be unconditionally stable. They are indispensable for post-closure simulations as the time scales at play are relatively large (hundred and up to thousands of years, Figure 2.2). Implicit methods solve a matrix system of equations with complex and computationally expensive mathematical procedures. They are contrasting with explicit methods which approximate the solution with a step by step procedure, using the previous solution in time to calculate the next. Explicit methods are computationally fast but are constrained by a small time step to remain stable which makes them impractical for modelling large time scales.

Discontinuity modelling: Single fractures and fracture networks present in the rock mass are one of the most influent features on safety (Tsang, 1991). They have a considerable impact on the stress response of the rock mass (Rutqvist et al., 2009a, 2001a), on the potential of radionuclides transport (Neretnieks, 2006) and on the bentonite full saturation time (Dessirier et al., 2017).

Numerically, there are two ways to represent fractures:

Effective continuum models. Fractures are not represented explicitly, their THM properties are homogenized on a representative volume which approximates their behaviour (Guvanasen and Chan, 2000, Oda, 1986, Stietel et al., 1996). Weak regions (elements) can be inserted pre-simulation to represent pre-existing fractures or inserted during simulation if specific conditions are satisfied according to a damage model (Drucker-Prager, Mohr-Coulomb, ...).

Discontinuum models. Fractures are represented explicitly and so is their deformation, propagation and coalescence.

A common conclusion of comparative modelling studies (Birkholzer et al., 2005b, Millard et al., 1995, Rutqvist et al., 2001b), is that there is excellent agreement on the calculated temperature fields, a relatively good agreement on the overall stress fields but an inconsistency in the hydraulic results. This is due to the specificities of the fundamental differences in numerical approaches and algorithms employed to model fractures.

Because the discontinuities are one of the most challenging aspect of THM modelling, in this section a continuum/discontinuum classification is adopted as presented by Jing (2003). The reviewed numerical methods are those employed commercially and in the scientific literature for the modelling of coupled thermo-hydro-mechanical processes in the context of geological waste disposal of radioactive waste. This review aims to compare i) the adequacy of a particular method to address a specific class of THM problems and ii) the number of key capabilities that a given code possess.

Strong couplings are the most difficult to implement and they reflect on how the code is structured whereas weak couplings may be incorporated within any code with relatively small implementation efforts. Therefore the review looks in priority at what strong couplings are present if not all and how they are implemented. For a broader insight on numerical codes employed in rock mechanics, refer to the reviews of Jing (2003) and Bobet et al. (2009). Details on the numerical codes mentioned in the following sections and throughout the thesis are available in the Appendix.

2.2.1 Continuum Methods

2.2.1.1 The Finite Element Method

The Finite Element Method (FEM) is certainly the most popular numerical method in continuum rock mechanics. The FEM divides the domain into a finite number of smaller volumes formed by an assembly of nodes called elements. The most common finite elements are three-noded triangles (2D) and four-noded tetrahedrons (3D). The PDEs are approximated at the element level using an approximation function or “shape function” that distributes the unknowns depending on the element topology. A global matrix system is obtained, the system is then discretized in time and may be solved implicitly or explicitly.

The FEM is the most employed by the numerical modelling community and thus benefits from mature technologies, expertise and well verified commercial codes (ABAQUS, COMSOL), research open source platforms (OpenGeoSys, Fluidity, IC-FERST, CAST3M) and specialised research codes (CODE-BRIGHT, COMPASS, FRACON, MOTIF, ROCMAS, THAMES).

2.2.1.2 The Finite Difference Method

Another popular continuum method and also the oldest (Jing, 2003) is the Finite Difference Method (FDM, Wheel 1996). In the FDM, to obtain the solution of the objective function, the partial derivatives of the PDE are replaced with differences of the objective function over spatial intervals in all directions. like in FEM, the domain is spatially discretized with a computational grid. For a given point of the grid the differences are evaluated with his direct neighbours in all directions. In FDM the grid is most often regular to conveniently evaluate the differences. This makes the FDM computationally effective and also the simplest formulation to implement. Moreover, the local approximation of the FDM makes the method suited to non-linear mechanical behaviours. However, solving on non regular grids or representing discontinuities explicitly is not straightforward with the FDM. The only purely FDM code in this review is the commercial software FLAC3D developed by Itasca Consulting Group.

2.2.1.3 The Cellular Automata

The cellular automata (CA) was originally developed for micro-fracturing of rocks under uniaxial compression (Feng et al., 2006). It is inspired by the self-organization theory in biology which holds that the state of a cell depends on itself but also on the state of its neighbours. When the CA is applied to rock mechanics the domain is discretized into cells and the state of the rock is formed by the interaction of information between adjacent cells at the previous time step, with information such as stress or displacement. Thus, the behaviour of a cell is considered to be local and this approach is in essence a finite difference method. The numerical code associated with the CA is the Cellular Automata: EPCA, developed at the Chinese Academy of Sciences, Wuhan.

2.2.1.4 The Finite Volume Method

The Finite Volume Method (FVM) employs the same direct approximation of PDEs as of the FDM but in an "integral sense" (Jing, 2003), the objective function is expressed at the finite volume level which is a small volume surrounding each nodal point of the computational grid. In the FVM, the formulation stays the same for every number of spatial dimensions. The divergence terms in the PDE are converted from volume to surface integrals and are evaluated as fluxes entering and leaving the finite volume and its neighbours. The FVM is particularly suited to fluid dynamics because the flux approach yields straightforward conservation as opposed to the FEM where normal gradients may differ across element interfaces and local mass conservation may be lost. Another advantage of the FVM is that the formulation may easily be used on unstructured grids. The computer codes with finite volume capabilities are Fluidity, IC-FERST, QPAC, TOUGH2 and TOUGH-FLAC.

2.2.1.5 The Boundary Element Method

The Boundary Element Method (BEM, Wilde and Aliabadi 1999), is a continuum method which represents solid domains by their boundaries, this makes them particularly suited to fracturing problems. The initiation, growth and coalescence of fractures is represented explicitly by the boundary elements.

On one hand, the advantage of the BEM is that only the domain boundaries need to be discretized, making the BEM more computationally effective than other continuum methods. On the other hand, the boundary dominant approach of the BEM encounters difficulties to model complex domain effects (Lee and Jing, 2004) such as i) initial/residual stress, ii) fields and body forces, iii) non-linear deformations and iv) non-linear distribution of domain properties. Lee and Jing (2004) proposed an approach to overcome domain integral limitations of the BEM by supporting it with FEM or FDM type of methods. Thus, the BEM alone is not a suitable method to capture material heterogeneities and their space, time, strain, temperature, saturation and fluid pressure variability. Boundary element methods are based on implicit solvers but to capture fracture propagation they may rely on an explicit scheme, see details of the BEM software FRACOD.

2.2.2 Discontinuum Methods: Discrete Element Methods

The term Discrete Element Method (DEM) includes all numerical methods that treat a given problem as an assembly of interacting bodies or discrete elements. In rock mechanics problems, the blocks of rock carved out by the fracture system are the discrete elements and fractures are represented by the voids separating the blocks.

DEM methods may be split into two different categories based on their time-marching procedure: Explicit DEM and implicit DEM also known as Discontinuous Deformation Analysis (DDA).

The modelling of a dead-end fracture contained within a rock body is not necessarily within the ability of DEM methods. Yet this may be achieved with a sub-discretization of the discrete elements with finite elements, this technology is available in advanced explicit DEM codes (Solidity, UDEC, 3DEC) and in the DDA (Jing, 1998).

2.2.2.1 Explicit DEM

The explicit DEM (Jing and Stephansson, 2007) or distinct element method as introduced by Cundall and Strack (1979) has an explicit time integration scheme with the deformation of discrete elements handled in an FDM fashion. As explained by Lei (2016) and Jing and Stephansson (2007), the basic computational sequence of an explicit DEM can be summarised with the following steps:

1. A contact detection algorithm identifies and updates all the contacts between the different elements composing the discrete system.
2. The contact forces are computed based on the contact configuration and contact law.
3. The resulting acceleration induced by the contact force is calculated with Newton's second law for each discrete element.

4. The displacements of each discrete element are obtained with a step by step time integration scheme (explicit) and positions of the elements are updated.

2.2.2.2 Discontinuous Deformation Analysis

In the Discontinuous Deformation Analysis (DDA, Shi 1992) the transient solution is obtained by implicitly solving a matrix system. The fundamental difference with explicit DEM is that instead of using Newton's second law for each element, the DDA minimizes the potential energy of the whole element system by solving it implicitly.

In the explicit DEM, contacts are resolved by interpenetration of elements resulting in a contact force (Munjiza and Andrews, 2000) while in the DDA, interpenetration is prevented by contact springs that are taken into account in the matrix system (Jing, 1998).

The DDA has thermo-mechanical (Jiao et al., 2015) and hydro-mechanical coupling capabilities (Jing et al., 2001, Morgan and Aral, 2015). However to the author's knowledge, the DDA has not been applied yet in the context of Geological Disposal Facilities and there is no prevalent numerical code regrouping THM coupling capabilities.

2.3 Current Research background

2.3.1 Fluidity & IC-FERST

Fluidity (Piggott et al., 2008) is an Open Source multiphase computational fluid dynamics code capable of numerically solving the Navier-Stokes equation on unstructured finite elements in all dimensions. IC-FERST is the branch of Fluidity developed mostly for reservoir simulation in two and three dimensions. IC-FERST can solve multiphase Darcy equations for porous (Gomes et al., 2017, Jackson et al., 2015, Salinas et al., 2018) and fractured rock media (Su et al., 2015).

An attractive feature of the Fluidity framework is the unstructured adaptive mesh optimization (García et al., 2011), able to locate spatial heterogeneities and to dynamically refine the mesh locally. This allows the necessary precision to be focussed where needed rather than re-generating a uniformly sized mesh, saving previous computational time and memory. For instance, the heterogeneity may be the maximum pressure gradient, the fluid phase interface (Jackson et al., 2015, Salinas et al., 2018) or pre-defined fractures (Obeysekara et al., 2018, Su et al., 2015), see Figure 2.12.

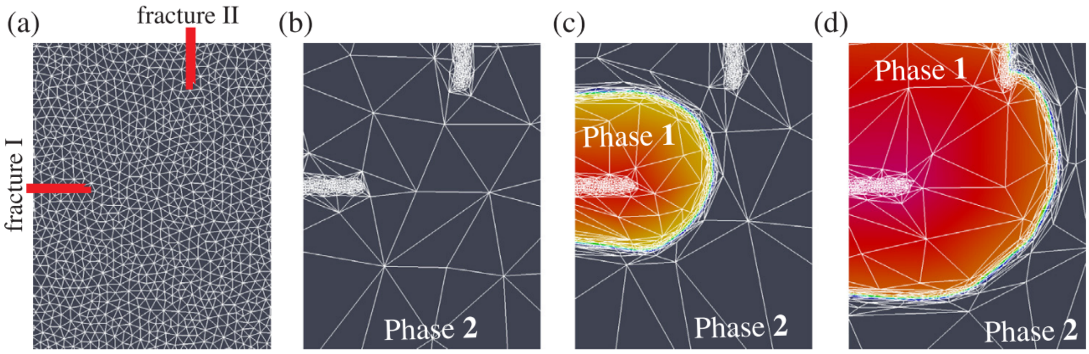

FIGURE 2.12: Adaptive mesh two-phase flow calculation: water injection (phase 1) in a oil saturated (phase 2) porous media. (a) At the start of the simulation, the domain of an oil-saturated fractured porous rock is discretised using a fixed unstructured mesh; (b) after an initial mesh adaptation, mesh is refined at the fracture and coarsened in the matrix; (c) penetration of the water phase with additional refinement at interface between the two fluid phases; (d) further displacement of oil with water and flow into fracture. Note: the red line in (a) indicates the position of pre-existing fractures (Obeysekara et al., 2018).

2.3.2 Solidity

Solidity is an Open Source, multi-purpose explicit mechanical solver based on the combined Finite-Discrete Element Method (FEMDEM or FDEM). The FEMDEM was pioneered by A. Munjiza in the 1990's at Swansea University and later on at Queen Mary University (Munjiza, 2004, Munjiza and Andrews, 2000, Munjiza et al., 1999, 2003, 1995). A fruitful collaboration between A. Munjiza (Queen Mary University), J.P. Latham and J. Xiang (Imperial College London) began in 2004 (Latham et al., 2013, Munjiza et al., 2010, Xiang et al., 2009a,b).

The FEMDEM combines the continuum based FEM with the discontinuum based explicit DEM. In FEMDEM multi-body interactions can be handled with a classic explicit DEM approach whilst each body is discretized with finite elements and solved accordingly. The DEM part handles behaviours such as translation, rotation, mechanical or thermal contact interactions while the FEM part calculates internal stress, strain, fracturing or heat transfer. The contact interaction between discrete bodies is calculated via the penalty function method (Munjiza, 2004, Munjiza and Andrews, 2000) relying on an infinitesimal overlap between the contacting discrete meshes to calculate the contact forces. Development efforts at Imperial College led to the release of a three-dimensional version with a large strain FEM formulation (Xiang et al., 2009a), a plasticity model (Karantzoulis, 2017) and fracture models (Guo, 2014, Guo et al., 2013, Lei, 2016, Lei et al., 2016).

When using the fracture model joint elements are inserted between triangular (2D) or tetrahedral finite elements (3D) pre-simulation as shown on Figure 2.13.

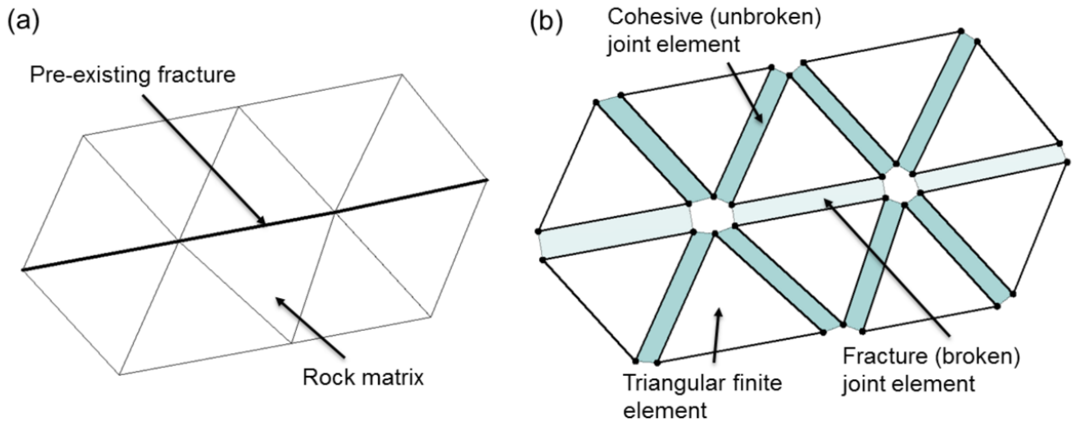

Figure 2.13: Insertion of joint elements in 2-D: (a) continuous FEM formulation (b) discontinuous FEM formulation. From Lei (2016)

The joint elements are 4 noded in 2D and 8 noded in 3D. They may be cohesive (i.e. unbroken) to represent the intact rock or broken to represent new or pre-existing fractures. While in tension, joint elements act as springs until they are broken which is analogous to the approach used in the DDA and in the explicit DEM codes 3DEC and UDEC. While in compression, joint elements will not penetrate each other significantly thanks to the contact force calculated with the penalty function method (Guo, 2014).

For the non-linear fracturing process, a cohesive zone model (Munjiza et al., 1999) handles the transitional elasto-plastic behaviour of joint elements (Figure 2.14).

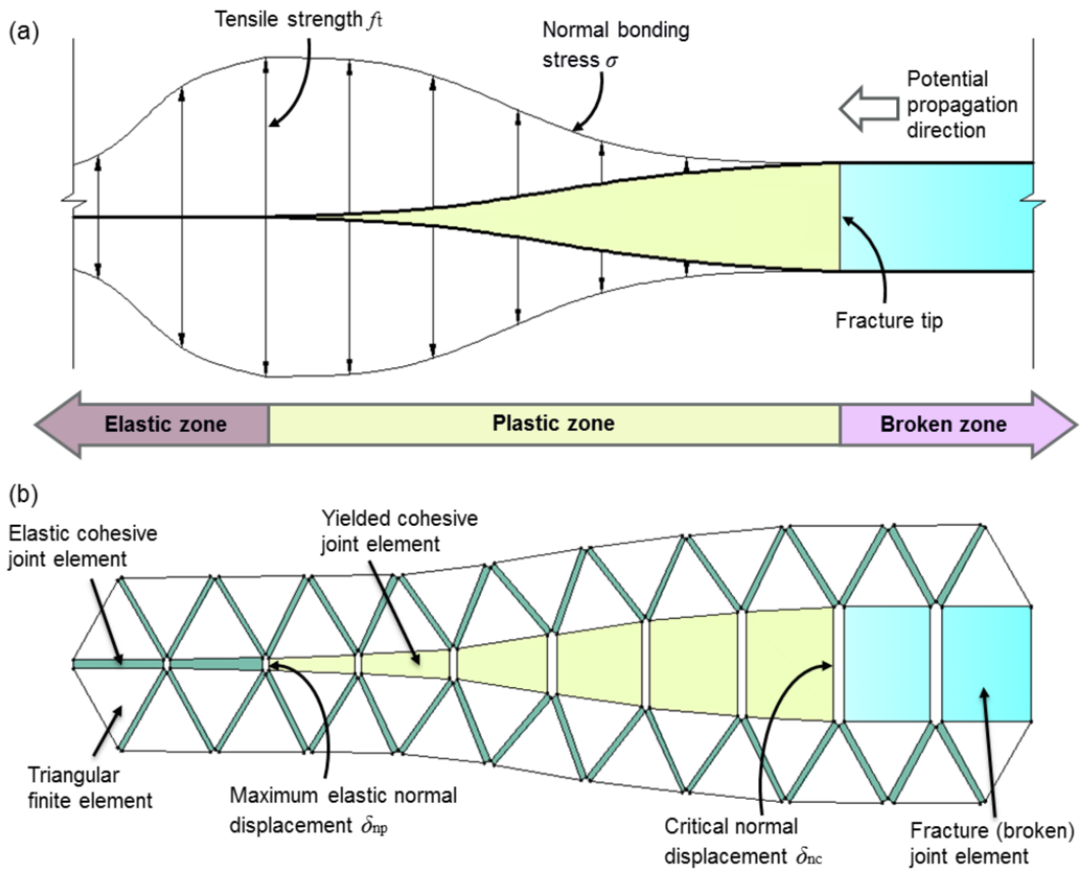

FIGURE 2.14: Cohesive zone model. (a) Schematic model of the transition between elastic, plastic and broken zones, (b) representation of the cohesive zone model in FEMDEM (Lei, 2016).

With such developments Solidity can capture the heterogeneity of the stress distribution in fractured rocks, the interaction of rock matrix blocks and the deformation, propagation and coalescence of rough fractures (Lei et al., 2017a, 2015, 2014, 2017c).

With regard to the above mentioned, it must be noted that inserting joint elements changes the formulation of Solidity from hybrid (discontinuum-continuum, respectively DEM and FEM) to fully discontinuum. When using the fracture model Solidity can be considered as an explicit DEM with the only difference being that the deformation of single elements are handled with FEM and not FDM (refer to section 2.2.2.1). Additionally, note that in the thesis Solidity will be employed without the fracture model and on a single solid body. In that case, the DEM part of the hybrid method is not recruited and Solidity will be referred as a continuum method (See Chapter 4).

2.3.3 Fluidity-Solidity: A Hybrid Approach

Simultaneously, while the the above features were in development and validation, an architecture for the joint use of Fluidity and Solidity was created (Viré et al., 2012). This led to the modelling of fluid-structure interaction with immersed body type of methods (Viré et al. 2012, 2015, 2013 and Yang et al. 2016, Figure 2.15), gas-rock interaction for blasting (Yang et al. 2017, Figure 2.16) and fluid-fracture/matrix interactions including flow in fractured rock (Obeysekara et al. 2017, 2018, Figure 2.17) and hydro-fracturing (Obeysekara 2018, Figure 2.18). The Fluidity-Solidity architecture will be employed to model coupled THM processes in porous, partially saturated fractured rock media.

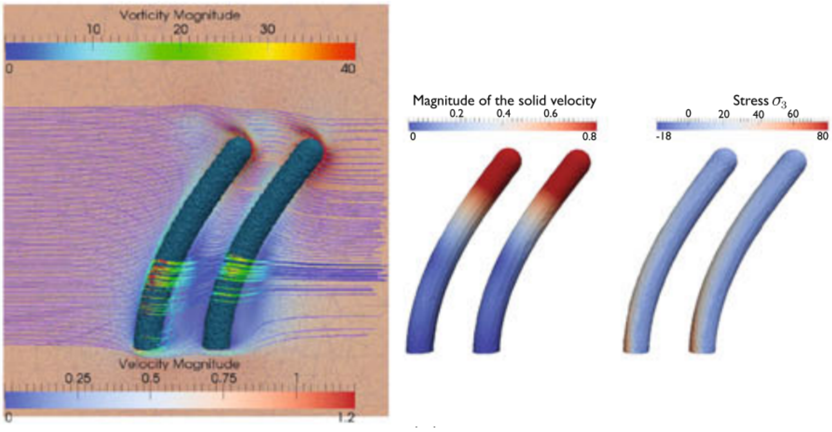

FIGURE 2.15: Flow past two flexible fibres (Viré et al., 2012).

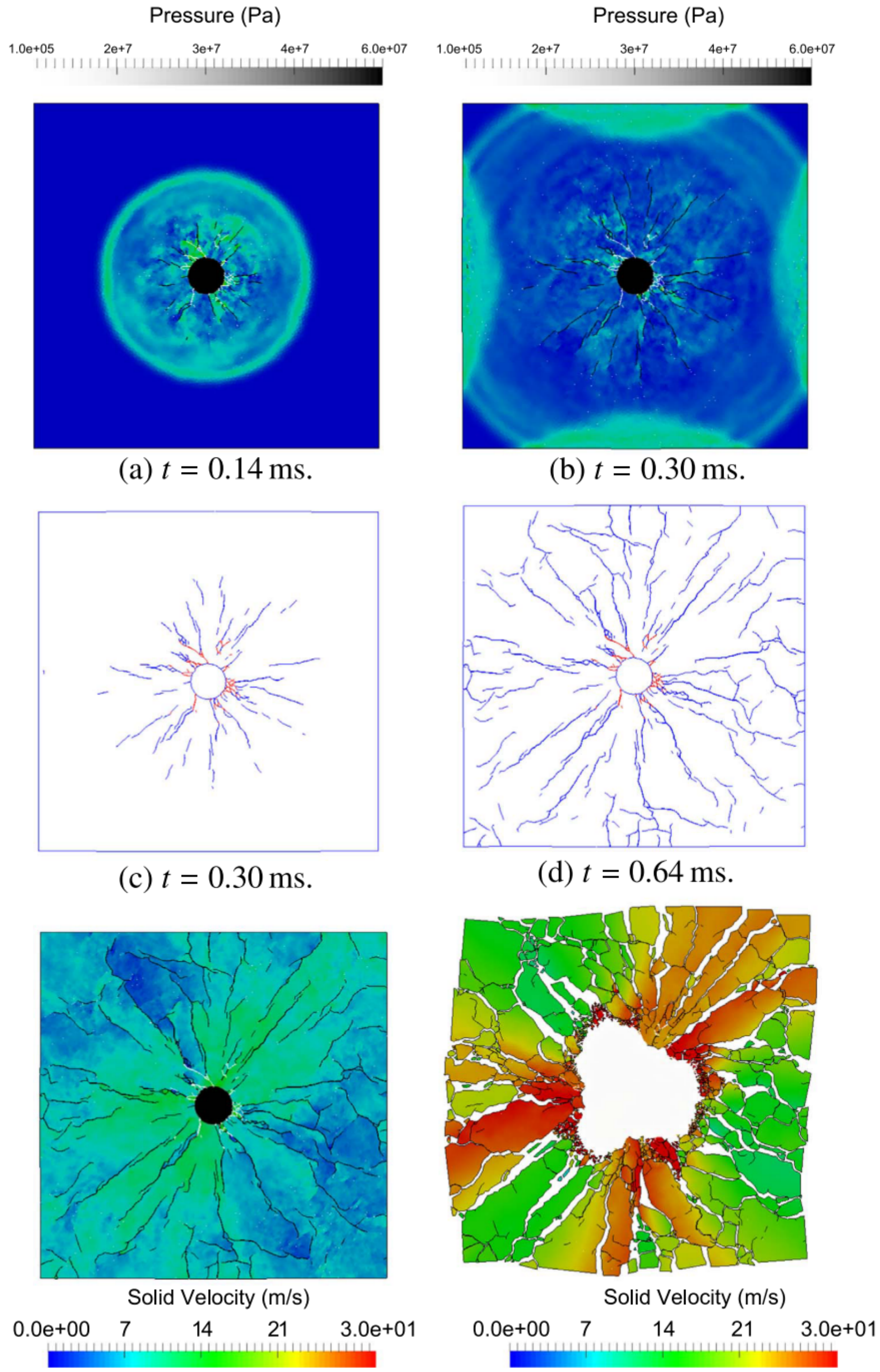

(a) $t = 0.14$ ms. (b) $t = 0.30$ ms.

(c) $t = 0.30$ ms. (d) $t = 0.64$ ms.

(e) $t = 0.64$ ms. (f) $t = 5.70$ ms.

FIGURE 2.16: The snapshots of the fluid pressure (a,b), fracture pattern (c,d) and solid velocity (e,f) inside the square rock block submitted to a blasting charge (Yang et al., 2017).

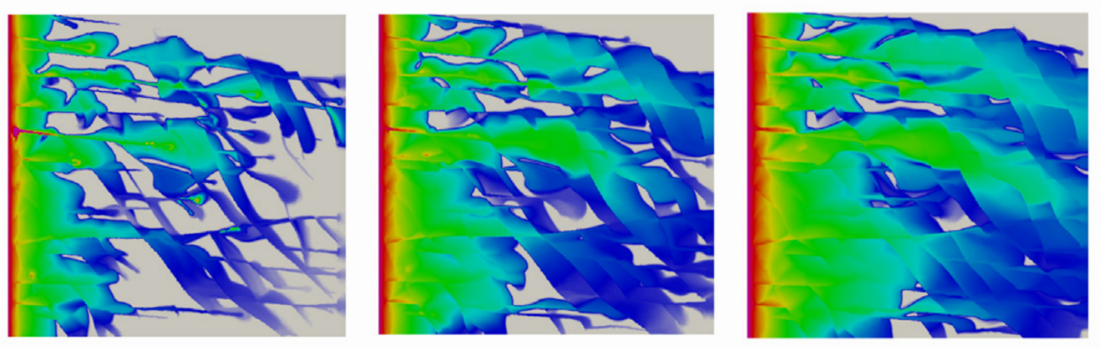

Figure 2.17: Evolution of the water saturation field during the injection of water into an initially oil-saturated fractured rock under in situ stress conditions (Obeysekara et al., 2018).

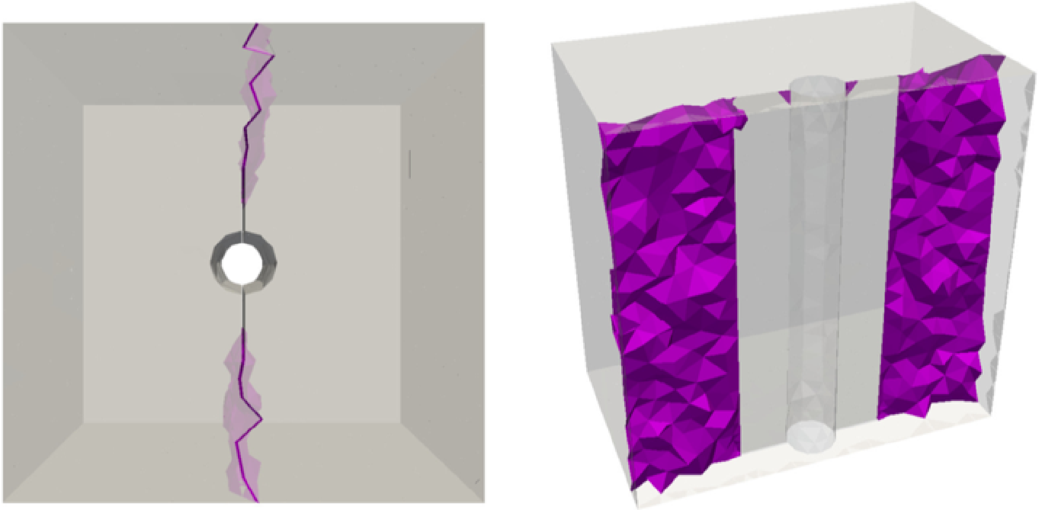

(A) Top view (B) Side view

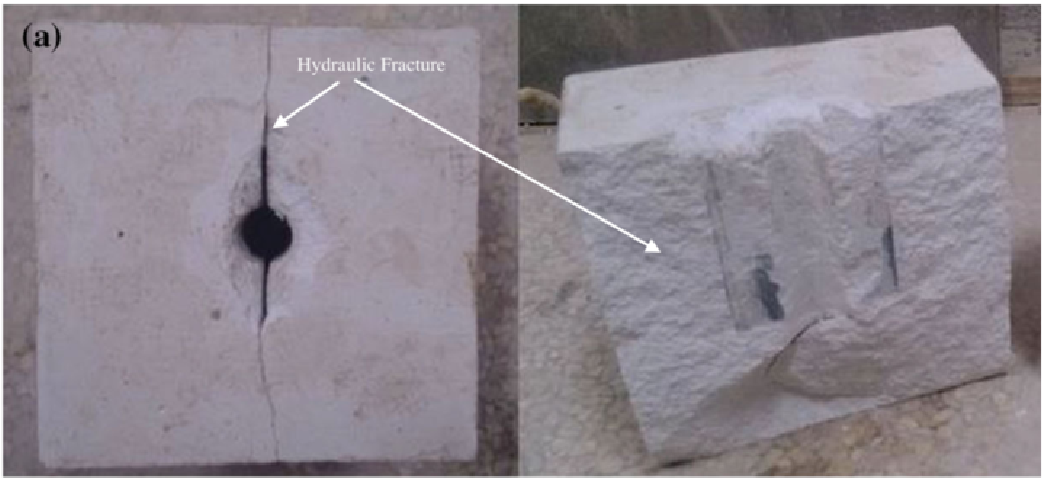

Figure 2.18: Validation against experiments of fluid injection into a borehole with pre-existing flaws (Obeysekara, 2018).

2.4 Comparison of THM Numerical Codes

2.4.1 Key numerical features, comparative table 2.1

3D: Three dimensionality is common and largely tested within the FEM, FDM, FVM and the explicit DEM but in the less popular DDA and BEM, advanced methods and codes for THM modelling are mostly in two dimensions. It is however likely that 3D technology for the DDA and BEM will emerge in the next few years.

Multiphase flow: In domain continuum methods, there is no obstacle to the implementation of multiphase flow, therefore this feature will be found in any mature software. On the contrary, for discontinuum approaches modelling the hydraulic continuum across discrete elements is challenging and this results in limited features in comparison to FEM or FVM. At the exception of 3DEC, in the BEM and the DEM, only single phase fluid flow in fractures is considered. Note that multiphase flow in fractures is not a relevant feature to implement.

Heterogeneity and multi-material modelling: Except for the BEM, all methods can handle multi-material configurations and heterogeneous properties in the rock mass. In continuum methods, the discontinuities between materials are at best represented with slide lines, planar boundaries or insertion of joint elements. All those techniques are aimed at preserving the continuum approach at the material's interfaces. This makes continuum methods less flexible than their discontinuum counterparts, where materials may be apart or contacting and interact within all degrees of freedom. However, preserving the continuity allows straight-forward formulations for THM behaviours across material interfaces such as porous media flow across the bentonite-rock interface.

Approach		**Method**	**Code Name**	**3D**	**Multiphase flow**	**Heterogeneity Modelling**	**Multi-material Modelling**
Continuum	Domain	FEM	ABAQUS	✓	✓	✓	✓
			CASTEM				
			CODE-BRIGHT				
			COMPASS				
			COMSOL				
			FRACON				
			MOTIF				
			OpenGeoSys				
			ROCMAS				
			THAMES	✗			
		FDM	EPCA	✓	✗		
			FLAC3D		✓		
		FVM	QPAC				
		FDM & FVM	TOUGH2-FLAC3D				
	Boundary	BEM	FRACOD	✗	✗	✗	✗
Discontinuum		Explicit DEM	3DEC, UDEC	✓		✓	✓
		DDA	✗	✗			

TABLE 2.1: Comparative table of numerical codes - Key numerical features. See the Appendix for details on numerical codes.

2.4.2 Fracture Capabilities, comparative table 2.2

Continuum Domain Methods

The FEM, FDM, FVM and CA may be referred to as continuum domain methods because their space discretization takes place over the whole domain considered as opposed to continuum boundary methods or BEM where only the boundaries of the domain are discretized.

Most continuum domain numerical codes (ABAQUS, THAMES, ROCMAS, MOTIF, FRACON, COMSOL and FLAC3D) have implemented features to allow the explicit representation of discontinuities with interface elements, joint elements, slide lines or areas with specific boundary conditions. However such solutions are limited because:

(i) they are defined manually when setting up the simulation and there is no automatic scheme to recognize new discontinuities and their interactions,

(ii) they can only take into account several discontinuities as they will encounter difficulties when dealing with many intersecting fractures,

(iii) they are limited to small displacements and/or rotation because of the continuum domain formulation.

Hence they may only be used to represent important discontinuities in the rock mass with a predictable behaviour such as faults or major fractures. Complex, explicit fractures and fracturing cannot be represented with domain continuum methods with the exception of the extended finite element method (X-FEM, Fries and Belytschko 2010).

The X-FEM is a feature existing in the FEM and the only rigorous approach for fracturing in continuum domain methods and it can be found in ABAQUS and CAST3M. In the X-FEM, a discontinuous function enriches the FEM continuum solution (Figure 2.19a). The enrichment allows for the solution to be approximated on cut elements and therefore no re-meshing is required to model a fracture which is a significant computational advantage. Since the void space created by a fracture is not spatially discretized (Figure 2.19b), an additional approach is necessary for hydraulic calculation across the discontinuity. Such approach for hydro-mechanical coupling exist with finite volumes (Figure 2.20, Wang 2015) but it has not yet being applied to the THM modelling of GDFs.

(A) Closed fracture (B) Open fracture

FIGURE 2.19: Fracture representation in the X-FEM method, enriched elements are marked in grey. Modified from Fries and Belytschko (2010).

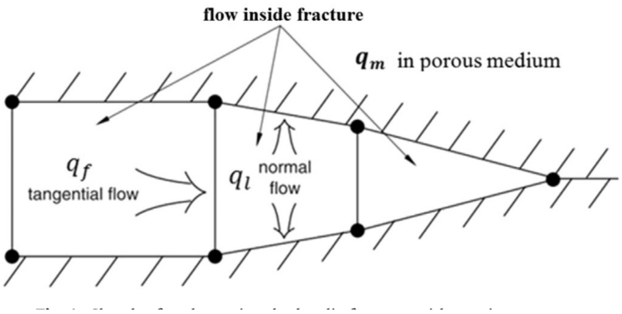

FIGURE 2.20: Fluid flow inside a fracture with the X-FEM (Wang, 2015).

Continuum Boundary Methods

Regarding continuum boundary methods or BEM, the two-dimensional FRACOD is perhaps the most widely recognized code available and it has proven to be a rigorous method for the quantitative assessment of fractures (Hudson et al., 2008, Rutqvist et al., 2009a, 2001a,b). It is worth mentioning that, the formulation employed by FRACOD in Rutqvist et al. (2009a) included a sub-critical crack growth model for creep, a time-dependent process. Results only showed insignificant sub-critical crack growth during the first 100 years of thermal loading. This suggests that a sub-critical crack growth model is not necessary for THM analysis of the heating up phase.

With FRACOD, the BEM can perform THM coupled analysis and allow fluid-fracture interaction with a finite volume approach as shown on Figure 2.21. Yet this will be limited to linear behaviour within the domain as it goes with the BEM. In conclusion, the BEM is an accurate tool for purely fracturing problems and a method of interest for benchmarking on fundamental test cases with other methods.

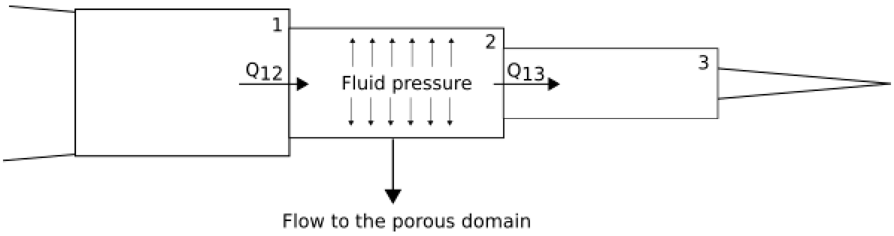

FIGURE 2.21: Subdivision of the fracture into flow elements in FRACOD, after Shen et al. (2013).

Discontinuum Methods

The power of all DEM approaches resides in their capacity to handle relatively large number of fractures. However, the modelling of coupled THM processes in DEM have not reached the same level of maturity compared to their continuum counterparts.

The DEM framework is not designed to embed hydraulic capabilities, their implementation is not straight forward and as a result DEM codes are often limited to fluid flow modelling in fractures, neglecting porous media flow and fracture-matrix flow interactions (Jing, 2003).

With the explicit DEM codes UDEC (Itasca, 2018) and 3DEC (Cappa et al., 2008) a discretization with tetrahedral and triangular elements can be employed, analogous to the DDA. Fluid flow in fractures is resolved with a network of fluid domains located where there is a contact between grid points or between an edge and a grid point (Figure 2.22). Domains are considered of uniform pressure and fluid may flow from one domain to its neighbours, creating a discrete network of interconnected pressure points solved by FDM. The flow is governed by the pressure differential between neighbouring domains and is controlled by the aperture of the rock joint according to the cubic law for flow between parallel plates (Snow, 1965).

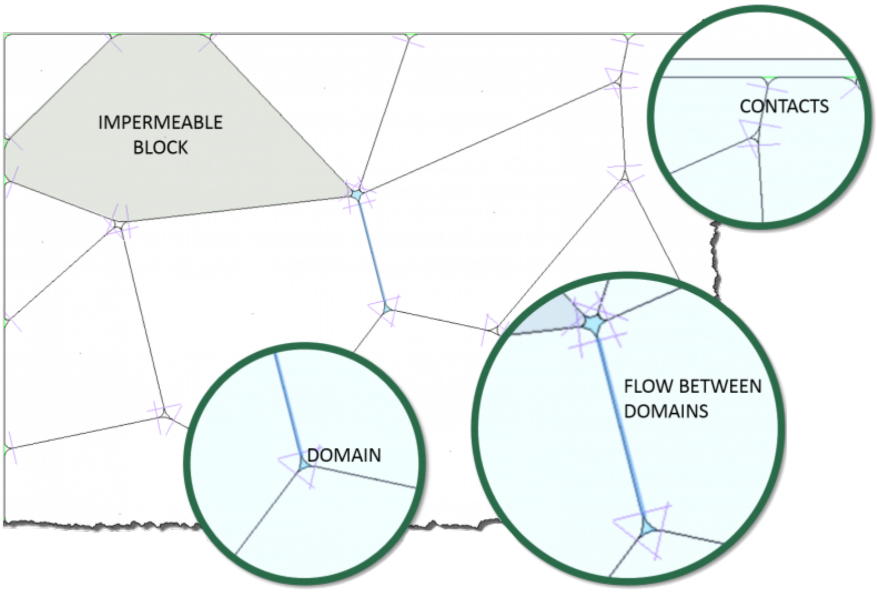

FIGURE 2.22: Fluid flow in-between discrete elements (Itasca, 2018)

Blocks are considered impermeable in UDEC but a steady-state pore pressure may be applied as a boundary condition. In 3DEC saturated porous media flow is considered within the rock blocks. In both codes, the fluid flow model may be coupled with the mechanical and thermal models (Cappa et al., 2008, Karatela and Taheri, 2018) with the compressibility and the thermal expansion of the saturated material being taken into account.

A similar approach for flow in-between discrete elements has been presented in the DDA (Jing et al. 2001, Figure 2.23) and with FVM instead of FDM (Morgan and Aral 2015, Figure 2.24). Due to its implicit nature, the DDA can easily integrate the flow equations in a matrix form compatible with the pre-existing matrix system of mechanical equations.

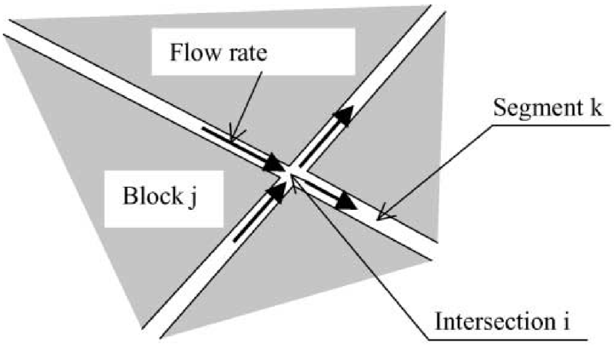

FIGURE 2.23: Flow in an idealized fracture intersection (Jing et al., 2001).The flow is calculated for each segment with the differential pressure of each intersection and the segment's mean aperture.

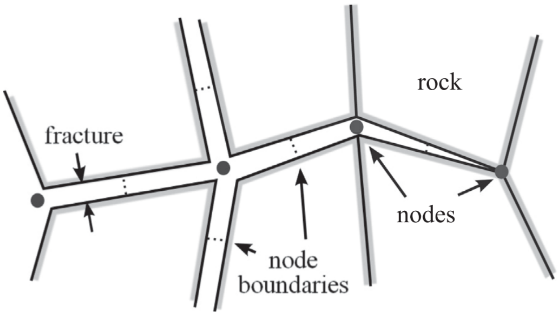

Figure 2.24: Flow in idealised fractures with the FVM method (Morgan and Aral, 2015).

Conclusion

The advantage of the domain methods for discontinuity modelling, is that they do not need to model the fractures explicitly. Effective continuum models are of low computational cost and offer a good approximation of the overall behaviour of a continuum, given that their calibration is accurate. Consequently, the continuum approach is the preferred choice for large scale THM modelling.

With the X-FEM, the BEM and the DEM, the explicit fractures and fracturing processes are fully represented. However, when introducing a fracture, a supplementary spatial discretization for the fluid domain is necessary. It may be achieved with a discrete system of nodal pressures solved by FDM (UDEC, 3DEC) or with volumes domains in the fractures solved by FVM (X-FEM, FRACOD, DDA).

To achieve accuracy in the prediction of fractures in the discontinuum methods, the mesh needs to be sufficiently refined otherwise results may be inconsistent from one mesh to the other and the hydraulic results drawn from fracture aperture and geometry will be impacted. Refining the mesh will come at a greater computational cost. Therefore, when modelling fractured rock masses, the preferred scale of DEM methods is substantially smaller to that of continuum methods.

This will not apply for the BEM due to its boundary approach, nor for the X-FEM because the enrichment function cuts across the elements and thus the mesh does not need to be as fine as for the discontinuum methods.

Additionally, the X-FEM conserves the FEM continuum quality in the intact rock domain (Wang, 2015) and fluid equations can be solved traditionally with FEM. Thus together with the FVM approach in the fractures (Figure 2.20) the fluid domain is not interrupted and fluid interactions between rock matrix and fractures can be captured (Wang, 2015).

Approach		Method	Code Name	Fracture representation	Fracturing process	H→M Fluid-fracture interaction
Continuum	Domain	FEM	ABAQUS	Damage model & X-FEM	X-FEM	✗
			CASTEM	Damage model & X-FEM	X-FEM	✗
			CODE-BRIGHT	Damage model	✗	✗
			COMPASS	✗	✗	✗
			COMSOL	Damage model & insertion of planar internal boundaries	✗	✓ Fluid pressure on planar boundaries
			FRACON	Insertion of joint elements	✗	✗
			MOTIF	Insertion of joint elements	✗	✓ Fluid pressure on joint elements
			OpenGeoSys	Damage model	✗	✗
			ROCMAS	Damage model	✗	✗
			THAMES	Insertion of joint elements	✗	✗
		FDM	EPCA	Damage model & insertion of weak elements	✗	✗
			FLAC3D	Damage model & insertion of weak elements	✗	✗
		FVM	QPAC	Damage model	✗	✗
		FDM & FVM	TOUGH2-FLAC3D	Damage model & insertion of weak elements	✗	✗
	Boundary	BEM	FRACOD	Boundary elements	✓	✓ Effective stress at the boundary
Discontinuum		Explicit DEM	3DEC UDEC	Void space between discrete elements	Bonded Block Model	✓ Effective stress on element boundary
		DDA	✗			

TABLE 2.2: Comparative table of numerical codes - Fracture capabilities. See the Appendix for details on numerical codes.

2.4.3 THM coupling capabilities, comparative table 2.3

T➞H: Buoyancy flow is driven by the changes of fluid density as a function of temperature, this a weakly coupled process and any code with a porous media flow formulation will be able to include this coupling. As a result the codes lacking this coupling are found in the discontinuum category.

H➞T: Heat convection also depends on the fluid capabilities and thus is generally found within continuum methods.

M➞H: Fractures affect the permeability of the domain, they may be dealt with using effective continuum models or with discontinuum models which are all based on the cubic law (Snow, 1965). The poro-elastic M➞H coupling i.e. the deformation in the porous rock inducing fluid pressure changes is omitted in the review.

H➞M: The changes in pore pressure will be converted into effective stress onto the rock matrix and the deformations in the rock will induce changes in porosity and pore pressure. This part of the poro-elastic theory is standard in continuum rock mechanics and thus can be found in all continuum codes. For the BEM (FRACOD) and the DEM codes the fluid pressure is only applied at the fractures. Pressure is exerted on the boundary elements for the BEM and on the discrete elements boundaries for the DEM. As seen previously in the DEM, flow is most often solved in-between the discrete elements only. Based on the cubic law we can predict that the fluid pressure will only be significant where there is a fracture opening. Consequently this approach will only be appropriate for low porosity rocks, where fluid flow in the pores can be neglected.

T➞M: Thermal expansion is naturally being taken into account in all codes as it is the most important source of mechanical stress in the vicinity of a deposition hole.

M➞T: The influence of deformation of the rock mass on the temperature field is of no significance in radioactive waste repository applications and in a large majority of rock mechanics and engineering problems.

Approach		**Method**	**Code Name**	**T→H Buoyancy flow & Thermal expansion**	**H→T Heat convection**	**M→H Fracture dependent permeability**	**H→M Poro-elastic formulation**	**T→M Thermal expansion**	**M→T**
Continuum	Domain	FEM	ABAQUS	✓	✗	Effective continuum	✓	✓	✗
			CAST3M		✓				
			CODE-BRIGHT		✗				
			COMPASS		✗				
			COMSOL		✓				
			FRACON		✗				
			MOTIF		✓				
			OpenGeoSys		✗				
			ROCMAS		✗				
			THAMES		✗				
		FDM	EPCA		✗				
			FLAC3D		✗				
		FVM	QPAC		✓				
		FDM & FVM	TOUGH2-FLAC3D		✓				
	Boundary	BEM	FRACOD	✗	✗	Cubic Law	✗		
Discontinuum		Explicit DEM	3DEC, UDEC	✓	✓				
		DDA	✗	✗	✗				

Table 2.3: Comparative table of numerical codes - THM coupled processes. See the Appendix for details on numerical codes.

2.4.4 Coupling scheme, comparative table 2.4

The choice of an implicit time marching procedure for solving thermal and hydraulic equations is mandatory for post closure applications and this is a unanimous choice among the codes reviewed. For mechanical solvers however, the type of time integration scheme varies.

Fully implicit solvers are the only ones able to solve THM coupled equations monolithically. The THM matrix equations may be assembled in a single system and solved at once. However, this will only be possible if all three THM processes have the same time step requirements. If not, the smallest time step must be used to preserve stability. This is computationally inefficient in GDF performance applications because mechanical equations usually require a much smaller time step for convergence than the thermal and hydraulic equations (Rutqvist et al., 2009b). The difference will be of several orders of magnitude if non-linearity is considered. Consequently, even for codes with fully implicit solvers a sequential approach is always preferred to model THM coupled processes (CODE-BRIGHT, OpenGeoSys, ROCMAS).

The sequential solution procedure iterates between thermal, hydraulic and mechanical processes and an appropriate time step is chosen for each process. Thermal and hydraulic equations have similar time steps requirements and thus they may be solved monolithically, making solely the TH-M coupling sequential. In TH-M sequential couplings the fluid and thermal equations are solved first. Then, coupling informations such as fluid pressure and temperature are transferred to the mechanical solver which will iterate for a fixed number of times or until mechanical equilibrium is attained. This configuration is employed by all of the THM codes in this review, illustrations of the sequential iteration process are presented on Figure 2.25, and in the Appendix on Figures A.2 and A.5. Thermal and/or hydraulic equations are solved in one temporal loop and mechanical equations in another. Between each loop, the necessary information is passed on to ensure the THM coupling.

Due to the size of the mechanical time step in explicit methods, running a real time simulation cannot be considered for large time scales. For instance, time increments for 3D explicit DEM fracturing of rock are typically below the micro-second. To reduce the mechanical computational time, a quasi-static approach known as the ”load factoring” technique may be employed (Prior, 1994). Developed for the modelling of the industrial metal forming process, it allows for the mechanical loading boundary conditions to be applied over a much shorter period of time compared to reality, reducing the simulation time. It must be noted that if the loading speed is increased too much, the kinetic energy generated will affect the solution, creating stress waves and instabilities. To avoid such scenario, the undesirable kinetic energy generated by the load scaling must be kept several orders of magnitude under the strain energy (Prior, 1994).

This approach is particularly relevant to repository modelling as the post closure temperature variations are of the order of hundred degree Celsius over a hundred years, inducing a slow deformation rate. The quasi-static approach is a mandatory route for all codes relying only on explicit geomechanics (COMPASS, MOTIF, FLAC3D, TOUGH-FLAC, 3DEC and UDEC). Implicit geomechanics codes may iterate on the real time scales of interest if they consider linear geomechanics but if non-linear mechanical behaviours such as fracturing are taken into account (X-FEM, DDA, BEM) the time-step will be so constrained that performing a real time simulation will become impractical and the quasi-static route must be followed.

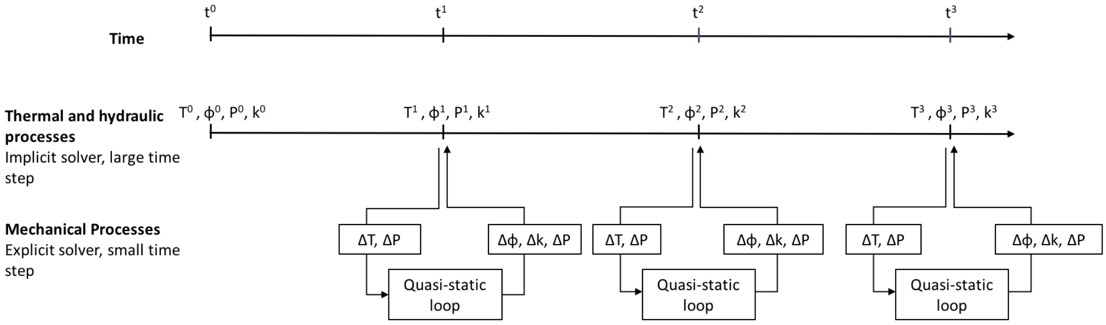

FIGURE 2.25: Illustration of the sequential, quasi-static iteration for the coupling of THM processes in Fluidity-Solidity. With T the temperature, ϕ the porosity, k the hydraulic conductivity and P the fluid pressure.

Approach		**Method**	**Code Name**	**Thermal equilibrium**	**Coupling scheme**	**Time marching procedure**		
						Thermal	**Hydraulic**	**Mechanical**
Continuum	Domain	FEM	ABAQUS	✓	M/S	I	I	I or E
			CAST3M	✗	S			I
			CODE-BRIGHT	✓	M/S			I
			COMPASS	✓	S			E
			COMSOL	✗	M/S			I
			FRACON	✓	M/S			I
			MOTIF	✓	S			E
			OpenGeoSys	✓	M/S			I
			ROCMAS	✓	S			I
			THAMES	✓	M/S			I
		FDM	EPCA	✓	S			I
			FLAC3D	✓	S			E
		FVM	QPAC	✓	M/S			I
		FDM & FVM	TOUGH2-FLAC3D	✓	S			E
	Boundary	BEM	FRACOD	✓	S			I and E
Discontinuum		E DEM	3DEC, UDEC	✗	S			E
		DDA	✗	✓	S			I

Table 2.4: Coupling scheme, comparative table. ‘M’ stands for Monolithic and ‘S’ stands for Sequential. ‘I’ stands for Implicit and ‘E’ for Explicit. See the Appendix for details on numerical codes.

2.5 Conclusion and Novelty of the Proposed Hybrid Approach

Continuum domain numerical codes possess the most rigorous THM modelling capabilities, they are the most efficient for the assessment of larger scale, overall processes occurring in the rock mass.

Given that the same effective continuum model is used, domain continuum methods are expected to agree on the results. Whereas for the continuum boundary and discontinuum methods, due to the variety of their formulation, in depth calibration work will be necessary for them to produce consensual results on the fracturing and hydraulic processes. Nevertheless, their explicit representation of fractures is necessary to understand the THM behaviour of fractured rock masses at the small scale.

The Fluidity-Solidity architecture enables a powerful hybrid method that has a continuum approach for the fluid processes and discontinuum approach for the mechanical processes. This allows for the best representation to be used for each of the processes.

Moreover, the Fluidity-Solidity framework has the following capabilities:

- Three-dimensionality
- Multiphase flow in fractures and porous matrix
- Heterogeneity modelling
- Multi-material modelling
- All THM couplings listed in Table 2.3

Assembling all the above capabilities in one numerical tool results in a computationally expensive method. The mesh requirements to represent fractures accurately in Solidity adds to the necessary fluid mesh refinement at the fractures positions for the sake of conservation of the Fluidity-Solidity interpolation. In consequence, this hybrid method is appropriate to small scale problems where the accuracy of THM coupled processes in fractured porous media is necessary and the associated numerical cost is justified. This explains the choice of the thermal spalling problem as the application case of this research work.

The literature review thereby confirms the novelty and potential of the planned programme of code development to successfully bring the thermal processes within the Fluidity-Solidity framework and to create a new versatile platform for THM applications with special emphasis on small scale processes.

Chapter 3

Thermal Developments in the Geomechanical Solver

3.1 Finite Element Equations for Heat Transfer

This section contains the finite element theory for heat transfer that has been the basis for code development in Solidity. The presented conduction heat transfer equations are modified from Nikishkov (2010).

3.1.1 Problem Statement

Let us consider an isotropic body with non-temperature dependent heat transfer properties, the equation of heat transfer has the following form:

$$\rho C\frac{\partial \mathbf{T}}{\partial t} - (\frac{\partial \mathbf{q}^x}{\partial x} + \frac{\partial \mathbf{q}^y}{\partial y} + \frac{\partial \mathbf{q}^z}{\partial z}) = \mathbf{Q} \tag{3.1}$$

With $\mathbf{q}^x, \mathbf{q}^y, \mathbf{q}^z$ components of the heat flow through an unit area; $\mathbf{T}$ is the temperature field; ρ is the material density ; C is the heat capacity; $\mathbf{Q}$ is the inner heat generation vector and t is time. According to Fourier's law, the components of the heat flow can be expressed as follows:

$$\mathbf{q}^x = -\overline{\overline{\kappa}}\frac{\partial \mathbf{T}}{\partial x}, \quad \mathbf{q}^y = -\overline{\overline{\kappa}}\frac{\partial \mathbf{T}}{\partial y}, \quad \mathbf{q}^z = -\overline{\overline{\kappa}}\frac{\partial \mathbf{T}}{\partial z} \tag{3.2}$$

With $\overline{\overline{\kappa}}$ the thermal conductivity matrix, the combination of the above expressions yields

$$\rho C \frac{\partial \mathbf{T}}{\partial t} + \nabla \cdot (\overline{\overline{\kappa}} \nabla \mathbf{T}) = \mathbf{Q} \tag{3.3}$$

The following formulation is easily derived with anisotropic heat transfer properties however, constant properties are used to keep the equations simple. If an isotropic thermal conductivity is considered $\overline{\overline{\kappa}} = \kappa \mathbf{I}$ with $\mathbf{I}$ the identity matrix, we have

$$\rho C \frac{\partial \mathbf{T}}{\partial t} + \kappa \nabla^2 \mathbf{T} s = \mathbf{Q} \tag{3.4}$$

Which may also be written as

$$\rho C \frac{\partial \mathbf{T}}{\partial t} + \kappa \, (\frac{\partial^2 \mathbf{T}}{\partial x^2} + \frac{\partial^2 \mathbf{T}}{\partial y^2} + \frac{\partial^2 \mathbf{T}}{\partial z^2}) = \mathbf{Q} \tag{3.5}$$

3.1.2 Finite Element Discretisation

The domain V is divided into finite elements connected at nodes, the boundary of the domain is noted Γ. Interpolation functions are used for calculation of temperature inside each finite element composed of n_e nodes:

$$\mathbf{T} = \mathbf{N}\{T\}, \quad \mathbf{N} = [N_1 \; N_2 \; ... \; N_{n_e}], \quad \{T\}^\top = \{T_1 \; T_2 \; ... \; T_{n_e}\} \tag{3.6}$$

In this formulation, $\mathbf{T}$ is the matrix of temperature distribution inside the finite element, $\{T\}$ is the vector of temperatures at the nodes, $\mathbf{N}$ is the interpolation or shape function vector. The spatial gradient of the shape function $\mathbf{B}$ is defined as follows:

$$\begin{pmatrix} \frac{\partial \mathbf{T}}{\partial x} \\ \\ \frac{\partial \mathbf{T}}{\partial y} \\ \\ \frac{\partial \mathbf{T}}{\partial z} \\ \end{pmatrix} = \begin{bmatrix} \frac{\partial N_1}{\partial x} & \frac{\partial N_2}{\partial x} & \cdots \\ \\ \frac{\partial N_1}{\partial y} & \frac{\partial N_2}{\partial y} & \cdots \\ \\ \frac{\partial N_1}{\partial z} & \frac{\partial N_2}{\partial z} & \cdots \\ \end{bmatrix} \{T\} = \mathbf{B}\{T\} \tag{3.7}$$

Applying the Galerkin discretisation gives:

$$\int_V \left[\rho C \frac{\partial T_i}{\partial t} - (\frac{\partial q_i^x}{\partial x} + \frac{\partial q_i^y}{\partial y} + \frac{\partial q_i^z}{\partial z}) \right] \; N_i \; dV = \int_V Q_i \; N_i \; dV \tag{3.8}$$

Where $i = 1, \cdots, n_e$ represent each set of equations in the finite element. Applying expression 3.7 and the divergence theorem yields

$$\int_V \rho C \frac{\partial T_i}{\partial t} \, N_i \, dV + \int_V B_{ij} \, \{q_i\} \, dV = -\int_\Gamma \{q_i\}^\top \{n_i\} \, N_i \, d\Gamma + \int_V Q_i \, N_i \, dV \tag{3.9}$$

With

$$\{q_i\}^\top = \{q_i^x \quad q_i^y \quad q_i^z\}, \quad \{n_i\}^\top = \{n_i^x \quad n_i^y \quad n_i^z\} \tag{3.10}$$

Where $\{n_i\}$ is an outer normal to the surface of the body. Also, it is worth noting that

$$\{q_i\} = -k \, B_{ij} \, T_i \tag{3.11}$$

After insertion of expression 3.11 into equation 3.9, the following boundary conditions are introduced:

- Initial temperature $T(x, y, z, t = 0) = T_0(x, y, z)$
- Dirichlet boundary condition $T(x, y, z, t) = T_{\mathcal{D}}(x, y, z, t)$ with $T_{\mathcal{D}}$ the specified temperature on $\Gamma_{\mathcal{D}}$
- Neumann boundary condition $\mathbf{q}^x n^x + \mathbf{q}^y n^y + \mathbf{q}^z n^z = \mathbf{q}_{\mathcal{N}}$ with $\mathbf{q}_{\mathcal{N}}$ the specified heat flow on $\Gamma_{\mathcal{N}}$
- Convection boundary condition $\mathbf{q}^x n^x + \mathbf{q}^y n^y + \mathbf{q}^z n^z = h(T_e - T_s)$ on Γ_{cv}, T_s being the solid temperature on the boundary, T_e the temperature of the environment in which the solid is placed and h is the convection coefficient
- Contact heat transfer boundary condition $\mathbf{q}^x n^x + \mathbf{q}^y n^y + \mathbf{q}^z n^z = \mathbf{q}^c$ on the contact area Γ_c

We obtain

$$\begin{aligned} &\int_V \rho C \, \frac{\partial T_i}{\partial t} \, N_i \, dV + \int_V \kappa \, B_{ij} \, B_{ji} \, T_i \, dV \\ &= \int_{\Gamma_{\mathcal{N}}} q_i^{\mathcal{N}} \, N_i \, d\Gamma + \int_{\Gamma_{cv}} q_i^{cv} \, N_i \, d\Gamma + \int_{\Gamma_c} q_i^c \, N_i \, d\Gamma + \int_V Q_i \, N_i \, dV \end{aligned} \tag{3.12}$$

Finally we write the condensed matrix expression of the finite element model:

$$M_{ij} \, \dot{T}_i + K_{ij} \, T_i = \mathcal{B}_i^{\mathcal{N}} + \mathcal{B}_i^{cv} + \mathcal{B}_i^c + \mathcal{Q}_i \tag{3.13}$$

With

$$
\begin{aligned}
M_{ij} &= \int_V \rho C \; N_i \; N_j \; dV \\
K_{ij} &= \int_V \kappa \; B_{ij} \; B_{ji} \; dV \\
\mathcal{B}_i^{\mathcal{N}} &= \int_{\Gamma_{\mathcal{N}}} q_i^{\mathcal{N}} \; N_i \; d\Gamma \\
\mathcal{B}_i^{cv} &= \int_{\Gamma_{cv}} q_i^{cv} \; N_i \; d\Gamma \\
\mathcal{B}_i^{c} &= \int_{\Gamma_c} q_i^{c} \; N_i \; d\Gamma \\
\mathcal{Q}_i &= \int_V Q_i \; N_i \; dV
\end{aligned}
\tag{3.14}
$$

For simplicity, all boundary conditions are regrouped under one term

$$\mathcal{B}_i = \mathcal{B}_i^{\mathcal{N}} + \mathcal{B}_i^{cv} + \mathcal{B}_i^{c} \tag{3.15}$$

3.1.3 Temporal Integration

The differential equation 3.13 needs to be integrated with respect to time to obtain a transient solution of the heat transfer equation. Consider a simple one dimensional differential equation of the form

$$w_t = w_{xx} \tag{3.16}$$

with $w_t = \delta w / \delta t$ the time derivative and $w_{xx} = \delta^2 w / \delta t^2$ the spatial gradient.

When evaluating the differential equation at discrete time intervals n, the spatial derivative may be evaluated as a combination of the known value of w at time level n or of the as-yet unknown value of w at $n+1$ depending on the parameter θ

$$w_t^{n+1} = (1-\theta) w_{xx}^n + \theta w_{xx}^{n+1}, \quad 0 \leq \theta \leq 1 \tag{3.17}$$

Using the simplest approximation of the time derivative, this yields

$$w^{n+1} = w^n + \Delta t \left[(1-\theta) w_{xx}^n + \theta w_{xx}^{n+1} \right] \tag{3.18}$$

As w_{xx}^{n+1} is unknown at time n, a $\theta = 1$ the equation will be solved implicitly whereas if $\theta = 0$ the solution is straight forward and is said to be explicit.

The theta method applied to our thermal differential equation 3.13 gives:

$$(M_{ij}^n - \theta \Delta t K_{ij}^n) T_i^{n+1} \ = [M_{ij}^n + (1-\theta)\Delta t K_{ij}^n] T_i^n + \mathcal{B}_i^n + \mathcal{Q}_i^n, \quad 0 \leq \theta \leq 1 \tag{3.19}$$

The θ-family time integration methods are of the most commonly used as they offer flexibility between explicit and implicit methods. For $\theta = 1$, the fully implicit backward difference (or backward Euler) method is obtained which is unconditionally stable, i.e. there is no restriction on the time step size. For $\theta = 0$, we have the conditionally stable explicit scheme known as forward difference. Finally, for different $\theta > 0$ and $\theta < 1$ the above equation will refer to mixed implicit-explicit methods with $\theta = 1/2$ being the Crank-Nicholson method.

For the forward difference, equation 3.19 gives

$$M_{ij}^n T_i^{n+1} \ = (M_{ij}^n + \Delta t K_{ij}^n) T_i^n + \mathcal{B}_i^n + \mathcal{Q}_i^n \tag{3.20}$$

To obtain T^{n+1} the matrix $[M]$ must be inverted. The most straight forward solution is to use the row-sum technique to obtain a diagonal lumped mass matrix:

$$L_{ii} = \sum_{j=1}^{n_e} M_{ii}, \quad \forall i \neq j \implies L_{ij} = 0 \tag{3.21}$$

As the Solidity solver is explicit, an explicit solver was first developed with the forward difference scheme. Second the solver was completed with an implicit scheme using the PETSc toolkit (Abhyankar et al., 2018) in order to solve matrix systems of equations and perform implicit calculations.

3.2 Thermal Contact between Discrete Elements

The research presented in this section is extracted from a publication by the author of this thesis, Joulin et al. (2016) published in the proceedings of the 7th International Conference on Discrete Element Methods (DEM7).

This work presents a novel approach for dealing with heat transfer contact interactions in the FEMDEM and in the explicit DEM. The approach is based on mesh penetration techniques (Munjiza and Andrews, 2000) which allows two meshes of two different solids to experience a small overlap. The penetration is a consequence of the time step and the velocities of the particles which controls the amount of penetration that will occur. From the overlap the contact force is drawn (see Section 2.2.2.1). When there is overlap, the surface of contact can be computed numerically. This allows for contact heat flux and heat conduction inside and between solid bodies to be linked. This works also presents a model for contact heat transfer interaction terms to be inserted in the matrix system of the heat equation and thus to solve contact heat transfer implicitly.

3.2.1 Thermal Contact

The the heat flux across the apparent surface area of two solids in contact is defined as follows (Mikic and Rohsenow, 1966):

$$q^c = \frac{\Delta T_c}{R_c} \tag{3.22}$$

R_c is the contact heat resistance and ΔT_c the apparent temperature drop at the contact. This definition introduces a fictional apparent temperature drop at the interface. In reality, there is no real discontinuity of the temperature distribution through the solids' contacts. There is a continuous distribution of temperature extending through the contact interface from both solids. As shown on Figure 3.1, defining the temperature drop as the difference in the temperature obtained by extrapolating the temperature profiles in the two regions of the interface enables the use of the contact heat resistance to simplify the complex heat processes occurring at the boundary.

3.2.2 Contact surface Area

The presented method evaluates the contact area between two contacting solids based on the penetration of boundary meshes, see Figure 3.2. A contact surface is obtained for both solids, the overall contact surface is the average of these two values.

When the solids are meshed, a couple of contacting elements are selected, one is called the contactor element, the other one is called the target element. The boundary surface of the target element in contact with the whole contactor element's volume is calculated, then the opposite calculation is performed.

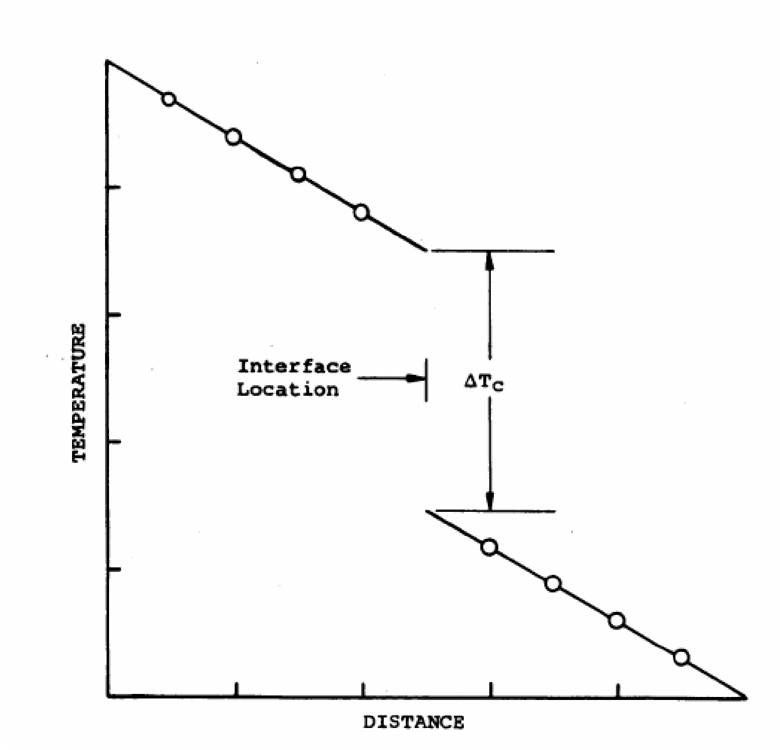

FIGURE 3.1: Definition of the contact temperature drop (Mikic and Rohsenow, 1966).

Each solid is meshed with four-noded tetrahedral elements, the algorithm loops on each face of the target element and the intersection surface with the contactor's volume is drawn on each target's face (and vice versa), see Figure 3.3a.

Two surface areas are obtained, one describing the contact area on the target, the other on the contactor, which we call respectively S_{tar} and S_{con}, the contact area is set to be the average of these two. Note that only the faces of the target element located on the boundary of the solid can be selected for surface calculation.

Figure 3.4 shows boundary elements from a first solid A, contacting a boundary element from a second solid B. For purposes of explanation of the surface calculation, consider the blue element to be the target element and red elements to be selected successively as contactor elements. Note that for clarity, the relative penetration size has been intentionally exaggerated on the figures.

Then consider that the target element from solid B possesses only one face located on the boundary of solid B, this face is highlighted on Figure 3.3b. The algorithm will intersect this face with all three contactor element volumes from solid A in order to reconstruct the surface area of contact. Therefore, three S_{tar} contact areas are obtained, see figure

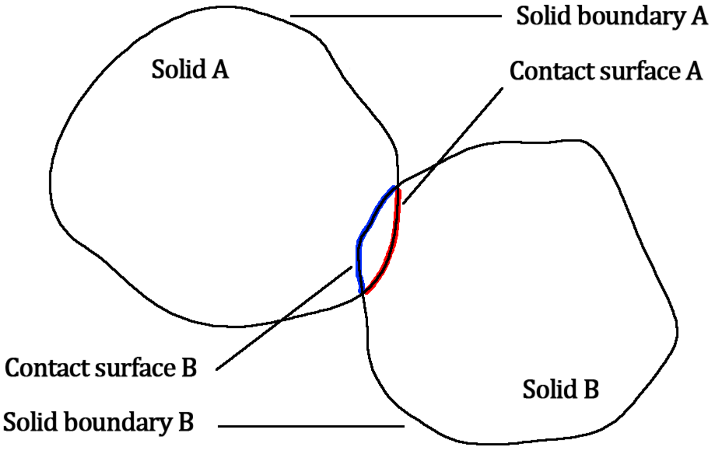

Figure 3.2: Contact overlap between two solids' boundaries.

3.3c. At last, the opposite calculation is performed. Contactor and target elements roles are swapped and surfaces S_{con} are obtained.

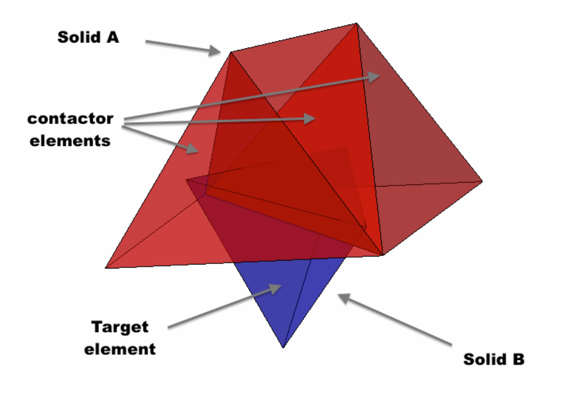

(A) Penetration between target and contactor tetrahedral elements

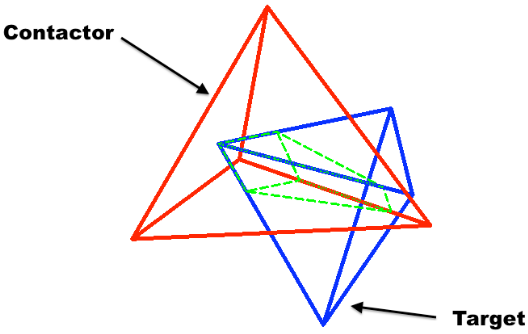

(B) Intersection lines of the contact

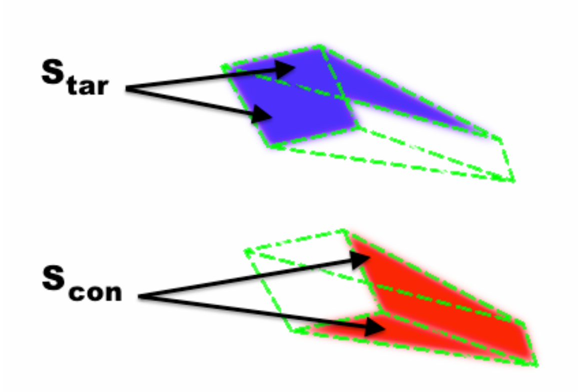

(C) Intersection volume

Figure 3.3: Element contact.

(A) Penetration between target and contactor tetrahedral elements

(B) Boundary face of target element

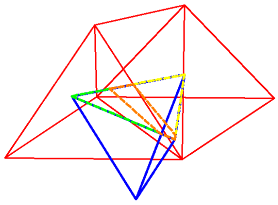

(C) Contact boundary surfaces of the target element

FIGURE 3.4: Element to element surface calculation for two contacting solids.

3.2.3 Computation of Heat Fluxes

Heat fluxes are calculated between each couples of contacting tetrahedral elements from two contacting solids meshes. The total contact heat flux temperature contribution to the heat transfer equation (Equation 3.13) is:

$$\mathcal{B}_i^c = \sum_{k=1}^{n_c} \mathcal{B}_i^{c,k} = \frac{1}{4R_c^k} \Delta T_c^k \ S_c^k \tag{3.23}$$

With n_c the number of contacts for which node i is involved, ΔT_c^k is the temperature drop and S_c^k is the contact surface of the contact k . The contribution is equally distributed between the four nodes for each tetrahedra hence the $\frac{1}{4}$ factor.

Figure 3.5 shows the contact heat transfer for two isolated contacting tetrahedral elements. Each element is composed of four nodes, the total contribution of the contact heat flux is for a node of element 1:

$$\mathcal{B}_1^c = \frac{1}{4R_c} (\frac{T_{11} + T_{12} + T_{13} + T_{14}}{4} - \frac{T_{21} + T_{22} + T_{23} + T_{24}}{4}) \ S_c \tag{3.24}$$

And for a node of element 2:

$$\mathcal{B}_2^c = -\mathcal{B}_1^c \tag{3.25}$$

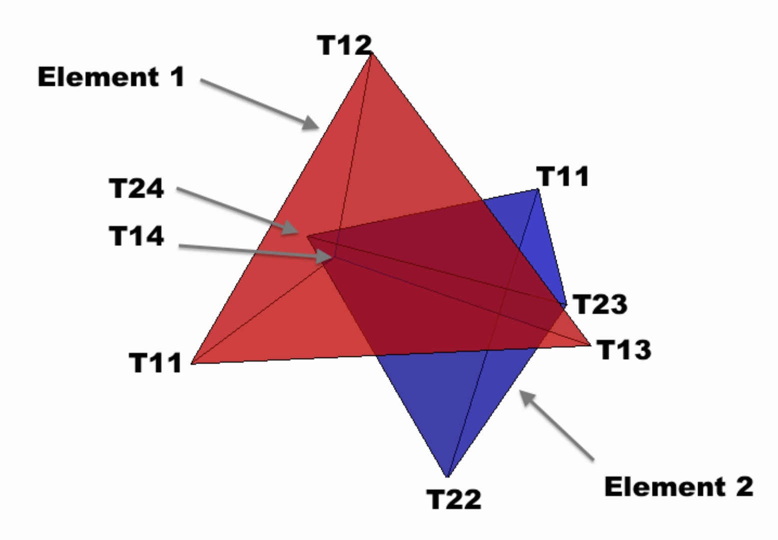

FIGURE 3.5: Nodal temperatures of two overlapping tetrahedral elements.

We can summarise the method with the following expression:

$$\mathcal{B}_i^c = \sum_{k=1}^{n_c} \frac{1}{16R_c^k} \sum_{l=1}^{4} (T_{con,l}^k - T_{tar,l}^k)\ S_c^k \tag{3.26}$$

With $T_{con,l}^k$ and $T_{tar,l}^k$ the nodal temperatures of the target and the contactor elements involved in the k contact.

3.2.4 Implicit Solver: Contact Interaction Matrix

In order to incorporate the contact heat transfer in the PETSc implicit solver, the contact contribution must be taken into account in the matrix system defined in Equation 3.13. To write equation 3.26 in a matrix form, we define the contact interaction term $\mathcal{B}_i^c$ as follows:

$$\mathcal{B}_i^c = \mathcal{C}_{ij}\ T_i \tag{3.27}$$

With $\mathcal{C}$ the contact heat transfer interaction $[n_e; n_e]$ sparse matrix containing node interactions between elements of separate bodies, n_e is the total number of nodes. We can decompose the contact interaction matrix into a sum of n_c sub sparse interaction

$[n_e; n_e]$ matrixes:

$$\begin{aligned} &\mathcal{C}_{ij} = \sum_{k=1}^{n_c} \frac{1}{16 R_c^k} \gamma_{ij}^k \; S_c^k \\ &\gamma_{ij}^k = +1 \quad if \quad i = j \\ &\gamma_{ij}^k = -1 \quad if \quad i \neq j \end{aligned} \tag{3.28}$$

With $i, j \in [1, 2, ...n_e]$ nodal indexes of the target and contactor elements of the considered contact couples. Finally, we rewrite the matrix equation 3.13 for a contact heat transfer problem:

$$M_{ij} \; \dot{T}_i + K_{ij} \; T_i = \mathcal{C}_{ij} \; T_i \tag{3.29}$$

3.3 Validation of Heat Conduction and Contact Heat Transfer Models

The validation work presented in this section contains:

i) The validation of the heat conduction model for a continuous solid with the FEM (Solidity) presented in Section 3.1, associated results are referred as ‘FEM’

ii) The validation of the contact heat transfer model with the hybrid FEMDEM (Solidity) presented in Section 3.2, associated results are referred as ‘FEMDEM’

iii) The validation of the contact heat transfer model (‘FEMDEM’) versus a DEM solution

For i) and ii) validation is performed against a one dimensional analytical solution for conduction heat transfer. For i) heat transfer is calculated through one continuous solid and for ii) the heat transfer is calculated through two contacting solids with a perfect contact condition, i.e. there is no resistance for heat to transfer across the contact. In such conditions, i) and ii) are expected to produce the same result. Finally with iii), the FEMDEM results are compared with a DEM solution to test the model in a complex contact configuration.

3.3.1 One Dimensional Heat Transfer: Analytical Solution

Consider a finite slab of length L and of an initial temperature of T_0 (Figure 3.6). The left side of the slab is insulated while the right side is exposed to a Dirichlet boundary condition with an imposed temperature T_D. There is no inner heat generation in the slab. The one-dimensional transient conduction equation for this problem is:

$$\frac{\partial^2 T}{\partial x^2} = \frac{1}{\alpha}\frac{\partial T}{\partial t}, \quad \alpha = \frac{c}{k} \tag{3.30}$$

With α the thermal diffusivity, k the thermal conductivity and c the heat capacity. The solution is given by Incropera et al. (2011):

$$\begin{aligned}
&\theta = \sum_{n=1}^{\infty} \frac{4\sin(n-\pi/2)}{2(n-\pi/2)+\sin[2(n-\pi/2)]}\cos[(n-\pi/2)X]e^{-(n-\pi/2)^2 F_o}, \\
&\theta = \frac{T-T_D}{T_i-T_D}, \\
&X = \frac{x}{L}, \\
&F_o = \frac{\alpha t}{L^2}
\end{aligned} \tag{3.31}$$

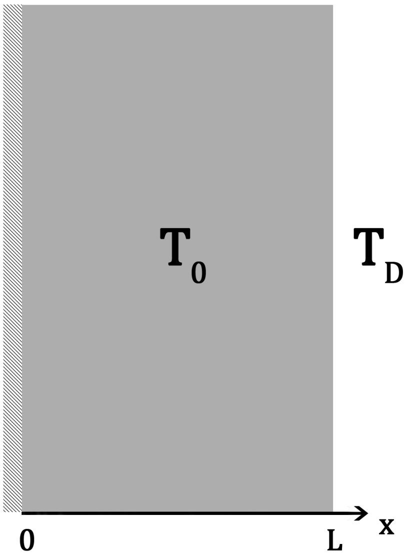

FIGURE 3.6: Boundary conditions for heat conduction in a slab.

3.3.2 Perfect contact validation

For the FEM simulation i) a 3D bar of a length of 1 m is used (Figure 3.7a and 3.7b). The solid bar has an initial temperature of $0°C$ and a temperature of $1°C$ is imposed at the right hand end face of the bar, all other faces are considered adiabatic.

The FEMDEM simulation ii) is a composition of two 0.5 m bars contacting at one end (Figure 3.7c and 3.7d). The solid bars have an initial temperature of $0°C$ and a temperature of $1°C$ is imposed at the right hand end face of the right hand bar. The contacting faces have a contact heat flux boundary condition and the rest of the faces are insulated.

The two solids meshes are overlapping and heat is flowing in the longitudinal direction, as shown on figure 3.8. To simulate a perfect contact the heat resistance is set to a relatively low value. Results show a very good agreement and are presented on Figure 3.9 and Table 3.2.

bar width, (m)	0.1
mesh size, (m)	5.10^{-2}
time step, (s)	10^{-3}
Thermal conductivity, κ ($W.(m.K)^{-1}$)	1
Specific heat capacity, c ($J.(Kg.K)^{-1}$)	1
Density, ρ ($kg.m^{-3}$)	100
Contact heat resistance, R_c ($m.K.W^{-1}$)	0.001

TABLE 3.1: Simulation parameters i) and ii) simulations.

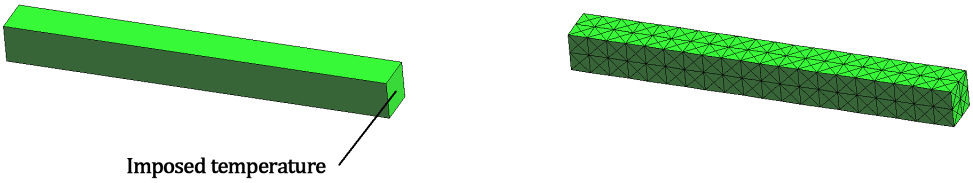

(A) A single bar of 1m,
FEM configuration for i)

(B) mesh for i)

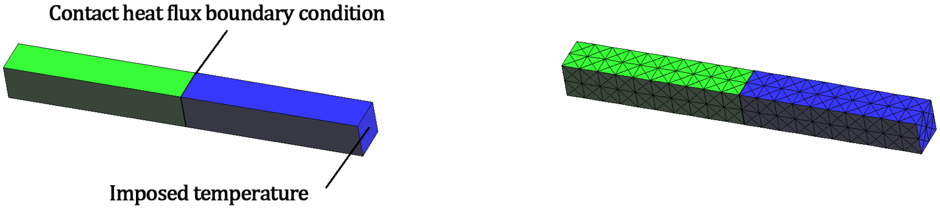

(C) Two contacting bars of 0.5m,
FEMDEM configuration for ii)

(D) mesh for ii)

FIGURE 3.7: Continous & hybrid configurations for validation test.

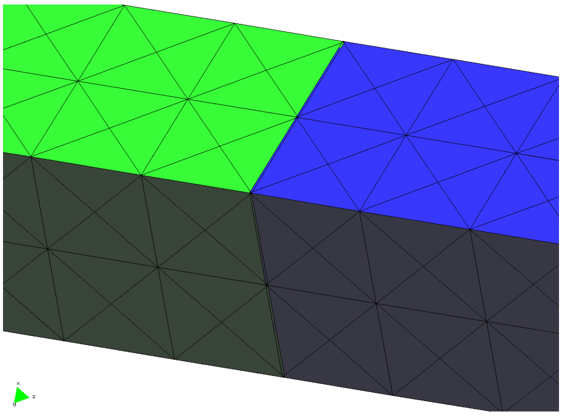

FIGURE 3.8: FEMDEM contact overlap close-up.

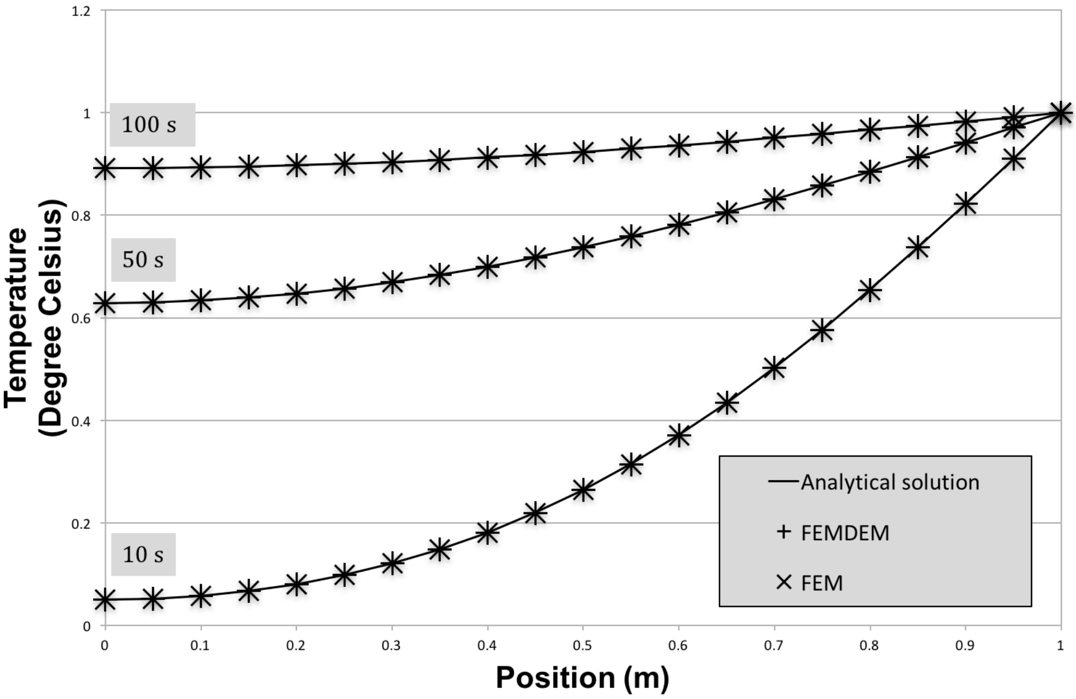

FIGURE 3.9: Temperature profiles for the analytical solution, FEM and FEMDEM simulations at times 10s , 50s and 100s.

Times	Average absolute FEM error i)	Average absolute FEMDEM error ii)
10s	0.062%	0.062%
50s	0.013%	0.013%
100s	0.0044%	0.0044%

TABLE 3.2: Average error of FEM and FEMDEM simulations compared to the Analytical solution.

3.4 Validation of the Contact Heat Transfer Versus a DEM Model

3.4.1 The pipe Network DEM Model

The pipe-network model presented by Feng et al. (2008, 2009) is designed for the modelling of large numbers of circular particles in 2D that represent infinite or long pipes.This method is presented in the culture of the discrete element method and is introduced here to form the basis of a validation study of the contact heat transfer model.

Consider two circular particles A and B having respectively T_A and T_B as average temperatures, the thermal resistances of the two pipes are respectively R_A and R_B. The total thermal resistance is:

$$R_{AB} = R_A + R_B + R_c^* \tag{3.32}$$

With R_c^* the contact thermal resistance for the pipe network model. The contact zone of the discrete thermal element is represented by an arc on the boundary of the element which is defined with its half angle α_i (Figure 3.10). For angles of contact below 30°, the discrete element thermal resistance can be approximated with high accuracy by the formula :

$$R_A = \frac{1}{\pi\kappa_A}\left(-ln\alpha_A + \frac{3}{2} + \frac{\alpha_A^2}{36}\right) \tag{3.33}$$

With κ_A the thermal conductivity of particle A.

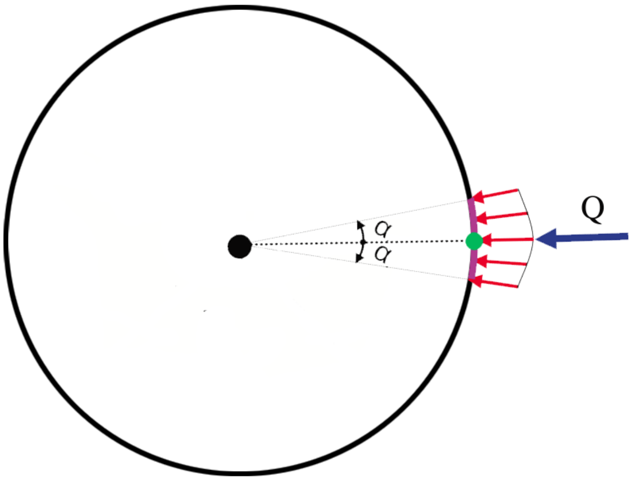

FIGURE 3.10: Contact heat flux for the discrete thermal element, modified from Feng et al. (2008)

The boundaries of the particles are insulated and heat transfers only through the contact zone. For two contacting discrete thermal element (see Figure 3.11) the heat flow between the two particles Q_{AB} is defined as follows :

$$(T_B - T_A) = R_{AB}\, Q_{AB} \tag{3.34}$$

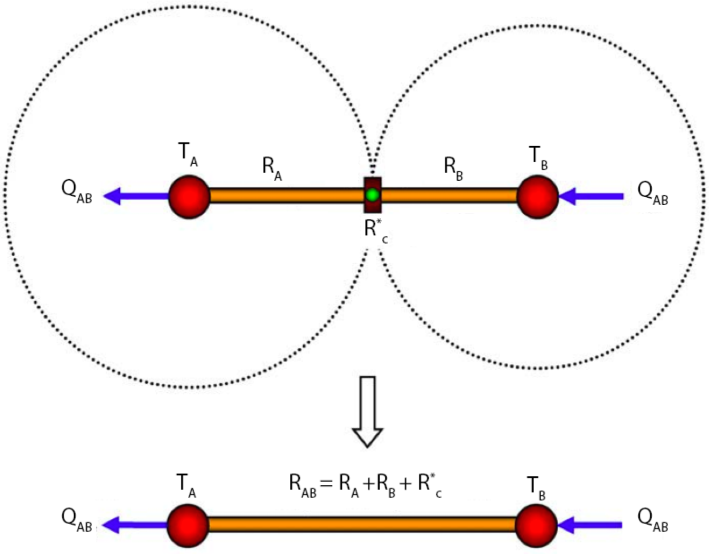

FIGURE 3.11: Pipe network model: two particles with thermal contact, modified from Feng et al. (2009).

The forward difference explicit time integration is used to solve the transient problem:

$$C_A \dot{T}_A^0 = Q_{AB} \tag{3.35}$$

$\dot{T}_A$ being the time derivative of the average temperature and C_A the total heat capacity of the particle A:

$$C_A = \pi \rho c_p r_A^2 \tag{3.36}$$

With c_p the heat capacity and r_A the particle's radius.

3.4.2 Homogenisation of the Heat Resistance

As demonstrated by equations 3.22, 3.13 and 3.34, 3.35, the FEMDEM and the Pipe network model approaches for the heat resistance differ and therefore an adjustment is required. The same contact heat flux contribution needs to be taken in account into the heat diffusion equation, therefore the following condition has to be fulfilled:

$$Q_{AB} = \frac{1}{w_{cyl}} \mathcal{B}^c \tag{3.37}$$

The left hand side of the above equation is the heat flux contribution from the Pipe network model extended from a 2D disc to an hypothetical 3D cylinder of a width represented by w_{cyl}; the right hand side correspond to the FEMDEM model. Therefore:

$$\frac{T_B^0 - T_A^0}{R_{AB}} = \frac{1}{w_{cyl}} \frac{\Delta T_c \, S_c}{R_c} \tag{3.38}$$

and

$$R_{AB} = \frac{R_c \, w_{cyl}}{S_c} - R_A - R_B \tag{3.39}$$

This conclusion also implies that $T_B - T_A = \Delta T_c$, i.e. the average particle temperature difference is equal to the local temperature difference at the contact zone and such is the main approximation of the discrete element approach, this condition will only be verified when the thermal conductivities are high compared to the contact heat resistance.

To make sure this assumption is acceptable in the following simulation, a ΔT_c calculation based on the average particle temperature difference has also been implemented in FEMDEM, in addition to the ΔT_c local temperature gap calculation.

3.4.3 FEMDEM Simulation Settings

Consider two contacting thin cylinders of the same radius r and width w_{cyl}. The two finite element meshes are overlapping at the contact zone (Figure 3.12). Simulation parameters are summarized in Table 3.3.

Two different FEMDEM simulations were performed, the first with a contact heat flux calculated with the local temperatures ('local ΔT'), the second calculated with the average particle temperatures ('average ΔT') .

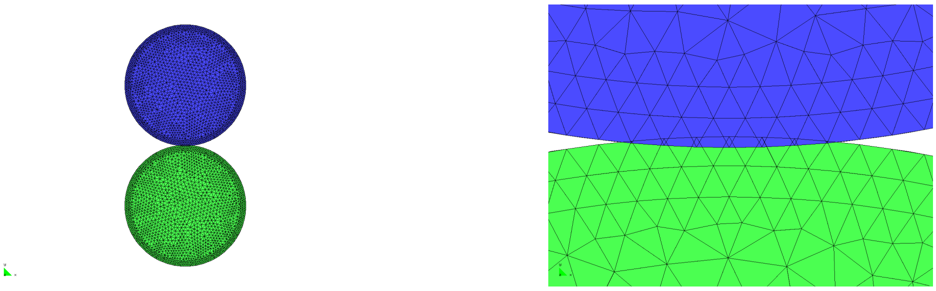

(A) FEMDEM mesh (B) FEMDEM mesh contact overlap close-up

Figure 3.12: FEMDEM mesh of two contacting cylindrical particles with a contact overalp.

Particle radius, r, (m)	1
mesh size, (m)	8.10^{-2}
time step, (s)	1.10^{-3}
Thermal conductivity, κ $(W.(m.K)^{-1})$	1
Thermal capacity, c $(J.(Kg.K)^{-1})$	1
Density, ρ $kg.m^{-3}$	100
Contact heat resistance, R_c $(m.K.W^{-1})$	1
Mesh penetration, p (m)	1.10^{-2}
Computed contact surface, (m)	$3.85\ 10^{-2}$
Initial temperature of particle A $(°C)$	0
Initial temperature particle B $(°C)$	0

Table 3.3: Simulation parameters for the FEMDEM simulation.

The accuracy of the computed contact surface S_c is validated against a theoretical surface formula S_c^{th} obtained from the overlap of two circles :

$$\sin\alpha_A^{th} = \frac{1}{2\ d\ r_A}\left(4\ d^2\ r_A^2 - (d^2 - r_A^2 + r_B^2)^2\right) \tag{3.40}$$

$$S_c^{th} = 2\ \alpha_A^{th}\ r_A\ L \tag{3.41}$$

With $d = r_A + r_B - p$, p being the penetration of the two meshes and L the thickness of the cylinder. For the actual configuration the theoretical surface is $S_c^{th} = 0.02\ m^2$, the error of the computed contact surface is of 4%.

This error is only due to the finite element approximation of the domain. The error of the contact surface reduces to 0.4% with a twice smaller mesh. Nevertheless, to reduce errors for this validation test, the computed contact surface is transformed into the equivalent contact half angle and then imputed in the pipe network model by means of the formula:

$$\alpha_A = \frac{S_c}{2\ w_{cyl}\ r_A} \tag{3.42}$$

Results are presented for particle B on figure 3.13. There is an average error of 7.6 % between the pipe-network model and the original FEMDEM (with a local temperature difference) against an average error of 0.63 % with FEMDEM and the average particle temperature difference. In this configuration, it is evident that the main assumption of the pipe-network model, being the consideration of the particle's temperature to be uniform, is not valid as the heat conductivity is relatively small. To rectify this error, consider now the same configuration with a heat conductivity a hundred times greater, results are presented on figure 3.15. In this case, both FEMDEM simulations produce the same result with an average error of 0.7 %, hence the pipe-network approximation can here be considered valid.

In summary, the foregoing examples show that when significantly varying temperatures exist in the contacting bodies, the FEMDEM code can capture the complexity of the time history, giving quite different results to when the assumption of average temperature within the particle is imposed.

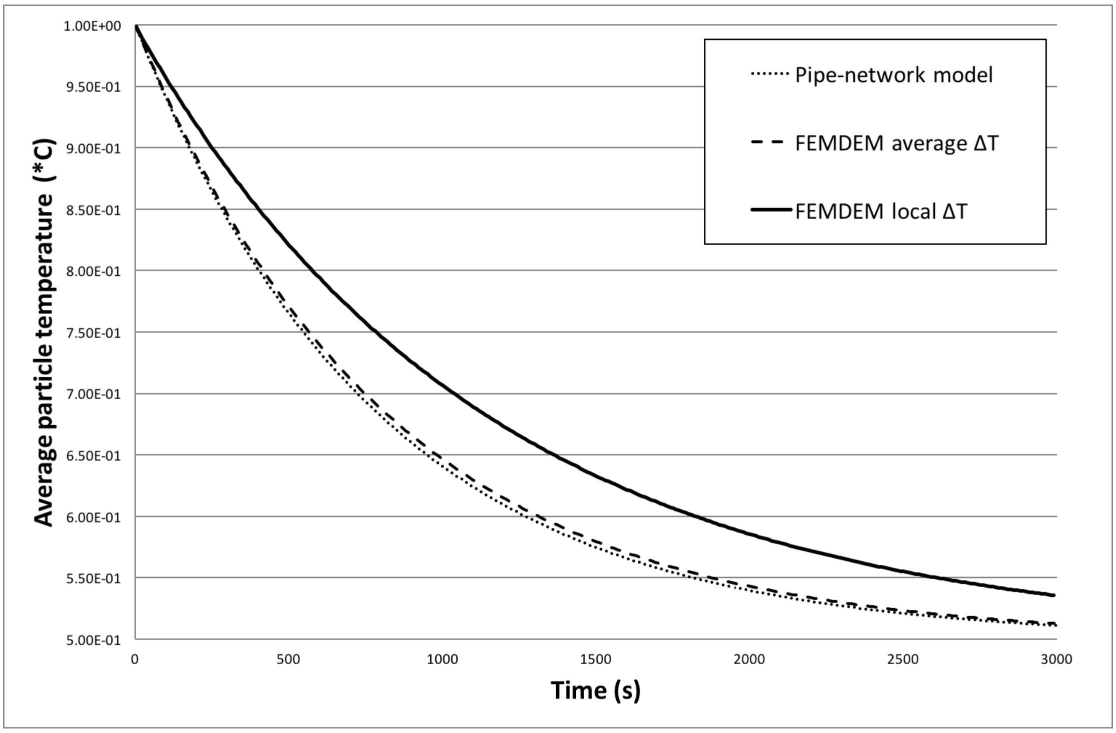

FIGURE 3.13: Average temperature evolution of particle j over time

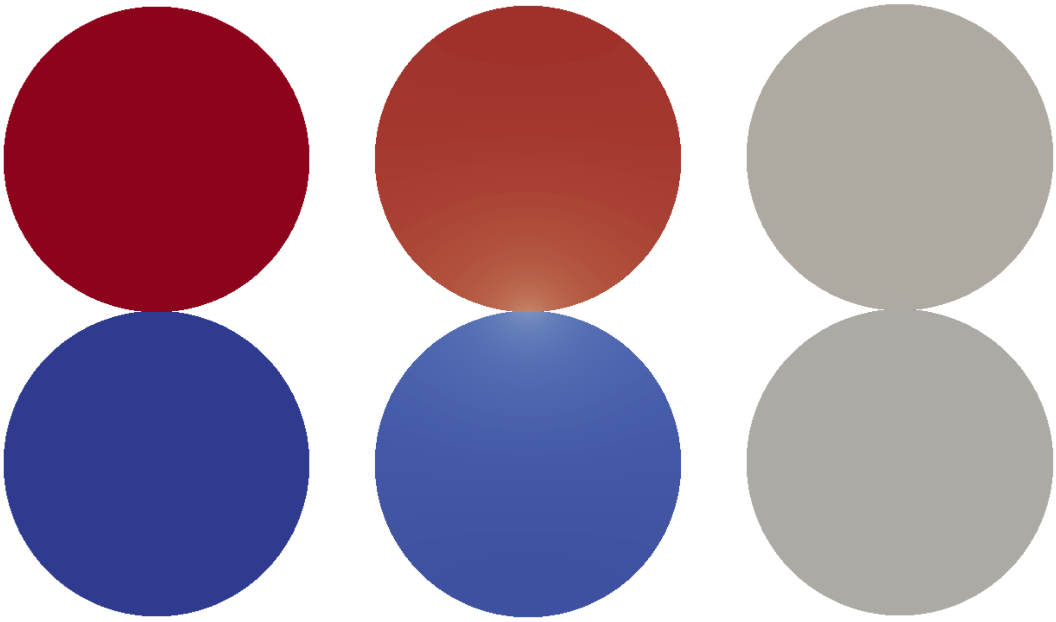

FIGURE 3.14: Initial, transient and final state of the pipe-network validation simulation

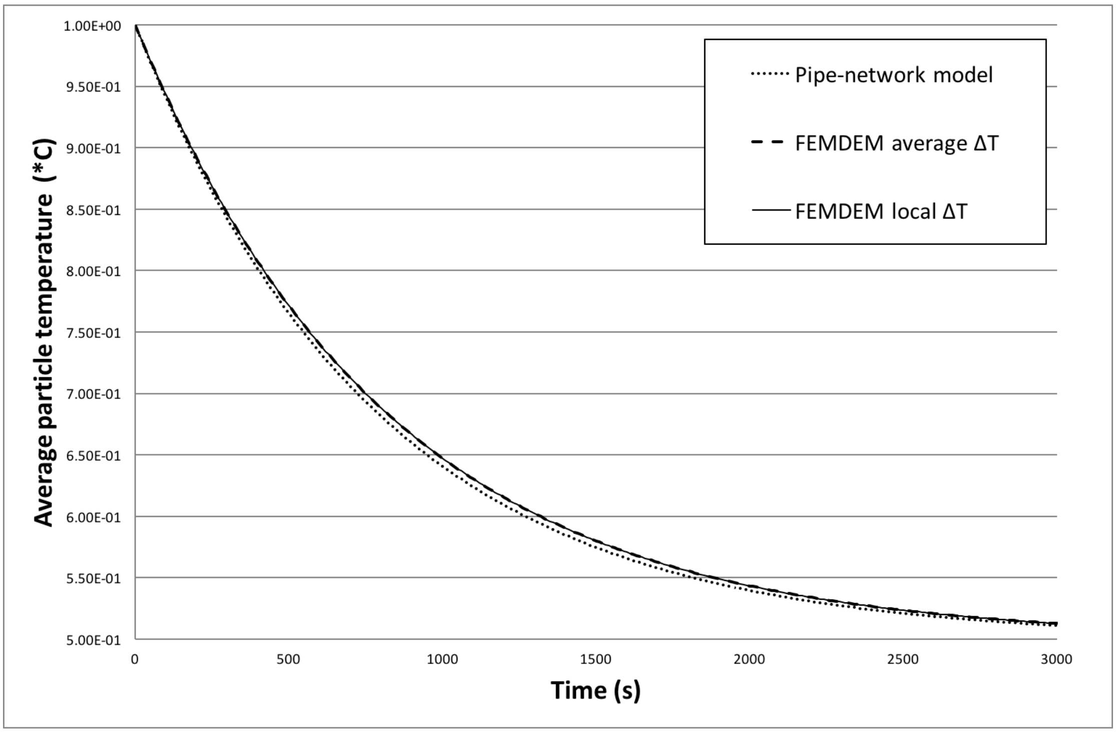

FIGURE 3.15: Average temperature evolution of particle j over time with an increased heat conductivity

3.5 Multi-body simulation

This section presents a static multi-body heat transfer simulation with 2,000 particles packed into a cylindrical container which is heated from the outside.

To obtain such a configuration, the particles are deposited into the container using the FEMDEM code. After all the particles are deposited, the temperature of the container is constrained to 300°C.

The particles deposited are metal nuts and their mesh is composed of 192 elements (Figure 3.16). Figures 3.17 and 3.19 show the heat transfer simulation with heating of the metal nuts from 0°C to 300°C.

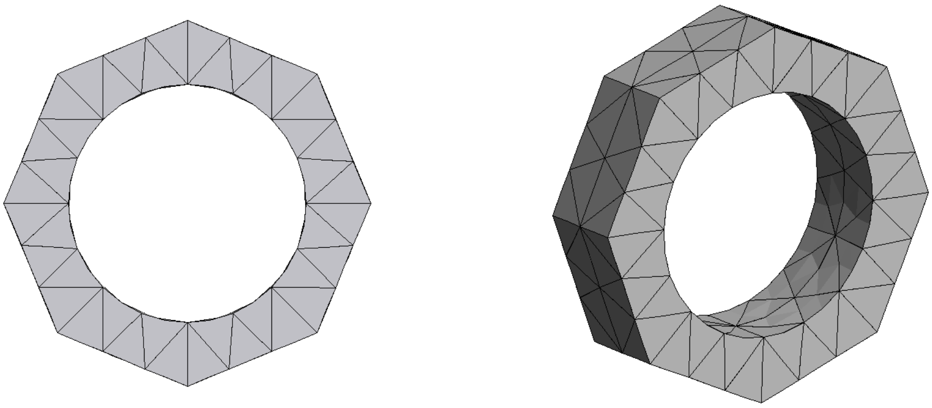

FIGURE 3.16: Particle mesh (metal nut), 192 elements.

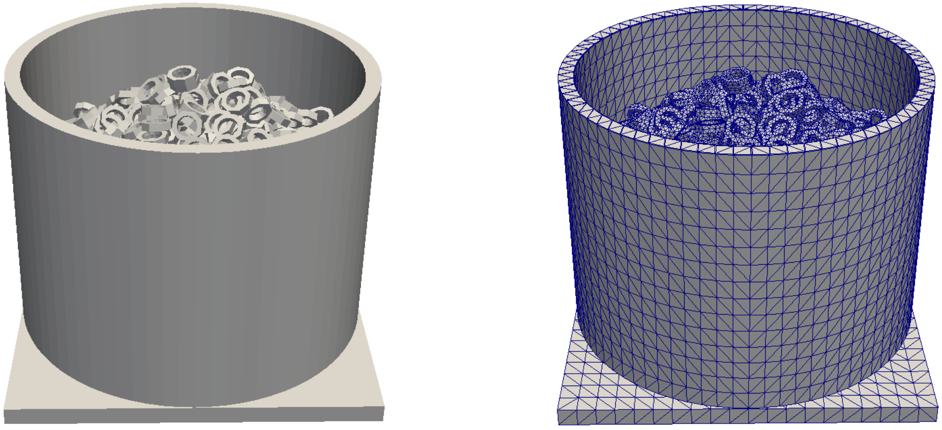

(A) Metal nuts and cylindrical container

(B) Mesh view

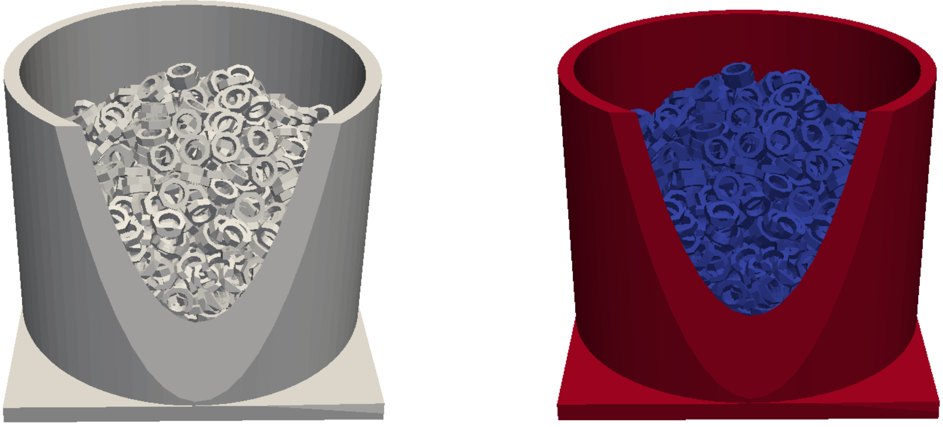

(C) Cross section view

(D) Initial conditions blue: $0^\circ C$, red: $300^\circ C$

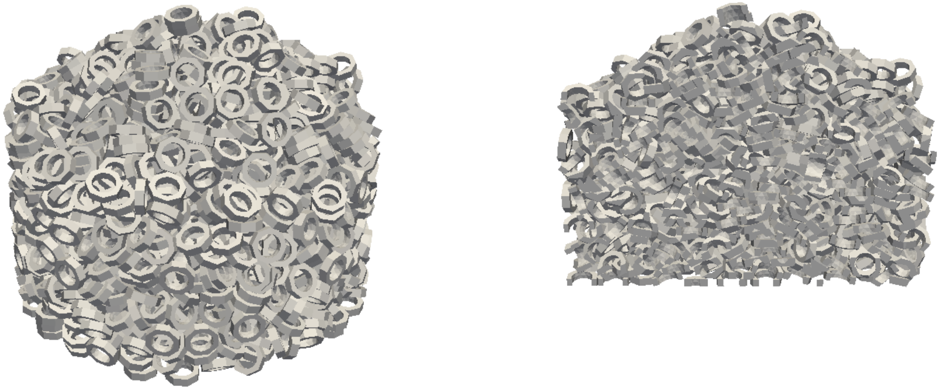

(E) Nuts packing only

(F) Nuts packing only (cross section view)

FIGURE 3.17: Thermal simulation setup of 2,000 metal nuts inside a cylindrical container.

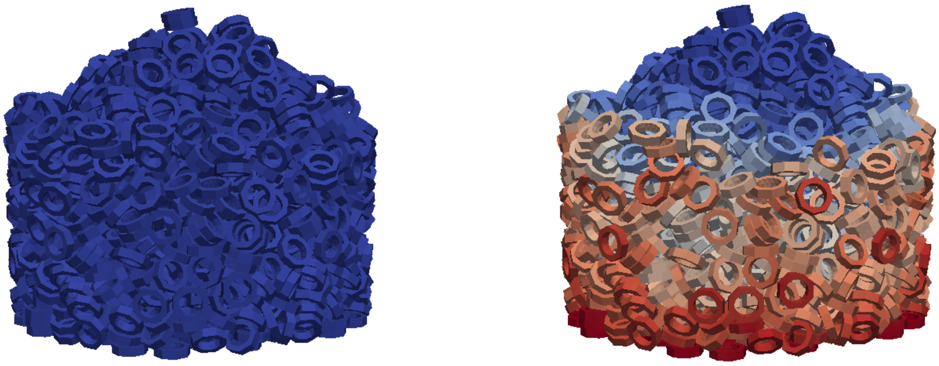

(A) Initial state (B) 1 time step

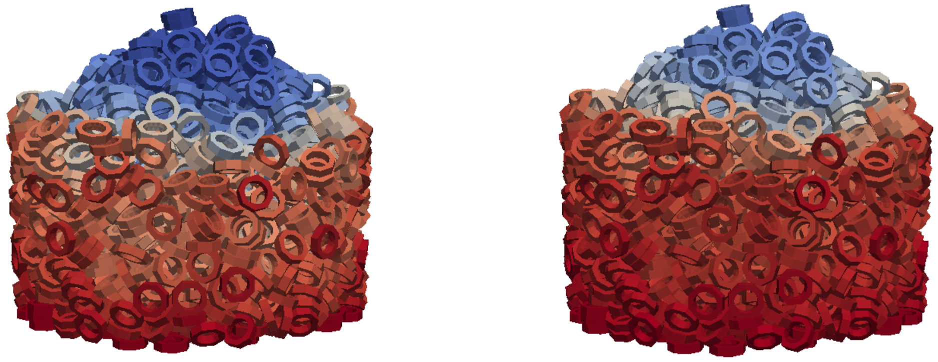

(C) 2 time steps (D) 3 time steps

(E) 10 time steps (F) 30 time steps

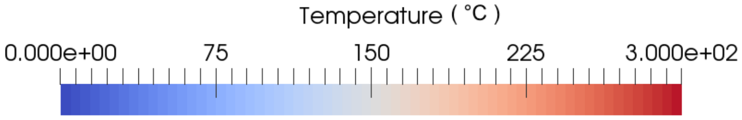

FIGURE 3.18: Heating up simulation of 2,000 metal nuts.

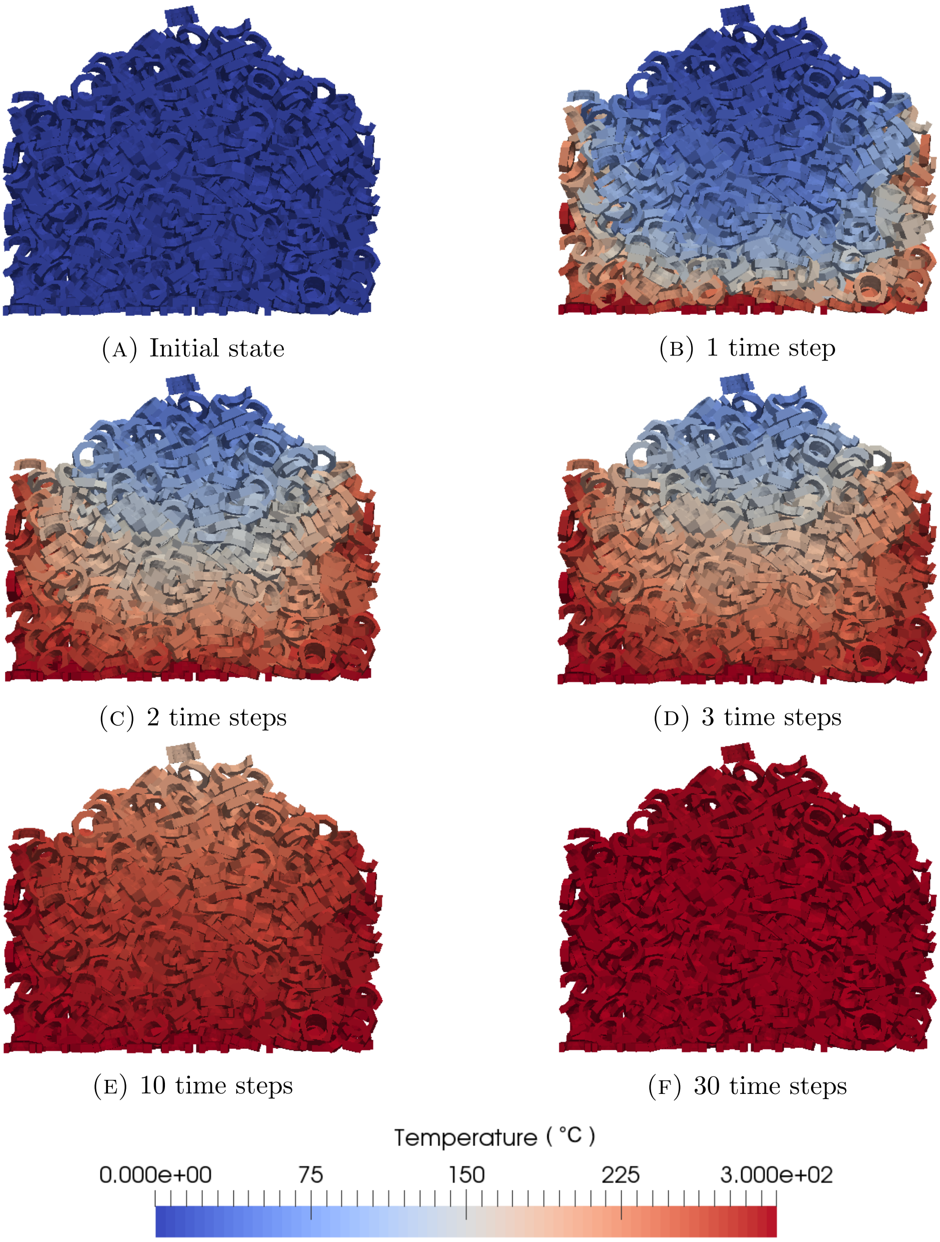
(A) Initial state

(B) 1 time step

(C) 2 time steps

(D) 3 time steps

(E) 10 time steps

(F) 30 time steps

FIGURE 3.19: Heating up simulation of 2,000 metal nuts (cross section view).

3.6 Conclusion

In this section, a conduction heat transfer model and a contact heat transfer model have been presented. Two validation tests have demonstrated the model's accuracy. Both models may be solved with a fully explicit forward difference scheme or with an implicit scheme with PETSc. Finally, a multi-body simulation demonstrated Solidity's ability to compute the thermal distribution in large particle systems.

However it must be emphasised that in a multi-body simulation, there is a multitude of possible contact configurations that might involve element surfaces, edges or summits. In a deposition simulation for instance, some particles may come to rest on edge-to-edge contact which will produce a infinitesimal surface area and heat transfer that is not representative of reality.

The contact heat transfer model calculates the apparent contact surface as opposed to the real contact surface of non-conforming rough surfaces (Yovanovich, 2005). In the event of modelling solids with complex shapes and curves, the apparent surface area calculation can only be as good as the mesh approximation of the solid's boundary. For this reason, boundary meshes will need to be refined when performing simulations with complex particles shapes and this will greatly impact the computational cost of simulations (Figure 3.20).

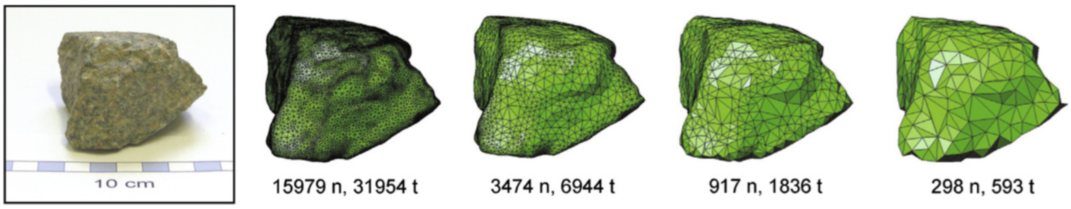

FIGURE 3.20: Mesh refinement of a granite aggregate with a complex shape, n is the number of nodes and t is the number of triangular boundary elements (Latham et al., 2008).

Moreover, the contact heat transfer model has proven to be accurate in capturing the intersection polygon of two contacting meshes from which the contact surface is drawn. Whilst the amount of mesh penetration is designed to be infinitesimal (Munjiza and Andrews, 2000), it will still impact the size of the intersection polygon, contact surface and contact heat transfer. Hence, it is important to investigate the sensitivity of the surface calculation to the mesh penetration.

In conclusion, for any contact heat transfer problem there needs to be an accurate investigation of the different types of contact configurations that may occur and if they are consistent with reality. The contact heat transfer model must be complemented with a systematic approach of calibration, sensitivity analysis and mesh refinement procedures.

3.7 Contact Heat Transfer in Fractured Rocks

Fractured rocks are a particular class of discrete systems where the blocks of rock carved out by the fractures are the discrete bodies, as shown on Figure 3.21. In such configuration, the contact heat transfer model can enable the heat to flow across fractures. For the FEMDEM, this implies that a discontinuous mechanical approach can be employed whilst preserving heat transfer across the discontinuities. Furthermore, heating can induce new fractures and open or close pre-existing fractures. When combining the contact heat transfer with thermo-mechanical coupling (Chapter 4) closing fractures can allow heat to flow whilst opening fractures will interrupt the heat conduction. The method also has an interest when studying heat transfer and fluid flow in non-conforming rough fractures, fully resolving the fracture walls will enable to simulate their complex interactions.

Experimental results by Lin et al. (1991) suggest that fluid-filled fractures do not have a significant impact on the heat transfer around a GDF. In such conditions, the thermal processes are best described with a continuum approach. Thus, contact heat transfer model is most appropriate to represent highly fractured dry rocks where closed fractures conduct heat whilst open, air-filled fractures are heat resisting. Nevertheless, since the focus of the thesis also includes hydraulic processes, priority has been given to THM coupling features and no further work is conducted on the contact heat transfer model.

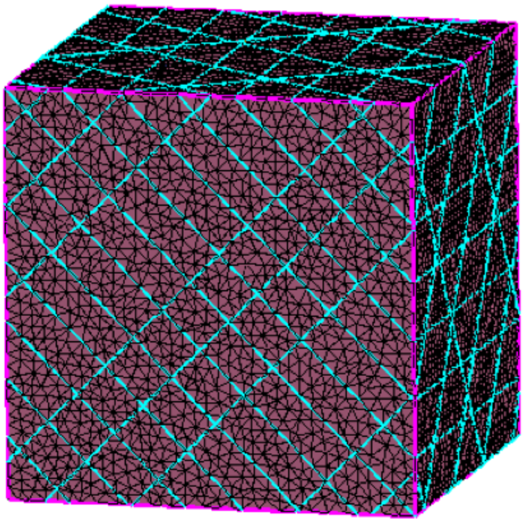

FIGURE 3.21: FEMDEM model of rock blocks intersected by two orthogonal fracture sets.

Chapter 4

Thermo-Mechanical Coupling

Thermally induced deformations and fracturing are significant concerns in many engineering fields such as engine design, nuclear fission reactors, geothermal energy and hydrocarbon production and radioactive waste disposal. When a material is exposed to a temperature gradient, it will deform and cracks may appear, the prediction of those cracks is key into making robust, efficient and safe designs.

In geothermal energy exploitation, the injections cycles of cool water in the hot reservoir are likely to induce fractures (Yaseen, 2004) and in hydrocarbon production, thermal shocks are found to enhance the hydraulic fracturing efficiency (Enayatpour et al., 2013). In such applications, the fractures increase the permeability of the reservoirs and have a positive influence on production.

On the contrary, in the context of radioactive waste disposal fractures are undesirable as initiating new cracks in the rock is potentially creating new flow pathways for radionuclides to be transported into the biosphere. As high temperatures are expected in the vicinity of a GDF, predicting thermally induced deformations and failure is of importance for safe disposal of the radioactive waste.

As seen in the literature review chapter, Section 2.4, Table 2.3 and 2.2, the thermo-mechanical coupling is a common feature among numerical simulators but thermally induced fracturing can only be performed with methods that represent fractures explicitly. Thus thermal fracturing exists in the X-FEM (Duflot, 2008, Liu et al., 2014, Zamani and Eslami, 2010), in the BEM method (Giannopoulos and Anifantis, 2005, Rinne et al., 2013, Shen, 2018), explicit DEM (Kwon et al., 2013), DDA (Jiao et al., 2015) and finally two-dimensional FEMDEM (Yan and Zheng, 2017).

Additionally, thermo-mechanical coupling and thermal fracturing capabilities are found within the particle based method, a sub-class of distinct element methods (explicit DEM), originally developed to model the behaviour of granular materials (Cundall and Strack, 1979). In particle based methods, the discrete elements are all disks in 2D and spheres in 3D. They are considered rigid thus only the element interaction needs to be solved. As a result, this method benefits from a low computational cost and large number of particles can be used. This makes particle based methods advantageous in micro-fracturing where the particle approach is a good approximation of the micro structure of rocks (Koyama et al., 2013).

To model fracture mechanics in particle based methods, Potyondy and Cundall (2004) developed a bonded particle model (BPM) where intact materials are represented by an assembly of bonded particles which may break under certain stress intensity. Within this framework, Wanne and Young (2008) proposed an extension of the BPM with thermo-elastic bonds for the thermal fracturing of granites. To resolve heat conduction in the particle system, Feng et al. (2008) presented a 2D model where contacting circular particles share heat flux bonds with their neighbours, such models also exist in 3D using spherical particles (Rickelt et al., 2009). When combining the thermal and bonded particle type of models, thermal fracturing was achieved by Xia et al. (2015, 2014) for circular particles and by André et al. (2017) for spherical particles.

Among particle based methods we also find the peridynamic method (Silling, 2000) which principal advantage is that its governing equations stay valid over discontinuities. Within the peridynamic framework, Wang et al. (2018) recently developed a thermo-mechanical model for the thermal cracking of rocks.

This chapter is focused on the thermo-mechanical coupling developments within the geomechanical solver. The thermal model introduced in Chapter 3 is coupled with the existing finite strain model of the FEMDEM approach (Xiang et al., 2009a) and its fracture model (Guo, 2014). The thermo-elastic theory for large deformations is presented first, then the thermal stress is validated against analytical solutions and finally, a three-dimensional validation of thermally induced fracturing is presented.

4.1 Thermo-Elastic Theory for Finite Strain FEMDEM

4.1.1 Deformation Gradient F

We define $\mathbf{X}$ as the vector of the initial positions in the element and $\mathbf{x}$ the vector of current positions (Xiang et al., 2009a), we write:

$$\mathbf{X} = \begin{bmatrix} X \\ Y \\ Z \end{bmatrix} = \mathbf{X}_{on}\mathbf{N} \tag{4.1}$$

$$\mathbf{x} = \begin{bmatrix} x \\ y \\ z \end{bmatrix} = \mathbf{x}_{cn}\mathbf{N} \tag{4.2}$$

$\mathbf{N} = [N_1 \ N_2 \ ... \ N_{n_e}]$ is the shape function or interpolation function, n_e the number of nodes in the element, $\mathbf{X}_{on}$ and $\mathbf{x}_{cn}$ are respectively the original and current position arrays

$$\mathbf{X}_{cn} = \begin{bmatrix} X_1 & X_2 & ... & X_{n_e} \\ Y_1 & Y_2 & ... & Y_{n_e} \\ Z_1 & Z_2 & ... & Z_{n_e} \end{bmatrix} \tag{4.3}$$

$$\mathbf{x}_{on} = \begin{bmatrix} x_1 & x_2 & ... & x_{n_e} \\ y_1 & y_2 & ... & y_{n_e} \\ z_1 & z_2 & ... & z_{n_e} \end{bmatrix} \tag{4.4}$$

The deformation gradient tensor links the current position to the initial element positions:

$$\mathbf{F} = \frac{\partial \mathbf{x}}{\partial \mathbf{X}} = \mathbf{x}_{cn}\frac{\partial \mathbf{N}}{\partial \mathbf{X}} \tag{4.5}$$

The determinant of the matrix F is called the Jacobian

$$J = det(\mathbf{F}) \tag{4.6}$$

From here we define the left Cauchy-Green tensor:

$$\mathbf{B} = \mathbf{F}\mathbf{F}^{\top} \tag{4.7}$$

4.1.2 Velocity Gradient L

We introduce the velocity vector as

$$\mathbf{v} = \begin{bmatrix} v_x \\ v_y \\ v_z \end{bmatrix} = \mathbf{v}_{cn}\mathbf{N} \tag{4.8}$$

With $\mathbf{v}_{cn}$

$$\mathbf{v} = \begin{bmatrix} v_{x,1} & v_{x,2} & \cdots & v_{x,n_e} \\ v_{y,1} & v_{y,2} & \cdots & v_{y,n_e} \\ v_{z,1} & v_{z,2} & \cdots & v_{z,n_e} \end{bmatrix} = \mathbf{v}_{cn}\mathbf{N} \tag{4.9}$$

The velocity gradient is

$$\mathbf{L} = \nabla\mathbf{v} = \frac{\partial\mathbf{v}}{\partial\mathbf{x}} = \mathbf{v}_{cn}\frac{\partial\mathbf{N}}{\partial\mathbf{x}} \tag{4.10}$$

We can also write the velocity gradient in terms of the deformation gradient with

$$\dot{\mathbf{F}} = \frac{\partial\mathbf{F}}{\partial t} = \frac{\partial}{\partial t}(\frac{\partial\mathbf{x}}{\partial\mathbf{X}}) = \frac{\partial}{\partial\mathbf{X}}(\frac{\partial\mathbf{x}}{\partial t}) = \frac{\partial\mathbf{v}}{\partial\mathbf{X}} \tag{4.11}$$

$$\dot{\mathbf{F}} = \frac{\partial\mathbf{v}}{\partial\mathbf{X}} = \frac{\partial\mathbf{v}}{\partial\mathbf{x}}\frac{\partial\mathbf{x}}{\partial\mathbf{X}} \tag{4.12}$$

Hence

$$\dot{\mathbf{F}} = \mathbf{L}.\mathbf{F} \tag{4.13}$$

And

$$\mathbf{L} = \dot{\mathbf{F}}.\mathbf{F}^{-1} \tag{4.14}$$

Finally, we write the rate of deformation matrix as:

$$\mathbf{D} = \frac{1}{2}(\mathbf{L} + \mathbf{L}^{\top}) \tag{4.15}$$

4.1.3 Thermal Expansion

The linear thermal expansion coefficient corresponds to the one-dimensional change in length for a given temperature change and is noted α. According to the concept of multiplicative split of the deformation gradient (Vujosevic and Lubarda, 2002), the deformation gradient may be decomposed into an thermal component $\mathbf{F}_T$ and an elastic $\mathbf{F}_e$ component:

$$\mathbf{F} = \mathbf{F}_T \mathbf{F}_e \tag{4.16}$$

With

$$\mathbf{F}_T = \Upsilon(T)\mathbf{I} \tag{4.17}$$

For an isotropic material, $\Upsilon = \Upsilon(T)$ is the ratio linking the variation of temperature to a deformation in a principal direction and $\mathbf{I}$ is the identity matrix. We also deduct from the expression of the velocity gradient (4.14) that

$$\mathbf{L}_T = \frac{\dot{\Upsilon}}{\Upsilon}\mathbf{I} = \frac{1}{\Upsilon}\frac{\partial \Upsilon}{\partial t}\mathbf{I} = \frac{1}{\Upsilon}\frac{\partial \Upsilon}{\partial T}\frac{\partial T}{\partial t}\mathbf{I} \tag{4.18}$$

Consider now the volume V_T resulting from a thermal expansion event of an initial volume V_0 from a temperature T_0 to T

$$dV_T = det(\mathbf{F}_T)dV_0 \tag{4.19}$$

According to the relationship $\dot{J} = J \ . \ tr(\mathbf{L})$ (Ogden, 1997), the time derivative of the above expression is:

$$\frac{d}{dt}(dV_T) = tr(\mathbf{L}_T)dV_0 \tag{4.20}$$

Integrating equation 4.18 yields

$$\frac{d}{dt}(dV_T) = \frac{3}{\Upsilon}\frac{\partial \Upsilon}{\partial T}\frac{\partial T}{\partial t}dV_0 \tag{4.21}$$

The traditional temperature dependent thermal expansion coefficient is:

$$\alpha(T) = \frac{1}{\Upsilon}\frac{\partial \Upsilon}{\partial T} \tag{4.22}$$

Hence

$$\frac{d}{dt}(dV_T) = 3\alpha(T)\frac{\partial T}{\partial t}dV_0 \tag{4.23}$$

Integrating equation 4.22 over the temperature change gives

$$\Upsilon(T) = exp\left(\int_{T_0}^{T} \alpha(T)dT\right) \tag{4.24}$$

If the thermal coefficient is considered independent of temperature i.e. $\alpha(T) = \alpha$ and $\alpha|T - T_0| << 1$ we can admit the following approximation (Vujosevic and Lubarda, 2002)

$$\Upsilon(T) = 1 + \alpha\Delta T, \quad \Delta T = T - T_0 \tag{4.25}$$

4.1.4 Thermo-Elastic Tensors

Let us now rewrite the previous tensors in terms of the thermo-elastic decomposition. We start with developing equation 4.25 into equation 4.16

$$\mathbf{F} = (1 + \alpha\Delta T)\mathbf{F}_e \tag{4.26}$$

The Jacobian becomes

$$J = det(\mathbf{F}) = det(\mathbf{F}_T)\ .\ det(\mathbf{F}_e) = (1 + \alpha\Delta T)^3 det(\mathbf{F}_e) \tag{4.27}$$

We may also write

$$J = J_T J_e \tag{4.28}$$

The velocity gradient tensor becomes

$$\mathbf{L} = \dot{\mathbf{F}}.\mathbf{F}^{-1} = \left[\mathbf{F}_T\dot{\mathbf{F}}_e + \mathbf{F}_e\dot{\mathbf{F}}_T\right]\left[\mathbf{F}_T\mathbf{F}_e\right]^{-1} = \dot{\mathbf{F}}_T\mathbf{F}_T^{-1} + \dot{\mathbf{F}}_e\mathbf{F}_e^{-1} \tag{4.29}$$

Note that there is commutativity of the matrix product in the above development because both $\mathbf{F}_T$ and $\dot{\mathbf{F}}_T$ are a product between a scalar and the identity matrix. We obtain

$$\mathbf{L} = \mathbf{L}_T + \mathbf{L}_e \tag{4.30}$$

The left Cauchy-Green tensor becomes

$$\mathbf{B} = \mathbf{F}\mathbf{F}^{\top} = \mathbf{F}_T\mathbf{F}_e(\mathbf{F}_T\mathbf{F}_e)^{\top} \tag{4.31}$$

And

$$\mathbf{B} = \mathbf{B}_T \mathbf{B}_e \tag{4.32}$$

Finally, the rate of deformation matrix becomes

$$\mathbf{D} = \frac{1}{2}(\mathbf{L} + \mathbf{L}^\top) = \mathbf{D}_T + \mathbf{D}_e \tag{4.33}$$

4.1.5 Cauchy Stress

The Cauchy stress is defined as force per unit area and is necessary to solve the momentum equation. As given by Xiang et al. (2009a):

$$\mathbf{C} = \frac{\mu}{J}(\mathbf{B} - \mathbf{I}) + \frac{\lambda}{J}(\ln J)\mathbf{I} + \mathbf{C}_D \tag{4.34}$$

With λ and μ the Lamé coefficients and $\mathbf{C}_D$ the dissipative part of the stress defined as:

$$\mathbf{T}_D = 2\eta\mathbf{D} \tag{4.35}$$

With η the viscosity of the material considered.

4.1.6 Analysis of Stress Response

Now considering only internal forces caused by the thermal expansion we have

$$\mathbf{C}_T = \frac{\mu}{J_T}(\mathbf{B}_T - \mathbf{I}) + \frac{\lambda}{J_T}(\ln J_T)\mathbf{I} + \mathbf{C}_{D_T} \tag{4.36}$$

With J_T the volume change induced by thermal expansion:

$$J_T = det(\mathbf{F}_T) = (1 + \alpha\Delta T)^3 \tag{4.37}$$

Which yields

$$\begin{aligned}\mathbf{C}_T = \Bigg[& \frac{\mu}{(1+\alpha\Delta T)^3}((1+\alpha\Delta T)^2 - 1) \\ & + \frac{\lambda}{(1+\alpha\Delta T)^3}\ln(1+\alpha\Delta T)^3 \\ & + \frac{2\eta\alpha}{1+\alpha\Delta T}\frac{\partial T}{\partial t}\Bigg]\mathbf{I}\end{aligned} \tag{4.38}$$

We can use the two above expressions to perform a validation test, controlling the volumetric expansion with J_T and the associated stress with $\mathbf{C}_T$.

4.2 Validation Work

As discussed in Section 2.3, Solidity can solve the mechanical equations with an hybrid continuum-discontinuum FEMDEM approach or with a discontinuum explicit DEM approach (fracture model). In this Section, the thermo-mechanical coupling implemented in Solidity will be verified for both.

4.2.1 Cauchy Stress Validation

To make sure that the thermo-mechanical coupling model presented in this chapter is implemented correctly, the Cauchy stress response to a temperature change is verified. A single finite element is fixed in all directions and subjected to a temperature change. The Cauchy stress generated by thermal expansion at the element level is compared to the analytical result (Equation 4.38).

With the parameters given in Table 4.1 the Cauchy stress in all 3 directions is of 3.332 MPa and the value computed with Solidity for one element is of 3.332 MPa. Note that we do not consider here the transient term of the Cauchy stress which is associated with the dissipative part of the stress and depends on how fast the temperature changes.

Young's Modulus, E (GPa)	20
Poisson's ratio, ν (-)	0.2
Lamé first parameter, λ (GPa)	5.56
Lamé second parameter, μ (GPa)	8.33
Thermal expansion coefficient, α ($/°C$)	1×10^{-6}
Temperature change, ΔT ($°C$)	100

TABLE 4.1: Mechanical and thermal parameters for validation

4.2.2 Thermal Expansion Validation

The thermal expansion of a material for a given temperature change is verified. Consider cubical solid with 1 meter edges meshed with two different element sizes, (A) 1 m and (B) 0.1 m (Figure 4.1).

A simulation is performed with the thermo-mechanical properties and temperature change listed in Table 4.1. The temperature is increased uniformly from 0 $°C$ to 100 $°C$ over 0.1 s with an integration time step of 1.0×10^{-5} s for (A) and of 1.0×10^{-6} s for (B).

For the given temperature increase, the 1 m^3 cube expands to reach a volume of $1 * \mathbf{J}_T = (1+\alpha\Delta T)^3 = 1.003003$ m^3. This value is in accord with the simulation results for model (A) and (B), as shown on Figure 4.2, results are in agreement with the analytical solution. Note that no significant thermal stress is generated in this configuration because the temperature is increased uniformly and the cube is free to expand.

(A) mesh size = 1 m (B) mesh size = 0.1 m

Figure 4.1: Finite element model of the cube with two different mesh sizes

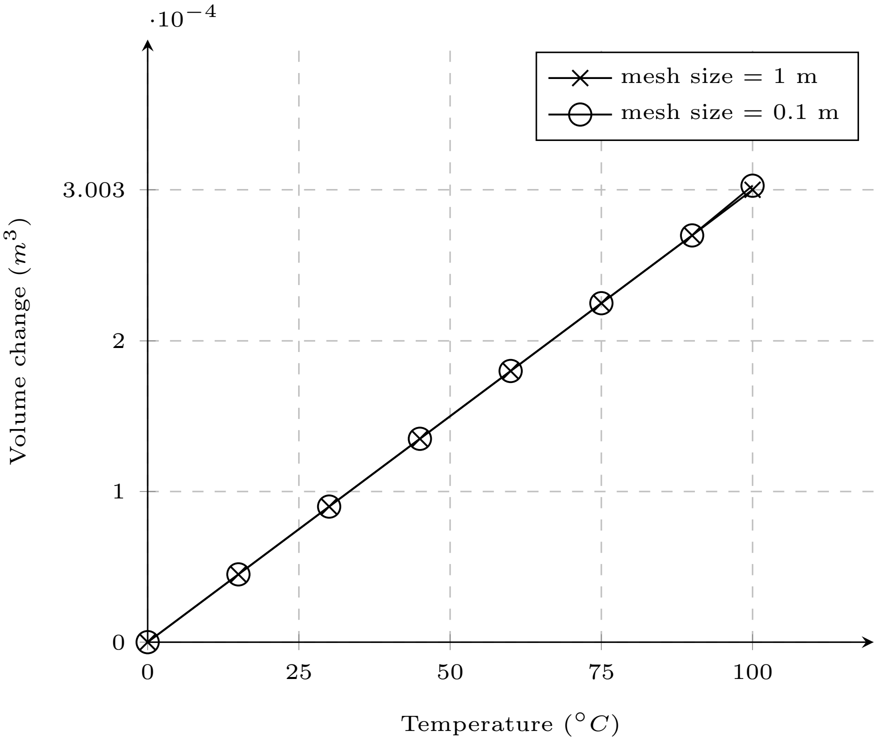

FIGURE 4.2: Temperature versus volume change of the cube for two different mesh sizes

4.2.3 Thermal Stress Validation: Hollow Cylinder

Now that the implementation of the TM model is verified, a validation of the thermal stress field is performed. A thermal-gradient must be present in order to generate differential thermal stress in the material.

Consider a hollow and thin cylinder as presented on Figure 4.3, with an inner and outer radii respectively a and b and a height h. A Dirichlet boundary condition is applied on the inner boundary of the thin cylinder with a temperature T_a and on the outer boundary with a temperature T_b. The faces normal to the Z direction are considered adiabatic.

For this problem, the temperature and stress solution are given by Noda et al. (2003):

$$T(r) = T_a + (T_b - T_a)\frac{\ln a}{\ln b}$$

$$\sigma_{rr} = \frac{\alpha E}{2}(T_b - T_a)\left[-\frac{\ln(r/a)}{\ln(b/a)} + \left(1 - \frac{a^2}{b^2}\right)\frac{b^2}{b^2 - a^2}\right] \tag{4.39}$$

$$\sigma_{\theta\theta} = \frac{\alpha E}{2}(T_b - T_a)\left[-\frac{1 + \ln(r/a)}{\ln(b/a)} + \left(1 + \frac{a^2}{b^2}\right)\frac{b^2}{b^2 - a^2}\right]$$

To validate the above analytical solution the hollow cylinder is meshed with 0.005m finite elements, see Figure 4.3. Note that when employing the hybrid FEMDEM on a single body, the discontinuum part is not recruited and the solver only uses the FEM. Thereby, two simulations are performed, one with the FEM solver (referred as 'continuum'), the other with the explicit DEM fracture model (referred as 'discontinuum'). Simulations are performed with an integration time step of $5.0 \times 10^{-9}s$ and the total simulation time is of $5.0 \times 10^{-3}s$. Material properties and boundary conditions are listed on Table 4.2. Temperature, radial and transverse thermal stress results are respectively presented on Figure 4.4, 4.5 and 4.6, good agreement is observed between simulation results and analytical solution.

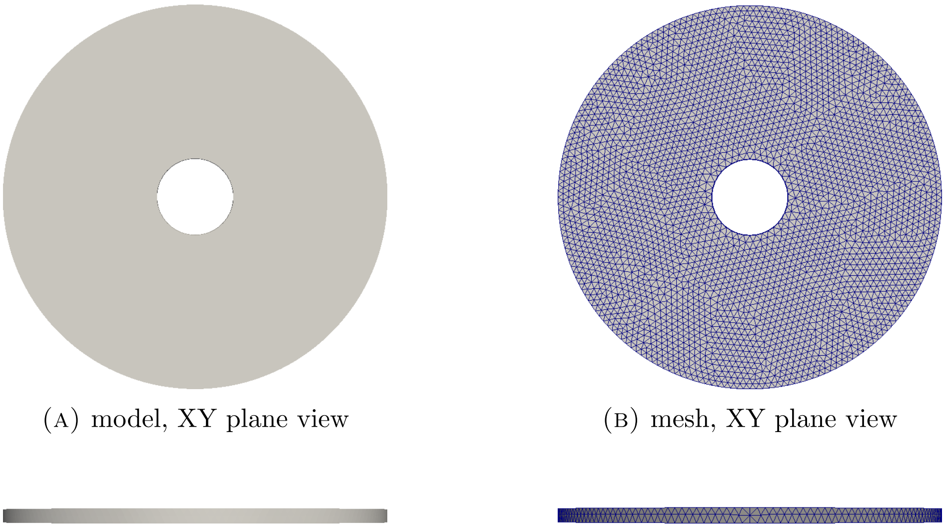

(A) model, XY plane view

(B) mesh, XY plane view

(C) model, XZ plane view

(D) mesh, XZ plane view

FIGURE 4.3: 3D model of the hollow cylinder

Geometry

Inner radius, a (m)	0.03
Outer radius, b (m)	0.15
Height, h (m)	0.01

Mechanical

Young's Modulus, E (GPa)	20
Poisson's ratio, ν	0.2
Internal cohesion, (MPa)	20
Tensile strength, (MPa)	10
Fracture penalty number, (GPa)	10^3
Fracture normal energy release rate	50
Fracture shear energy release rate	100
Internal friction (rad)	577

Thermal

Thermal expansion coefficient, α ($/°C$)	5×10^{-6}
Initial temperature, ΔT ($°C$)	0
Inner temperature, T_a ($°C$)	0
Outer temperature, T_b ($°C$)	100

Table 4.2: Mechanical and thermal parameters for validation.

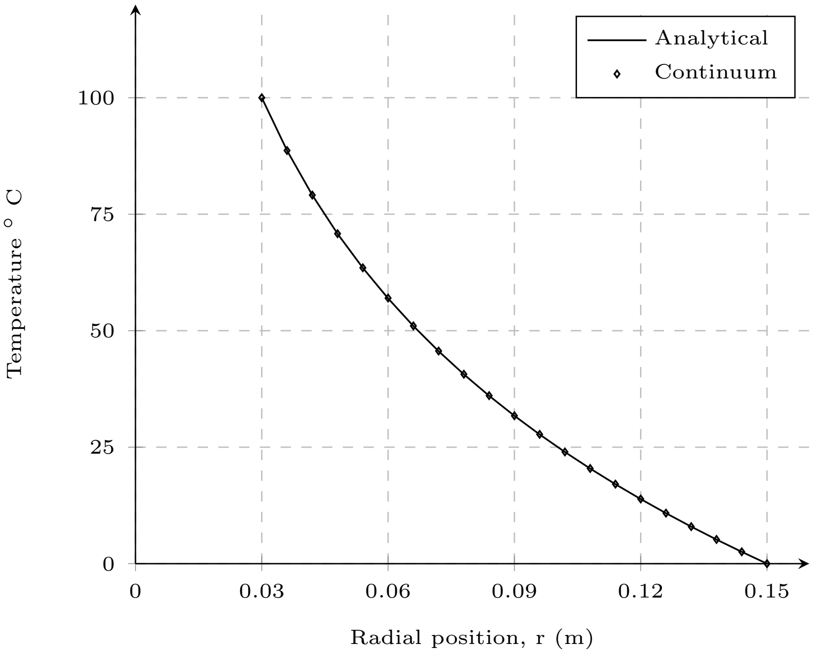

Figure 4.4: Steady state temperature profile in the hollow cylinder

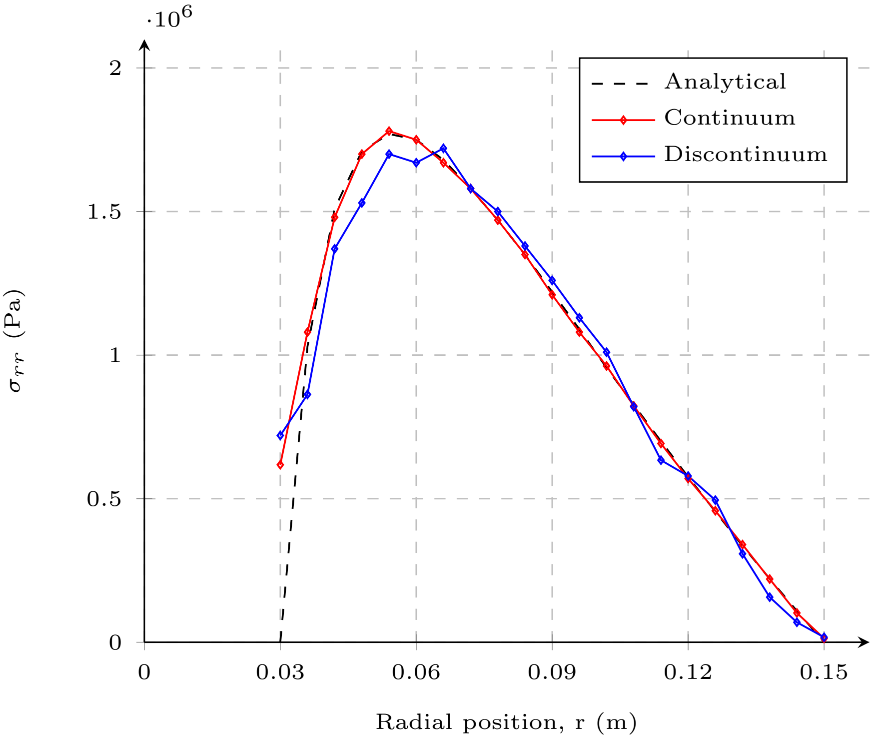

Figure 4.5: Radial thermal stress σ_{rr} in the hollow cylinder

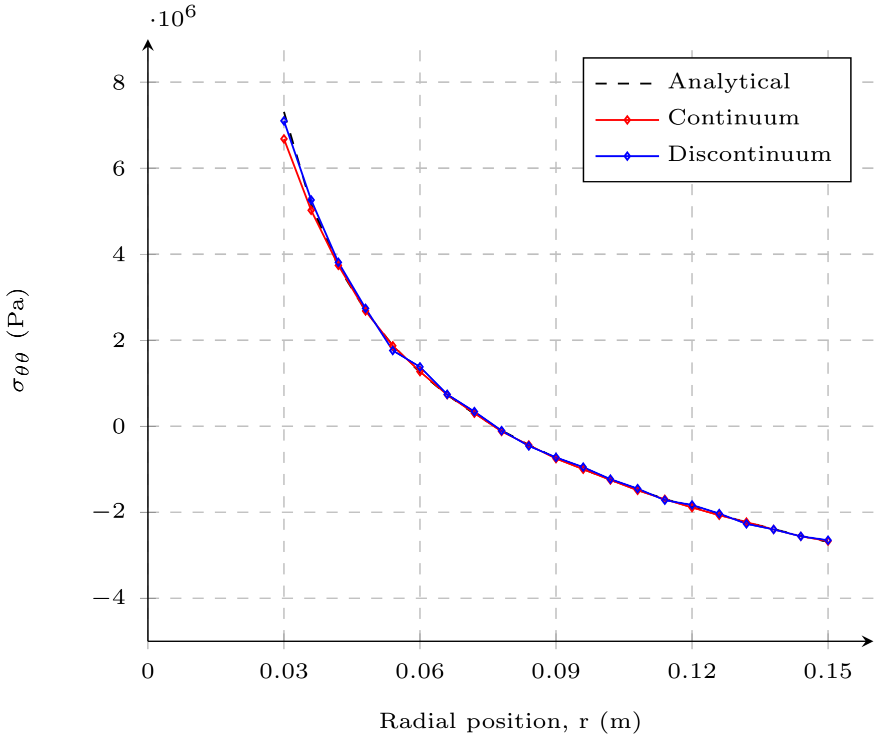

FIGURE 4.6: Transverse thermal stress $\sigma_{\theta\theta}$ in the hollow cylinder

4.2.4 Thermal Fracturing Validation: Hollow cylinder

Now that the stress field has been validated against Equation 4.39, this analytical solution is used again to dimension a simulation that will generate a fracture. For a tensile fracture to appear, the thermal stress in the transverse direction ($\sigma_{\theta\theta}$) must exceed the tensile strength of the material.

The thermal expansion coefficient of the material is increased sixfold, the maximal $\sigma_{\theta\theta}$ that will be generated in the cylinder is now higher than the tensile strength of the material, as highlighted on Figure 4.7, fractures are expected to initiate on the outer boundary of the cylinder. Note that on Figure 4.7, only the continuum stress profile is compared to the analytical solution because when fractures are generated in the discontinuum simulation, the stress field is perturbed.

Graphical results of the discontinuum simulation are presented on Figure 4.8. The first two cracks appear on the outer boundary of the cylinder (4.8b) and propagate to the centre of the cylinder (4.8c). Then, several cracks initiate in the inner boundary of the cylinder, three of them propagate outward (4.8d) and two of them cut through to the outer boundary of the cylinder (4.8e).

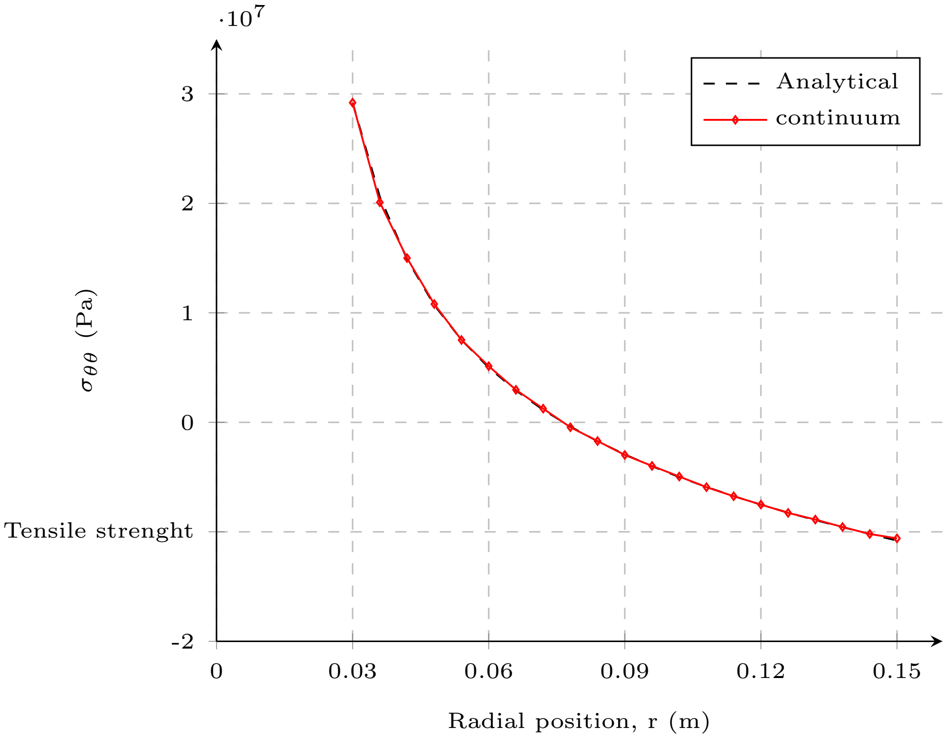

FIGURE 4.7: Transverse thermal stress $\sigma_{\theta\theta}$ in the hollow cylinder

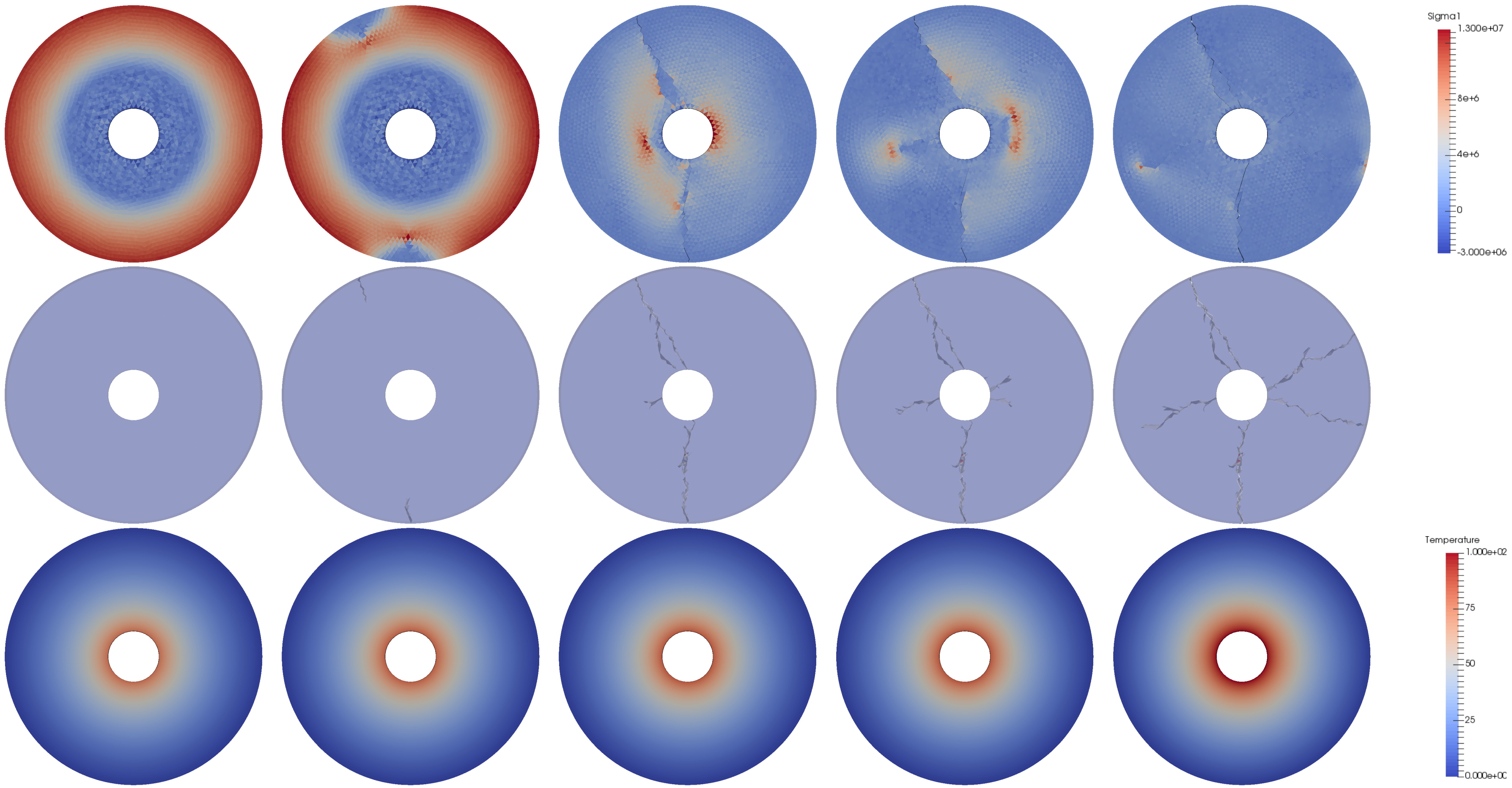

(A) t = 3.950 ms (B) t = 4.109 ms (C) t = 4.199 ms (D) t = 4.220 ms (E) t = 5.0 ms

FIGURE 4.8: Thermal fracturing of the hollow cylinder at different times (A-E). First row is the maximal principal stress (σ_1), second row is the crack pattern and third row is the temperature field displayed on the continuum mesh

4.2.5 Thermal Stress Validation: Concentric cylinders

The cracking of reinforced concrete structures under thermal stress was investigated numerically and experimentally by Abdalla (2006), this work has been the basis for validation of some of the numerical methods presented in the introduction of this chapter (Wang et al., 2018, Yan and Zheng, 2017). Reinforcements in concrete are often made of steel which has a higher thermal expansion coefficient. Upon heating, the steel exerts a pressure on the concrete cover and induces fracturing, see Figure 4.9.

(A) Experimental model

(B) Experimental results after heating

Figure 4.9: Thermal cracking due to differential thermal expansion of a reinforcement embedded in concrete (Abdalla, 2006).

A solution of the radial stress is given in Abdalla (2006):

$$\begin{aligned} \sigma_{\theta\theta} &= \frac{a^2(b^2+r^2)}{r^2(b^2-a^2)}p \\ p &= \frac{(\alpha_a-\alpha_b)\Delta T E_a}{E_a/E_b(\beta+\nu_b)+(1-\nu_a)} \\ \beta &= \frac{b^2+a^2}{b^2-a^2} \end{aligned} \tag{4.40}$$

First, this expression is verified with the continuum and discontinuum models using coefficients of thermal expansion ten time smaller than the experiment: $\alpha_a = 7.2 \times 10^{-7}/°C$ and $\alpha_b = 2.2 \times 10^{-6}/°C$. Then, the discontinuum model is employed with the thermal expansion coefficients of the experiment (Table 4.3) and the fracture pattern is compared to the experiment.

The model presented on Figure 4.10 is meshed with 0.005 m finite elements, for all simulation an integration time step of $5.0 \times 10^{-9}s$ is used. The total simulation time is of $5.5 \times 10^{-3} s$ and temperature is increased uniformly from $0°C$ to $100°C$ over a time of $5.0 \times 10^{-3} s$.

Results are presented on Figure 4.11 for σ_{rr} and on Figure 4.12 or $\sigma_{\theta\theta}$. The stress profiles show that the tangential stress is maximal for $r = a$, this is where fracture is expected to initiate when using the experimental thermal expansion coefficients $\alpha_a = 7.2 \times 10^{-6}/°C$ and $\alpha_b = 2.2 \times 10^{-5}/°C$. Simulation results of the thermal fracturing simulation performed with the the experimental thermal expansion coefficients is shown on Figure 4.13.

In summary, Figure 4.12 shows good agreement between the stress profile and the analytical solution. Moreover, the final fracture pattern (Figure 4.13e) is consistent with experimental results (Figure 4.9b) in the sense that radial cracks propagate in the concrete, from the interface with steel and up to the outer boundary. In the light of the several successful validations performed in this chapter, the thermo-mechanical strong coupling is considered complete.

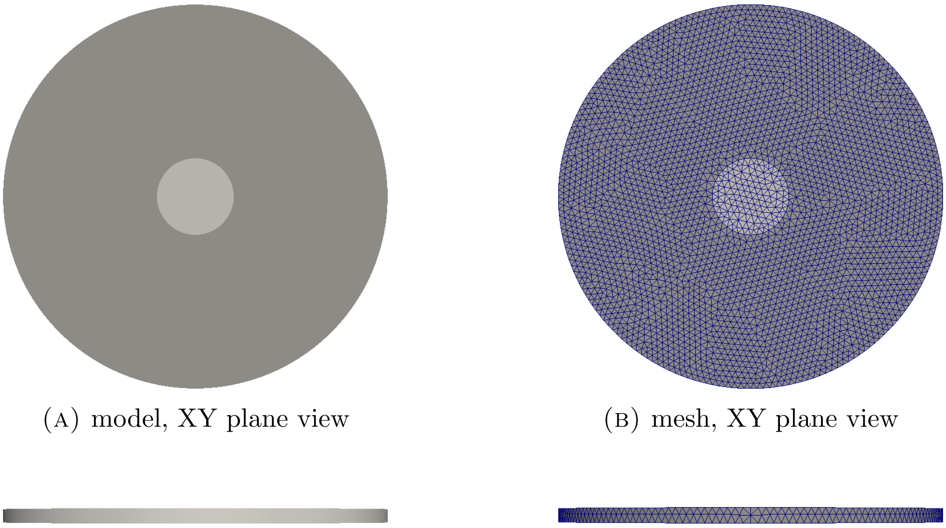

(A) model, XY plane view

(B) mesh, XY plane view

(C) model, XZ plane view

(D) mesh, XZ plane view

Figure 4.10: 3D model of the concrete reinforcement.

Geometry	Outer cylinder: Concrete	Inner cylinder: Steel
Radius (m)	b = 0.03	a = 0.15
Height, h (m)	0.01	0.01

Mechanical

Young's Modulus, E (GPa)	20	40
Poisson's ratio, ν	0.2	0.3
Density, ρ (kg/m^3)	2300	2300
Internal cohesion, (MPa)	20	20
Tensile strength, (MPa)	10	20
Fracture penalty number, (GPa)	4.10^3	4.10^3
Contact penalty number, (GPa)	40	40
Fracture normal energy release rate	50	100
Fracture shear energy release rate	100	100
Internal friction (rad)	577	577

Thermal

Thermal expansion coefficient, α ($/^\circ C$)	7.0×10^{-6}	2.2×10^{-5}
Initial temperature, T_0 ($^\circ C$)	0	
Temperature increase, Δ_T ($^\circ C$)	100	

Table 4.3: Mechanical and thermal parameters for validation

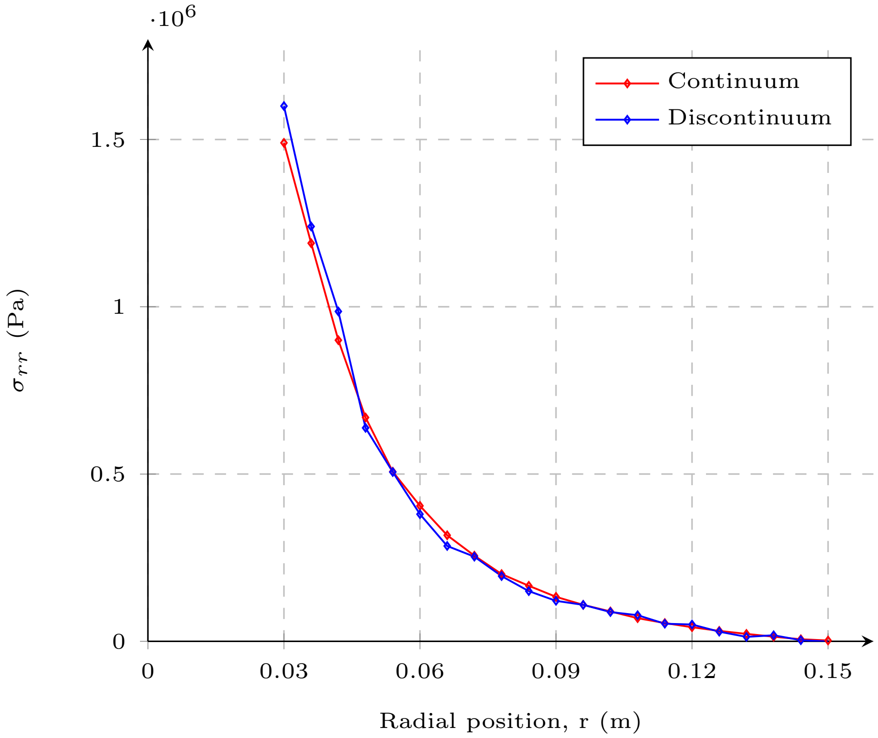

FIGURE 4.11: Radial stress σ_{rr} in the outer cylinder

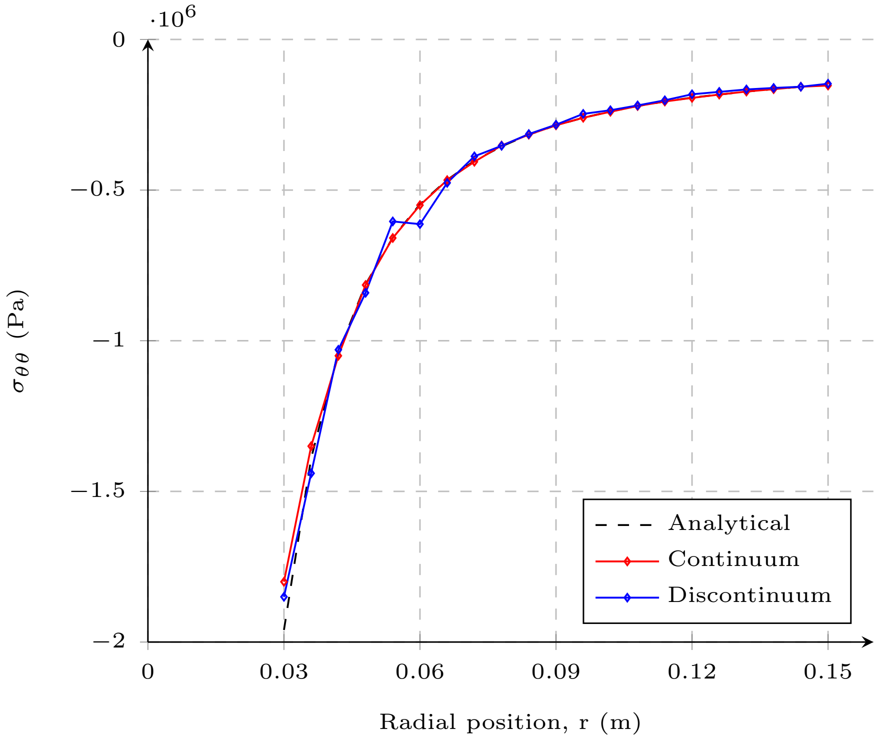

FIGURE 4.12: Tangential stress $\sigma_{\theta\theta}$ in the outer cylinder

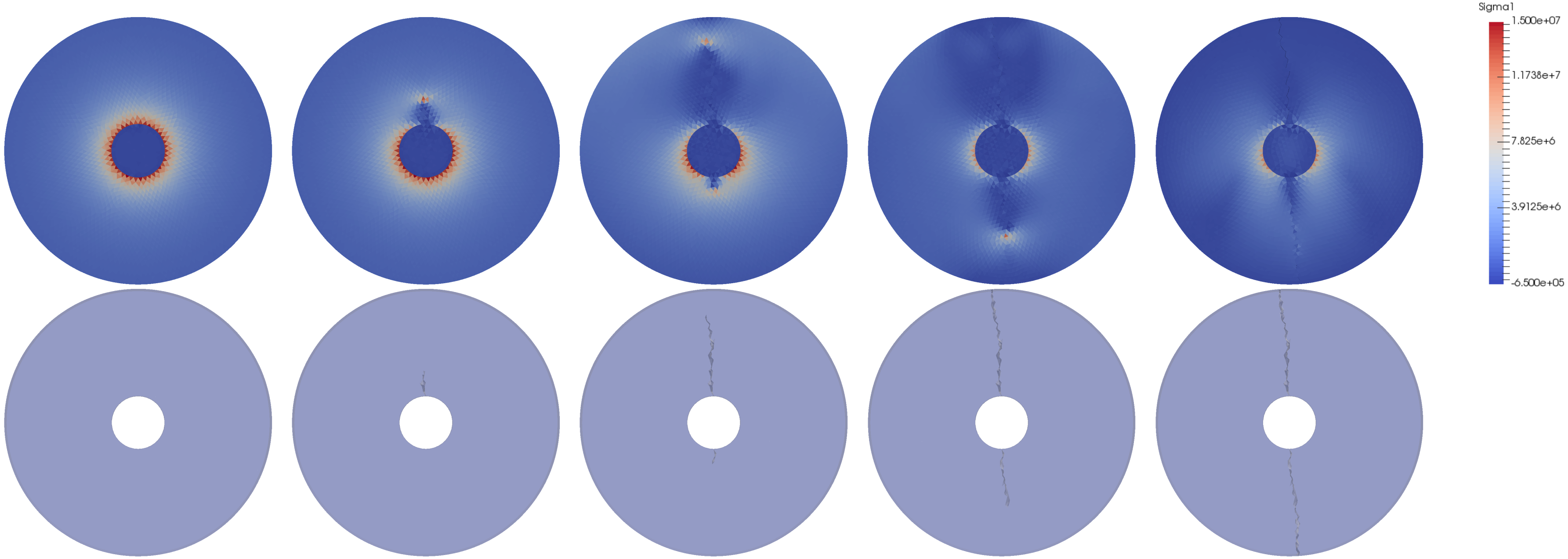

(A) t = 3.650 ms
T = 73.00°C

(B) t = 3.680 ms
T = 73.59°C

(C) t = 3.731 ms
T = 74.61°C

(D) t = 3.761 ms
T = 75.23°C

(E) t = 5.5 ms
T = 100.00°C

FIGURE 4.13: Thermal fracturing of the reinforced concrete cylinder at different times (A-E). First row is the maximal principal stress (σ_1) and second row is the crack pattern

Chapter 5

Thermal Coupling in the Dual Code Framework

This chapter puts forward the details, implementation and validation of a new numerical method to couple heat transfer between the thermo-hydraulic solver and the thermo-mechanical solver of the Fluidity-Solidity architecture. The main part of the research introduced in this chapter is specific to fluid-structure interaction (FSI) problems which focus on the behaviour of solids and their surrounding fluid. Thus the developments and validations are mostly presented in a FSI context which is not the main focus of the thesis. Nevertheless, the numerical method proposed in this chapter can also be applied to THM coupled process in fractured porous media, that aspect is discussed but it will only be demonstrated in the next chapter.

5.1 Literature Review: FSI Numerical Methods

Many engineering fields rely on inputs from FSI numerical methods in areas such as nuclear energy (Buchan et al., 2014), coastal engineering (Latham et al., 2009), rock blasting (Yang et al., 2017) or aerodynamics (Jindal et al., 2005). In FSI problems, the solid can be considered static, mobile, deformable, brittle, porous etc, and the fluid can be compressible, incompressible, turbulent, etc. This explains the great variety of numerical approaches, each one most suited to a specific configuration. We find in the literature four types of criterion to classify FSI methods (Sections 5.1.1 to 5.1.4), in most cases the criterion are independent which reflects on the multitude of possible combinations.

5.1.1 Mathematical Formulation

The first classification is based on the mathematical formulation of space. Numerical methods aim to render the behaviour of a physical phenomena by computing the associated quantity (velocity, temperature,...) for a given media (fluid, gas or solid) at different points of space and time, the given numerical problem is said to be discretised in space and time. The space discretisation corresponds to an assembly of connected points forming the computational mesh or grid whereas, the time discretisation is a succession of points in time, together they form the computational system. Upon solving the computational system, the physical quantity is obtained at the points where and when it was discretised. To achieve the space discretisation, there are three types of formulations:

The Lagrangian formulation, where the computational system is fixed to the represented physical phenomena (Figure 5.1a). This is particularly helpful when dealing with solids as the mesh will move and deform like the solid does. The drawback of this method is its inability to capture the large deformations of the material, because as the shape of the material changes the computational grid is deformed as well and may no longer be suitable to describe the material's behaviour. Hence, this method is mostly suited to solid mechanics where deformations are much smaller than in fluids. When dealing with FSI problems a full Lagrangian approach may be adopted, while solids are represented traditionally, the fluid is described with a large number of particles, this is known as the Smoothed Particle Hydrodynamics (SPH) method (Rafiee and Thiagarajan, 2009, Ryzhakov et al., 2010).

The Eulerian formulation, where the computational system is fixed in space and the media is moving within (Figure 5.1b), this easily represents the behaviour of a fluid within its container. More specifically the media is treated as a continuum which means the container or domain is filled with fluid(s). However, Eulerian methods do not introduce interfaces structurally (for example: an air-water interface) and in order to capture interfaces accurately, the mesh will have to be refined where they are (García et al., 2011). An Eulerian only approach may be adopted for FSI problems, for example this is achieved by Coquerelle and Cottet (2008) with an immersed boundary method and by Dunne and Rannacher (2006) with a Cartesian grid method.

The Arbitrary Lagrangian-Eulerian scheme, ALE (Donea et al., 2004, Hübner et al., 2004, Udaykumar et al., 2001, Van Loon et al., 2007). Designed specifically for FSI problems, the ALE scheme describes the computational domain as a continuum but allows to have either the continuum moving with respect to the mesh or to have the mesh moving with the continuum. Large deformations of the fluid can be handled whilst an interface is kept moving to account for the presence of a solid (Figure 5.1c). ALE methods are said to be boundary-conforming and when dealing with moving solids, re-meshing techniques must be employed to maintain a sharp fluid-solid interface. Such techniques are generally associated with a significant computational cost.

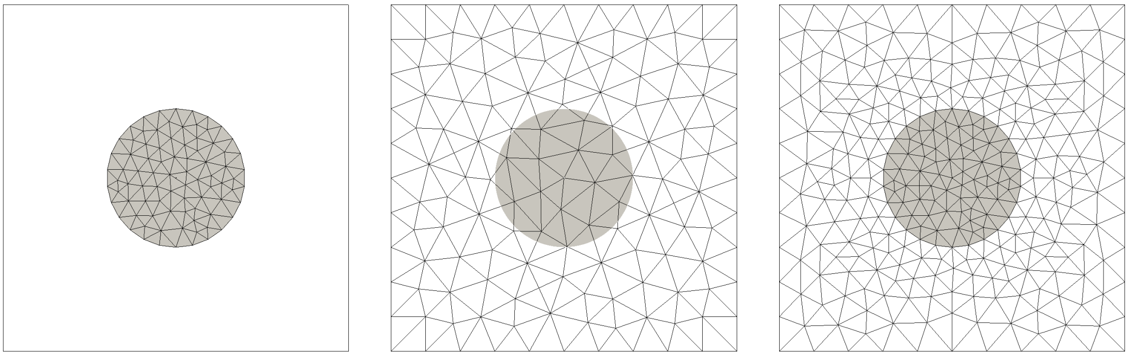

(A) Lagrangian (B) Eulerian (C) ALE

FIGURE 5.1: Different methods for the spatial representation of a circular field in two dimensions

5.1.2 Coupling Scheme

The second criteria distinguishes between the computational system solving methods. The system comprises of distinct equations relative to the hydraulic, mechanical and thermal processes. In the monolithic or strong coupling approach (Coquerelle and Cottet, 2008, Gibou and Min, 2012, Hübner et al., 2004, Peskin, 1972, Ryzhakov et al., 2010) the system of equations is solved at once, using the same numerical solver.

On the other hand, the loose, partitioned, fractional or weak coupling approach (Apte et al., 2009, Farhat et al., 1998, Gibou and Min, 2012, Jaiman et al., 2006, Rutqvist et al., 2002, Viré et al., 2012, 2015, 2013) is composed of separate solvers. Each one in charge of solving their respective equations. Hence, there is an iteration process between the two solvers, this relies on the introduction of a coupling term in the fluid and the solid equations to allow the exchange of information at each time iteration.

In a comparison of monolithic and loose methods, Michler et al. (2004) argues that the iteration process of partitioned methods produces staggered results over time. Consequently, they must comply to a restriction on the time step size in order to achieve accuracy. On the contrary, monolithic methods are unconditionally stable and may achieve accuracy for larger time steps.

However, despite conditional stability, loosely coupled approaches can conserve the most appropriate formulation for hydraulic and mechanical processes (respectively Eulerian and Lagrangian). Fluid and solid solvers may also have different time-steps, hence the number of necessary iterations may be reduced to their respective minimum depending on the problem configuration. Furthermore, the loose approach is often preferred because fluid and solid numerical tools have been developed by research groups separately for many years, allowing the coming together of two mature technologies (Obeysekara, 2018, Rutqvist et al., 2002, Yang, 2018).

5.1.3 Body-Conformation of the Mesh

FSI numerical methods can be separated based on the body conformal character of their mesh. As explained by Mittal and Iaccarino (2005), in body-conforming methods there are first the Cartesian grid methods (Figure 5.2a) (Clark et al., 1986, DeZeeuw and Powell, 1993, Dunne and Rannacher, 2006, Russell and Wang, 2003, Udaykumar et al., 2001, 1999, 1996), originally introduced by Clark et al. (1986) with an Eulerian formulation where the cells of the grid are parametrised to account for the presence of a solid boundary. Second, there are the methods known as 'cut-cell' which split the cells to match the solid-fluid interface (DeZeeuw and Powell, 1993, Udaykumar et al., 2001, 1999, 1996).

For the Cartesian grid or cut-cell methods, the use of techniques that can track the boundary of the solid structure as a sharp interface are necessary and this may become computationally challenging when dealing with deformations or movement of the solid (Udaykumar et al., 1999). Such methods are often associated with the ALE formulation for which the body-conformity of the mesh is a requirement (Donea et al., 2004, Hübner et al., 2004, Udaykumar et al., 2001).

As opposed to the previous, the immersed boundary (Peskin, 1972 and Fadlun et al., 2000), volume penalization (Angot et al., 1999, Coquerelle and Cottet, 2008, Engels et al., 2015), fictitious domain (Apte et al., 2009, Glowinski et al., 1994, Van Loon et al., 2007), ghost-cell (Mittal et al., 2008), immersed body (Kajishima et al., 2001, Viré et al., 2012, 2013) or immersed shell methods (Viré et al., 2015, Yang et al., 2016) have grids that do not conform to the solid boundary (Figure 5.2b) . In such methods, the boundary conditions are modified in the fluid equation at the vicinity of the solid's boundary.

For body-conforming methods, the sharp fluid-solid interface makes resolving boundary conditions straightforward. Whereas for non-body conforming methods, the boundary is not introduced in a structural manner. Thus, to achieve sufficient accuracy at the solid boundary, non-body conformity requires projection methods (Farrell and Maddison, 2011, Pain et al., 2001) and local mesh refinement (García et al., 2011, Griffith et al., 2007) which also comes at a significant computational cost. Nevertheless, the task of mesh generation is significantly easier than for body-conforming methods especially when dealing with intricate solid boundaries or with moving solids.

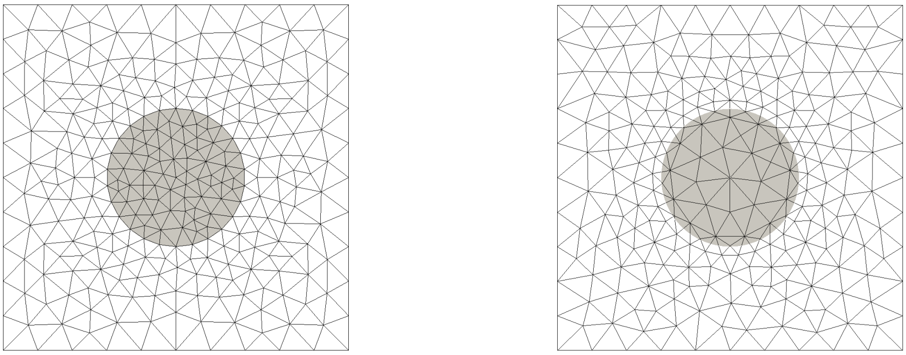

(A) Body-conforming mesh

(B) Non-body-conforming mesh with a refined mesh at the fluid-solid interface

FIGURE 5.2: Different type of fluid mesh in FSI numerical methods with an immersed solid (grey)

Note that the volume penalization method (Angot et al., 1999, Engels et al., 2015) has many similarities to the volume relaxation method (Kajishima et al., 2001, Viré et al., 2012) which is part of the research presented hereby. In volume penalization methods, the solid is seen as an impermeable barrier with the use of a 'volume penalisation' term in the momentum equation to enforce the boundary condition (similar to the volume relaxation in the immersed body method). In the original method (Angot et al., 1999), the relaxation coefficient is the inverse of very low permeability and Coquerelle and Cottet (2008), Engels et al. (2015) use an arbitrary large coefficient. In the original immersed body method Kajishima et al. (2001) the volume relaxation is employed to counter balance the fluid equation and relax to the solid velocity, this is done with a coefficient equal to the mass divided by the time step.

5.1.4 Forcing Term

According to Mittal and Iaccarino (2005), numerical methods can also be separated from the point of view of the implementation of the forcing term (also referred as source, penalty or relaxation term) into the Navier-Stokes equation. First, we have the continuous forcing approach where the source term is introduced together with the discretisation (immersed boundary, volume penalisation methods, immersed shell as by Yang et al. (2016)). Second, the discrete forcing approach has first the equations discretised with no account for the fluid-solid boundary until a supplementary term is introduced to account for its presence and thus correct the initial discretisation (immersed body, immersed shell as by Viré et al. (2015), cut-cell and Cartesian grid methods).

5.1.5 Heat Transfer in FSI Methods

The literature review has covered so far the general methods for fluid-structure interaction. They are typically developed for the coupling of momentum, the coupling of scalar fields such as temperature has received relatively less attention from the scientific community despite the fact that thermal problems in a wide range of FSI applications such heat exchangers, nuclear and chemical reactors, electronic equipment cooling or engine manufacture.

The reason for the low interest may be that in a large number of cases, thermal applications are dealt as conjugated heat transfer problems (CHT, Dorfman and Renner, 2009). Often in CHT problems we find (i) a fixed solid-fluid boundary, (ii) a boundary conforming mesh and (iii) a monolithic solver with a continuous forcing approach. Thus addressing a class of problems where the structure is fixed with a fluid flowing past.

On the contrary, the present approach is suited to the heat transfer of moving and deformable solids immersed in fluids. For this category of problems, Fadlun et al. (2000) implemented the traditional immersed boundary momentum coupling with the introduction of a passive scalar. Kim and Choi (2004) performed fluid-solid temperature coupling by introducing a heat source or sink as a relaxation term in the energy equation in the same way it is done for momentum coupling with the immersed body method (Kajishima et al., 2001). This method was pursued and developed in three dimensions leading to more accurate and advanced results for the study of convection heat transfer by Kim et al. (2008) and Yoon et al. (2010). However, those methods solely consider the solid as a heat source or sink and do not consider the fluid's influence on the solid, they are one-way coupled.

5.2 Fluid-Solid Coupling background

The research presented in this chapter is a continuation of the work on the Fluidity-Solidity coupled architecture initiated by Viré et al. (2012, 2015, 2013) and complemented by Yang et al. (2018, 2016) for momentum coupling with the Navier-Stokes equation and by Obeysekara et al. (2018, 2017, 2018) for the hydro-mechanical coupling in fractured porous media with Darcy's law.

The method has evolved from immersed body (Viré et al., 2012, 2013) to immersed shell (Viré et al., 2015, Yang et al., 2016) and is now loosely coupled, non-body conforming with a continuous forcing approach. Two separate solvers are employed for fluid and solid respectively of Eulerian (Fluidity) and Lagrangian formulation (Solidity), the method is also two-way coupled as the solid influences the fluid and vice versa.

Distinction must be made between:

(i) The physical domains of fluid (V_f) and solid (V_s) that are distinct and not superimposed (Figure 5.3).

(ii) The computational domains which comprises of:

  (a) A solid computational domain (V_s) solved with Solidity

(b) A fluid computation domain (V) solved with Fluidity. V encompasses the fluid physical domain (V_f) and the projection of the solid computational domain that we call V_s^f (see Figures 5.4 and 5.5). V is such that $V = V_f \cup V_s^f$.

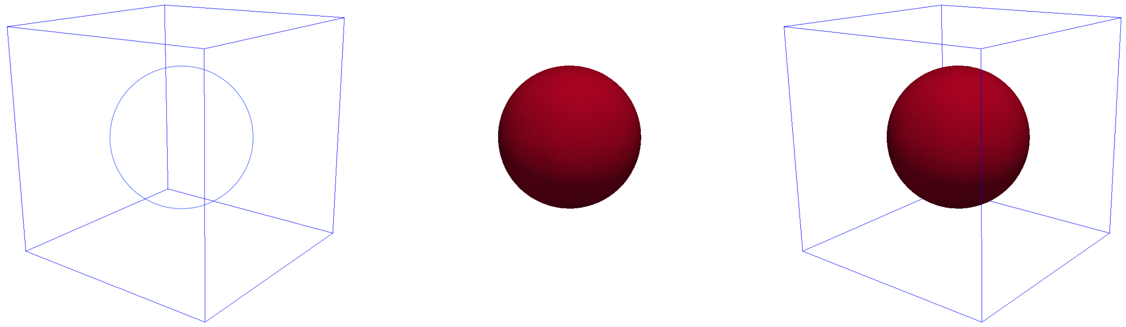

(A) Boundaries of the fluid physical domain V_f (B) Solid physical domain V_s (C) V_f and V_s

FIGURE 5.3: Configuration of fluid and solid physical domains in three dimensions.

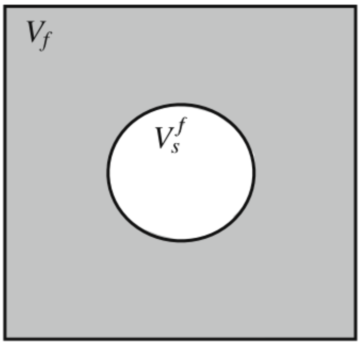

FIGURE 5.4: Two-dimensional schematic representation of the fluid computational domain V, with $V = V_f \cup V_s^f$ (Viré et al., 2012).

On the computational domain V, V_f is represented by a volume fraction of fluid α_f and V_s^f is represented by a volume fraction of solid or 'solid concentration' α_s (Figure 5.5) such that:

$$\alpha_f + \alpha_s = 1 \tag{5.1}$$

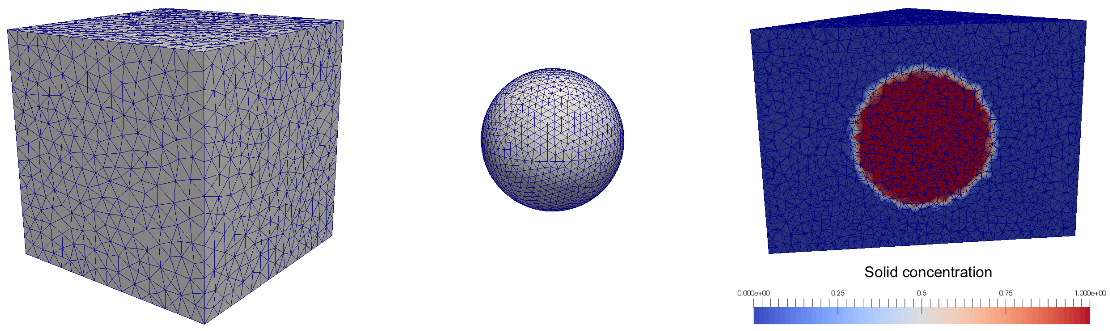

(A) Fluid computational domain V

(B) Solid computational domain V_s

(C) Solid concentration distribution on a cross section of the fluid computational domain

FIGURE 5.5: Computational domains.

A mesh to mesh Galerkin projection (Farrell and Maddison, 2011) ensures that information such as solid concentration or velocity is transferred from the solid to the fluid and vice-versa. In the original immersed body method (Kajishima et al., 2001) and in (Viré et al., 2012) the bulk velocity $\mathbf{u}_b = \alpha_s \mathbf{u}_s + \alpha_f \mathbf{u}_f$ is relaxed to the solid velocity $\mathbf{u}_s$ on V_s^f (with $\mathbf{u}_f$ the fluid velocity). This is achieved with a relaxation term inserted in the fluid momentum equation. The relaxation term or 'penalty force' is of the form $F_f = \alpha_s \beta(\mathbf{u}_s - \mathbf{u}_b)$, with β the relaxation factor which indicates how fast the fluid and solid velocities equal each other at the interface. For two way coupling, the opposite penalty force $F_s = \beta(\mathbf{u}_b - \mathbf{u}_s)$ is inserted in the solid momentum equation.

The drawback of this approach is that the penalty force is applied on the volume V_s^f ($\alpha_s > 0$) when it should only be acting at the fluid-solid boundary. Note that when developing the expression of the bulk velocity into the penalty force, we find that $F_f = \alpha_s \alpha_f \beta(\mathbf{u}_s - \mathbf{u}_f)$ with the product $\alpha_s \alpha_f$ only non-zero at the fluid-solid interface. This was used by Viré et al. (2015) to correct the immersed body approach by solving for $\mathbf{u}_f$ instead of $\mathbf{u}_b$ and by mapping the penalty force on a thin shell surrounding the solid (Figure 5.6). Instead of projecting the whole solid mesh onto the fluid mesh, only the shell mesh is projected (Figure 5.7). The coupling term becomes $F_f = \alpha_{sh} \beta(\mathbf{u}_f - \mathbf{u}_s)$ with α_{sh} the shell concentration. As a result, the penalty force only acts at fluid-solid boundary and vanishes inside the solid.

Finally, Yang et al. (2016) completed the immersed shell method with a continuous forcing approach, presented in Section 5.3.2. By multiplying the fluid equation with the fluid concentration α_f, the approach ensures that all the terms of the fluid equation disappear at the solid's position (i.e. $\alpha_f = 0$). However, for the fluid equation to be continuous over the fluid computational domain there needs to be a stabilisation term or 'body relaxation term' which was not introduced in the formulation until the present work.

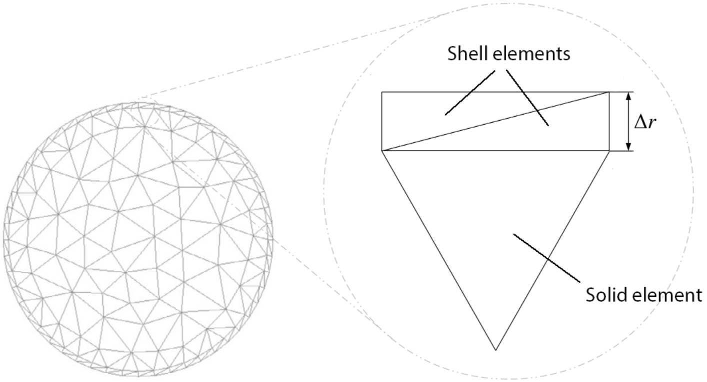

FIGURE 5.6: Geometry of the ring mesh in two dimensions. Left: the solid mesh with its surrounding shell mesh, right: a 3D solid element with its shell mesh. Δ_r is the ring mesh thickness (Yang et al., 2016)

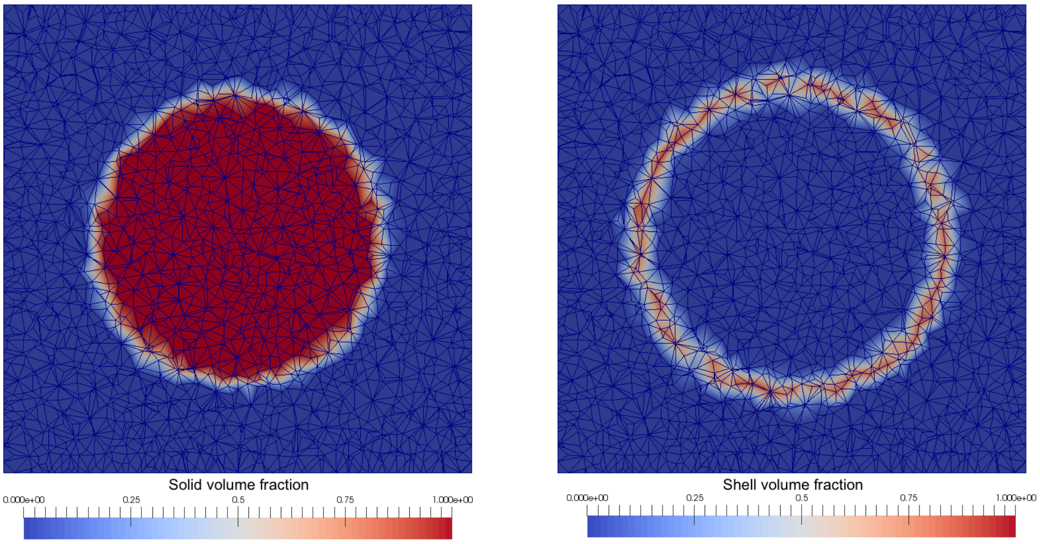

(A) Solid volume fraction α_s

(B) Shell volume fraction α_{sh}

FIGURE 5.7: Projection of the solid (A) and the shell mesh (B) onto the fluid mesh

5.3 Thermal Coupling Methodology

As for clarity and differentiation of the solid and fluid equations for heat transfer, constants and variables referring to the solid terms will adopt the subscript 's' whereas the subscript 'f' will be employed for the fluid terms. The governing equations used for the thermal coupling are the fluid thermal energy equation:

$$\rho_f C_f(\frac{\partial T_f}{\partial t} + \mathbf{u}_f \cdot \nabla T_f) + \nabla \cdot (\kappa_f \nabla T_f) = 0 \tag{5.2}$$

and the solid thermal energy equation:

$$\rho_s C_s \frac{\partial T_s}{\partial t} + \nabla \cdot (\kappa_s \nabla T_s) = 0 \tag{5.3}$$

Note that the heat transfer properties are considered as constants. This section covers both the immersed body and the immersed shell methods and explains why they are not sufficient to model two way coupled fluid-solid heat transfer. Finally, a combined immersed ring-body approach is proposed.

5.3.1 Immersed Body Method

For thermal coupling with the original immersed body method as introduced by Kajishima et al. (2001), a thermal coupling term s_c is introduced in the fluid thermal energy equation to account for the presence of the solid:

$$\rho_f C_f(\frac{\partial T_f}{\partial t} + \mathbf{u}_f \cdot \nabla T_f) + \nabla \cdot (\kappa_f \nabla T_f) - \alpha_s s_c = 0 \tag{5.4}$$

Discretising in time the equation 5.4 in the most fundamental way, with n the time increment, we find

$$\rho_f C_f \left(\frac{T_f^{n+1} - T_f^n}{\Delta t} + \mathbf{u}_f \cdot \nabla T_f^n \right) + \nabla \cdot (\kappa_f \nabla T_f^n) - \alpha_s^n s_c^n = 0 \tag{5.5}$$

$$T_f^{n+1} = T_f^n - \frac{\Delta t}{\rho_f C_f} \left(\mathbf{u}_f \cdot \nabla T_f^n + \nabla \cdot (\kappa_f \nabla T_f^n) \right) + \alpha_s^n \frac{\Delta t}{\rho_f C_f} s_c^n \tag{5.6}$$

We define T_f^* as the predicted temperature without the solid's contribution

$$T_f^{*n+1} = T_f^n - \frac{\Delta t}{\rho_f C_f} \left(\mathbf{u}_f \cdot \nabla T_f^n + \nabla \cdot (\kappa_f \nabla T_f^n) \right) \tag{5.7}$$

At the solid's positions, where ($\alpha_s = 1$), T_f^{*n+1} must be corrected to satisfy $T_f^{*n+1} = T_s^{n+1}$. We write

$$s_c^n = \frac{\rho_f C_f}{\Delta t}(T_s^{n+1} - T_f^{*n+1}) \tag{5.8}$$

for our condition to be satisfied, i.e. when we replace the above expression in equation 5.6. Equation 5.4 becomes

$$\rho_f C_f(\frac{\partial T_f}{\partial t} + \mathbf{u}_f \cdot \nabla T_f) + \nabla \cdot (\kappa_f \nabla T_f) - \alpha_s \frac{\rho_f C_f}{\Delta t}(T_s - T_f) = 0 \tag{5.9}$$

This method is one way coupled and only considers the solid as a heat source or sink. To implement two way coupling, one adds the equal and opposite coupling term in the solid equation as follows

$$\rho_s C_s \frac{\partial T_s}{\partial t} + \nabla \cdot (\kappa_s \nabla T_s) + s_c = 0 \tag{5.10}$$

However we can see how this strategy is not conservative when combining the fluid equation 5.4 with the solid equation 5.10 multiplied by the solid concentration to form the energy equation of the bulk temperature T_b

$$\rho_f C_f(\frac{\partial T_b}{\partial t} + \mathbf{u}_f \cdot \nabla T_b) + \nabla \cdot (\kappa_f \nabla T_b) + \alpha_s \left[\rho_s C_s \frac{\partial T_b}{\partial t} + \nabla \cdot (\kappa_s \nabla T_b)\right] = 0 \tag{5.11}$$

The coupling terms disappears but at the solid's positions ($\alpha_s > 0$) we are solving for both fluid and solid heat transfer equations. The energy equation of the fluid-solid system should be:

$$\begin{aligned} \alpha_f &\left[\rho_f C_f(\frac{\partial T_b}{\partial t} + \mathbf{u}_f \cdot \nabla T_b) + \nabla \cdot (\kappa_f \nabla T_b)\right] \\ +\alpha_s &\left[\rho_s C_s \frac{\partial T_b}{\partial t} + \nabla \cdot (\kappa_s \nabla T_b)\right] = 0 \end{aligned} \tag{5.12}$$

Which can also be written as

$$\begin{gathered} \rho_b C_b \frac{\partial T_b}{\partial t} + \alpha_f \rho_f C_f \mathbf{u}_f \cdot \nabla T_b + \nabla \cdot \kappa_b \nabla T_b = 0 \\ \rho_b = \alpha_f \rho_f + \alpha_s \rho_s \\ C_b = \alpha_f C_f + \alpha_s C_s \\ \kappa_b = \alpha_f \kappa_f + \alpha_s \kappa_s \end{gathered} \tag{5.13}$$

5.3.2 Immersed Shell Method

In this method the heat flux is relaxed through a thin shell surrounding the solid. The shell is formed by four-nodded elements constructed as an extension of the surface elements of the solid boundary, the ring thickness is noted Δ_r (Figure 5.6).

5.3.2.1 Spatial Discretisation of the Solid

Integrating equation 5.3 over the volume of solid gives

$$\int_{V_s} \left(\rho_s C_s \frac{\partial T_s}{\partial t} + \nabla \cdot (\kappa_s \nabla T_s) \right) N_s \; dV = 0 \tag{5.14}$$

Using the divergence theorem on the diffusion term we have

$$\int_{V_s} \nabla \cdot (\kappa_s \nabla T_s) N_s \; dV = -\int_{V_s} \kappa_s \nabla T_s N_s \; dV + \int_{\Gamma_s} n \cdot \kappa_s \nabla T_s \nabla N_s \; d\Gamma \tag{5.15}$$

Applying the divergence theorem on more time we obtain

$$\int_{V_s} \nabla \cdot (\kappa_s \nabla T_s) N_s dV = \int_{V_s} \nabla \cdot (\kappa_s \nabla T_s) N_s \; dV + \int_{\Gamma_s} n \cdot (\kappa_s \nabla T_s|_{fluid} - \kappa_s \nabla T_s|_{solid}) N_s \; d\Gamma \tag{5.16}$$

Finally we get

$$\int_{V_s} \left(\rho_s C_s \frac{\partial T_s}{\partial t} - \nabla \cdot (\kappa_s \nabla T_s) \right) N_s \; dV = \int_{\Gamma_s} n \cdot (\kappa_s \nabla T_s|_{fluid} - \kappa_s \nabla T_s|_{solid}) \; N_s \; d\Gamma \tag{5.17}$$

Continuing with the coupling term

$$\begin{aligned} \int_{\Gamma_s} n \cdot (\kappa_s \nabla T_s|_{fluid} - \kappa_s \nabla T_s|_{solid}) \;\; N_s \; dV = \int_{\Gamma_s} \kappa_s \Bigg[& n_x (\frac{\partial T_s}{\partial x}|_{fluid} - \frac{\partial T_s}{\partial x}|_{solid}) \\ & + n_y (\frac{\partial T_s}{\partial y}|_{fluid} - \frac{\partial T_s}{\partial y}|_{solid}) \\ & + n_z (\frac{\partial T_s}{\partial z}|_{fluid} - \frac{\partial T_s}{\partial z}|_{solid}) \Bigg] \; N_s \; d\Gamma. \end{aligned} \tag{5.18}$$

With the divergence theorem, we can approximate the fluid temperature derivatives next to the solid boundary using T_f

$$\int_{V_s} \frac{\partial T_s}{\partial x}|_{fluid} N_s \, dV = - \int_{V_s} \frac{\partial N_s}{\partial x} T_s \, dV + \int_{\Gamma_s} n_x T_f N_s \, d\Gamma \tag{5.19}$$

Similarly for the solid temperature derivatives using T_s at the boundary

$$\int_{V_s} \frac{\partial T_s}{\partial x}|_{solid} \; N_s \, dV = - \int_{V_s} \frac{\partial N_s}{\partial x} \; T_s \, dV + \int_{\Gamma_s} n_x T_s \; N_s \, d\Gamma \tag{5.20}$$

Then using equation 5.19 into equation 5.20 we obtain

$$\int_{V_s} \frac{\partial T_s}{\partial x}|_{fluid} \; N_s \, dV - \int_{V_s} \frac{\partial T_s}{\partial x}|_{solid} \; N_s \, dV = \int_{\Gamma_s} n_x (T_f - T_s) \; N_s \, d\Gamma \tag{5.21}$$

Using a simplified constant shape function N_s and with Δx_{wall} being the fluid element size around the wall and normal to it, the heat flux can be evaluated on the shell as

$$\frac{\partial T_s}{\partial x}|_{fluid} - \frac{\partial T_s}{\partial x}|_{solid} = \frac{n_x (T_f - T_s)}{\Delta x_{wall}}. \tag{5.22}$$

We can evaluate the terms in equation 5.21 over the shell of volume V_{sh} of thickness Δr using equation 5.22 to obtain:

$$\begin{aligned} &\int_{\Gamma_s} n_x \kappa_s (\frac{\partial T_s}{\partial x}|_{solid} - \frac{\partial T_s}{\partial x}|_{fluid}) \; N_s \, d\Gamma \\ \approx &\int_{V_{sh}} n_x \frac{1}{\Delta r} \kappa_s (\frac{\partial T_s}{\partial x}|_{solid} - \frac{\partial T_s}{\partial x}|_{fluid}) \; N_s \, dV \\ \approx &\int_{V_{sh}} \frac{n_x^2}{\Delta r \Delta x_{wall}} \kappa_s (T_s - T_f) \; N_s \, dV, \end{aligned} \tag{5.23}$$

Summing up in all directions, equation 5.18 becomes

$$\int_{\Gamma_s} n \cdot (\kappa_s \nabla T_s|_{fluid} - \kappa_s \nabla T_s|_{solid}) \; N_s \, dV = \int_{V_{sh}} \frac{1}{\Delta r \Delta x_{wall}} \kappa_s (T_f - T_s) \; N_s \, dV \tag{5.24}$$

Finally, the coupled solid energy equation is:

$$\int_{V_s} \left(\rho_s C_s \frac{\partial T_s}{\partial t} + \nabla \cdot (\kappa_s \nabla T_s) \right) N_s \, dV = \int_{V_{sh}} \frac{1}{\Delta r \Delta x_{wall}} \kappa_s (T_f - T_s) \; N_s \, dV \tag{5.25}$$

5.3.2.2 Spatial Discretisation of the Fluid

Integrating equation 5.2 over the fluid's volume

$$\int_{V_f} \left(\rho_f C_f (\frac{\partial T_f}{\partial t} + \mathbf{u}_f \cdot \nabla T_f) + \nabla \cdot (\kappa_f \nabla T_f) \right) \; N_f \; dV = 0 \tag{5.26}$$

Applying the same method as for the solid we get

$$\begin{aligned} &\int_{V_f} \nabla \cdot (\kappa_f \nabla T_f) N_s \; dV \\ =&\int_{V_f} \nabla \cdot (\kappa_f \nabla T_f) N_f \; dV + \int_{\Gamma_f} n \cdot (\kappa_f \nabla T_f|_{solid} - \kappa_f \nabla T_f|_{fluid}) \; N_f \; d\Gamma \end{aligned} \tag{5.27}$$

And

$$\begin{aligned} &\int_{V_f} \left(\rho_f C_f (\frac{\partial T_f}{\partial t} + \mathbf{u}_f \cdot \nabla T_f) + \nabla \cdot (\kappa_f \nabla T_f) \right) \; N_f \; dV \\ =&\int_{V_{sh}} \frac{1}{\Delta r \Delta x_{wall}} \kappa_f (T_s - T_f) \; N_f \; dV \end{aligned} \tag{5.28}$$

5.3.2.3 Conservation

In order to have the energy conserved in the system we must have the coupling terms equal and opposite, this may be achieved by the use of an mean conductivity $\kappa_e = \frac{\kappa_s + \kappa_f}{2}$ or harmonic conductivity $\frac{1}{\kappa_e} = \frac{1}{\kappa_s} + \frac{1}{\kappa_f}$, or a heat resistance $R_e = \frac{1}{k_e}$ specific to the fluid-solid interface heat transfer properties. We obtain the coupled fluid and solid equations:

$$\begin{aligned} &\int_{V_f} \left(\rho_f C_f (\frac{\partial T_f}{\partial t} + \mathbf{u}_f \cdot \nabla T_f) + \nabla \cdot (\kappa_f \nabla T_f) \right) \; N_f \; dV \\ =&\int_{V_{sh}} \frac{1}{\Delta r \Delta x_{wall}} \kappa_e (T_s - T_f) \; N_f \; dV \end{aligned} \tag{5.29}$$

and

$$\int_{V_s} \left(\rho_s C_s \frac{\partial T_s}{\partial t} + \nabla \cdot (\kappa_s \nabla T_s) \right) N_s \; dV = \int_{V_{sh}} \frac{1}{\Delta r \Delta x_{wall}} \kappa_e (T_f - T_s) \; N_s \; dV \tag{5.30}$$

When writing the energy equation of the fluid-solid system by adding equation 5.29 to 5.30, the coupling terms disappear and we obtain

$$\begin{aligned}&\int_{V_f}\left(\rho_f C_f(\frac{\partial T_f}{\partial t}+\mathbf{u}_f\cdot\nabla T_f)+\nabla\cdot(\kappa_f\nabla T_f)\right)\ N_f\ dV\\+&\int_{V_s}\left(\rho_s C_s\frac{\partial T_s}{\partial t}+\nabla\cdot(\kappa_s\nabla T_s)\right)N_s\ dV=0\end{aligned}\tag{5.31}$$

We can conclude that the immersed shell method is then conservative because we recover a correct expression of the fluid-solid equation when adding the fluid and the solid equations. However, we must bear in mind that the fluid computational domain embeds the solid. The fluid equation 5.29 is integrated over V_f but the fluid computational domain is $V = V_f \cup V_s^f$. Thus, there must be an additional term in the fluid equation to account for V_s^f. This is achieved in the next section with the immersed body method.

5.3.3 Combination of the Immersed Body and Shell Methods

To achieve immersed shell-body coupling, we start by multiplying the fluid equation by the fluid volume fraction:

$$\alpha_f\left(\rho_f C_f(\frac{\partial T_f}{\partial t}+\mathbf{u}_f\cdot\nabla T_f)+\nabla\cdot(\kappa_f\nabla T_f)\right)=0\tag{5.32}$$

This way, the fluid equation is solved only at the fluid's positions. Then, we add the immersed body coupling term, to relax the fluid to the solid temperature at the solid's position

$$\alpha_f\left(\rho_f C_f(\frac{\partial T_f}{\partial t}+u\cdot\nabla T_f)+\nabla\cdot(\kappa_f\nabla T_f)\right)+\alpha_s\beta_v(T_f-T_s)=0\tag{5.33}$$

With β_v the immersed body relaxation coefficient. We now integrate the above equation over the fluid computational domain V knowing that $\int_V \alpha_f\ dV = \int_{V_f} dV$ and $\int_V \alpha_s\ dV = \int_{V_s} dV$

$$\begin{aligned}&\int_{V_f}\left(\rho_f C_f(\frac{\partial T_f}{\partial t}+\mathbf{u}_f\cdot\nabla T_f)+\nabla\cdot(\kappa_f\nabla T_f)\right)N_f\ dV\\&=\int_{V_s}\sigma_v(T_s-T_f)\ N_f\ dV\end{aligned}\tag{5.34}$$

Developing the first term of the above equation with the immersed shell approach we have

$$\begin{aligned}&\int_{V_f}\left(\rho_f C_f(\frac{\partial T_f}{\partial t}+\mathbf{u}_f\cdot\nabla T_f)+\nabla\cdot(\kappa_f\nabla T_f)\right)N_f\ dV\\&=\int_{V_{sh}}\frac{1}{\Delta r\Delta x_{wall}}\kappa_e(T_s-T_f)N_f\ dV+\int_{V_s}\beta_v(T_s-T_f)\ N_f\ dV\end{aligned}\tag{5.35}$$

The above is coupled with the solid heat transfer equation:

$$\int_{V_s}\left(\rho_s C_s\frac{\partial T_s}{\partial t}-\nabla\cdot(\kappa_s\nabla T_s)\right)N_s\ dV=\int_{V_{sh}}\frac{1}{\Delta r\Delta x_{wall}}\kappa_e(T_f-T_s)N_s\ dV\tag{5.36}$$

In the immersed body method we had $\beta_v=\frac{\rho_f C_f}{\Delta t}$ but in the current configuration β_v can be chosen arbitrarily because the fluid equation is multiplied by α_f. In the immersed shell-body approach two separate projections are made, one for the shell coupling term and one for the body relaxation term. The projections are concurrent at the fluid-solid interface, as illustrated by Figure 5.7. The shell coupling term is essential for the conservation of the method therefore we must ensure that:

$$\beta_v<<\frac{1}{\Delta x_{wall}}\kappa_e\tag{5.37}$$

5.3.4 Implicit Treatment of the Coupling terms

This section presents the time discretised matrix equations for solving the fluid and solid equation implicitly.

5.3.4.1 Solid Matrix Equation

The time discretised solid energy equation 3.19 is rewritten with the shell coupling term for the solid, noted $\mathbf{r}_s$, with n the time increment

$$[\mathbf{M}_s^n-\theta_s\Delta t\mathbf{K}_s^n]\,T_s^{n+1}\ =[\mathbf{M}_s^n+\theta_s\Delta t\mathbf{K}_s^n]\,T_s^n+\mathcal{B}_s^n+\mathcal{Q}_s^n+\mathbf{r}_s^n\tag{5.38}$$

With

$$r_s^n=\int_{V_{sh}}\frac{\kappa_e}{\Delta r\Delta x_{wall}}(T_f^n-T_s^{n+1})\ N_s^n\ dV\tag{5.39}$$

We split r_s into a left and a right hand side part:

$$\begin{cases} lhs_s^n = \displaystyle\int_{V_{sh}} \frac{\kappa_e}{\Delta r \Delta x_{wall}} \; N_i \; dV \\ \\ rhs_s^n = \displaystyle\int_{V_{sh}} \frac{\kappa_e}{\Delta r \Delta x_{wall}} T_f^n \; N_i \; dV \end{cases} \tag{5.40}$$

Finally we have

$$\left[\mathbf{M}_s^n - \theta_s \Delta t \mathbf{K}_s^n + lhs_s^n\right] T_s^{n+1} \; = \left[\mathbf{M}_s^n + \theta_s \Delta t \mathbf{K}_s^n + rhs_s^n\right] T_s^n + \mathcal{B}_s^n + \mathcal{Q}_s^n \tag{5.41}$$

5.3.4.2 Fluid Matrix Equation

The spatial discretisation of the fluid advection-diffusion equation (5.2) yields the following matrix equation

$$\mathbf{M}_f \dot{T}_f + \mathbf{A}(\mathbf{u}_f) \; . \; T_f + \mathbf{K}_f T_f = \mathcal{B}_f + \mathcal{Q}_f + \mathbf{v}_f + \mathbf{r}_f \tag{5.42}$$

With $\mathbf{M}_f$ the fluid mass matrix, $\mathbf{A}(\mathbf{u}_f)$ the advection operator, $\mathbf{K}_f$ is the thermal diffusion operator, $\mathcal{B}_f$ is the vector accounting for thermal boundary conditions and $\mathcal{Q}_f$ the vector accounting for the source terms, $\mathbf{v}_f$ is the immersed body relaxation term and $\mathbf{r}_f$ is the fluid's shell coupling term. We have

$$\begin{aligned} M_{f_{ij}} &= \int_{V_f} \rho_f C_f \; N_{f_i} N_{f_j} \; dV \\ A_{ij} &= -\int_{V_f} \alpha_{f_i} B_{f_{ij}} \; . \; u_f N_{f_j} \; dV \\ K_{f_{ij}} &= \int_{V_f} \alpha_{f_i} \kappa_f \; B_{f_{ij}} B_{f_{ji}} \; dV \\ v_{f_i} &= \int_{V_s} \sigma_v (T_{si} - T_{bi}) N_{f_i} \; dV \\ r_{f_i} &= \int_{V_{sh}} \frac{\kappa_e}{\Delta r \Delta x_{wall}} (T_{si} - T_{f_i}) \; dV \end{aligned} \tag{5.43}$$

Applying the theta time integration scheme gives

$$\begin{aligned} &\left[\mathbf{M}_f^n + \theta_f \Delta t (\mathbf{A}^n(\mathbf{u}_f^n) + \mathbf{K}_f^n)\right] T_f^{n+1} \\ = &\left[\mathbf{M}_f^n + (1-\theta_f) \Delta t (\mathbf{A}^n(\mathbf{u}_f^n) + \mathbf{K}_f^n)\right] T_f^n + \mathcal{B}_f^n + \mathcal{Q}_f^n + \mathbf{v}_f^n + \mathbf{r}_f^n \end{aligned} \tag{5.44}$$

With the fluid coupling terms for the time increment n are

$$\begin{aligned}\mathbf{v}_f^n &= \int_{V_s} \beta_v (T_s^n - T_f^{n+1})\ N_f^n\ dV \\ \mathbf{r}_f^n &= \int_{V_{sh}} \frac{\kappa_e}{\Delta r \Delta x_{wall}} (T_s^n - T_f^{n+1})\ N_f^n\ dV\end{aligned} \tag{5.45}$$

As done for the solid equation, the coupling terms are separated between left and right hand side

$$\begin{cases} lhs_f^n = \displaystyle\int_V \alpha_s^n \sigma_v\ N_f^n\ dV + \int_{V_{sh}} \alpha_f^n \frac{\kappa_e}{\Delta r \Delta x_{wall}}\ dV \\ \\ rhs_f^n = \displaystyle\int_V \alpha_s^n \sigma_v T_s^n\ N_f^n\ dV + \int_{V_{sh}} \alpha_f^n \frac{\kappa_e}{\Delta r \Delta x_{wall}} T_s^n\ dV \end{cases} \tag{5.46}$$

Finally, equation 5.44 becomes

$$\begin{aligned} &\left[M_f^n + \theta_f \Delta t (A^n(u_f^n) + K_f^n) + lhs_f^n\right] T_f^{n+1} \\ = &\left[M_f^n + (1-\theta_f)\Delta t (A^n(u_f^n) + K_f^n) + rhs_f^n\right] T_f^n + \mathcal{B}_f^n + \mathcal{Q}_f^n \end{aligned} \tag{5.47}$$

5.3.5 Mesh to Mesh Projections

The coupling terms r_f and r_s are formed on the ring mesh and then projected to the fluid and solid respectively. The body relaxation term v_f and the solid concentration α_s are formed on the solid volume mesh and then projected to the fluid mesh.

The ring to solid mesh projection of r_s is straight forward since the ring mesh is grown from the solid mesh, for the ring to fluid mesh projection of r_f, v_f and α_s, the mesh-to-mesh projection is employed. The projection is identical to the one employed by Viré et al. (2012, 2013) for the immersed-body and by Viré et al. (2015), Yang et al. (2016) for the immersed shell.

This approach ensures that the volume integral of a given field $\mathcal{F}$ projected from the shell ($\mathcal{F}_r$) or volume mesh ($\mathcal{F}_v$) is conserved on the fluid mesh:

$$\int_{V_{sh}} \mathcal{F}_r\ dV = \int_V \mathcal{F}_f\ dV, \tag{5.48}$$

Or

$$\int_{V_s} \mathcal{F}_v\ dV = \int_V \mathcal{F}_f\ dV, \tag{5.49}$$

This is achieved by minimizing the L_2 norm of the interaction error of the solution of the following linear equation (Farrell and Maddison, 2011):

$$\int_{V_{sh}} \sum_{i=1}^{m_r} (\mathcal{F}_{sh})_i^r N_i^{sh} N_k^f \, dV = \int_V \sum_{j=1}^{m_f} (\mathcal{F}_f)_j^f N_j^f N_k^f \, dV \tag{5.50}$$

Or

$$\int_{V_s} \sum_{i=1}^{m_s} (\mathcal{F}_r)_i^s N_i^s N_k^f \, dV = \int_V \sum_{j=1}^{m_f} (\mathcal{F}_f)_j^f N_j^f N_k^f \, dV \tag{5.51}$$

With m the number of nodes of the considered mesh. For thermal coupling we have a total of three Galerkin projections: (I) projection from fluid to ring of T_b, (II) projection of r_f from ring to fluid mesh and finally (III) projection from v_f from solid volume mesh to fluid mesh. The other projections are straight forward: (i) for T_s from solid to ring mesh and (ii) for r_s from ring to solid mesh (see Figure 5.8).

5.3.6 Coupling Procedure

The flow chart below presents the coupling steps for the immersed shell-body method for thermal coupling within Fluidity-Solidity .

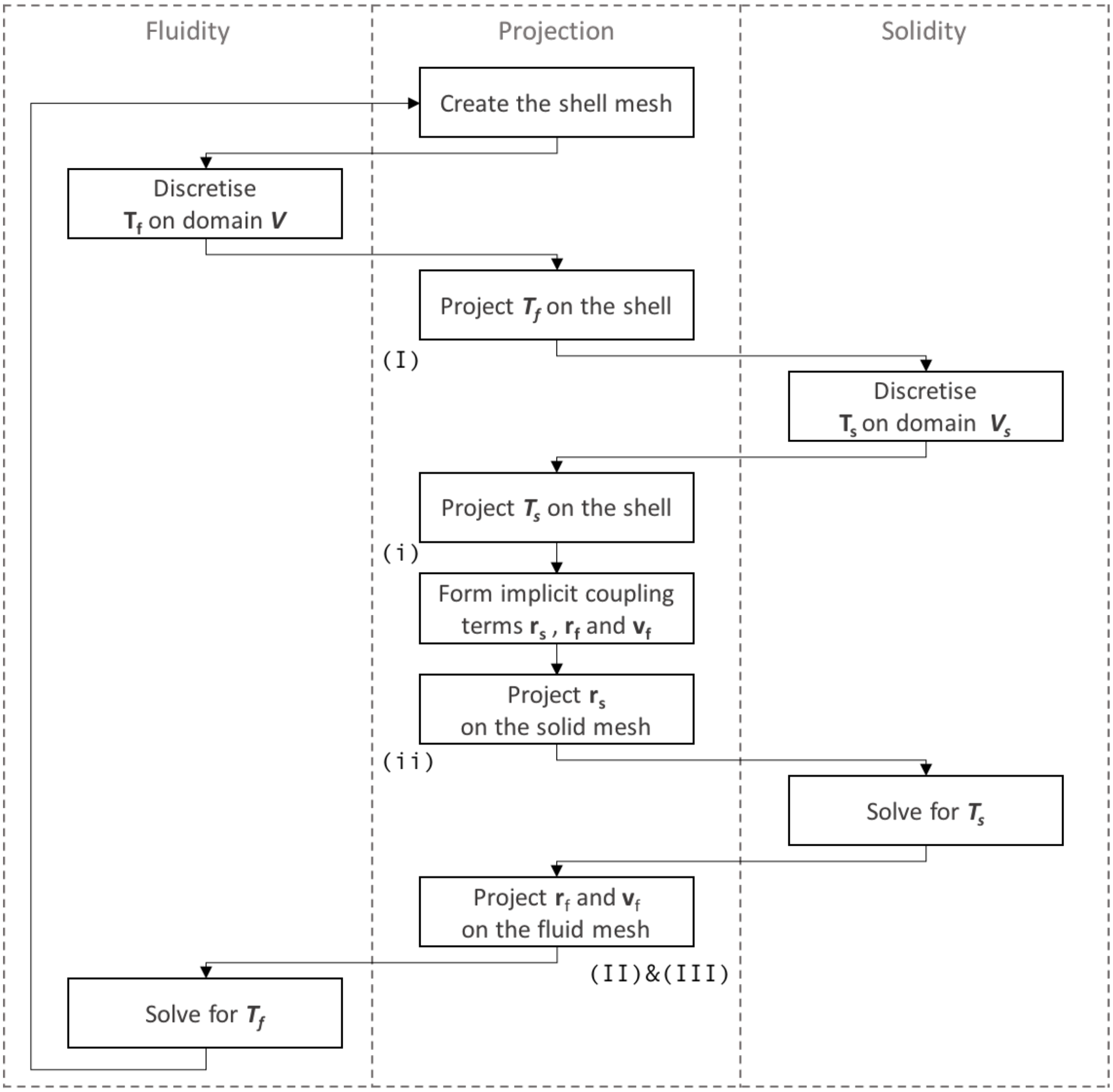

FIGURE 5.8: Flow chart of the ring-volume IB method. Upper-case Roman numerals correspond to the Galerkin mesh-to-mesh projection while lower-case Roman numerals correspond to the straight forward projections between the solid and the shell mesh.

5.4 Fluid-Solid Thermal Coupling for Fractured Porous Media

The fluid-solid coupling approach has been presented so far for the configuration of a solid immersed in a fluid domain where the solid is impermeable to the fluid. When considering a porous media, fluid and solid are present everywhere in the domain and the porosity defines the volume fraction of fluid and solid. When considering an open fracture space, the solid concentration is 0 and the fluid concentration is 1.

Most numerical THM codes reviewed in Chapter 2 consider the thermal equilibrium of the porous media (Table 2.4). This means that the rock matrix and the pore fluid are considered of the same temperature at all times. In that case, one energy equation with equivalent thermal properties can be used:

$$\begin{aligned} \rho_b C_b \frac{\partial T_b}{\partial t} + \phi \rho_f C_f \; u_f \cdot \nabla T_b + \nabla \cdot \kappa_b \nabla T_b = 0 \\ \rho_b = (1-\phi)\rho_s + \phi \rho_f \\ C_b = (1-\phi) C_s + \phi C_f \\ \kappa_b = (1-\phi)\kappa_s + \phi \kappa_f \end{aligned} \tag{5.52}$$

With ϕ the porosity and T_b the bulk temperature of the porous media. Without the thermal equilibrium we have two equations that are coupled in an immersed body fashion. For the pore fluid we have

$$\phi \left[\rho_f C_f \left(\frac{\partial T_f}{\partial t} + \; u_f \cdot \nabla T_f \right) + \nabla \cdot \kappa_f \nabla T_f) \right] + h_\phi (T_f - T_s) = 0 \tag{5.53}$$

and for the rock matrix

$$(1-\phi) \left[\rho_s C_s \frac{\partial T_s}{\partial t} + \nabla \cdot \kappa_s \nabla T_s) \right] + h_\phi (T_s - T_f) = 0 \tag{5.54}$$

With h_ϕ a convection coefficient describing how fast the heat is exchanged between the solid and the fluid in the porous media.

Because In Fluidity (IC-FERST), the thermal equilibrium equation (5.52) is already implemented and because the thermal equilibrium can largely be considered in radioactive waste repository modelling applications, no further work is performed on the thermal coupling model for porous media. To achieve THM coupling, it is sufficient to calculate the thermal processes in Fluidity and project the temperature on Solidity and then to perform thermo-mechanical coupling. There is no necessity to calculate thermal processes in Solidity. Such THM coupling is demonstrated in the following chapter.

5.5 Validation

In this section, the Fluidity-Solidity coupled heat transfer model is verified for a heat conduction problem with a solid sphere embedded in a cubical fluid domain. Then, a heat convection problem is presented for fluid flow past a solid sphere in a cubical enclosure.

5.5.1 Coupled Heat Conduction

This section presents the validation of the Fluidity-Solidity coupled heat transfer with the combined immersed ring-body method (Section 5.3.3). Consider a solid sphere of 5cm diameter embedded in a cubical fluid domain with edges of $8cm$(Figure 5.9). Solid and fluid are at the same initial temperature of $0°C$ and a Dirichlet boundary condition of $1°C$ is imposed on all faces of the cubical fluid domain (Figure 5.11). Heat is transferred from the fluid to the solid sphere until the whole coupled system reaches $1°C$, see Figures 5.12 and 5.13.

Parameters of the simulation are presented on Table 5.1. The same properties are purposely used for the fluid and solid. This allows the comparison of the fluid-solid results with a fluid only simulation. The fluid only simulation has the same properties as of Table 5.1 but has no embedded solid. Since we only consider heat conduction in this problem, the fluid-solid and fluid only solutions are expected to be the same.

To demonstrate the ability of the novel immersed ring-body method to achieve accuracy with mesh adaptivity at a reduced computational cost, a sensitivity analysis with different fluid meshes is performed. The solid mesh is kept the same with an element size of 0.005 m (Figure 5.10) whilst eight different fluid meshes are employed, they are numbered from M1 to M8 (Figure 5.14).

For the simulations with meshes M1 to M4 the ring size is of $\Delta_r = 0.005\ m$ while for meshes M5-M8 the ring size is of $\Delta_r = 0.0025\ m$. The fluid mesh size in the vicinity of the fluid-solid interface is chosen to be the same as the ring size. For the two sets of meshes M1-4 and M5-8, we first start with a uniform mesh of the same size as that of the ring (M1 and M5). Then, we use a mesh adapted to the size of the ring at the fluid-solid interface, the mesh size outside of the interface's vicinity is gradually increased to $L_0 = 0.01\ m$ (M2 and M6), $L_0 = 0.02\ m$ (M3 and M7) and $L_0 = 0.03\ m$ (M4 and M8), see Figure 5.14. The different mesh properties employed in the sensitivity analysis are summarised on Table 5.2.

The mesh adaptive process is performed prior to the heat transfer simulations and is presented for mesh M8 on Figure 5.15. Results from the sensitivity analysis are highlighted on Figures 5.20 to 5.26, note that mesh M5 was removed from the sensitivity analysis because of the unreasonable computational time caused by its the very fine mesh.

For each of the meshes:

1. A Fluidity-Solidity coupled simulation is performed.
2. A Fluidity 'fluid only' simulation is performed.

We note that all results display:

(i) A good agreement between the solid and the 'fluid only' temperature profiles. Note that small inaccuracies are observed for high values of L_0, the fluid mesh becomes too coarse on V_s^f for M4, M7 and M8 (Figures 5.23a to 5.26a). Nevertheless, this does not affect the results and the temperatures profiles are still coherent at the fluid-solid interface ($r = 0.05$ or $x = -0.05$ and $x = 0.05$ on Figures 5.23a to 5.26a).

(ii) a good agreement between the fluid results of the coupled simulation and the 'fluid only' results where $\alpha_s = 1$ or $\alpha_s = 0$, i.e. everywhere except at the fluid-solid interface. This is due to the transition between the ring and the volume relaxations terms (x = -0.05 and x = 0.05 on Figures 5.20a to 5.26a). Note that the incoherences between the temperature profiles are reduced for smaller ring sizes, Figures 5.24a to 5.26a.

Note that the fluid only simulations have all produced coherent results (Figure 5.16) thus we conclude that there is overall agreement between all simulations. To verify if the method is conservative and does not result in heat loss or gain, the transient evolution of the temperature integral over the whole domain is calculated (Figures 5.20b to 5.26b). For the fluid only simulation the integral is:

$$\int_V T_f \, dV \tag{5.55}$$

While for the coupled simulation we combine the fluid temperature at the fluid's positions (in Fluidity) and the solid temperature on the solid domain (in Solidity):

$$\int_V \alpha_f T_f \, dV + \int_{V_s} T_s \, dV \tag{5.56}$$

All coupled results show conservation of the temperature, with a maximal error below 0.8% (Figure 5.17). With mesh adaptivity, the computation time was reduced by four times for M1-M4 (Figure 5.18). We suppose a similar computational time reduction would have been found for M5-M8 if it had been practical to run M5 (Figure 5.19).

time step	$0.001\ s$
κ_f, κ_s	$1\ W.(m.K)^{-1}$
c_f, c_s	$1\ J.(Kg.K)^{-1}$
ρ_f, ρ_s	$100\ kg.m^{-3}$

TABLE 5.1: Heat conduction parameters for Solidity and Fluidity.

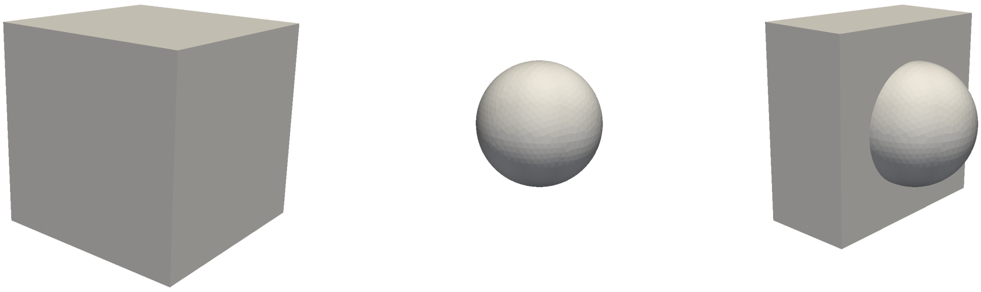

(A) Fluid domain (B) Solid domain (C) Cross-section view

FIGURE 5.9: Fluid and solid domain geometries for validation of the coupled heat conduction.

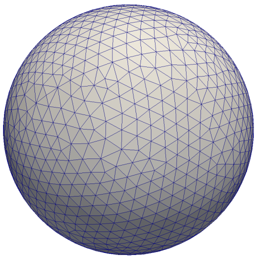

FIGURE 5.10: Solid mesh employed for the sensitivity analysis.

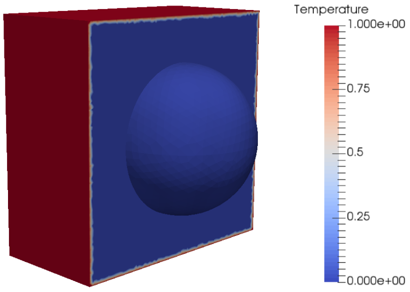

FIGURE 5.11: Initial temperature distribution (cross-section view).

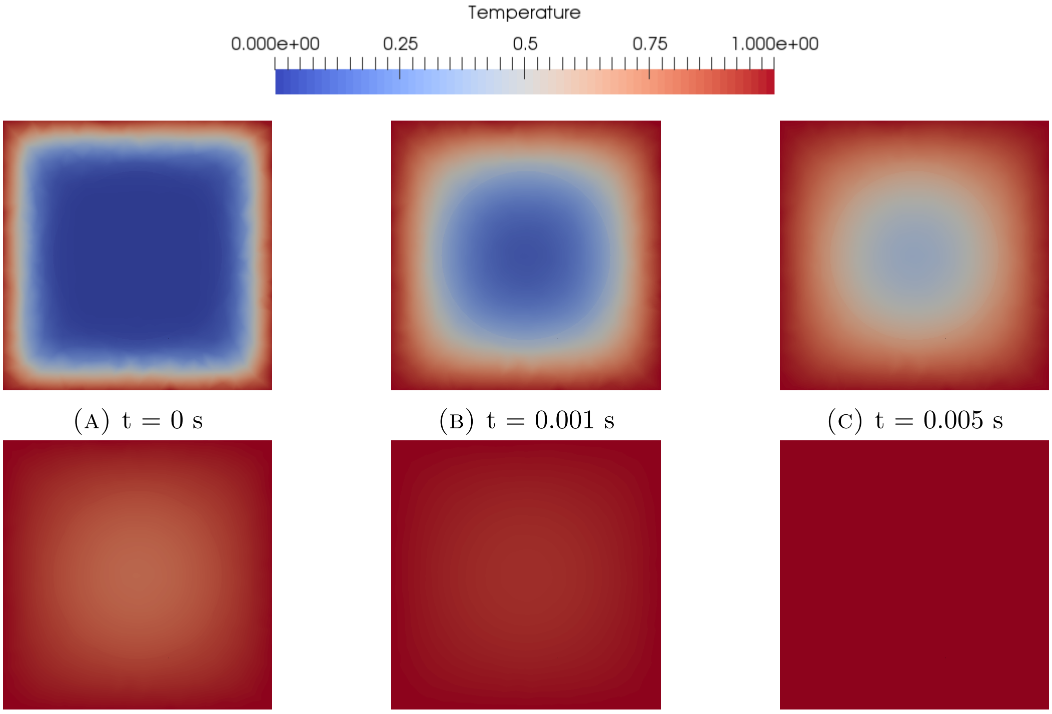

(A) t = 0 s (B) t = 0.001 s (C) t = 0.005 s

(D) t = 0.01 s (E) t = 0.03 s (F) t = 0.07 s

FIGURE 5.12: Temperature field evolution over time in a cross-section of the superimposed fluid and solid domains.

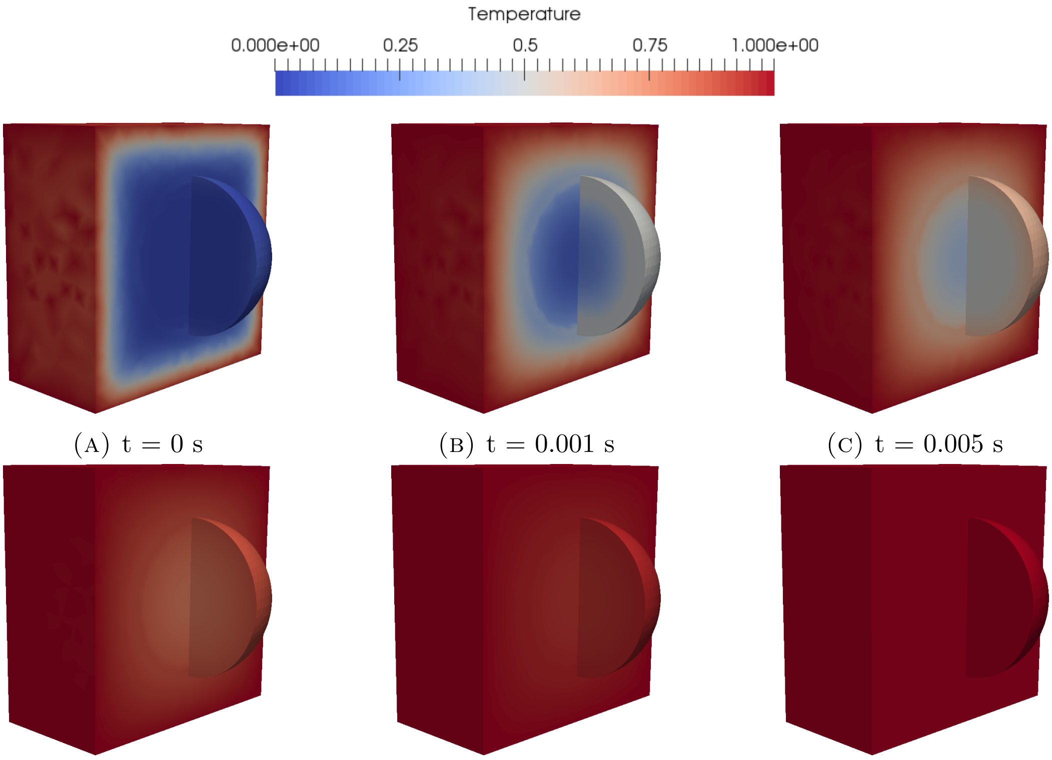

(A) t = 0 s

(B) t = 0.001 s

(C) t = 0.005 s

(D) t = 0.01 s

(E) t = 0.03 s

(F) t = 0.07 s

FIGURE 5.13: Temperature field evolution over time with normal cross-section planes for the superimposed fluid and solid domains.

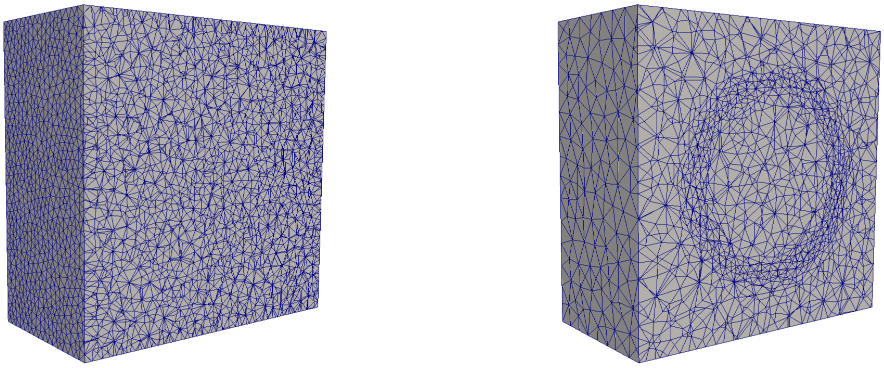

(A) M1: $L_0 = 0.005$ - no adapted mesh

(B) M2: $L_0 = 0.01$, $L_a = 0.005$

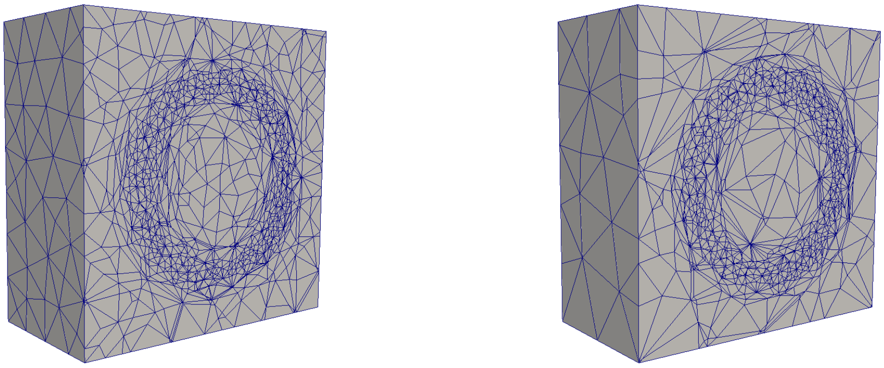

(C) M3: $L_0 = 0.02$, $L_a = 0.005$

(D) M:4 $L_0 = 0.03$, $L_a = 0.005$

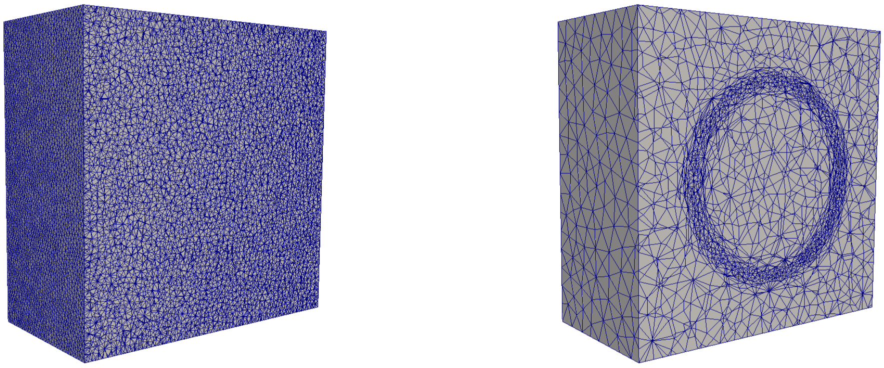

(E) M5: $L_0 = 0.0025$ - no adapted mesh

(F) M6: $L_0 = 0.01$, $L_a = 0.0025$

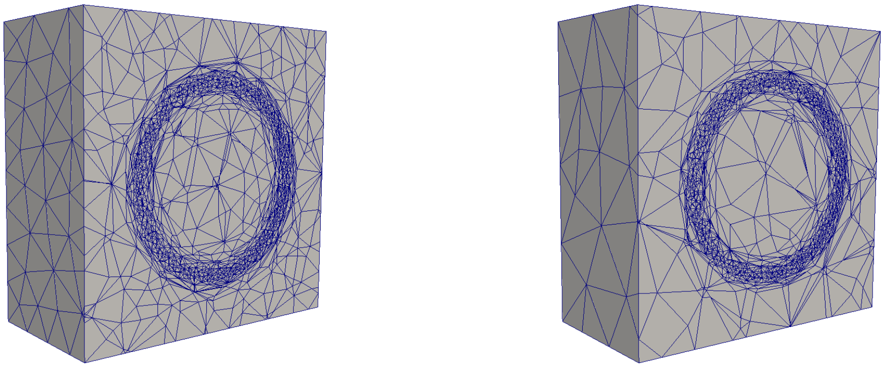

(G) M7: $L_0 = 0.02$, $L_a = 0.0025$

(H) M8: $L_0 = 0.03$, $L_0 = 0.0025$

FIGURE 5.14: Cross-section of the different meshes used for the sensitivity analysis of the immersed shell-body method. L_0 is the mesh size outside of the adapted zone and L_a is the size of the mesh adapted to the contour of the solid concentration.

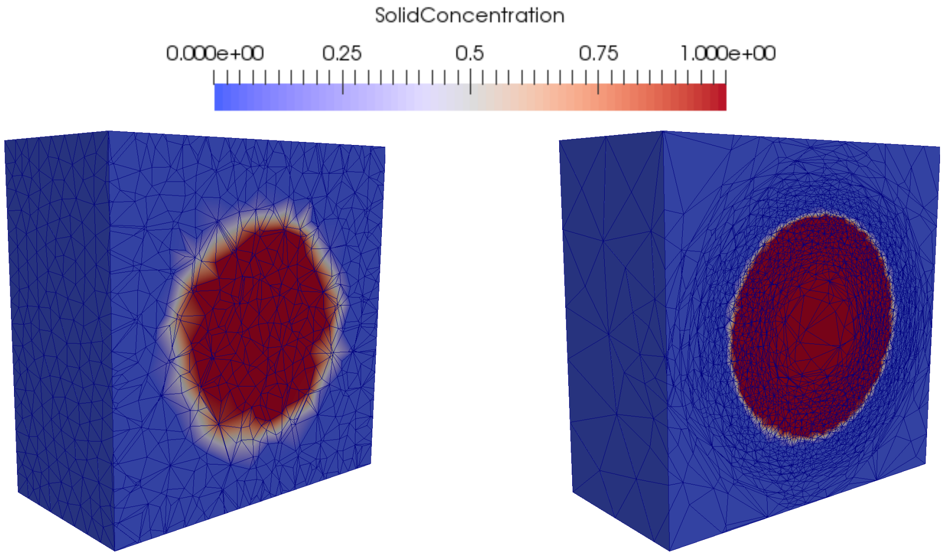

(A) Initial mesh

(B) 1 adaptive mesh iteration

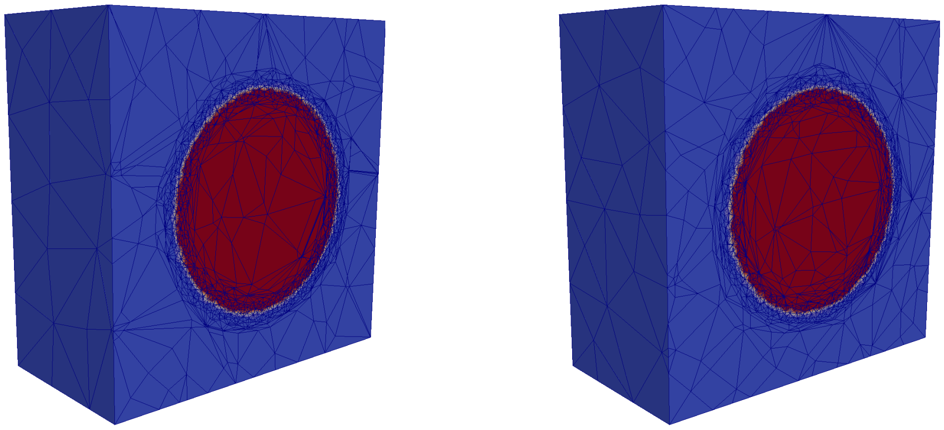

(C) 2 adaptive mesh iterations

(D) 3 adaptive mesh iterations

FIGURE 5.15: Solid concentration on a cross section of the fluid domain, the mesh is adapted to the contour of the projection of the embedded solid sphere volume for mesh M8: $L_0 = 0.03m$, $L_a = 0.0025m$.

	$L_0(m)$	$L_a(m)$	$\Delta r(m)$	$\Delta x_{wall}(m)$
M1	0.005	no adapted mesh	0.005	0.005
M2	0.01	0.005	0.005	0.005
M3	0.02	0.005	0.005	0.005
M4	0.03	0.005	0.005	0.005
M5	0.0025	no adapted mesh	0.0025	0.0025
M6	0.01	0.0025	0.0025	0.0025
M7	0.02	0.0025	0.0025	0.0025
M8	0.03	0.0025	0.0025	0.0025

TABLE 5.2: Mesh properties of the sensitivity analysis. With L_0 the mesh size outside of the adapted zone, L_a the size of the adapted mesh, Δr the shell thickness and Δx_{wall} the fluid mesh size in the vicinity of the shell.

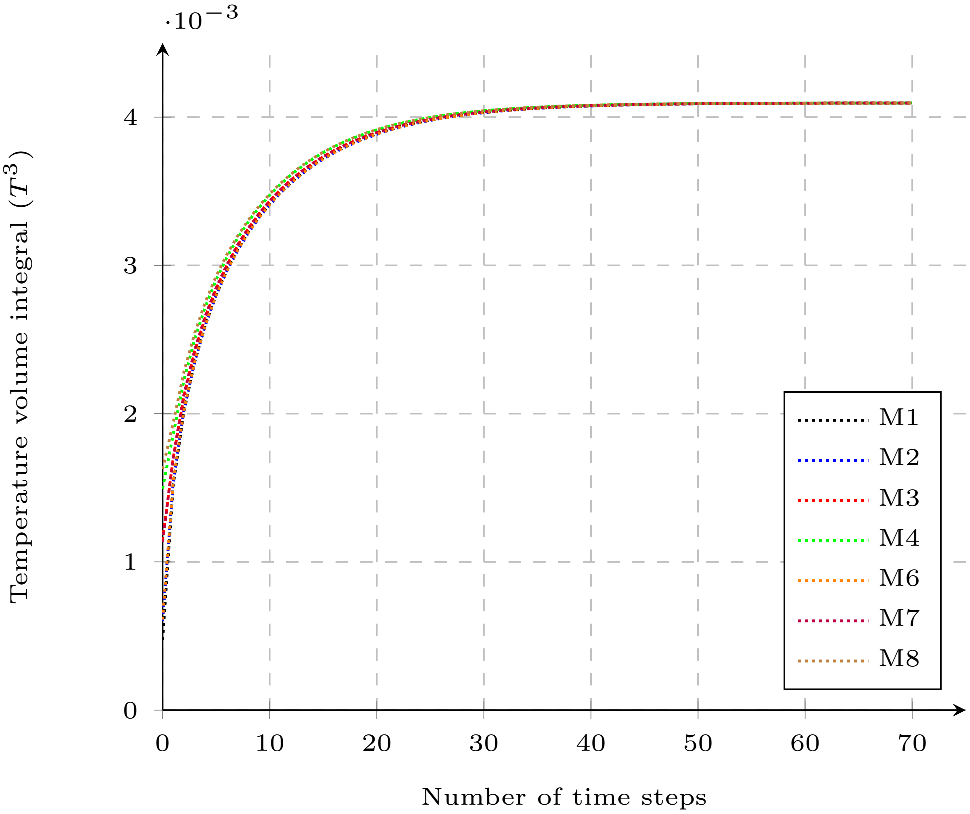

FIGURE 5.16: Temperature integral versus time-steps for the fluid only simulations.

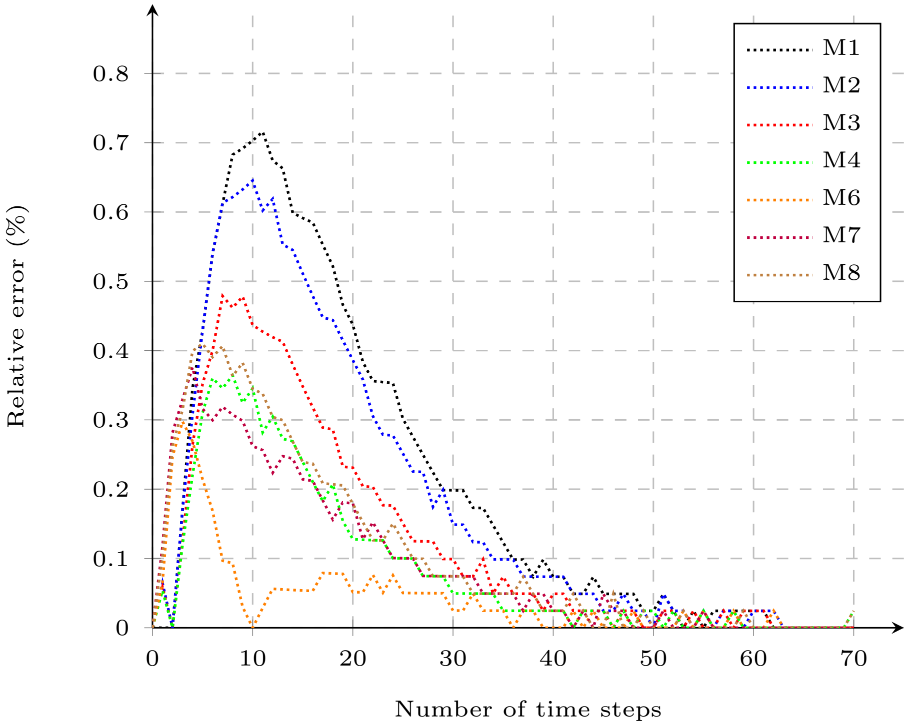

FIGURE 5.17: Absolute relative error per time step, between the temperature integrals of the coupled and the fluid only simulations.

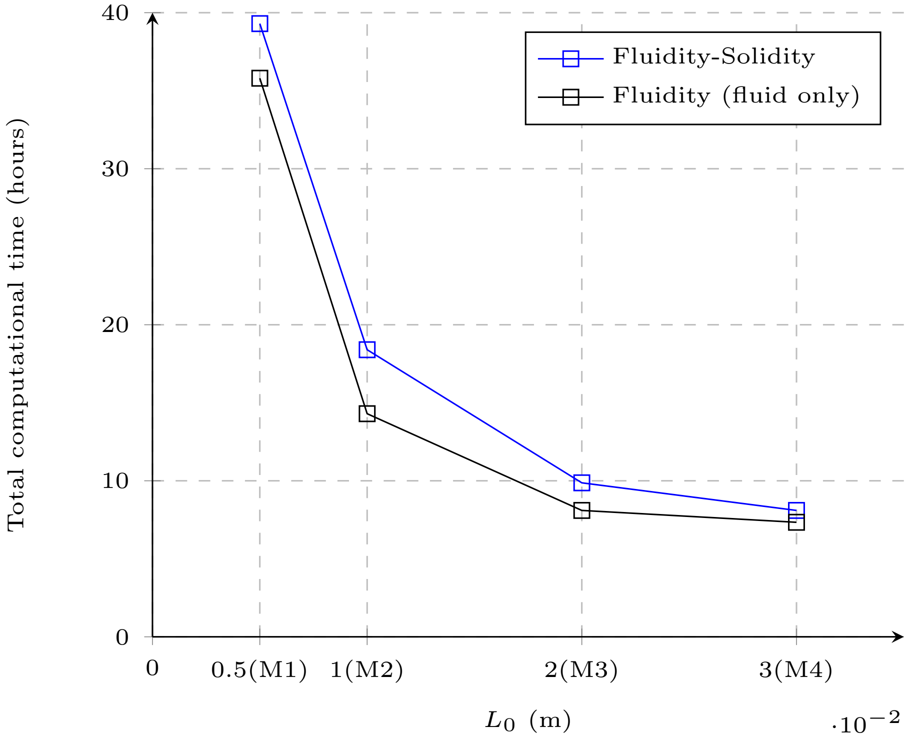

FIGURE 5.18: Mesh size L_0 versus the total computational time for fluid-solid and fluid only simulations (M1, M2, M3 and M4). Calculations are performed on a single Intel Xeon(R) CPU E5-2630 2.30GHz processor.

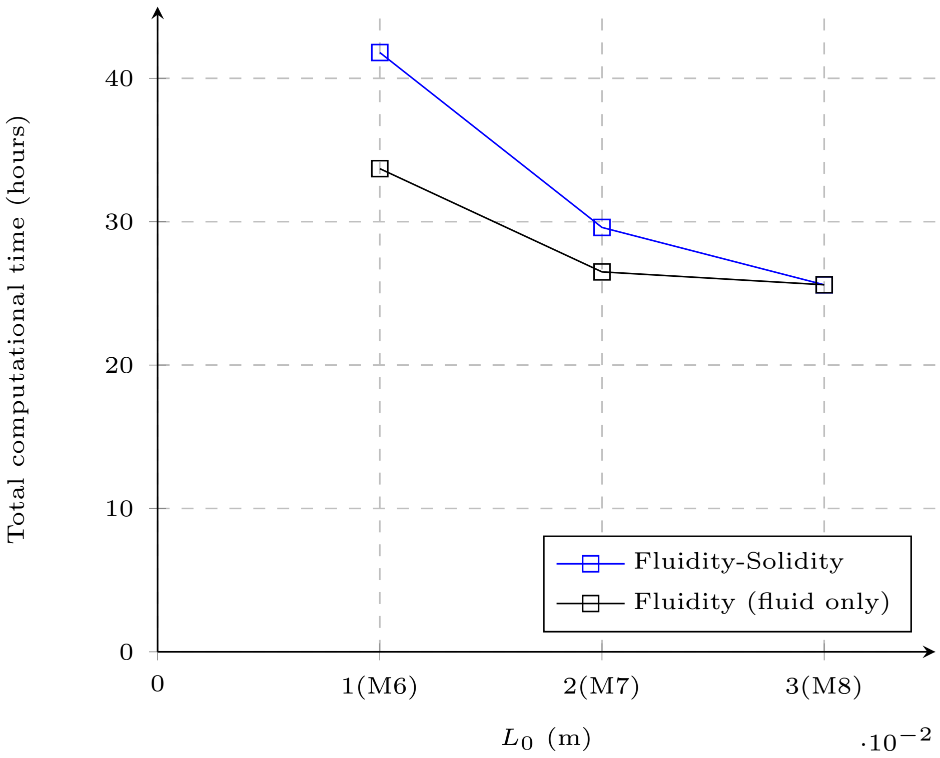

FIGURE 5.19: Mesh size L_0 versus the total computational time for fluid-solid and fluid only simulations (M6, M7 and M8). Calculations are performed on a single Intel Xeon(R) CPU E5-2630 2.30GHz processor.

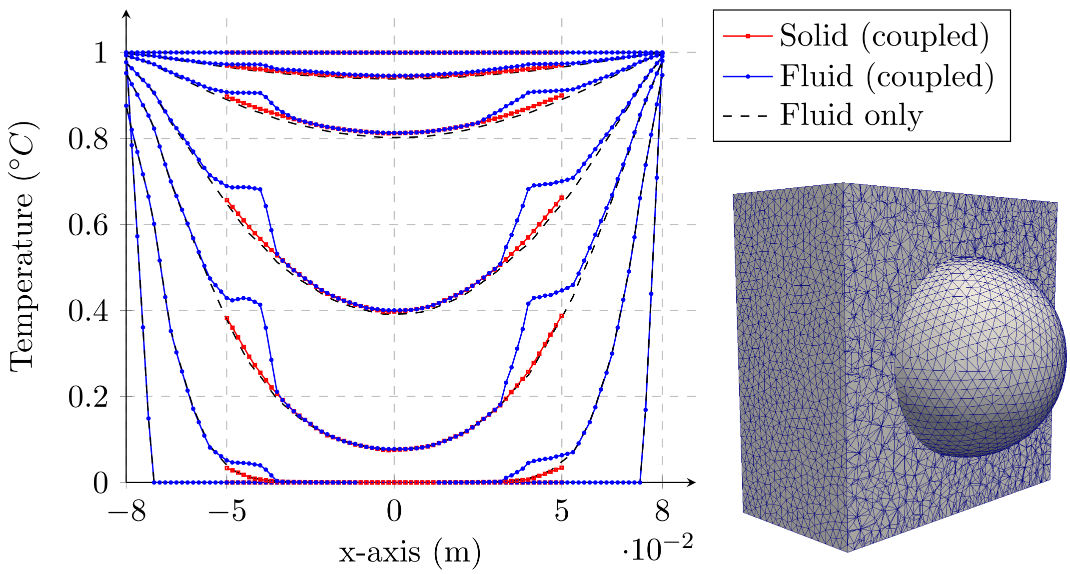

(A) Temperature profiles along the x-axis for time steps 0, 10, 20, 30 and 70 (bottom to top)

(B) Cross section of solid and fluid mesh (M1)

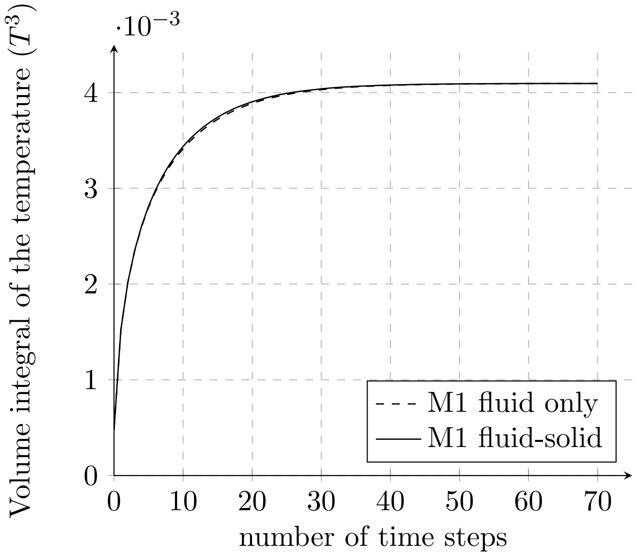

(C) Temperature integral versus time-steps

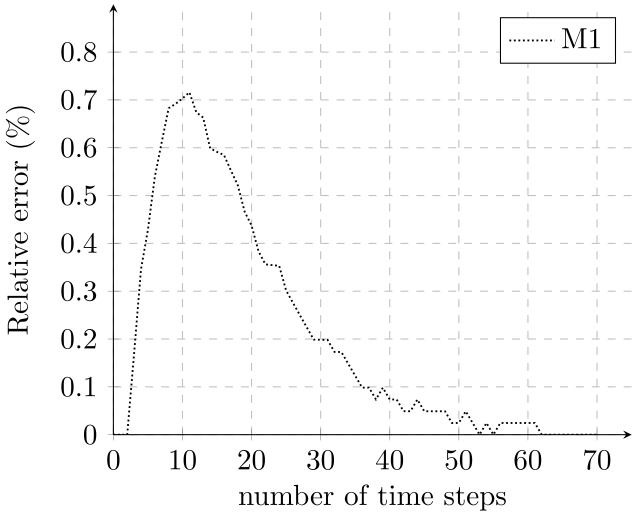

(D) Absolute relative error between the coupled and the fluid only simulation versus the number of time steps

FIGURE 5.20: Results for mesh M1

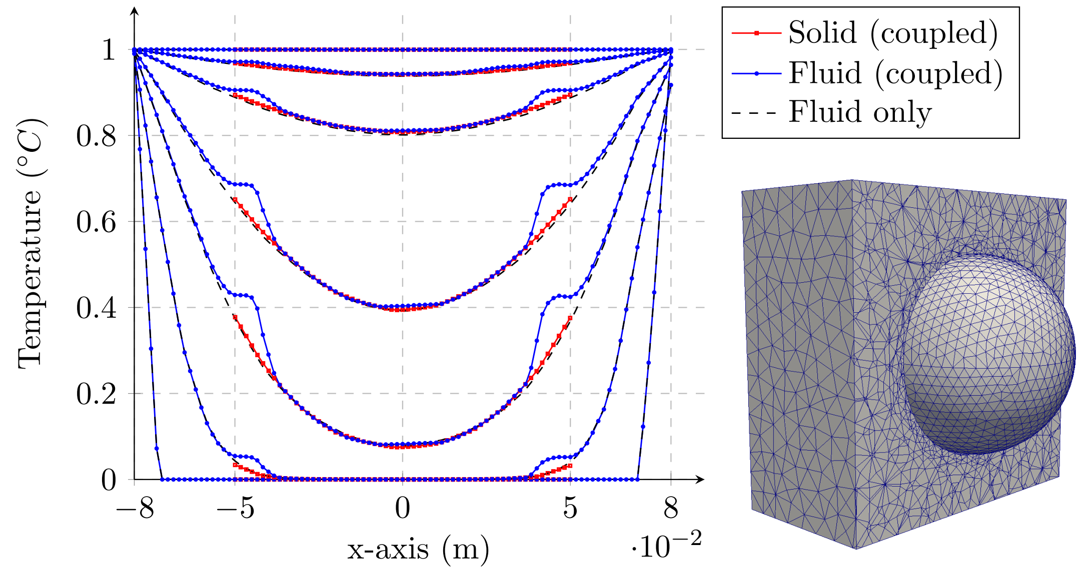

(A) Temperature profiles along the x-axis for time steps 0, 10, 20, 30 and 70 (bottom to top)

(B) Cross section of solid and fluid mesh (M2)

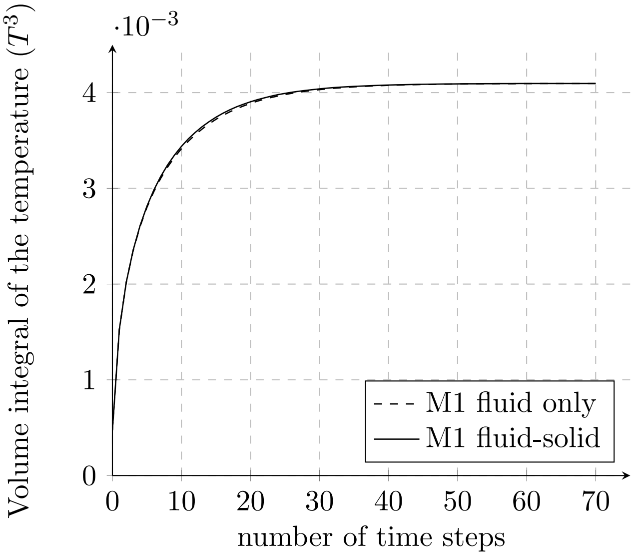

(C) Temperature integral versus time-steps

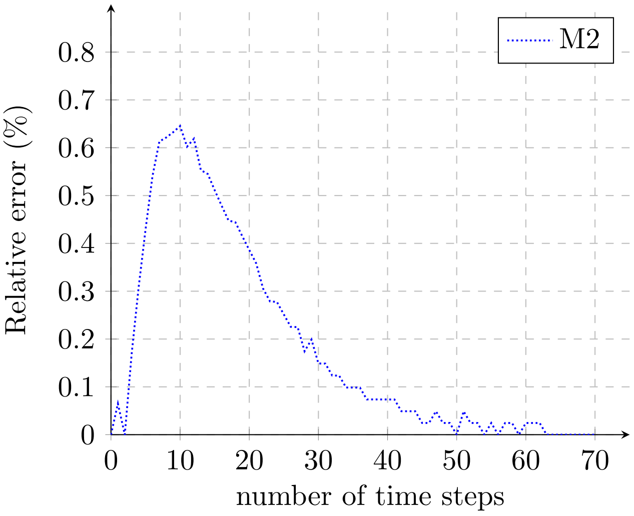

(D) Absolute relative error between the coupled and the fluid only simulation versus the number of time steps

FIGURE 5.21: Results for mesh M2

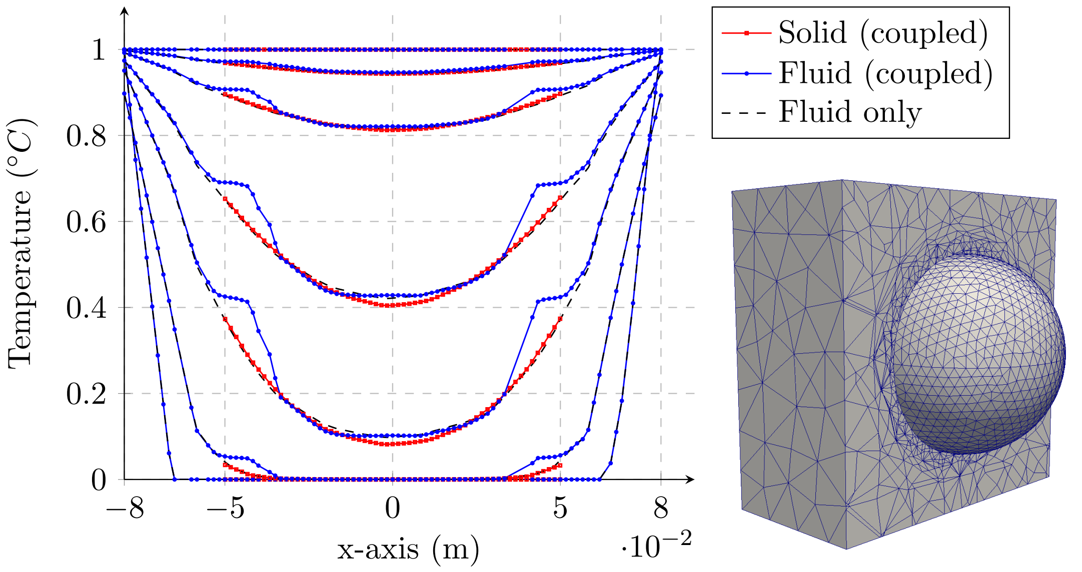

(A) Temperature profiles along the x-axis for time steps 0, 10, 20, 30 and 70 (bottom to top)

(B) Cross section of solid and fluid mesh (M3)

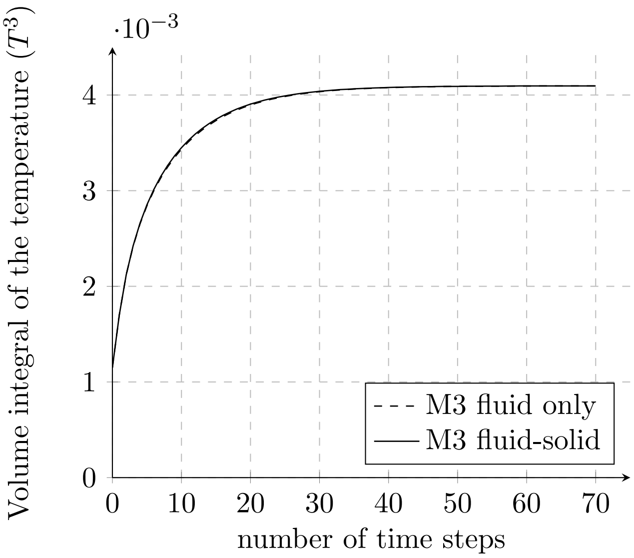

(C) Temperature integral versus time-steps

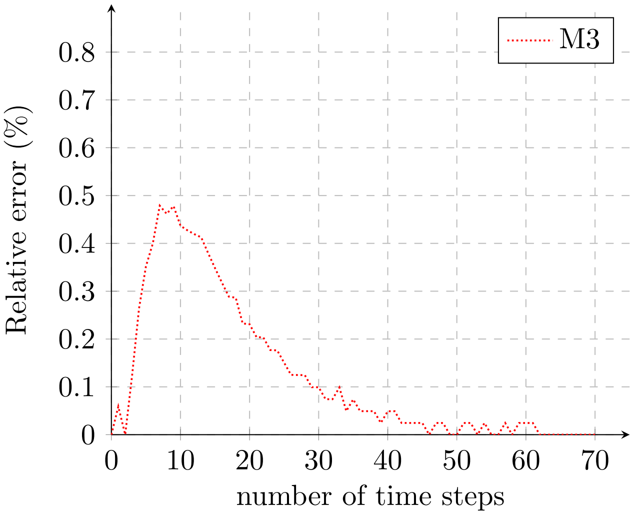

(D) Absolute relative error between the coupled and the fluid only simulation versus the number of time steps

FIGURE 5.22: Results for mesh M3

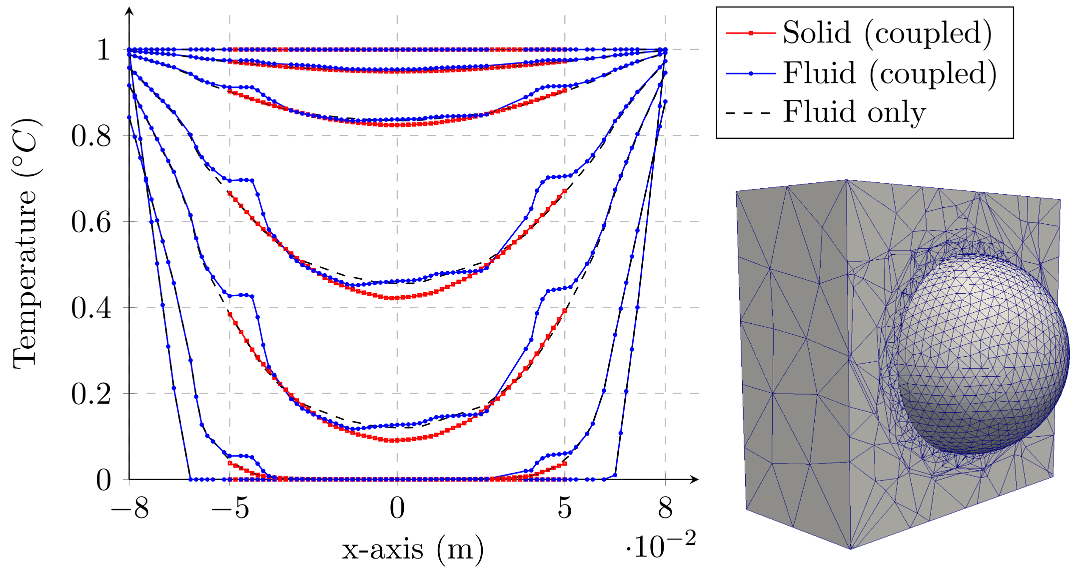

(A) Temperature profiles along the x-axis for time steps 0, 10, 20, 30 and 70 (bottom to top)

(B) Cross section of solid and fluid mesh (M4)

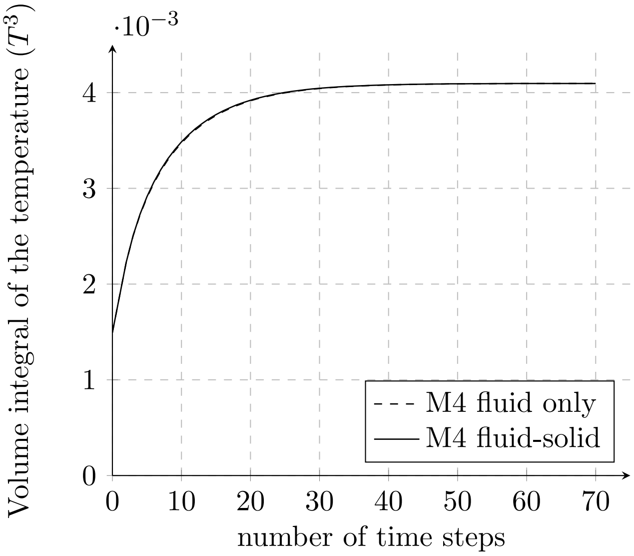

(C) Temperature integral versus time-steps

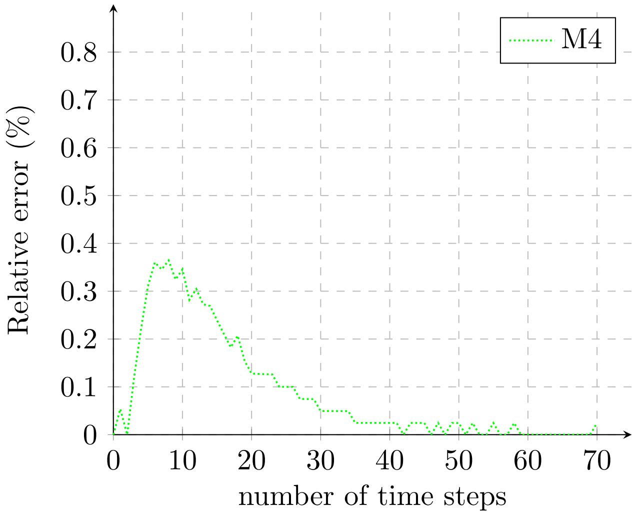

(D) Absolute relative error between the coupled and the fluid only simulation versus the number of time steps

FIGURE 5.23: Results for mesh M4

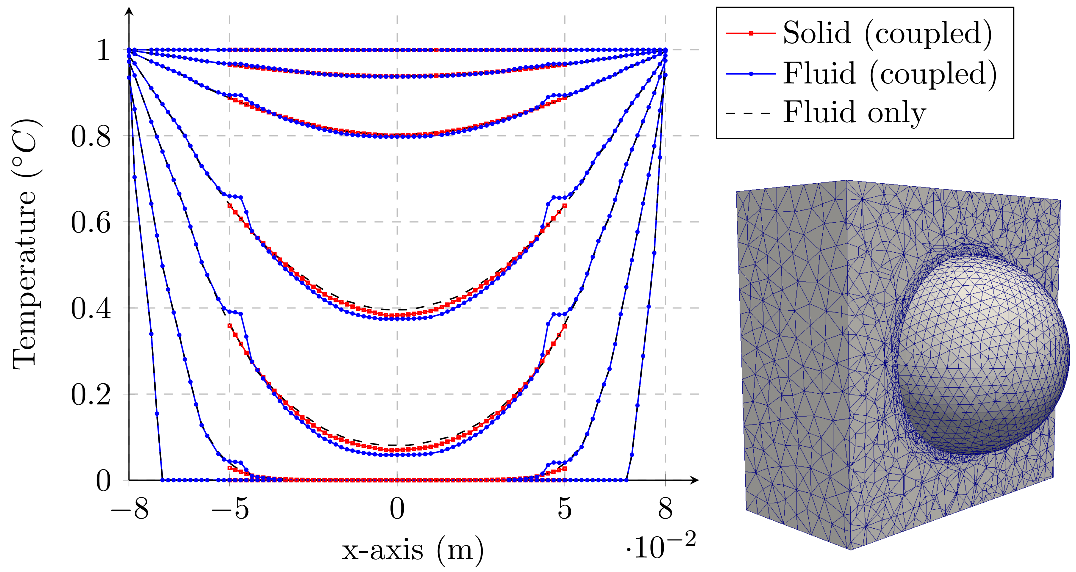

(A) Temperature profiles along the x-axis for time steps 0, 10, 20, 30 and 70 (bottom to top)

(B) Cross section of solid and fluid mesh (M6)

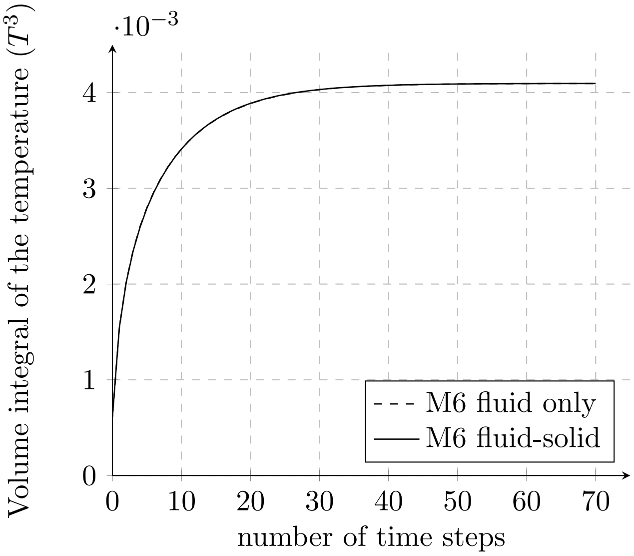

(C) Temperature integral versus time-steps

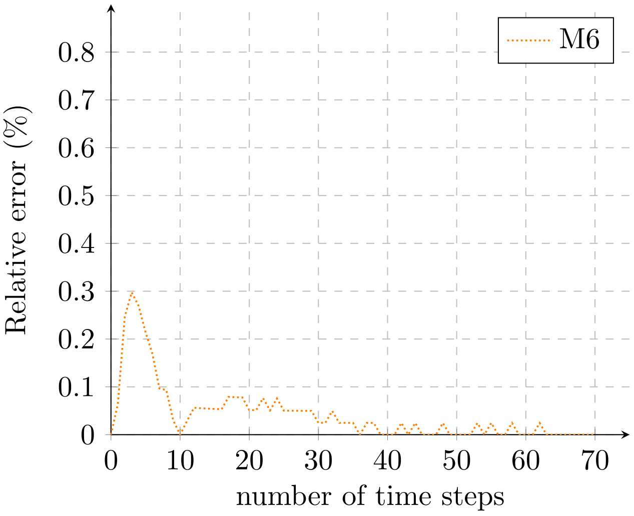

(D) Absolute relative error between the coupled and the fluid only simulation versus the number of time steps

FIGURE 5.24: Results for mesh M6

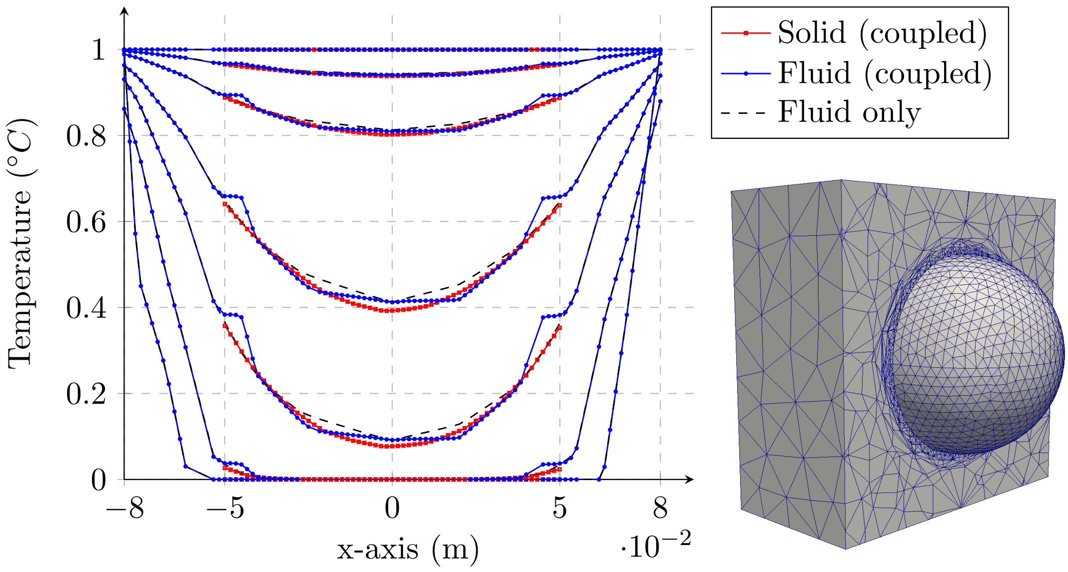

(A) Temperature profiles along the x-axis for time steps 0, 10, 20, 30 and 70 (bottom to top)

(B) Cross section of solid and fluid mesh (M7)

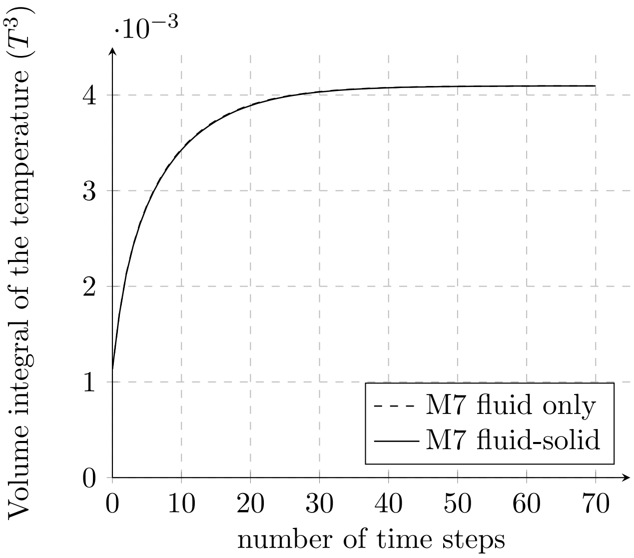

(C) Temperature integral versus time-steps

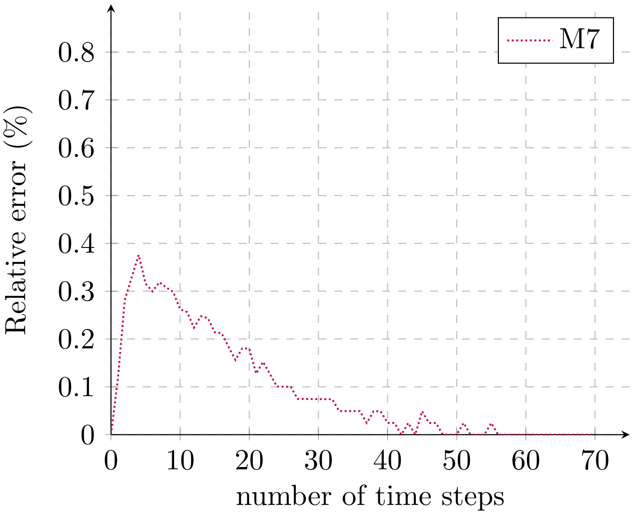

(D) Absolute relative error between the coupled and the fluid only simulation versus the number of time steps

Figure 5.25: Results for mesh M7

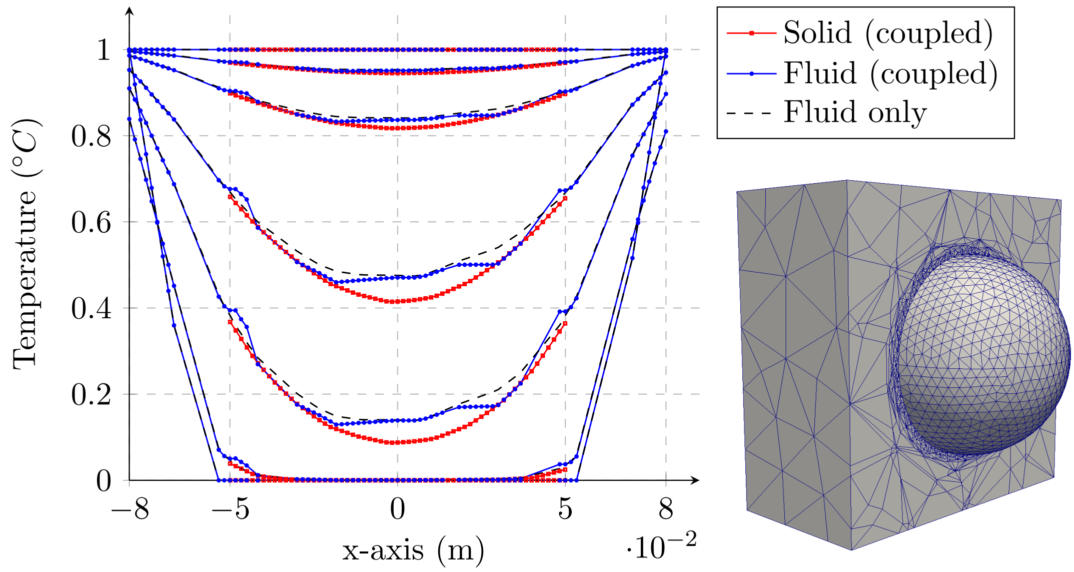

(A) Temperature profiles along the x-axis for time steps 0, 10, 20, 30 and 70 (bottom to top)

(B) Cross section of solid and fluid mesh (M8)

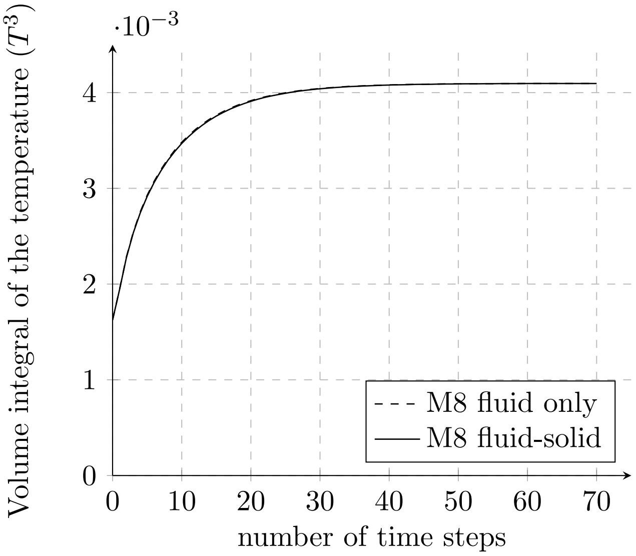

(C) Temperature integral versus time-steps

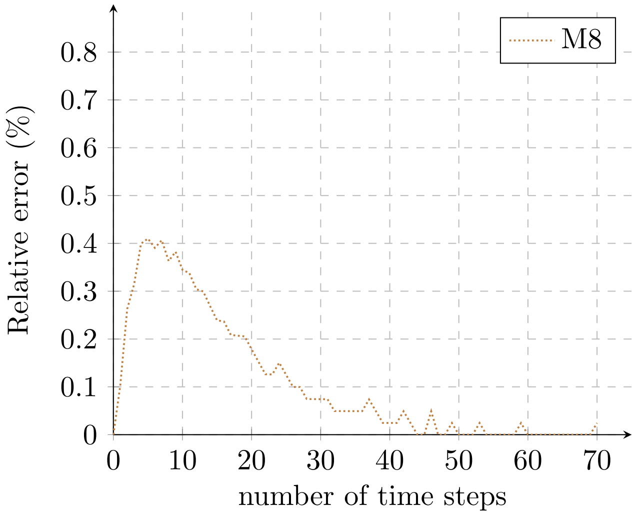

(D) Absolute relative error between the coupled and the fluid only simulation versus the number of time steps

FIGURE 5.26: Results for mesh M8

5.5.2 Coupled Heat Convection: Flow Past A Sphere

In this simulation a fixed solid sphere immersed in a moving fluid is considered. The immersed shell is used for the momentum coupling (Yang et al., 2016) and for thermal coupling, the immersed shell-body presented in this chapter is employed. The fluid domain is cubical with 0.4 m edges and the solid sphere embedded at its centre is of 0.05 m radius (Figure 5.27). The simulation parameters are presented on Table 5.3. Fluid and solid properties are chosen to be the same so the results of the coupled simulation can easily be compared with the results of a fluid only simulation. In the fluid only simulation, only the momentum coupling is enabled, thus only heat conduction is possible on V_s^f.

An adapted mesh is used for the fluid domain with $L_0 = 0.05\ m$ and $L_a = 0.005\ m$, the solid mesh size is of a uniform size of $0.005m$, see Figure 5.28. The fluid and solid are of an initial temperature of $0°C$ and fluid of a temperature of $1°C$ is injected from one of the faces of the fluid domain and is allowed to flow outside of the domain through the opposite face, all other faces impermeable. There is a differential pressure of 10 Pa between the inlet and the outlet.

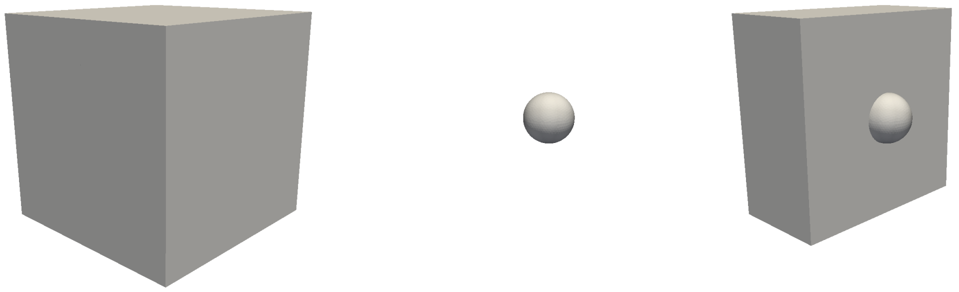
(A) Fluid domain (B) Solid domain (C) Cross-section view

FIGURE 5.27: Fluid and solid domain geometries for validation of the coupled heat conduction.

time step	$0.01\ s$
Δr	$0.005\ m$
κ_s, κ_f	$1\ W.(m.K)^{-1}$
c_f, c_s	$1\ J.(Kg.K)^{-1}$
ρ_f, ρ_s	$1000\ kg.m^{-3}$

TABLE 5.3: Simulation parameters for Solidity and Fluidity.

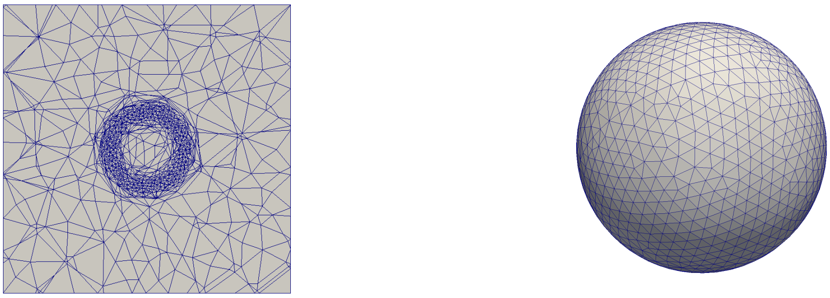

(A) Cross-section of the adapted fluid mesh (B) Solid mesh

FIGURE 5.28: Fluid and solid meshes for the coupled heat convection simulation

Graphical results are presented on Figure 5.29 for the fluid-only simulation, on Figure 5.30 and 5.31 for the coupled simulation. Temperature profiles are presented for different times on Figure 5.32, the time evolution of the temperature integral is presented on Figure 5.33 with the associated error.

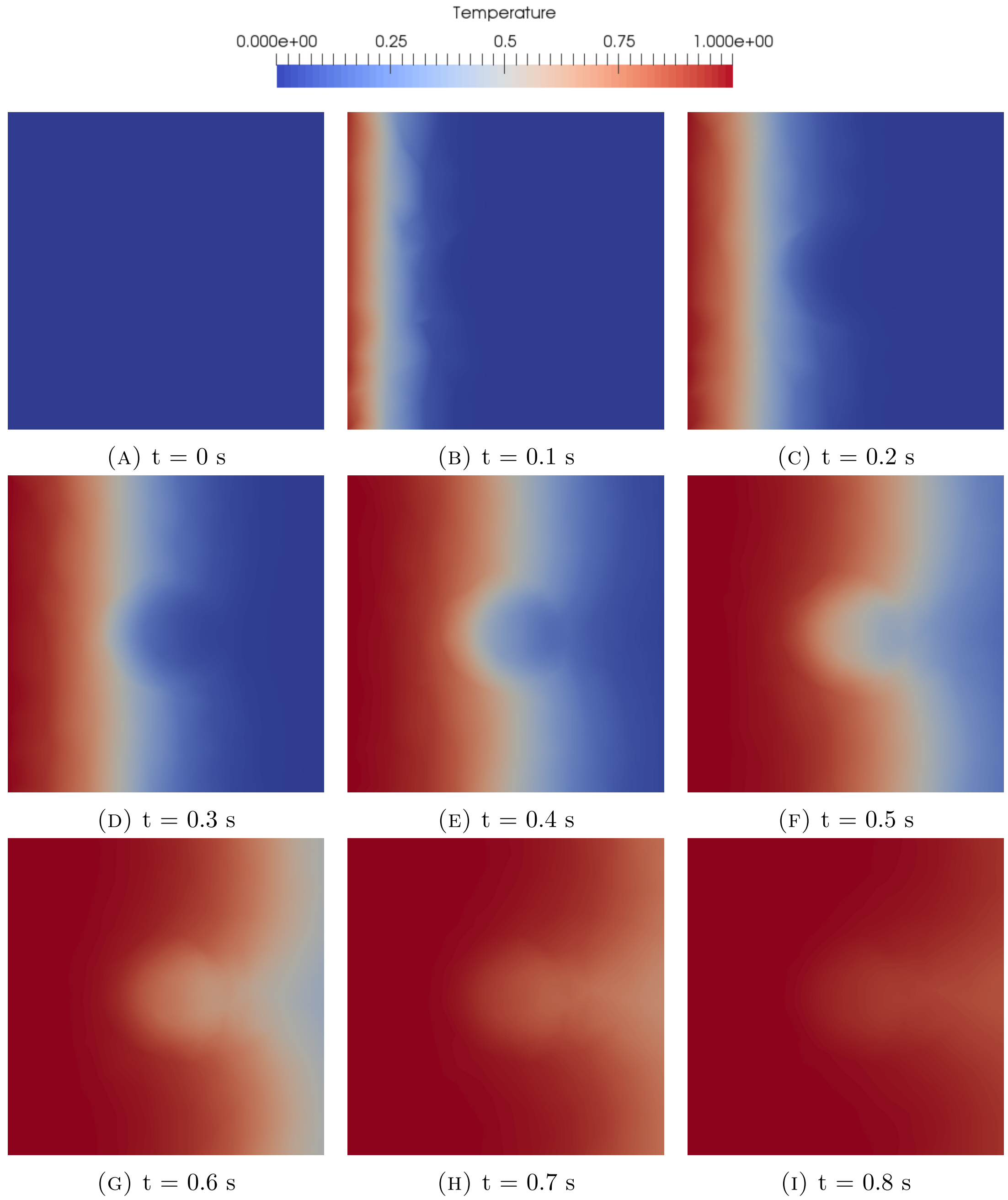

(A) t = 0 s (B) t = 0.1 s (C) t = 0.2 s

(D) t = 0.3 s (E) t = 0.4 s (F) t = 0.5 s

(G) t = 0.6 s (H) t = 0.7 s (I) t = 0.8 s

FIGURE 5.29: Temperature evolution over time in a cross-section for the fluid only simulation.

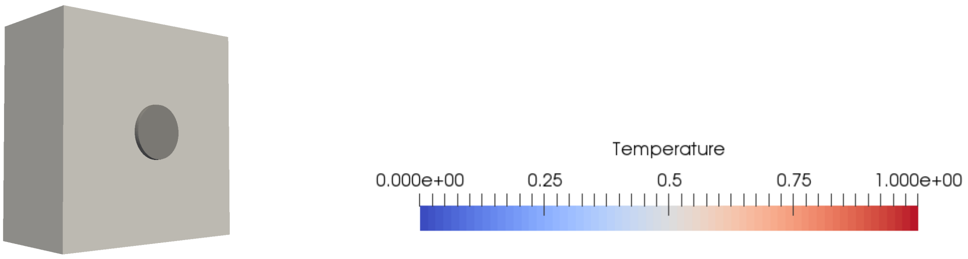

(A) Fluid domain cross section (light grey) and solid domain cross-section (dark grey)

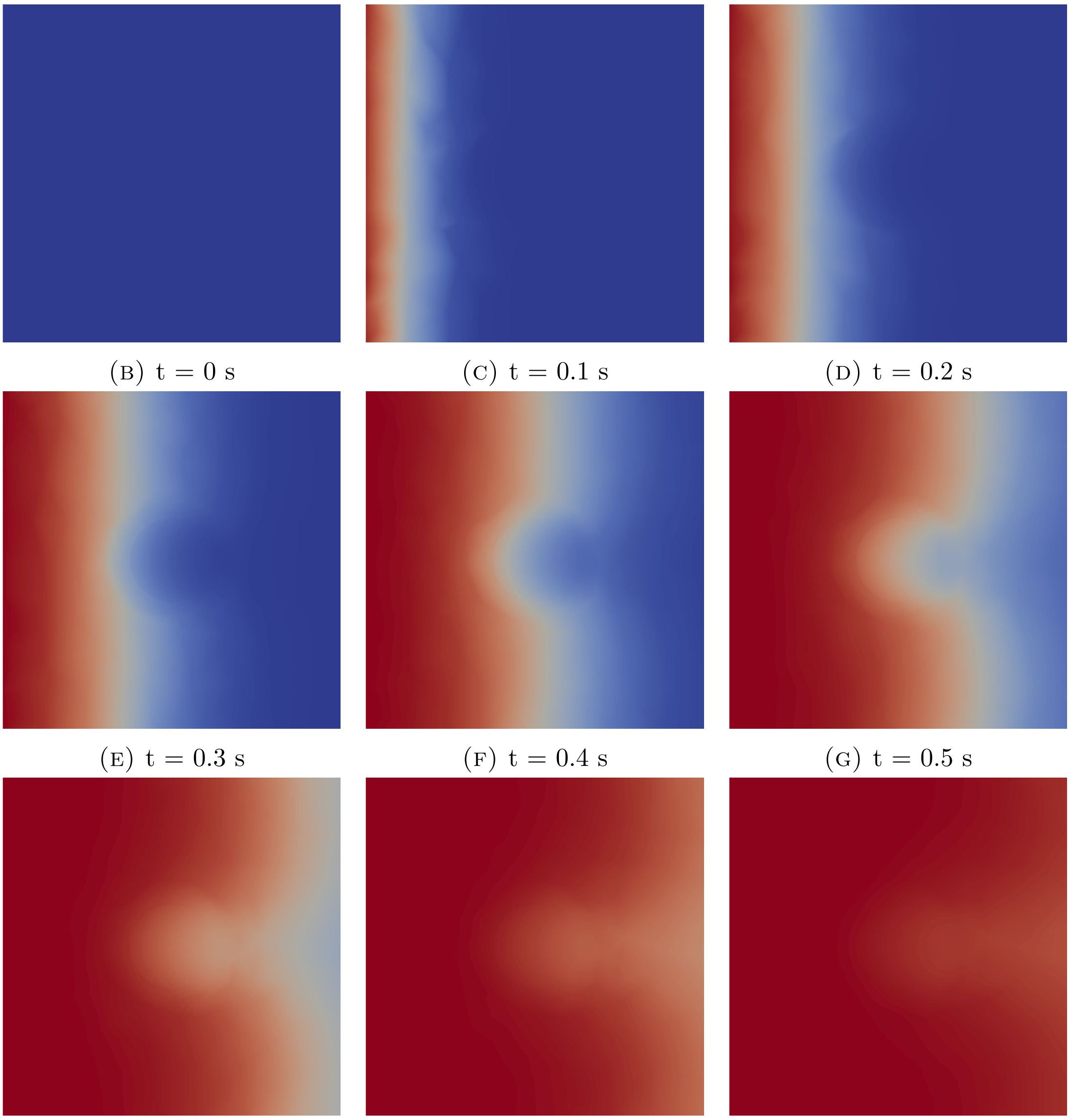

(B) t = 0 s

(C) t = 0.1 s

(D) t = 0.2 s

(E) t = 0.3 s

(F) t = 0.4 s

(G) t = 0.5 s

(H) t = 0.6 s

(I) t = 0.7 s

(J) t = 0.8 s

FIGURE 5.30: Temperature evolution over time in a cross-section for the coupled simulation. (A) shows the configuration of the cross-section, leaving the solid apparent on top of the fluid domain.

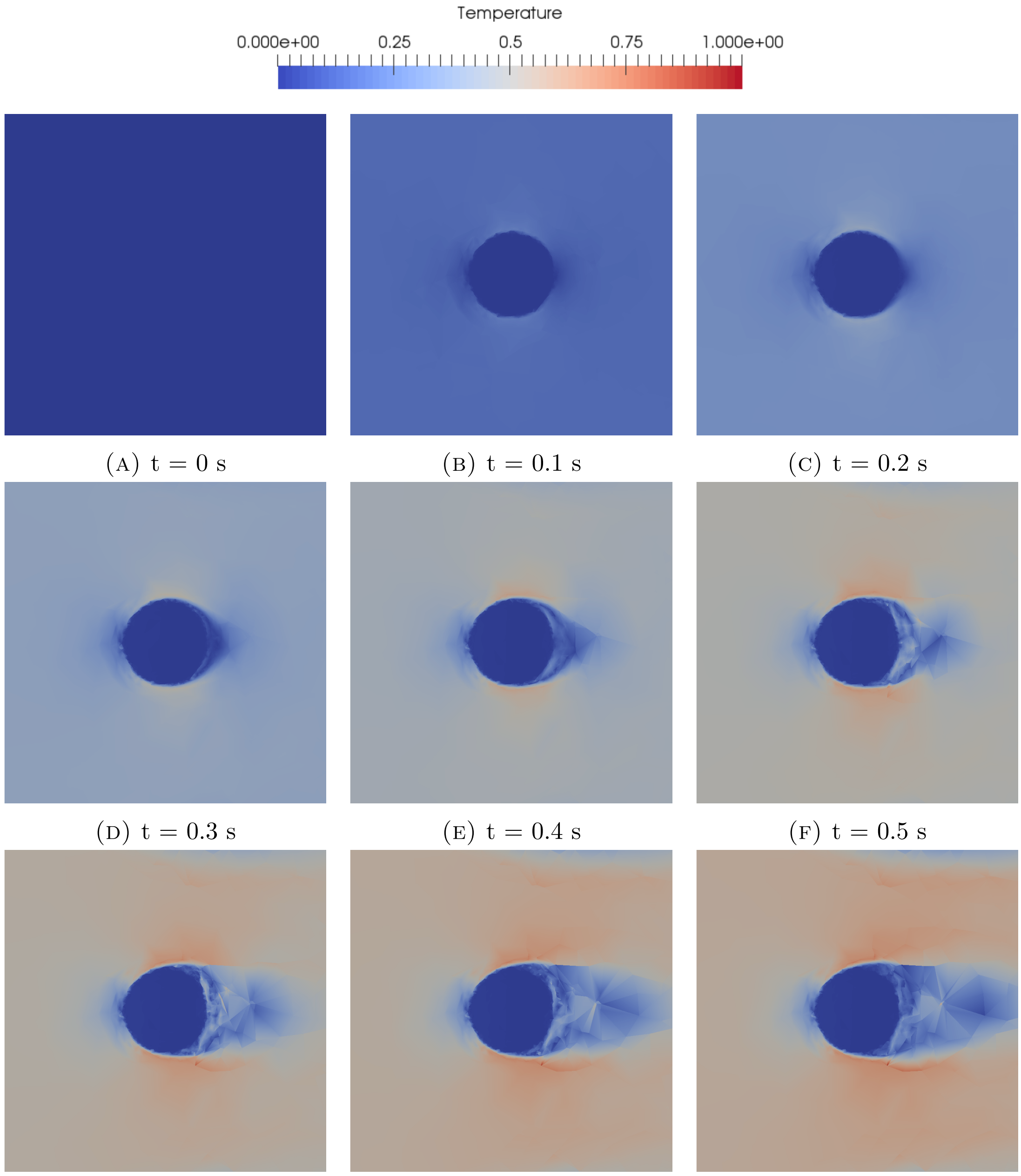

(A) t = 0 s (B) t = 0.1 s (C) t = 0.2 s

(D) t = 0.3 s (E) t = 0.4 s (F) t = 0.5 s

(G) t = 0.6 s (H) t = 0.7 s (I) t = 0.8 s

FIGURE 5.31: Velocity magnitude evolution over time in a cross-section of the fluid domain in the coupled simulation.

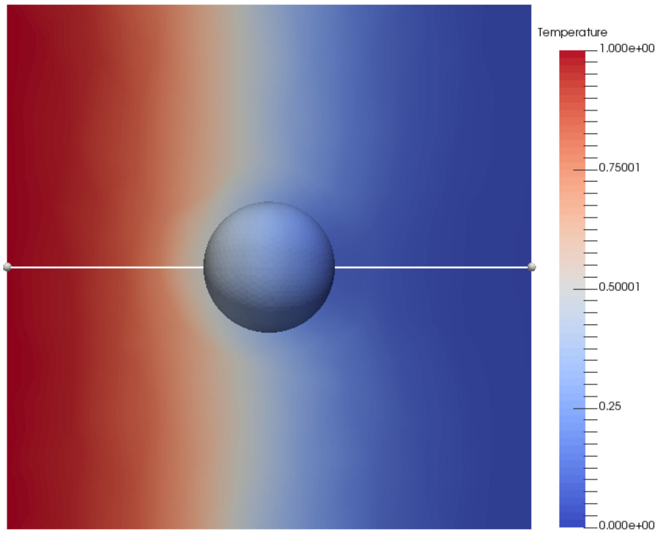

(A) Line of plot for the temperature profiles of (B)

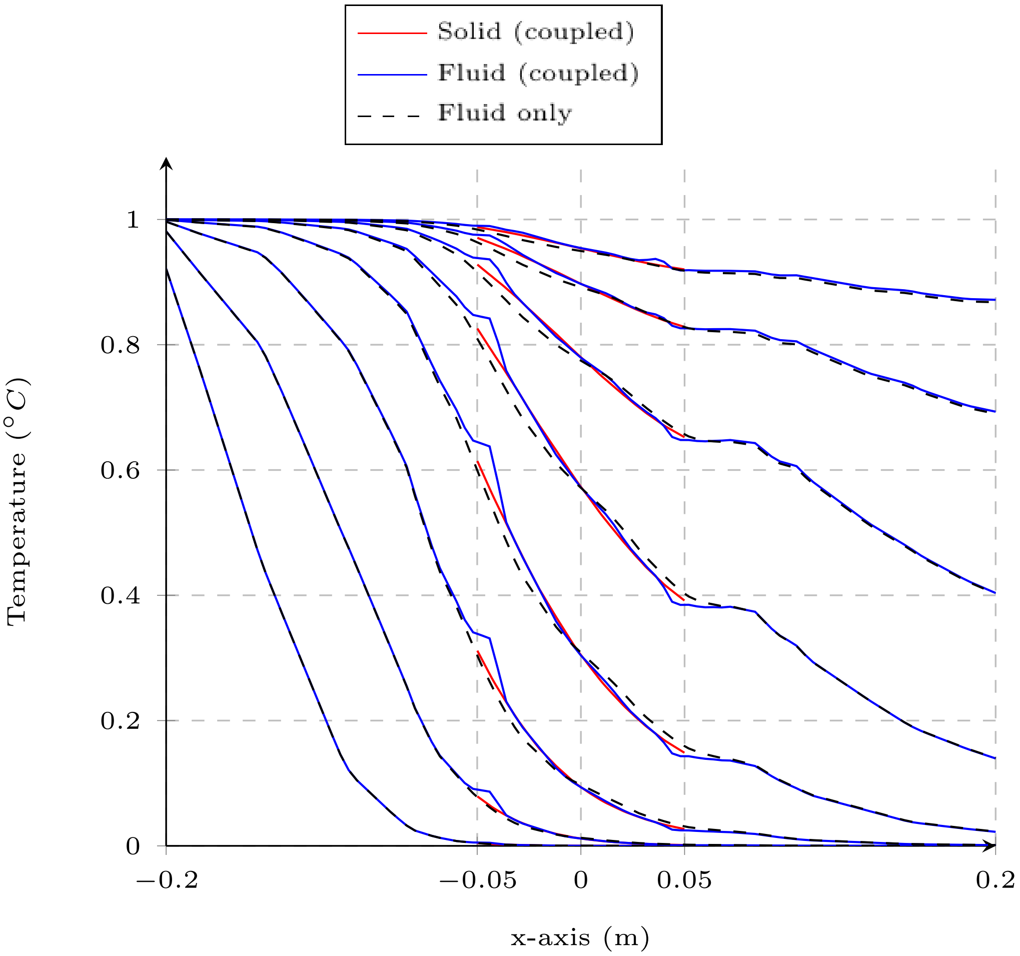

(B) Temperature profiles at times 0.1 s, 0.2 s, 0.3 s, 0.4 s, 0.6 s, 0.7 s, 0.8 s and 2 s (bottom to top)

Figure 5.32: Temperature profiles for the heat convection simulation.

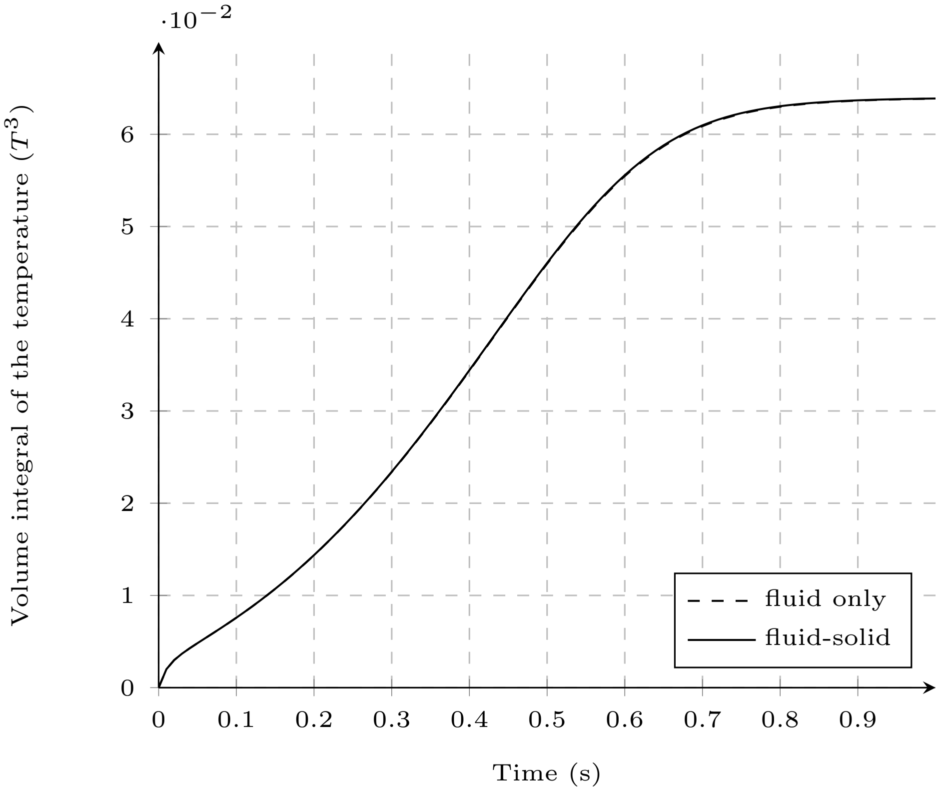

(A) Temperature integral versus time

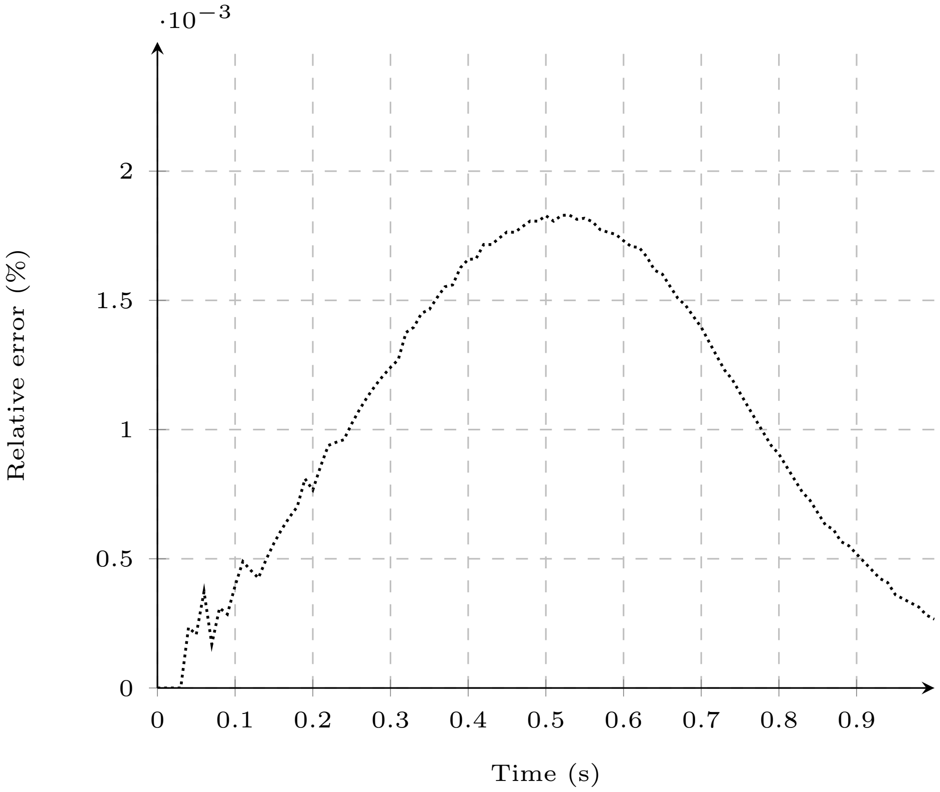

(B) Absolute relative error between the coupled and the fluid only simulation versus time

FIGURE 5.33: Temperature integrals for the heat convection simulation.

5.6 Concluding Remarks

In this Chapter the immersed body and the immersed shell method were investigated, after concluding that the methods alone were not sufficient to perform thermal coupling, an immersed shell-body method was presented. The immersed shell-body demonstrated high accuracy on the presented validations and also has proven to be compatible with adapted mesh. At present in the Fluidity-Solidity coupling, the shell and the volume mesh are projected separately on the fluid mesh. To gain in efficiency, the coupling term should be formed on the combined shell-volume mesh and projected at once. This should also remove the irregularities observed in the temperature profiles at the fluid-solid interfaces.

Chapter 6

Thermal Spalling Application

This chapter presents the foundation for the numerical modelling work necessary to address a THM coupled thermal spalling problem designed in collaboration with the Swedish nuclear fuel and waste management company (SKB). The investigation aims to provide insight on recent experimental findings whilst improving understanding and predictive capabilities of thermal spalling.

6.1 Problem statement

6.1.1 Spalling and Thermal Spalling Phenomena

Spalling is defined as stress-induced brittle failure at the boundary of an underground excavation. Failure occurs in thin slabs which form a V-shaped notch extending in the rock mass (Figures 6.1 and 6.2). Spalling may first take place after the construction phase of the repository as a response of the stress redistribution around the excavated volumes. Brittle failure may also be initiated or aggravated after deposition of the heat generating waste because of the thermal stress induced in the rock mass, the latter is referred to as thermal spalling. For spalling to initiate at a specific location, the spalling strength must be exceeded, which is defined as the compressive tangential stress ($\sigma_{\theta\theta}$) necessary for the rock to fail (Andersson, 2007, Martin, 2005).

(A) Rock slabs

(B) V-shaped notch

FIGURE 6.1: Spalling observations in the experimental deposition holes of the ASPE (Andersson, 2007).

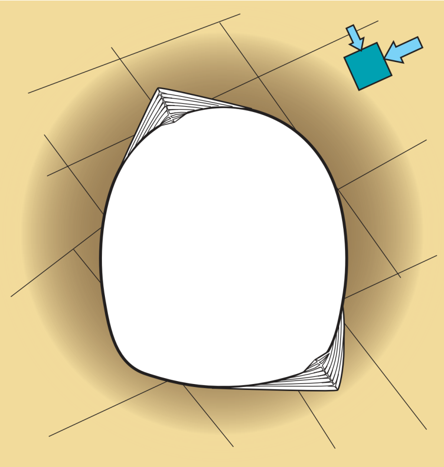

FIGURE 6.2: Schematic representation of stress-induced spalling (Martin, 2005).

6.1.2 Safety Concerns Associated with Spalling

The continuous process of thermally induced failure that occurs after deposition of the HLW canisters and closure of the repository is the main safety concern associated with spalling. A spalled zone with high hydraulic conductivity will increase the potential for radionuclide transport into the rock mass (Neretnieks, 2006).

Several in-situ experiments conducted by SKB examined the occurrence of spalling and the possibilities to minimize it. The Äspö Pillar Stability Experiment (APSE, Andersson 2007) provided evidence that a relatively small support pressure (of a few hundred KPa) applied on the walls of the deposition hole was sufficient to control thermal spalling, which confirmed the conclusions of previous numerical investigations (Birkholzer et al., 2005a, Cho et al., 2002).

As discussed in Section 2.1.3, the saturated rock environment allows the hydration of the bentonite which causes swelling, thereby preventing the aggravation of spalling. However, there is still a concern for dry deposition holes or conditions that do not allow the bentonite to reach full saturation and to provide a sufficient support pressure. If such conditions are sustained over time, the potential for spalling will increase as the thermal stress develop in the rock mass.

The CAPS experiment (Counterforce Applied to Prevent Spalling) was designed after the ASPE to determine if the small counterforce created by the deposition of bentonite pellets could be sufficient to suppress or reduce thermally induced spalling (Glamheden et al., 2010). Results showed that the pellets are not sufficient to prevent the excavation from failing, although they will keep slabs in place and limit the hydraulic conductivity of the spalled area. Glamheden et al. (2010) also reported that in experimental deposition holes appearing as dry, minor spalling occurred, whereas more continuous zones of failure were observed in holes appearing as wet. A possible explanation for the correlation between saturation and extent of spalling is the reduction of rock strength in the presence of water (see Section 6.1.4). It is important to note that the different saturation levels may not be the only cause explaining the observations, local heterogeneities in the rock mass and the presence of a shear zone may also have contributed (Glamheden et al., 2010).

Nevertheless, there is at present no final assessment of the direct causality link between the saturation levels in the rock mass and the initiation and propagation of spalling (Hökmark et al., 2010). Additionally, even in the event of bentonite swelling, there is no evidence that a sufficient support pressure will develop in time to suppress thermal spalling (Hökmark et al., 2010). Therefore, a scientific understanding of the THM processes involved in the time evolution of saturation in the bentonite as well as predictive capabilities are necessary.

6.1.3 Bentonite Saturation Time

To increase the scientific understanding of the hydraulic interaction in the three-barrier system, the Bentonite Rock Interaction Experiment (BRIE. Fransson et al., 2017) was conducted in the Äspö Hard Rock Laboratory, Sweden. Key findings of the experiments included that i) the emplacement of the bentonite causing a pronounced de-saturated zone around the experimental boreholes ii) that fractures provided the main wetting to the bentonite.

Numerical modelling was carried out as part of the BRIE (Holton and Hoch, 2017, Vidstrand et al., 2017). Discrete fracture networks generated stochastically were used to represent each fracture individually or to calculate effective porous medium properties for each grid block, both solved with TOUGH2 in three dimensions. Results showed that the large capillary pressure caused by the bentonite (up to 70MPa) is the driving force of the de-saturation of the surrounding rock and its re-saturation over time. The suction strength of the bentonite is a function of saturation and will be maximal at the time of deposition (Dueck and Nilsson, 2010, Vidstrand et al., 2017). Additionally, the following observations were made:

- Porous media flow had a significant impact on the bentonite saturation time even in sparsely fractured rocks,
- Saturation of the bentonite is highly heterogeneous and cannot be captured with an homogenous representation of the host rock hydraulic properties,
- Saturation time differences of about 40 years were observed between individual fracture and effective medium representations.

Two dimensional numerical simulations of the BRIE were also conducted by Dessirier et al. (2017) with TOUGH2, considering a 100 MPa initial suction strength. The results showed a desaturated zone extending on a distance of about 2/3 larger to that of the radius of the deposition hole considered (0.15 m). In addition, the bentonite saturation time was shown to be highly dependent on the presence of conductive fractures oriented towards and/or connected to the deposition hole. Dessirier et al. (2017) calculated a saturation time of a year for the buffer in the vicinity of a conductive fracture, whereas it would take up to 10 years at other positions (Figure 6.3).

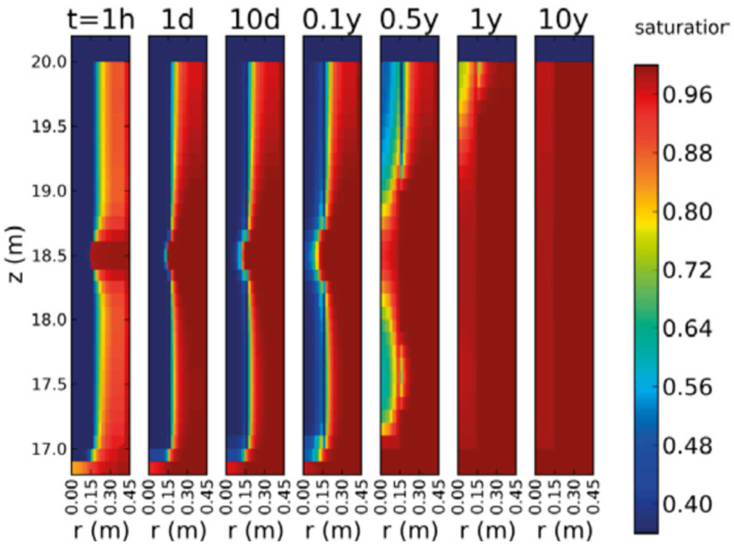

FIGURE 6.3: Evolution of saturation for a bentonite-rock model at different times after emplacement of the bentonite. A fracture is present at mid-height of the deposition hole Dessirier et al. (2017).

The assumption of uniformly flowing fractures intersecting the deposition hole horizontally is the most common scenario in the modelling (Åkesson et al., 2010, Dessirier et al., 2017, Hökmark et al., 2010). However, reviews by Tsang et al. (1998) and Black (2012) conclude that fracture flow in rocks occurs in channels rather than uniformly (Figure 6.4). Depending on the characteristics of the channelled flow, the saturation of the buffer in the fracture plane and vertically may not be as evenly distributed compared to with uniform flow. Heterogeneous wetting patterns could lead to uneven swelling pressures and may have significant consequences on spalling.

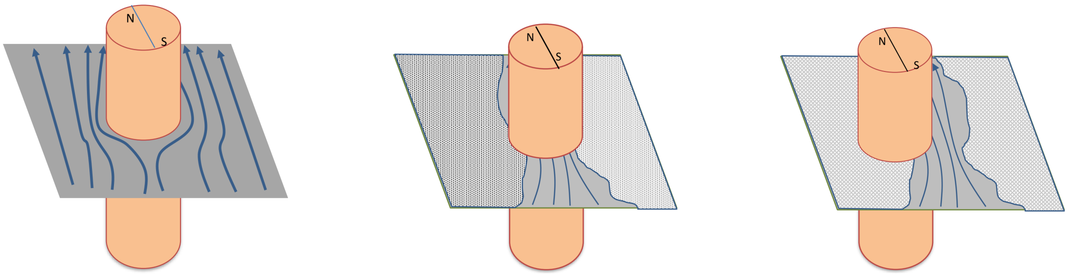

(A) Uniformly flowing fracture

(B) Disconnected channelled flow (the deposition hole interrupts the fracture flow)

(C) Grazing channelled flow

FIGURE 6.4: Different fracture flow scenarios. Arrows represent the expected flow direction after saturation of the bentonite buffer (Thatcher et al., 2018).

Thatcher et al. (2018) investigated channel flow re-saturation by performing THM coupled modelling in the bentonite with QPAC, considering heat conduction processes in a rigid rock mass and hydraulic processes in fractures only. The results showed saturation times differing by more than a factor of four depending on whether the flow was uniformly intersecting the entire circumference of the excavation or whether the flow was channelled over a smaller perimeter.

Additionally, Dessirier (2018) presented a three-dimensional analysis of the re-saturation problem with TOUGH2. The main objective of the study was to compare the impact of different modelling assumptions on the buffer saturation time: i) saturation via inflow from a single fracture versus porous media flow, ii) homogenous fracture flow versus channelled flow and iii) representation of the bentonite as an homogenised material versus representation of the bentonite in its deposition configuration i.e., with pellets and blocks (the compacted bentonite blocks surround the canister and bentonite pellets are inserted in the gap between the bentonite and the rock SKB, 2010b). The results showed that i) re-saturation by porous media flow is a viable scenario if there is no conductive fracture within a meter from the deposition hole wall, ii) flow channelling can affect the buffer re-saturation time significantly only if the area of intersection between the fracture and the excavation wall is restricted and iii) the pellet-filled gap distributes the water intake to the outer surface of the bentonite blocks. While the spaces between the bentonite pellets acting as flow pathways may prevent issues associated with uneven bentonite swelling caused by flow channelling, it is not known how long this effect will last as the pellets eventually homogenise with the blocks.

6.1.4 THM Coupled Processes in the Context of Thermal Spalling

Small scale simulations and experiments suggest that the de-saturation in the rock occurs within a small domain compared to the size of the excavations (Dessirier et al., 2017, Fransson et al., 2017). Assuming that there is no significant scale effect with respect to the BRIE experiment, a de-saturated zone extending up to a few meters away from the excavation walls can be expected for the full scale deposition hole (about 1.8 m diameter, SKB 2010a). Moreover, vertically distributed spalled zones are reportedly circa 10 cm deep and 30 cm wide (Andersson, 2007). It is important to put in perspective that the scale of the problem considered is relatively small compared to radioactive waste repository applications in general. Therefore, special attention must be paid to certain THM coupled processes as they may have a significant impact at the scale of interest:

Thermal→ Hydrological : Heating-cooling of the entrapped water and thermal expansion leading to fluctuations in fluid pressure.

On one hand, using a coupled thermo-hydro-mechanical approach on a heater test at the Kamashi Mine, Rutqvist et al. (2001b) observed in their models pore fluid pressure fluctuations in the order of 0.1 MPa. This is a relevant magnitude compared to the low in-situ fluid pressure but this wasn't concluded to be sufficient to induce any relevant mechanical effects such as fracture opening.

On the other hand, Andersson (2007) determined that changes in the tangential stress magnitude of only 1 MPa was sufficient to cause a yielding zone in the deposition hole wall. Andersson's observations suggest that without this thermally induced stress change further yielding and widening of the spalled zone would not occur.

Considering the stress sensitivity of spalling, it is worth investigating the magnitude of this coupling as this may have an impact depending on the specific in-situ conditions and properties, especially the canister power and the bentonite suction strength.

Hydrological→ Mechanical : Micro scale fluid-solid interactions.

In comparison to dry samples, an experimental study reported by Hudson et al. (2008) indicated an average reduction of 17% in rock strength for fully saturated samples containing 0.68% or 10% of saline solution (Figure 6.5). Similarly, laboratory tests performed within the CAPS experiment found a reduction of 10% in both the crack initiation stress and the uniaxial compressive strength of the rock between dry and wet samples (Glamheden et al., 2010). Both studies were conducted on samples from the Äspö diorite, the rock type considered in the modelling work of this chapter. Considering the stress sensitivity of spalling, the reduction of rock strength coupled with the increase in water content must be investigated.

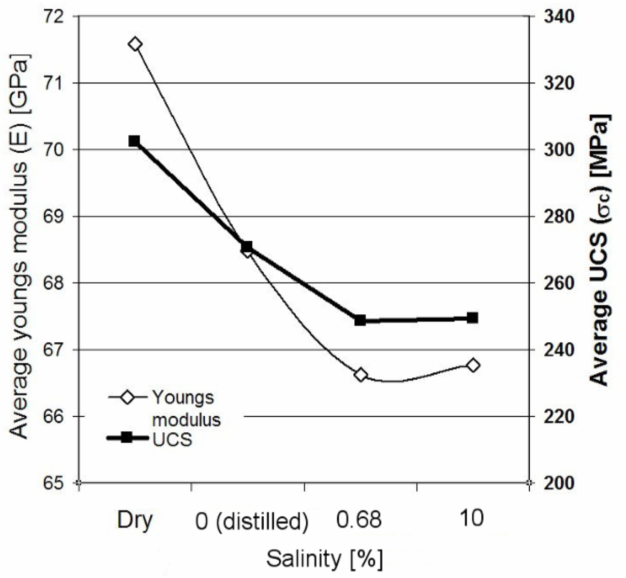

Figure 6.5: Mean Young's modulus and UCS (Uniaxial Compressive Strength) of Äspö diorite specimens in four different saturation conditions (Hudson et al., 2008).

Thermal→Mechanical→Hydrological: In the vicinity of the deposition hole, thermal stress influences the porosity of the media and the aperture of fractures. Depending on their orientation fractures may be compressed, dilated or sheared (Birkholzer et al., 2005b, Rutqvist et al., 2009b, Rutqvist and Tsang, 2003). The saturation time relies on the hydraulic conductivity of the porous and fractured rock, yet no numerical study considered their dependency to thermal and in-situ stresses, neither for single fractures or for the fracture networks of the excavation damage zone.

Hydrological→Mechanical→Thermal→Mechanical: When placing the waste canister, a 10 mm air gap is left between the canister surface and the bentonite blocks as part of the design (SKB, 2010b). Upon swelling, the bentonite will come in full contact with the canister. In dry conditions the maximal buffer temperature is significantly higher than in saturated conditions (Hökmark et al. 2010, Figure 6.11) and thus higher thermal stress can be expected.

6.1.5 Objectives

There is a plausible concurrence in time between positive factors preventing spalling (i.e. factors leading to bentonite swelling; and lowering maximal temperatures and thermal stress) and negative factors that have the potential to aggravate spalling (i.e. saturation dependent rock strength, fluctuations in fluid pressure, higher maximal temperatures and thermal stress). Changes in pore space and fracture aperture will also come into play but the nature of their contribution is to be determined.

In the literature, the saturation time and the thermal spalling have been investigated separately, the stress changes in the excavation have not been considered alongside the evolution of saturation and bentonite swelling with a THM coupled approach in the rock and the bentonite. Additionally, no study considered the impact of thermal stress on fracture aperture and saturation time.

In this work, a THM coupled time-dependent investigation of saturation and thermal spalling is proposed with the numerical method outlined in this thesis. The research aims at providing answers to the following interrogations:

- At what points in time and under which conditions can thermal spalling initiate before the bentonite buffer provides a sufficient support pressure?
- Can the saturation levels have a significant negative impact on the spalling phenomena at a certain point in time?
- In which proportions can the changes in pore space and fracture aperture influence the saturation time?
- What is the influence of pre-existing and propagating fractures on the distribution of thermal stress and thermal spalling?

The method is thought to be particularly suited to the investigation because the considered problem

- Is dependent on THM coupled processes,
- Has three dimensional implications because the THM conditions vary in the horizontal plane and along the vertical axis of the deposition hole,
- Involves multiphase flow during the saturation process of the bentonite-rock environment,
- Involves spatial heterogeneities,

- Has a three-material configuration: rock, bentonite buffer and waste canister,
- Occurs over large time scales: in certain cases considered in the modelling, the full saturation of the bentonite can take up to several thousands of years (Thatcher et al., 2018),
- Involves fractures: pre-existing fractures, EDZ fractures and spalling cracks. Such features have a strong influence on the saturation time due to their relatively high hydraulic conductivity compared to the porous media (Dessirier et al., 2017).

6.2 Numerical Model

6.2.1 Scope of the Analysis

The work presented in this chapter provides a preliminary insight into the investigation of thermal spalling and saturation, aiming to demonstrate the potential of the Fluidity-Solidity method to tackle the problem rather than making definitive conclusions, which will be the objective of future work. The following coupled process are considered:

- Multiphase flow
- Thermal expansion of the rock
- In-situ stress conditions in the rock mass
- Heat convection
- Multi-materiality for hydraulic and thermal processes
- Saturation dependent thermal properties

Primarily because of time constraints a number of coupled processes and features are not taken into account, they are:

- Multi-materiality for the mechanical processes
- Thermal expansion of the fluids
- Capillary pressure
- Poro-elasticity
- Pre-existing fractures and fracturing
- Hydro-mechanical coupling in fractures including saturation dependent mechanical properties

The thermal and hydraulic process are solved with Fluidity (IC-FERST) whilst the mechanical process are solved with Solidity. The model specifications, material properties and boundary conditions are presented in the following sections.

6.2.2 Thermal and Hydraulic Model (Fluidity)

Geometry

The size of the model must be large enough so that in-situ conditions at the boundary do not influence the thermal or hydraulic results. The heat wave generated by the canister will travel to the boundary and will be reflected back to the source. Additionally, the pressure gradient depends on the distance between the hydrostatic condition at the domain boundary and the atmospheric condition at the tunnel. The model was increased gradually until no significant difference in the thermal or hydraulic results could be observed over the total simulation time. The model extends up to 400 m away from the centre of the deposition hole, vertically and radially. As no heterogeneities are considered, the problem has a vertical symmetry plane orthogonal to the tunnel direction and centred on the deposition hole. Consequently, a vertically halved cylindrical geometry is chosen. Schemas of the model geometry are presented on Figures 6.6, 6.7 and 6.8.

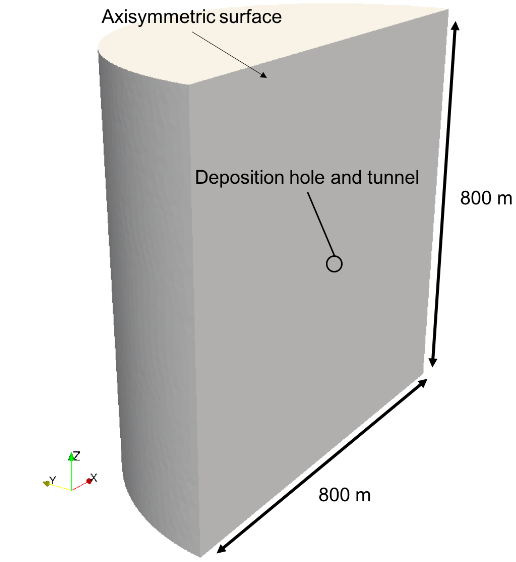

Figure 6.6: Fluidity model geometry

The thermo-hydraulic processes are modelled in the rock and in the bentonite which are treated as porous media domains. Since the waste canister is impermeable, it is preferable not to model its volume but instead consider the interface between the bentonite and the canister as a domain boundary. Dimensions for the different elements of the repository are taken standard (SKB 2010a, Figure 6.7). Note that to simplify the model, the 10 mm air gap between the canister surface and the bentonite blocks (SKB, 2010b) is not considered explicitly.

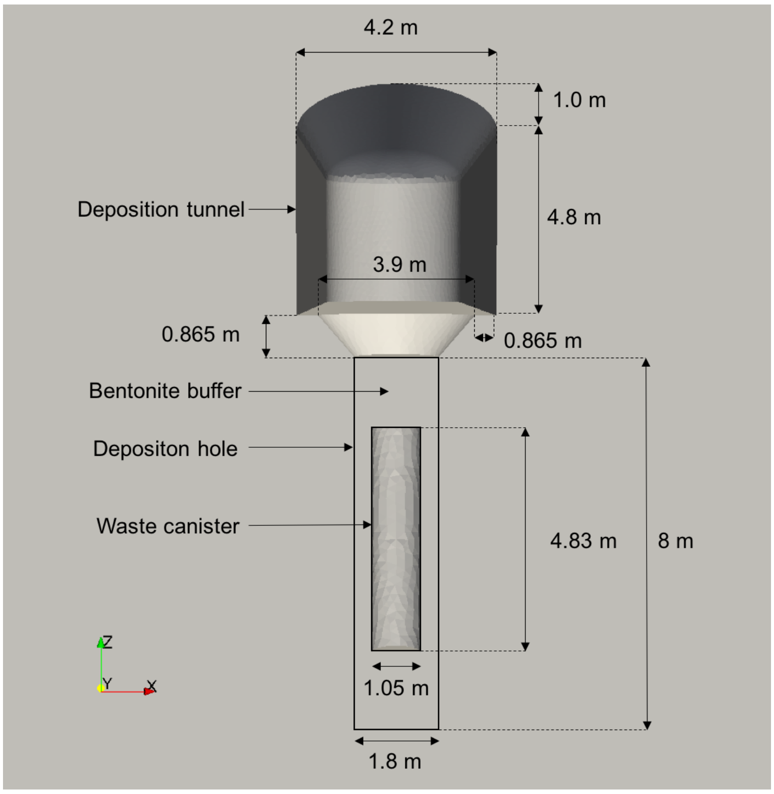

(A) XZ plane view

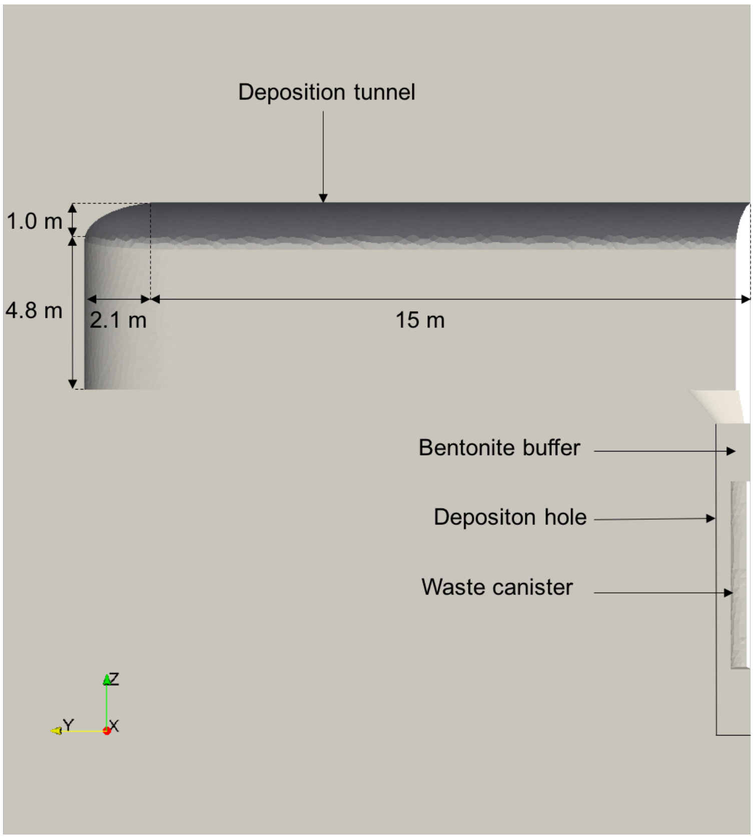

(B) YZ plane, cross-section view

FIGURE 6.7: Fluidity model geometry: close-up of the deposition hole and tunnel. Dimensions from SKB (2010a).

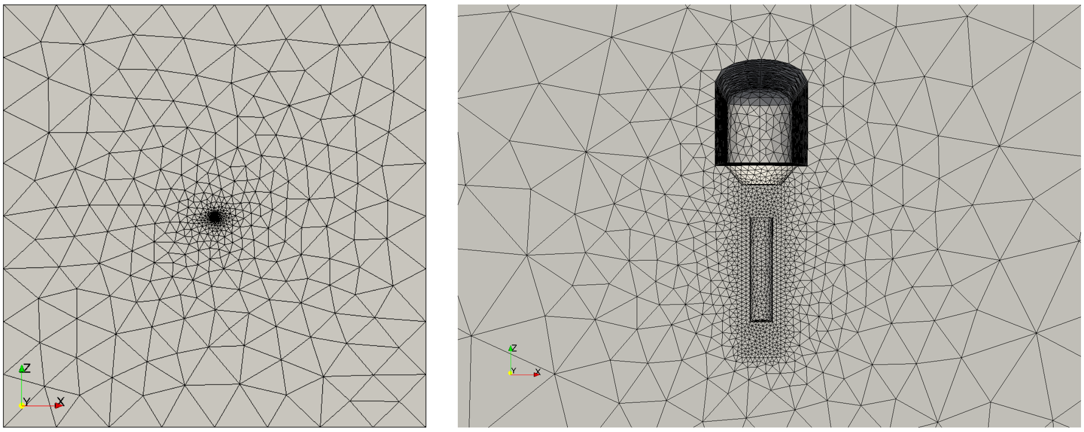

(A) Full model (B) Close-up

Figure 6.8: Fluidity model mesh in the XZ plane.

Hydraulic initial and boundary conditions

There is a no-flow condition on the axisymmetric plane and on the canister boundary, an atmospheric pressure condition at the tunnel and a hydrostatic pressure condition on all the other boundaries. At deposition time (t = 0), the host rock is considered fully saturated and the bentonite is saturated at 36%, see figure below.

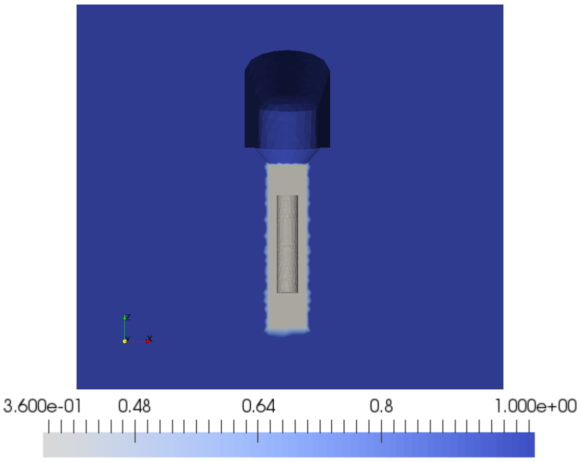

Figure 6.9: Initial saturation in the bentonite and host rock.

Material properties

Similar to the majority of the previously cited modelling work on saturation time, the hydraulic properties for the current modelling are taken from the BRIE (Fransson et al., 2017). Since the BRIE was a hydraulic experiment under iso-thermal conditions, thermal properties are taken from the CAPS experiment which was also conducted in the Äspö

Hard Rock Laboratory, at a similar depth (Glamheden et al., 2010). Thermal and hydraulic properties are summarised in Table 6.1.

	Host Rock	Buffer	Water	Air
Density ($Kg.m^{-3}$)	2750	1560	1000	1.276
Porosity	0.003	0.438		
Permeability (m^2)	1.0×10^{-19}	6.4×10^{-21}		
Cinematic viscosity ($Pa.s$)			7.0×10^{-4}	1.8×10^{-5}
Heat conductivity ($W.(m.K)^{-1}$)	2.6	0.7	0.6	0.03
Mass heat capacity ($J.(Kg.K)^{-1}$)	763.6	1381	4182	1005

TABLE 6.1: Thermal and hydraulic properties of the porous media domain for multi-phase simulation with Fluidity

Thermal initial and boundary conditions

For the present work, the thermal boundary conditions were simplified. First, the geothermal gradient is not represented in the initial temperature or the boundary conditions. The initial temperature is considered to be a uniform $15°C$ (Glamheden et al., 2010). Second, unresolved difficulties were encountered when imposing convection and flux boundary conditions and considering two phases. Thus, a temperature of $15°C$ is imposed at the tunnel boundary and an analytical solution of the temperature is imposed at the canister surface, all other boundaries are considered adiabatic.

The hottest point of the waste canister is found at canister mid-height however, in a dry deposition hole the air filled gap between the bentonite and the canister's vertical surfaces is thermally insulating. Thus the maximum buffer temperature is located at the top of the canister where there is direct contact with the bentonite (Hökmark et al., 2009). In the present configuration, results have shown that the bentonite stays dry during the large majority of the thermal effects, thus the expression of maximum buffer temperature T_{tot}^{dry} for a dry deposition hole is retained (Hökmark et al., 2010)

$$\Delta T_{tot}^{dry}(t) = 0.87 \frac{P(t)}{A\ \kappa_b^{dry}} R_0\ .\ ln(R_2/R_1) + 16\ .\ \frac{P(t)}{P_0} \tag{6.1}$$

$$\Delta T_{tot}^{wet}(t) = 0.87 \frac{P(t)}{A\ \kappa_b^{wet}} R_0\ .\ ln(R_2/R_1)$$

With R_0 the canister radius, R_1 the inner radius of the bentonite blocks (considering a 10mm air gap), R_2 the radius of the deposition hole, $\kappa_b^{dry} = 0.7\ W.(m.K)^{-1}$ and $\kappa_b^{wet} = 1.3\ W.(m.K)^{-1}$ the buffer heat conductivities, $A = 17.664\ m^2$ the canister surface, $P_0 = 1,700\ W$ the initial canister power and $P(t)$ time function of canister power expressed as (Hökmark et al., 2009)

$$P(t) = P_0 \sum_{i=1}^{7} a_i\ e^{(-t/t_i)} \tag{6.2}$$

Where $P_0 = 1,700W$ is the initial power, t_i are time constants and a_i dimensionless coefficients (see Table 6.2). The simplified boundary condition uses the following uniform temperature $T_{can}(t)$ at the canister boundary

$$T_{can}(t) = T_0 + \Delta T_{tot}^{dry}(t) \tag{6.3}$$

With T_0 the initial temperature of the rock domain. The transient evolution of the normalised canister power is plotted on Figure 6.10 and the transient evolution of T_{can} is plotted on Figure 6.11.

i	t_i (years)	a_i
1	20	0.060147
2	50	0.705024
3	200	-0.054753
4	500	0.249767
5	2,000	0.025407
6	5,000	-0.009227
7	20,000	0.023877

TABLE 6.2: Time constants and coefficients of the exponential power expression (Hökmark et al., 2009).

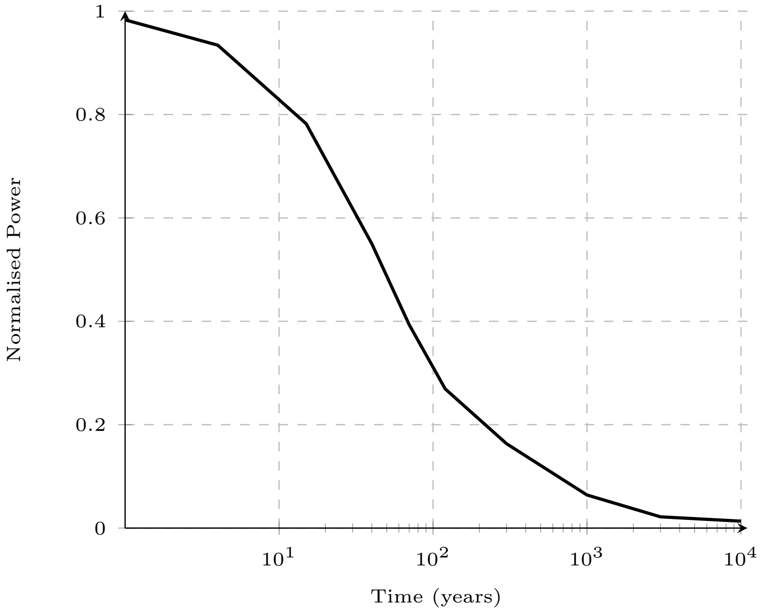

FIGURE 6.10: Transient evolution of the normalised canister power.

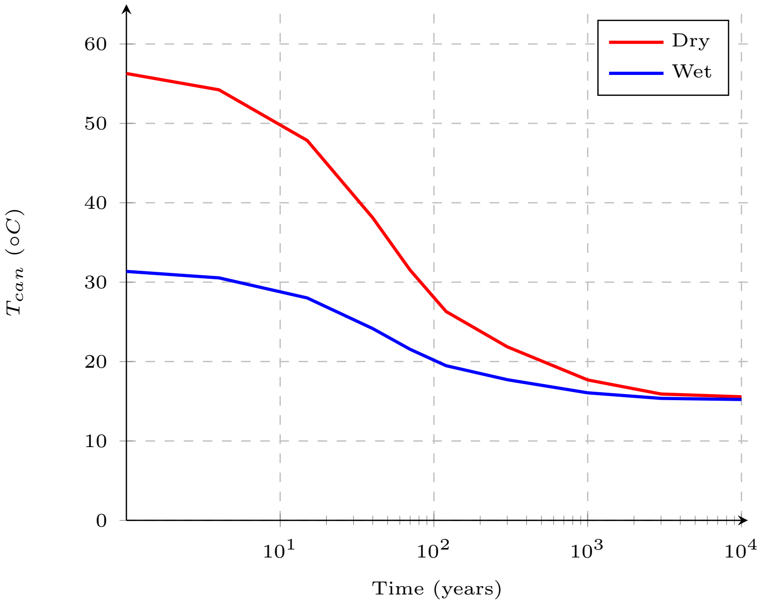

FIGURE 6.11: Transient evolution of the temperature boundary condition T_{can} imposed at the canister surface, for dry and wet conditions.

6.2.3 Geomechanical Model (Solidity)

Geometry

In geo-mechanical modelling, models must be sufficiently large to apply the in-situ stress conditions to the far field in order obtain the correct stress distribution at the zone of interest. For continuum numerical methods like the FEM, a coarse mesh is usually employed at the far-field and is refined in the zone of interest to reduce computational costs. This is however not currently possible with the fracture model of Solidity, elements must be of the same size for the contact force between elements to be consistent. Since relatively small elements are required to resolve fractures accurately, the model size is constrained for the computational cost to remain acceptable. Although the fracture model is not included in this study and a large model could be used, a smaller model is employed to prepare for future work.

Nevertheless, the mechanical model must still be sufficiently large to capture the thermal stresses caused by heating, the spalling cracks and pre-existing fractures. Thus the model chosen does not need to extent more than a few meters away from the deposition hole where the thermal changes will become insignificant and which will also embed the excavation damage zone and spalled areas. The model is chosen to be an axisymmetric hollow cylinder with an outer diameter corresponding to the width of the deposition tunnel, an inner diameter corresponding to the excavation (1.8 m) and a height superior to that of the deposition hole (8 m) so mechanical effects at the bottom of the excavation can be represented, as shown on Figure 6.12. The computational mesh employed in the geomechanical modelling is presented on Figure 6.13.

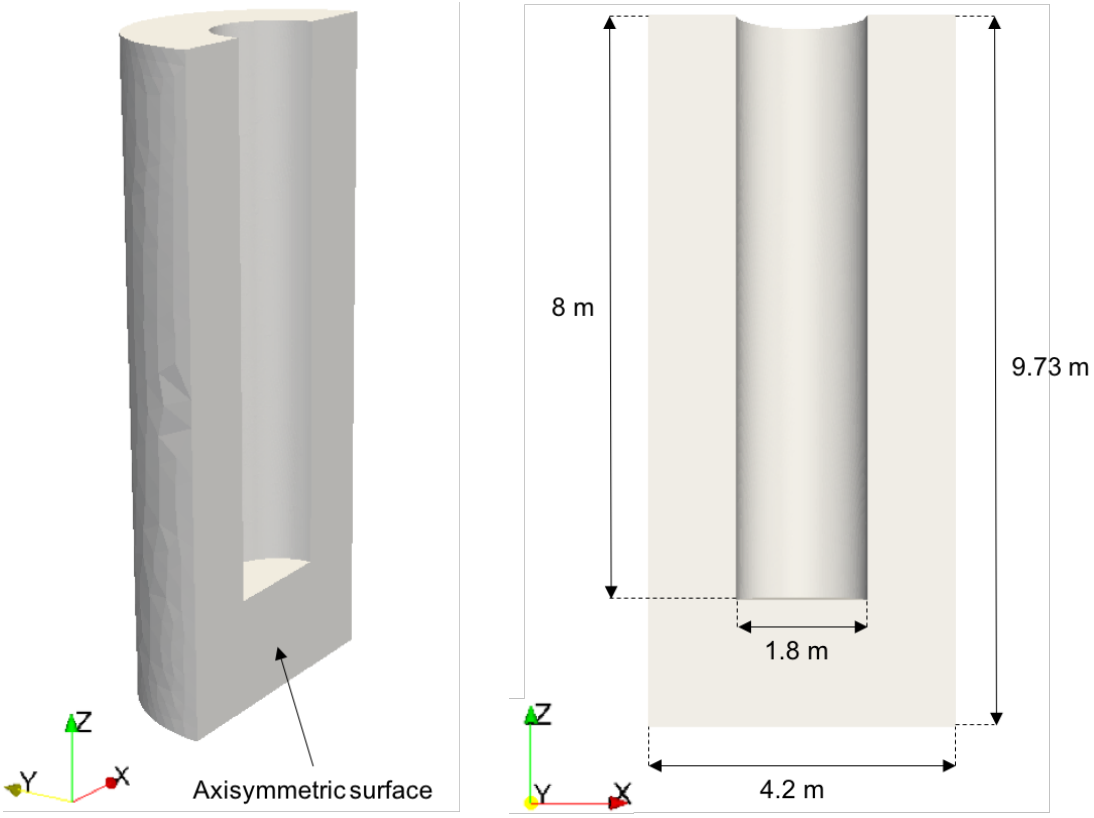

(A) Side View

(B) XZ plane view

FIGURE 6.12: Mechanical model geometry.

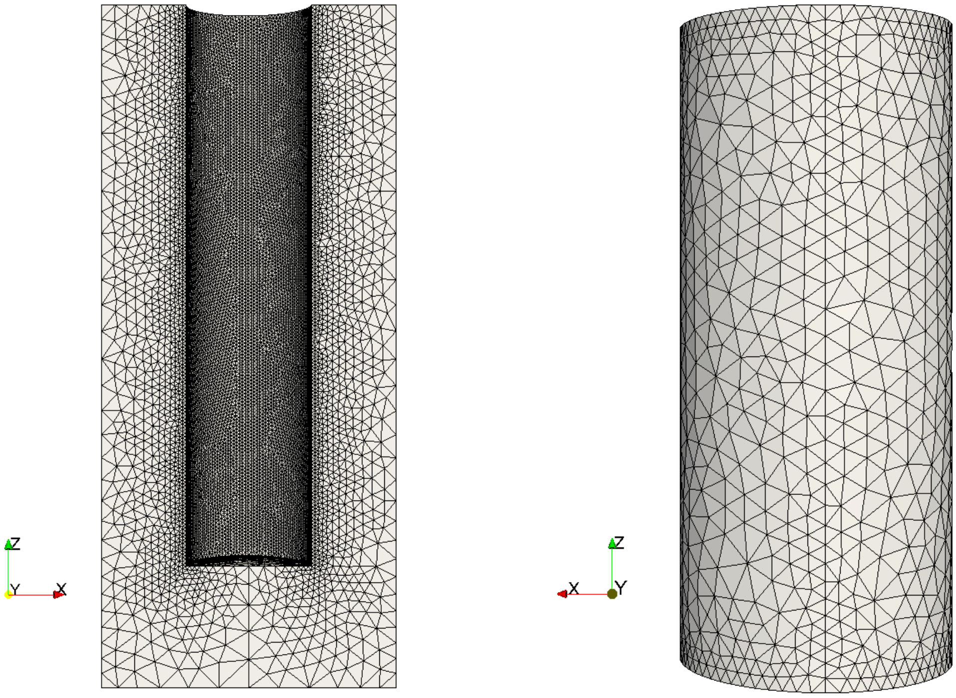

(A) XZ plane view, axisymmetric and excavation boundaries

(B) XZ plane view, radial boundary

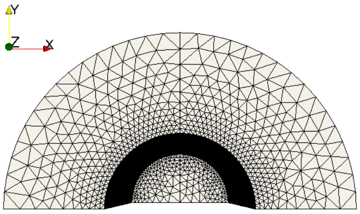

(C) XY plane view, excavation and top boundaries

FIGURE 6.13: Mechanical model mesh

Material properties

The rock properties are taken from the CAPS experiment (Glamheden et al., 2010), they are presented in Table 6.3.

Density $(Kg.m^{-3})$	2750
Young's modulus (GPa)	76
Poisson's ratio	0.25
Uniaxial compressive strength, UCS (MPa)	227
Crack initiation threshold, CI (MPa)	116
Linear thermal expansion coefficient (K^{-1})	7.0×10^{-6}

TABLE 6.3: Mechanical properties of the rock domain for simulation with Solidity (Glamheden et al., 2010)

Mechanical boundary conditions

To resolve the in-situ stress state without a far-field model, an analytical solution is applied as a boundary condition: the Kirsch equations which describe the stress field around a vertical circular excavation. As given by Zoback (2007), the Kirsch equations are:

$$\begin{aligned}
\sigma_{rr}(r,\theta) =& \frac{1}{2}(S_{Hmax}+S_{hmin}-2P_p)\left(1-\frac{R^2}{r^2}\right)\\
&+\frac{1}{2}(S_{Hmax}-S_{hmin})\left(1-\frac{4R^2}{r^2}+\frac{3R^4}{r^4}\right)\cos 2\theta\\
\\
\sigma_{\theta\theta}(r,\theta) =& \frac{1}{2}(S_{Hmax}+S_{hmin}-2P_p)\left(1+\frac{R^2}{r^2}\right)\\
&-\frac{1}{2}(S_{Hmax}-S_{hmin})\left(1+\frac{3R^4}{r^4}\right)\cos 2\theta\\
\\
\sigma_{r\theta}(r,\theta) =& -\frac{1}{2}(S_{Hmax}-S_{hmin})\left(1+\frac{2R^2}{r^2}-\frac{3R^4}{r^4}\right)\sin 2\theta\\
\\
\sigma_{zz}(r,\theta) =& S_v-2\nu(S_{Hmax}-S_{hmin})\frac{r^2}{R^2}\cos 2\theta
\end{aligned} \tag{6.4}$$

With σ_{rr}, $\sigma_{\theta\theta}$, $\sigma_{r\theta}$ and σ_{zz} the components of the stress tensor in cylindrical coordinates, R the radius of the excavation, P_p the pore pressure, S_v the vertical stress, S_{Hmax} and S_{hmin} respectively the maximal and minimal principal horizontal stresses, ν the Poisson ratio, r the radial position and θ the angular position measured from the direction of S_{Hmax}. The in-situ stress conditions are summarized in Table 6.4. Note that the vertical stress was not considered in the present simulation. The model is fixed in the normal direction of the axisymmetric plane.

S_{Hmax} (MPa)	41
S_{hmin} (MPa)	23
P_p (MPa)	4.9

TABLE 6.4: In-situ stress conditions (Glamheden et al., 2010).

6.2.4 Fluidity-Solidity Coupling

For the Fluidity-Solidity coupled simulations, the thermo-hydraulic and coupled model are super-imposed as showed on Figure 6.15. The temperature is projected from the Fluidity to the Solidity volume mesh, this enables the calculation of thermal stress in Solidity.

Thermo-hydraulic processes are calculated on real time whereas the mechanical processes are solved by iterating in a quasi-static loop as illustrated on Figure 6.14. At the first time step, the in-situ stress conditions are loaded on the mechanical model until equilibrium is reached. Then, the Fluidity-Solidity simulation starts. At the end of each Fluidity iteration, the new temperature field is projected to the mechanical model and thermal stresses are calculated in the quasi-static loop.

Fluidity uses an adaptive time step based on the convergence requirements of the hydraulic processes and on the temperature evolution. The latter ensures there is enough temporal resolution to capture the history of the thermal stress with the mechanical model. Therefore, the time step is relatively small during the heating phase when the thermal gradients are sharp; and relatively large when temperatures fall and convergence of the system is governed by the slow saturation process. The adaptive time step ranges from 12 hours to 100 years with a total simulation time of 4,000 years. In Solidity, a fixed time step of 1.0×10^{-6} seconds is used, the number of quasi-static iterations is scaled based on the maximal absolute temperature variation with for reference 4,000 iterations for $1°C$.

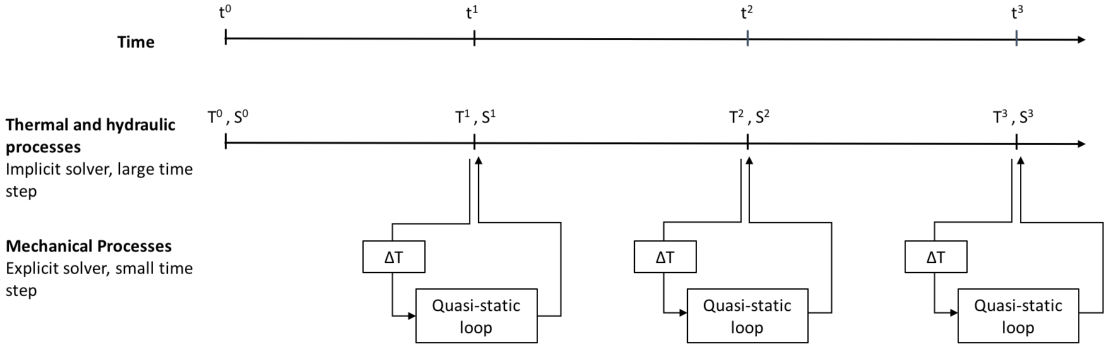

FIGURE 6.14: Illustration of the sequential, quasi-static iteration for the coupling of THM processes employed in Fluidity-Solidity for the thermal spalling application. With T the temperature and S the saturation of the porous media.

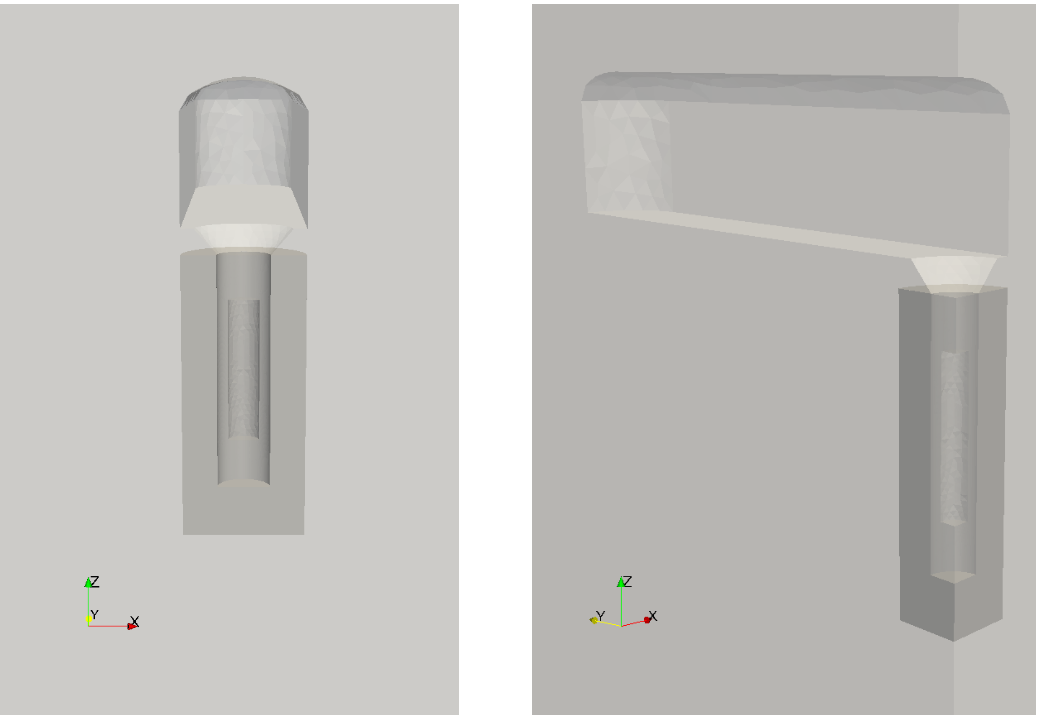

(A) XZ plane view (B) Cross-section view

Figure 6.15: Super-imposed thermo-hydraulic (light grey) and mechanical (dark grey) computational domains

6.3 Results

6.3.1 In-situ stress

Validation

For validation of the initial in-situ stress distribution, a 0.5 m thick section of the geomechanical model is used with the same mesh size as presented on Figure 6.16. S_{Hmax} is considered in the X direction and S_{hmin} in the Y direction. Failure is expected to occur at the excavation wall in the Y axis i.e., in the direction of S_{hmin} where the compressive stress is maximal (Zoback, 2007).

It is important to mention that Solidity is based on Cartesian coordinates and that stress results will be expressed in function of σ_{xx} and σ_{yy}. Also note that the stress convention adopted in the results considers compressive stress as positive. For reference, the horizontal stress components given by the Kirsch equations are plotted on Figure 6.17 in polar coordinates and on Figure 6.18 in Cartesian coordinates.

The stress distributions obtained from the simulations are compared with the Kirsch analytical solution and plotted along the Y axis on Figures 6.19 (σ_{xx}) and 6.20 (σ_{yy}), along the X axis on Figures 6.21 (σ_{xx}) and 6.22 (σ_{yy}) and in the XY direction on Figures 6.23 (σ_{xx}), 6.24 (σ_{yy}) and 6.25 (σ_{xy}) . Note that the stress tensor component σ_{xy} is not plotted on the X and Y axis because it is zero in those directions.

There is an overall good agreement between the analytical solution and the simulation results. Although it is likely that reducing the mesh size will further improve the agreement, the accuracy is deemed sufficient for the present analysis.

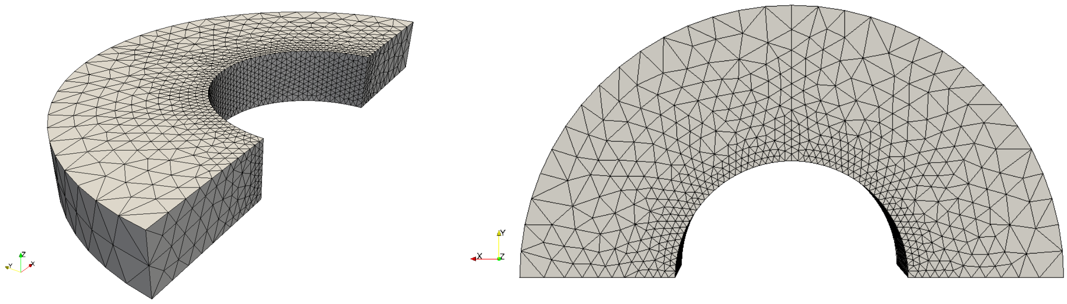

(A) Side view

(B) Top view

FIGURE 6.16: Geomechanical model for validation of the in-situ stress.

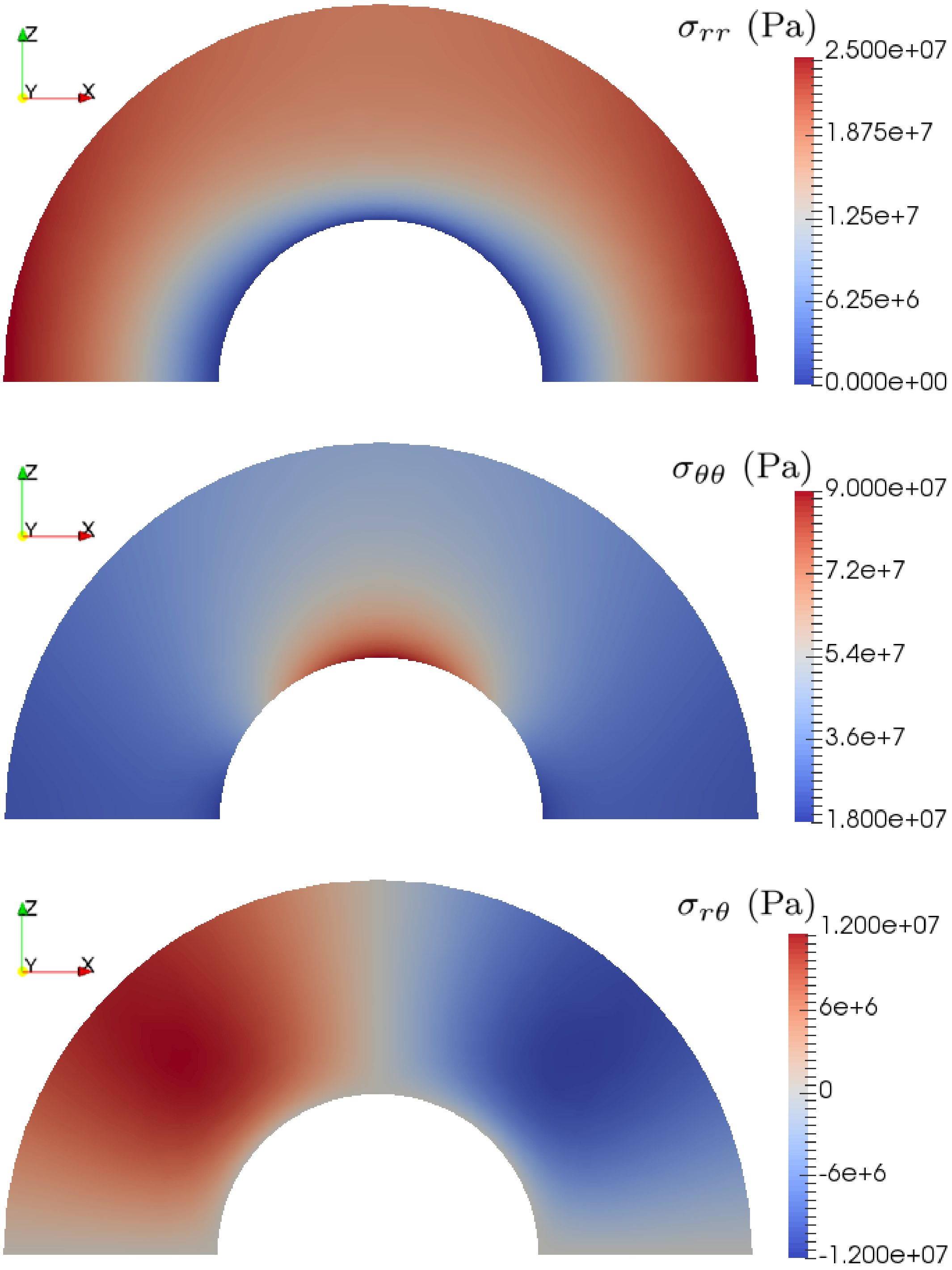

FIGURE 6.17: Analytical solution of the in-situ stress around a circular excavation in polar coordinates.

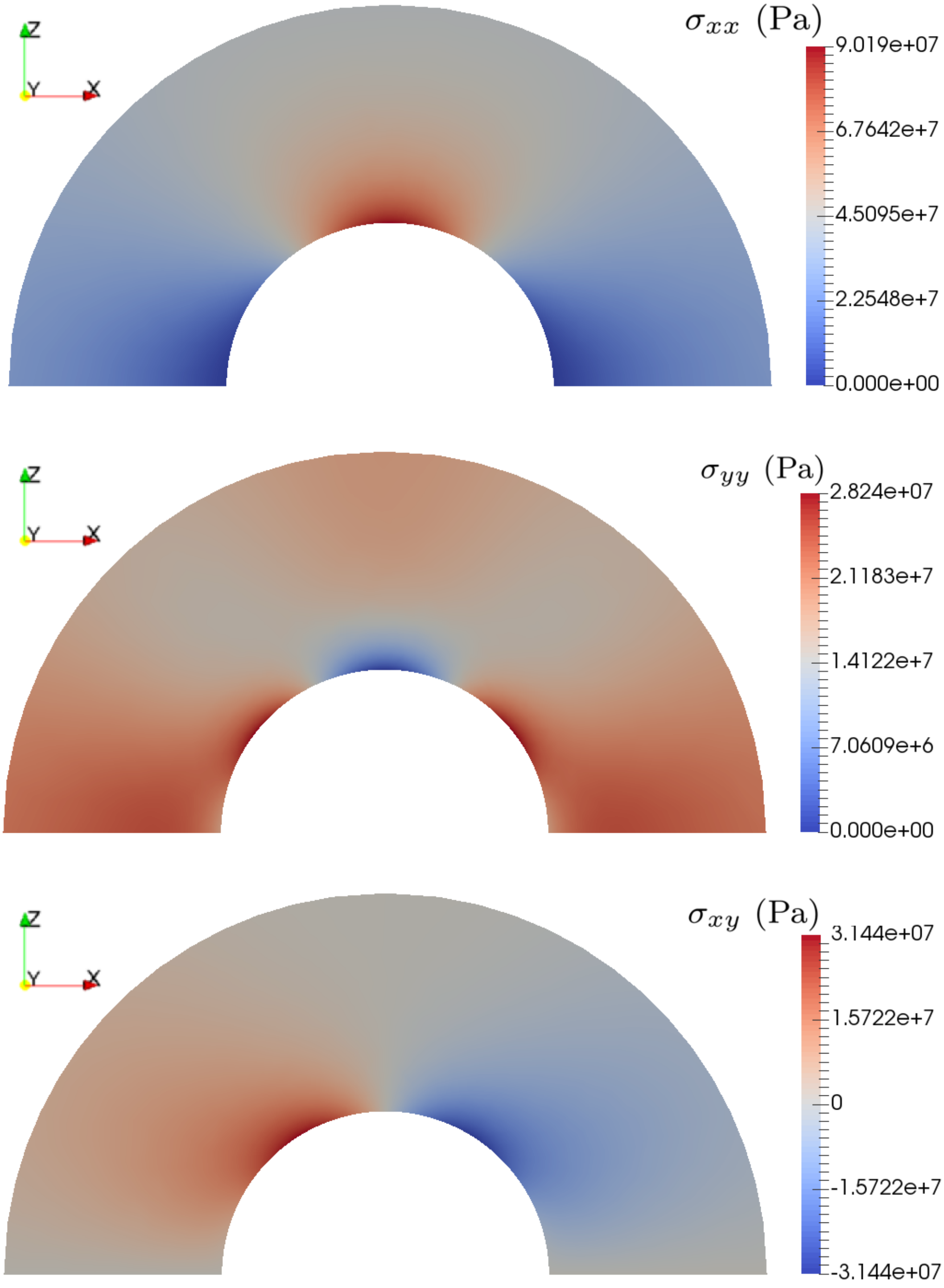

FIGURE 6.18: Analytical solution of the in-situ stress around a circular excavation in Cartesian coordinates.

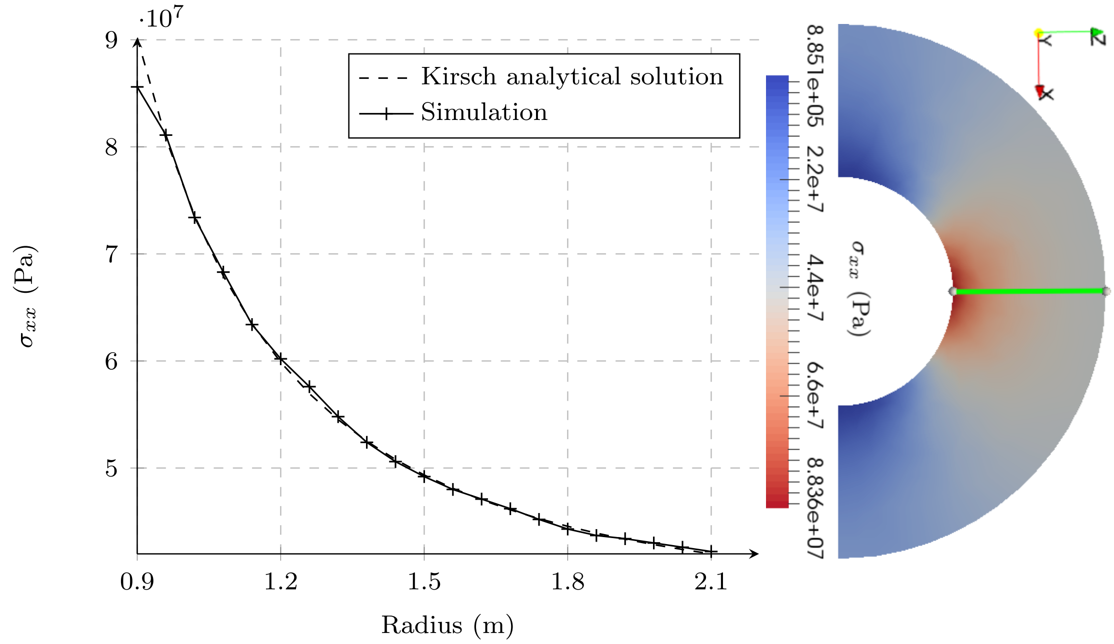

(A) Radius versus σ_{xx} along the plot line

(B) Spatial distribution results of σ_{xx} and plot line in the Y axis

Figure 6.19: Results for σ_{xx} and comparison with the analytical solution along the Y axis.

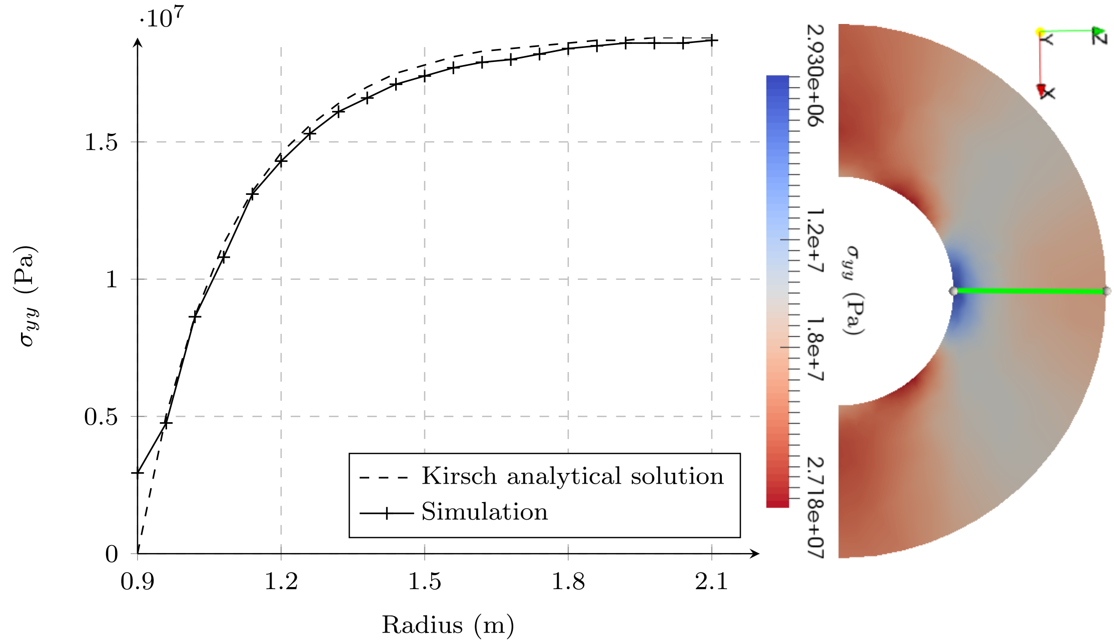

(A) Radius versus σ_{yy} along the plot line

(B) Spatial distribution results of σ_{yy} and plot line in the Y axis

Figure 6.20: Results for σ_{yy} and comparison with the analytical solution along the Y axis.

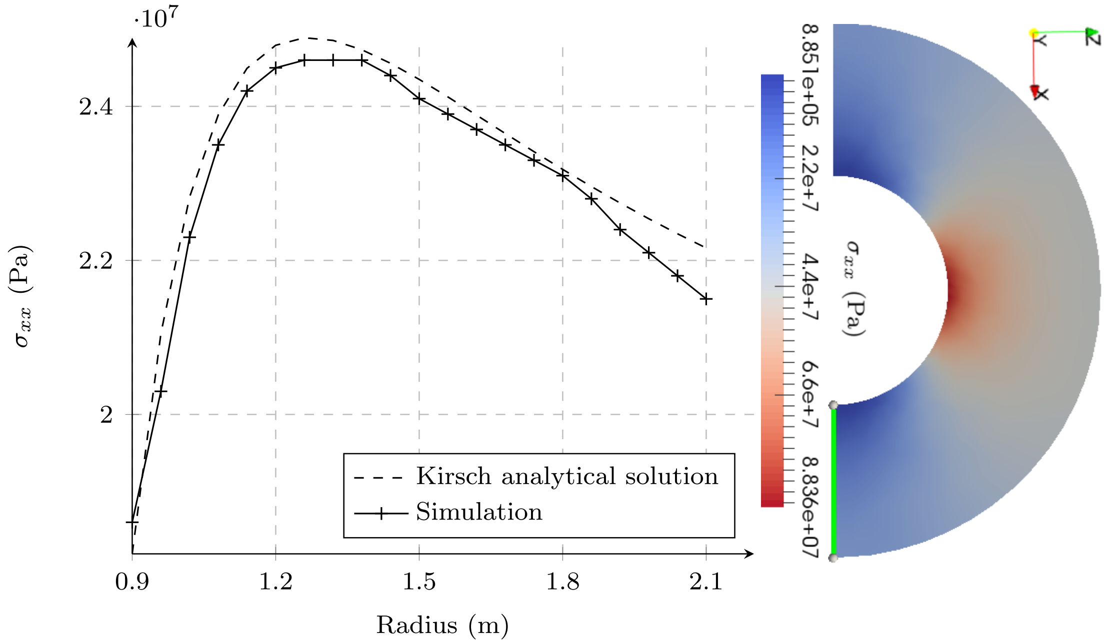

(A) Radius versus σ_{xx} along the plot line

(B) Spatial distribution results of σ_{xx} and plot line in the X axis

FIGURE 6.21: Results for σ_{xx} and comparison with the analytical solution along the X axis.

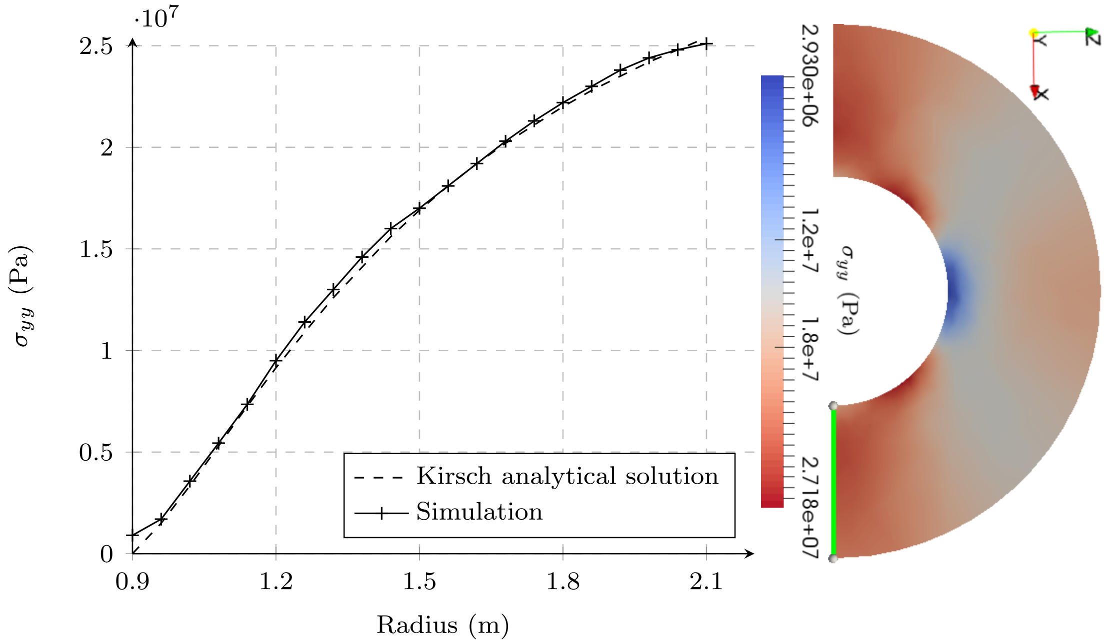

(A) Radius versus σ_{yy} along the plot line

(B) Spatial distribution results of σ_{yy} and plot line in the X axis

FIGURE 6.22: Results for σ_{yy} and comparison with the analytical solution along the X axis.

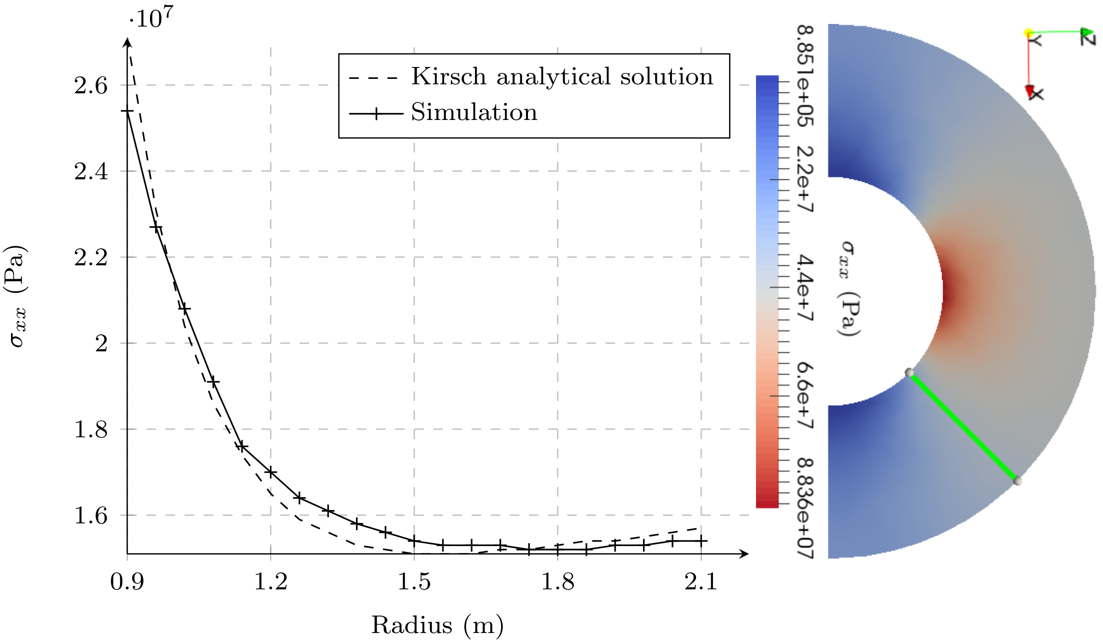

(A) Radius versus σ_{xx} along the plot line

(B) Spatial distribution results of σ_{xx} and plot line in the XY direction

FIGURE 6.23: Results for σ_{xx} and comparison with the analytical solution along the XY direction.

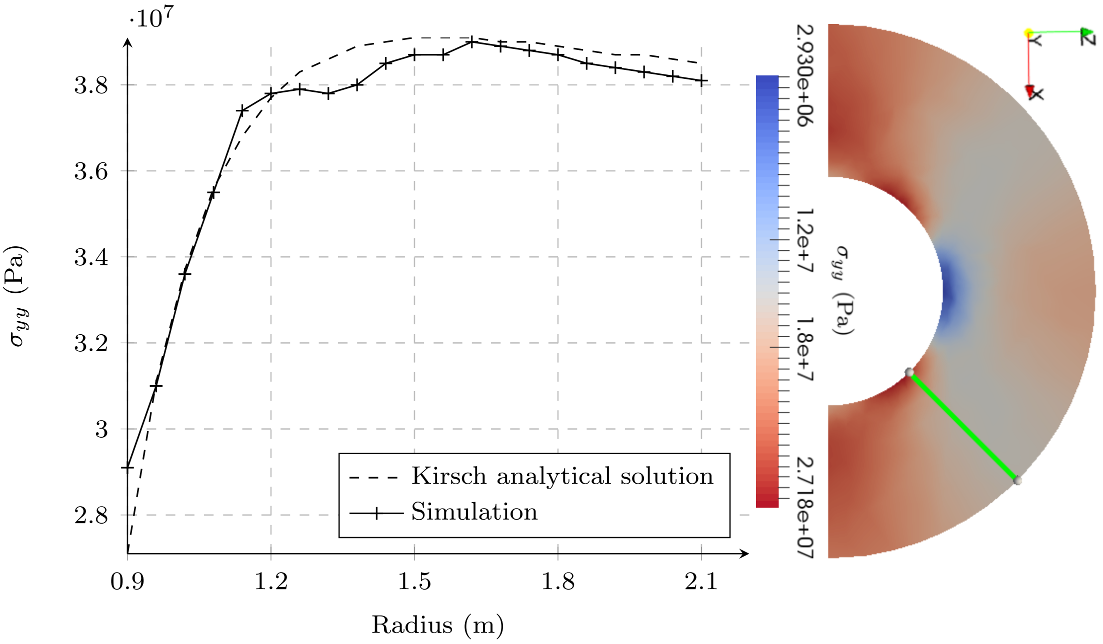

(A) Radius versus σ_{yy} along the plot line

(B) Spatial distribution results of σ_{yy} and plot line in the XY direction

FIGURE 6.24: Results for σ_{yy} and comparison with the analytical solution along the XY direction.

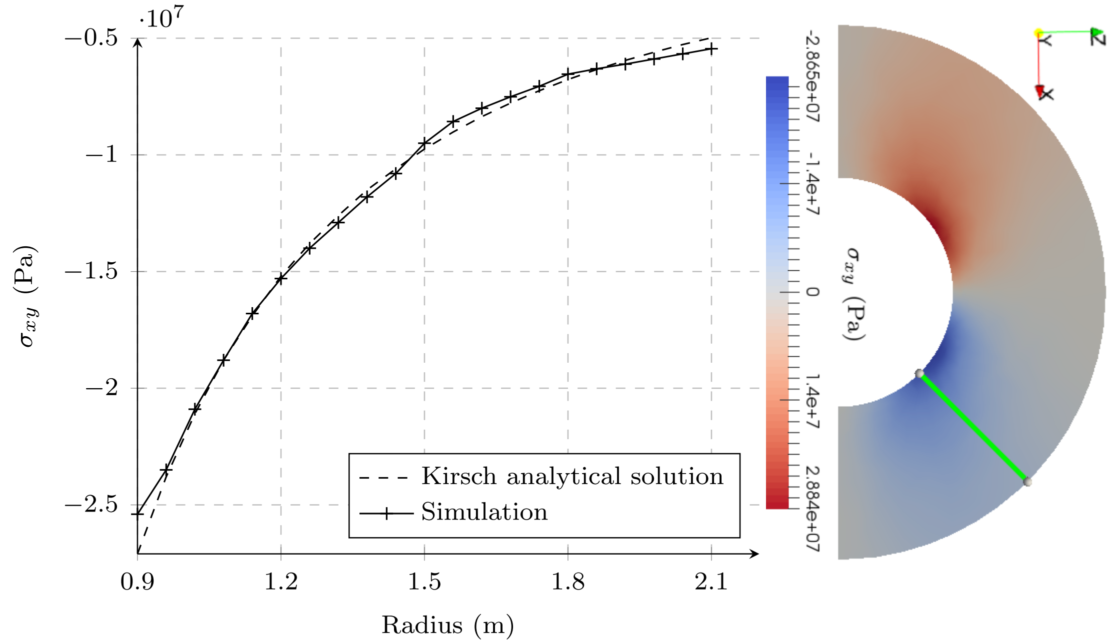

(A) Radius versus σ_{xy} along the plot line

(B) Spatial distribution of σ_{xy} and plot line in the XY direction

FIGURE 6.25: Results for σ_{xy} and comparison with the analytical solution along the XY direction.

Mechanical model

The in-situ stress conditions in the geomechanical model are presented on Figure 6.26. At the excavation wall in the Y axis, the radial stress σ_{rr} is minimal and equal to σ_{yy} (Figure 6.26b) and the tangential stress $\sigma_{\theta\theta}$ is maximal and equal to σ_{xx} (Figure 6.26a). Therefore, the distribution of σ_{xx} determines the potential for spalling, cracks will appear for a stress superior to the crack initiation threshold (CI, 116 MPa) and failure is expected if the stress exceeds the uniaxial compressive strength (UCS, 227 MPa).

Figure 6.27, show the vertical distribution of σ_{xx} at the excavation wall in the Y axis. The stress is not evenly distributed, it is maximal with 88.4 MPa at canister mid-height (4 m from the top of the excavation), smaller at the top of the excavation with 79.2 MPa and minimal at the bottom of the excavation with 50 MPa. Thus neither cracks nor failure would occur in the in-situ conditions.

It must be pointed out that the Kirsch equations are valid for a infinite circular excavation in the vertical direction. Applying the Kirsch equations to a hollow cylinder has produced accurate results. However, this technique is not suited for the part of the cylinder that is not hollow (Figure 6.12) and inaccuracies can be expected in the lower region of the model.

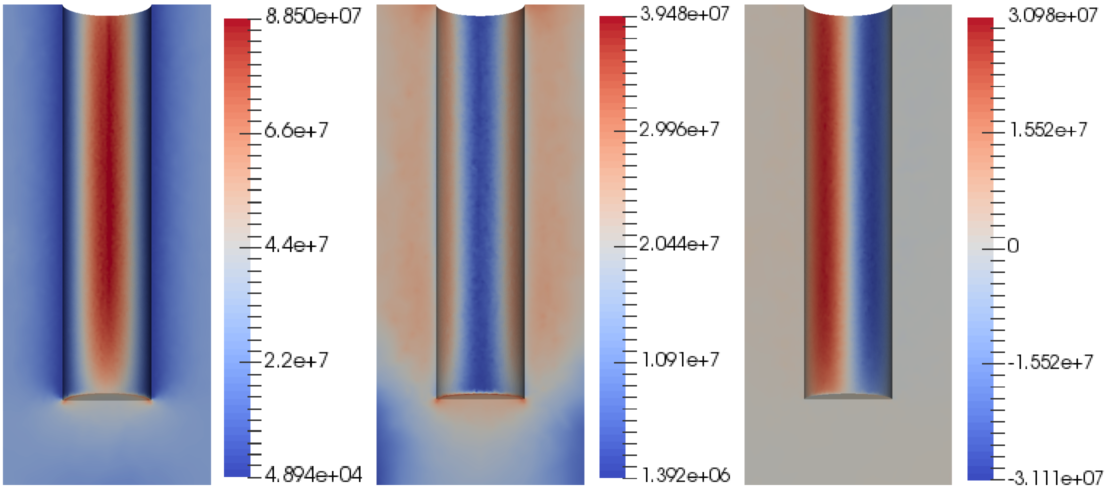

(A) σ_{xx} (Pa) (B) σ_{yy} (Pa) (C) σ_{xy} (Pa)

FIGURE 6.26: In situ-stress state in the rock as calculated with the geomechanical model.

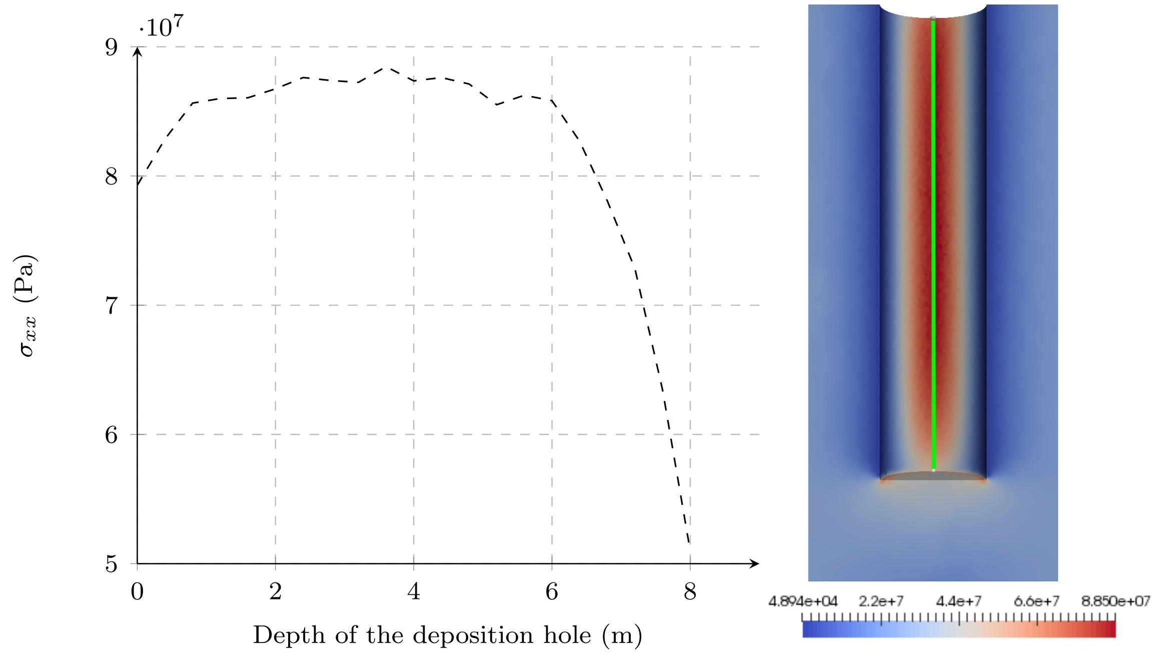

(A) Vertical distribution of σ_{xx}, with 0 depth at the top of the excavation

(B) Distribution of σ_{xx} on the excavation wall and vertical plot line

FIGURE 6.27: Vertical distribution of σ_{xx}.

6.3.2 Thermal evolution

The temperature distribution at different times is presented on Figure 6.28 for the thermo-hydraulic model (Fluidity) and on Figure 6.29 for the projected temperature on the geomechanical model (Solidity). The hottest temperature on the excavation wall is found at canister mid-height, which confirms results by Hökmark et al. (2009).

Therefore, the evolution of temperature is analysed in the horizontal plane of canister mid-height and along the Y axis for three different locations: at the bentonite-canister interface ($T_{ben-can}$), at the bentonite-rock interface and in the rock ($T_{ben-rock}$), 2.1 m away from the excavation wall which corresponds to the outer radius of the geomechanical model. The three temperature locations are shown on Figure 6.30.

For the three locations, Figure 6.31 presents the temperature evolution as a function of time and Figure 6.32 the temperature evolution in function of the number of time steps. Results indicate that the maximal temperature at the bentonite-rock interface $T_{ben-can}$ is attained after 60 days (88 time steps) whereas for $T_{ben-rock}$ and T_{rock} the maximum is reached at 1.8 years (107 time steps).

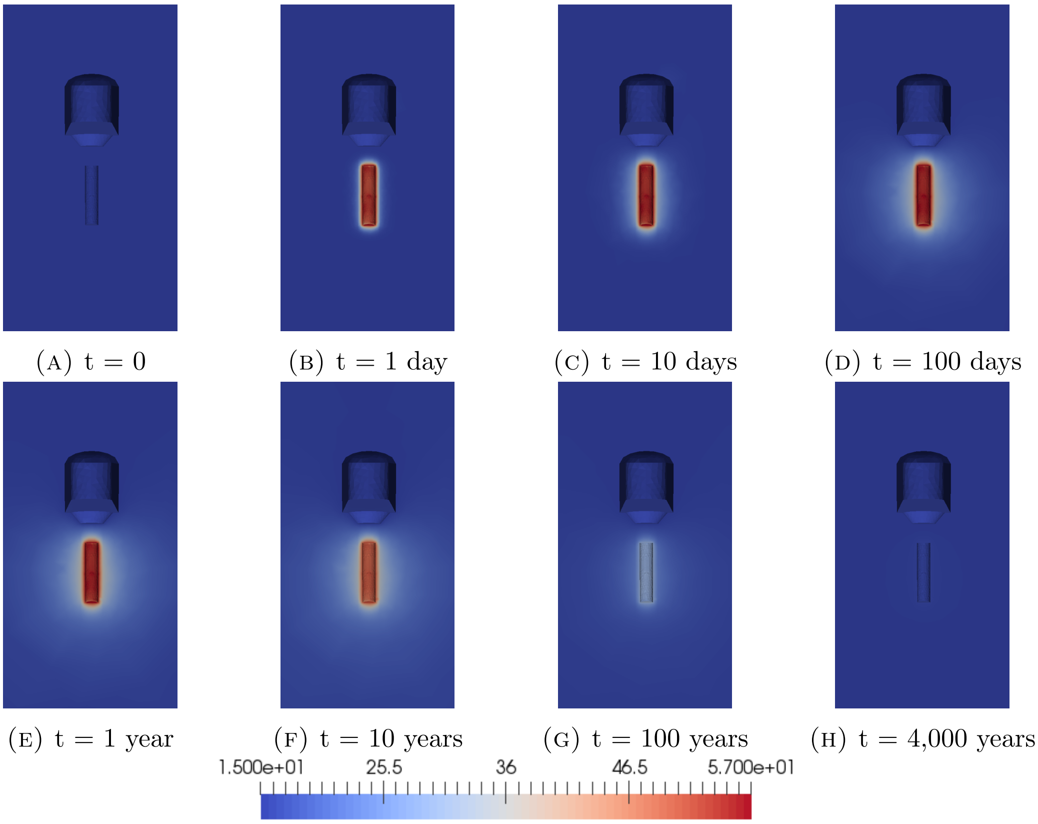
(A) t = 0 (B) t = 1 day (C) t = 10 days (D) t = 100 days

(E) t = 1 year (F) t = 10 years (G) t = 100 years (H) t = 4,000 years

FIGURE 6.28: Evolution of the temperature distribution in the thermo-hydraulic model (Fluidity).

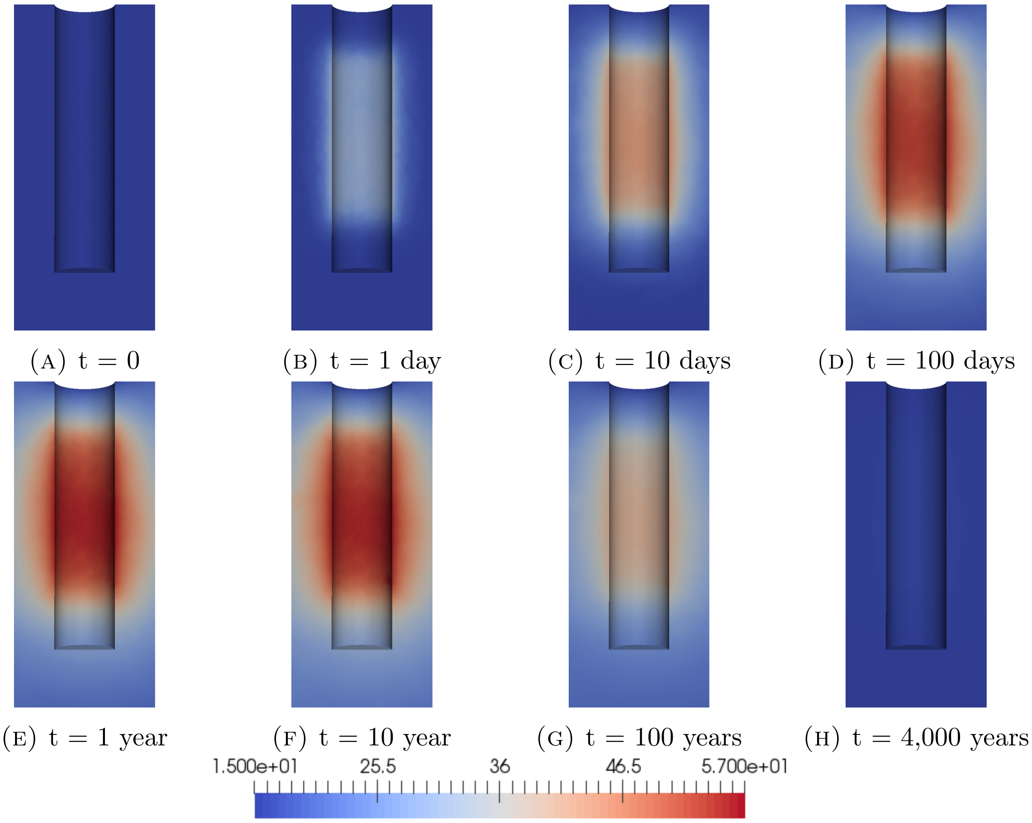
(A) t = 0 (B) t = 1 day (C) t = 10 days (D) t = 100 days

(E) t = 1 year (F) t = 10 year (G) t = 100 years (H) t = 4,000 years

FIGURE 6.29: Evolution of the temperature distribution projected on the geomechanical model (Solidity).

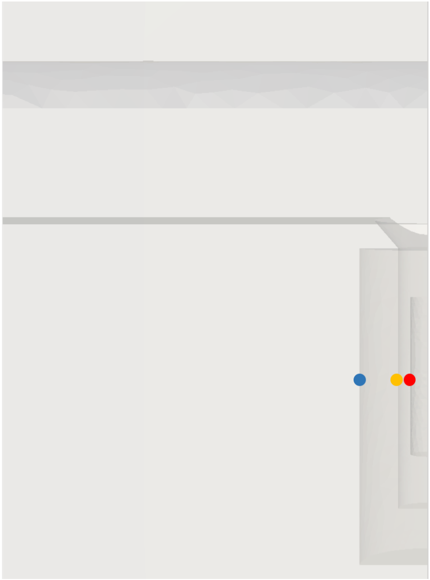

FIGURE 6.30: Positions of $T_{can-ben}$ (red), $T_{ben-rock}$ (orange) and T_{rock} (blue).

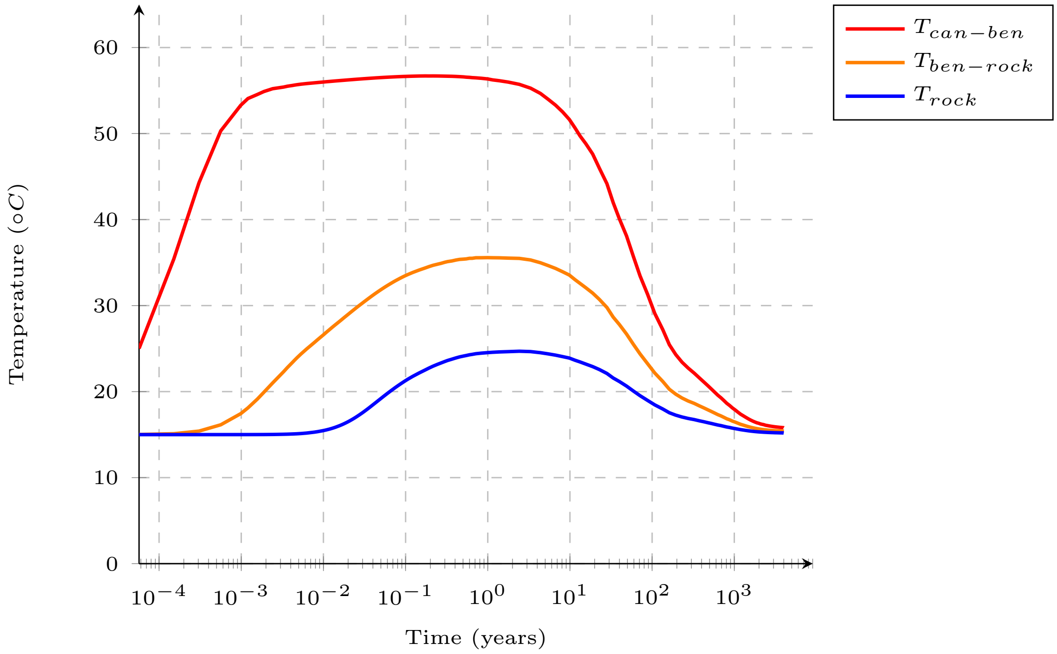

Figure 6.31: Temperature versus time at three different locations.

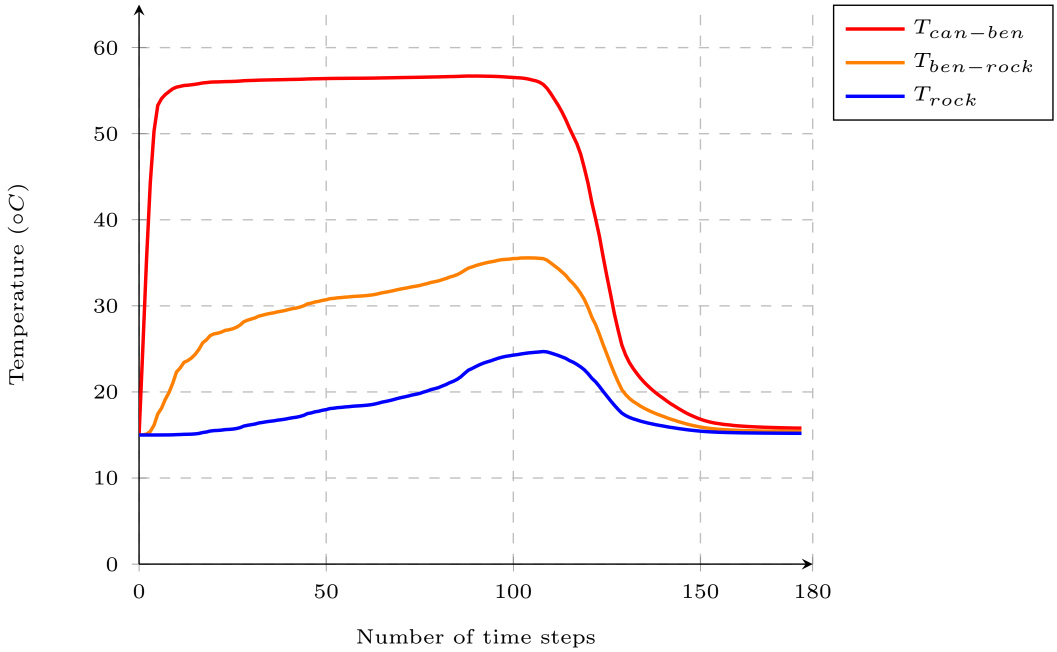

Figure 6.32: Temperature versus number of time steps at three different locations.

6.3.3 Mechanical processes

With rising and falling temperatures modelled with the thermo-hydraulic model, the corresponding thermal stress is calculated with the geomechanical model at each time step. Figure 6.33 shows $\Delta\sigma_{xx}$, the stress variation of σ_{xx} over time with for reference the in-situ stress state. Results indicate that the stress variation caused by heating corresponds to the zone of highest temperatures which is centred at canister mid-height (Figure 6.29).

The maximal value of $\Delta\sigma_{xx}$ on the excavation wall is of about 6.4 MPa and is attained at t=10 days (44 time steps), see Figure 6.33c. The maximal $\Delta\sigma_{xx}$ is obtained much earlier than the highest temperatures in the rock (1.8 years, 107 time steps), this is probably the result of the stress contribution from thermal gradients. According to equation 4.39 (Chapter 4), the radial stress at the excavation wall increases with ΔT, the temperature difference between T_{rock} and $T_{ben-rock}$. Figure 6.34, shows the evolution of ΔT over time, it is maximal at t=10 days and decreases slightly until the peak temperature at t=1.8 years before returning to almost zero during the following 4,000 years.

Figures 6.35 and 6.36 show the stress profiles of σ_{xx} along the Y axis at canister mid-height for different times. Figure 6.35 shows stress at times between t=0 and t=10 days (i.e. during thermal stress loading) whilst Figure 6.36 shows stress between t=10 days and t=4,000 years (i.e. during thermal stress un-loading).

The maximal compressive stress, on the excavation wall at canister mid-height, obtained as a result of heating is of 93.2 MPa (at t = 10 days) which is an increase of about 4% compared to the in-situ stress state. The maximal stress is still significantly below the crack and failure thresholds thus no thermal spalling would occur in the present configuration.

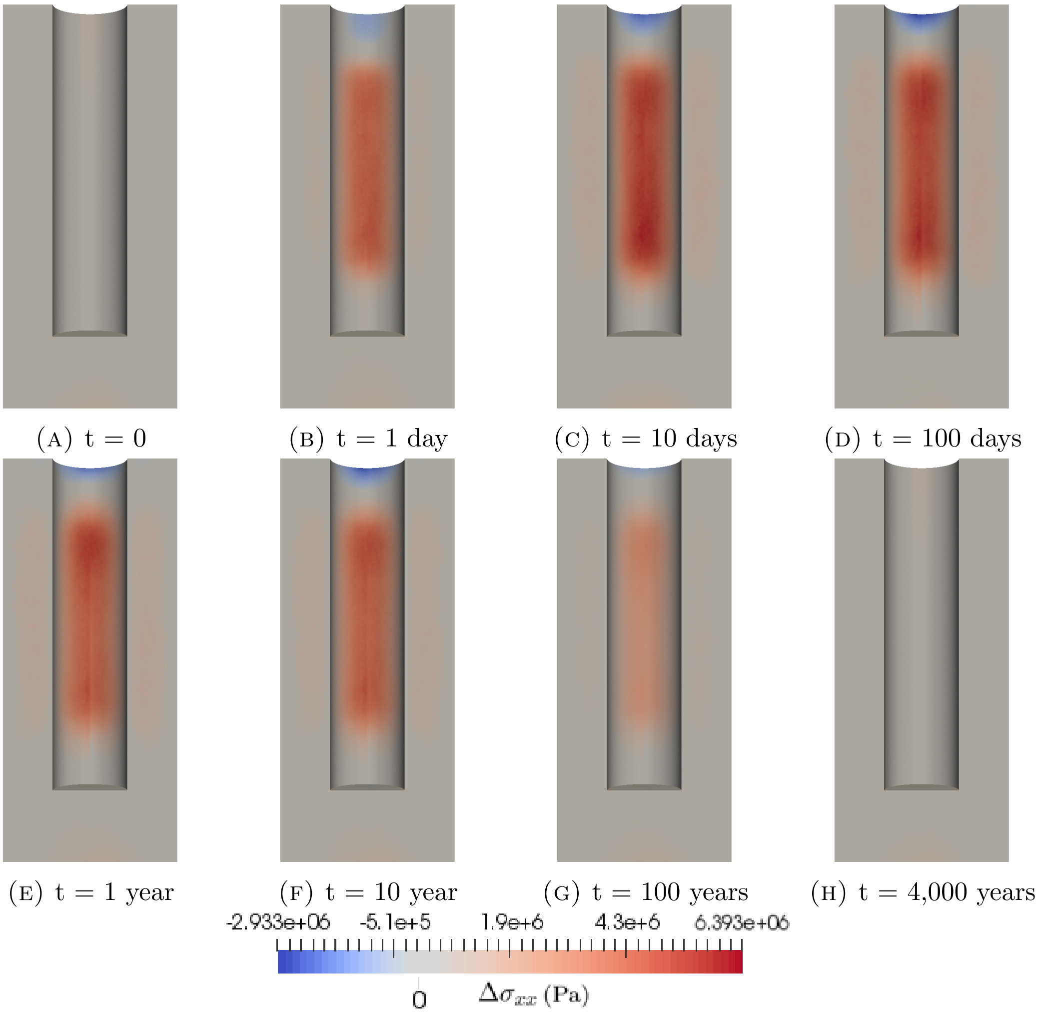
(A) t = 0 (B) t = 1 day (C) t = 10 days (D) t = 100 days

(E) t = 1 year (F) t = 10 year (G) t = 100 years (H) t = 4,000 years

FIGURE 6.33: Variation of σ_{xx} from the initial in-situ conditions (Figure 6.26a) during heating and cooling.

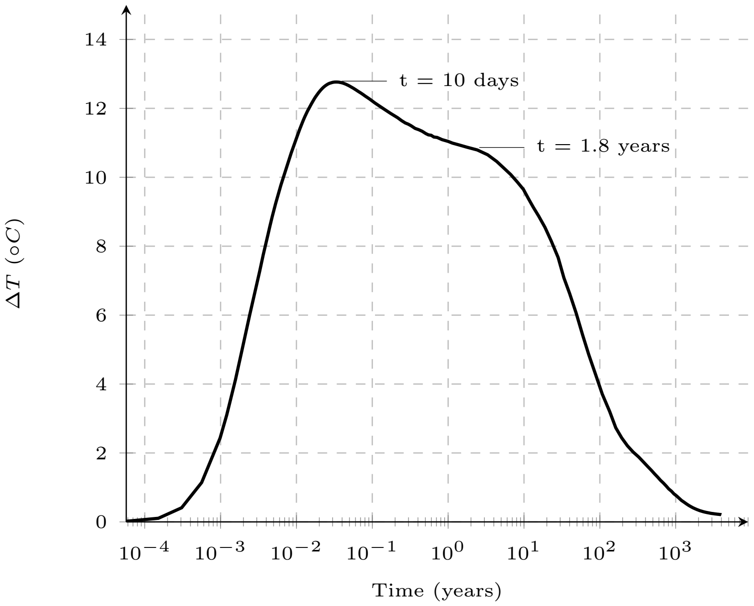

FIGURE 6.34: Temperature difference $\Delta T = T_{ben-rock} - T_{rock}$ versus time.

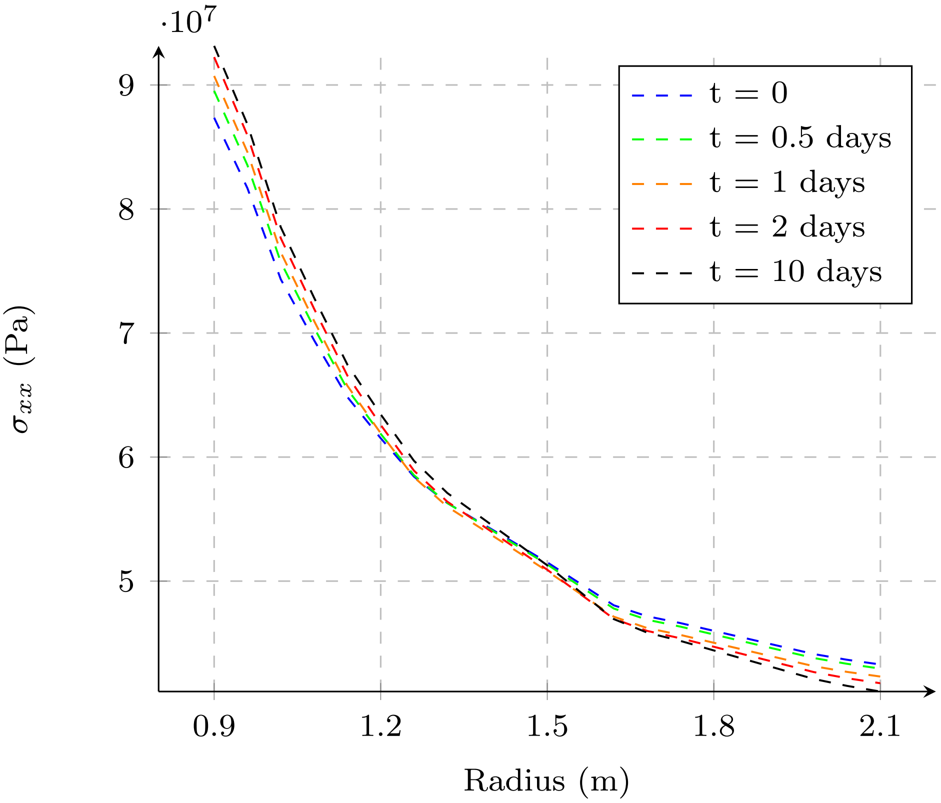

FIGURE 6.35: σ_{xx} along the Y axis at canister mid-height: thermal stress loading.

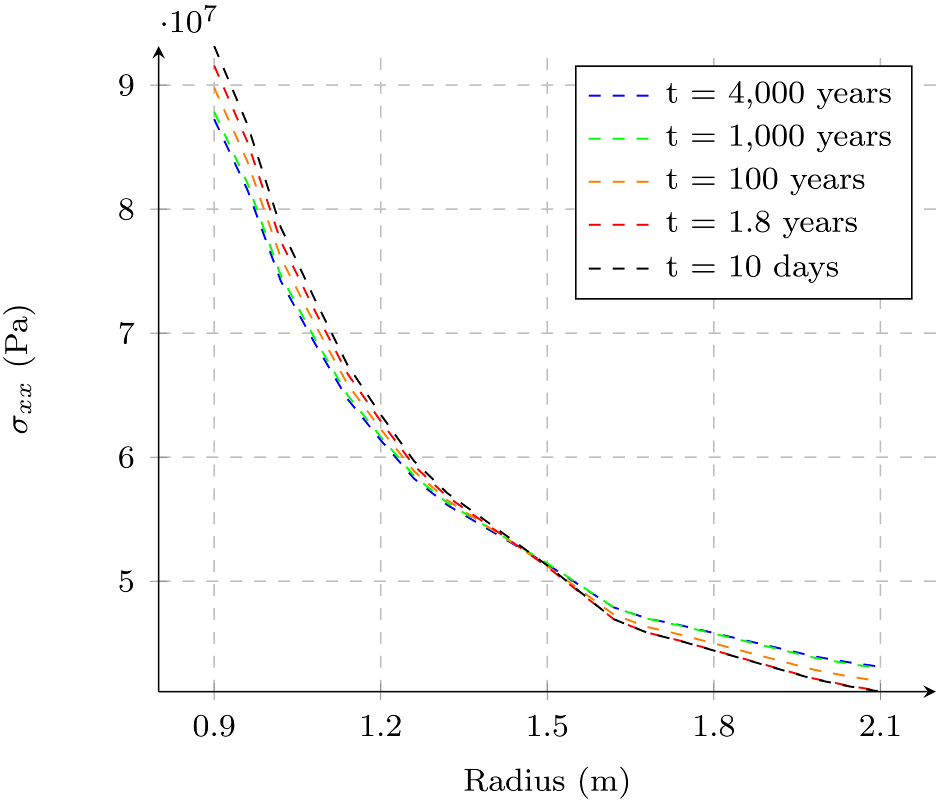

FIGURE 6.36: σ_{xx} along the Y axis at canister mid-height: thermal stress unloading.

6.3.4 Evolution of Saturation

Because no fractures are considered in the modelling, the saturation of the bentonite only occurs via porous media flow. Additionally, because the capillary pressure is not taken into account, the only driving force for saturation is the weight of the column of water. Due to the very low permeability of the rock and the bentonite, the saturation process is occurring very slowly.

Figure 6.37, shows the saturation levels at different times in the deposition hole. Significant changes in saturation for the bentonite regions in contact with the rock can be observed after 100 days whereas the volume directly below the canister will stay unsaturated even after 4,000 years (Figure 6.37h). Results also show partial saturation over the canister surface with relatively minor evolution between 100 and 4,000 years (Figures 6.37f-6.37h). This is observed because the air trapped below is escaping upward along the bentonite-canister boundary.

Figure 6.38 shows the saturation evolution over time for two points at canister mid-height in the YZ plane, $S_{can-ben}$ at the bentonite-canister interface, S_{ben} in the bentonite at equal distance from the excavation wall and the canister, and $S_{ben-rock}$ at the bentonite-rock interface. Results indicate very different evolution of saturation over time for the three locations considered, this suggests a sustained heterogeneous distribution of wetting in the horizontal plane that will certainly influence the swelling pressure of the bentonite.

The evolution of saturation at the bentonite-rock interface $S_{ben-rock}$ and the evolution of ΔT are plotted together on Figure 6.39. According to Figure 6.38, the bentonite-rock interface has the shortest saturation time, thus the bentonite will at best swell according to $S_{ben-rock}$. Additionally, ΔT has shown to be correlated with the maximal compressive strength at the excavation wall. Figure 6.39 clearly shows that no bentonite support pressure can possibly be expected when the thermal stress is maximal. When $S_{ben-rock}$ reaches 90% saturation i.e. at t = 1,000 years, the temperature gradient is close to null (Figure 6.39) and the stress at the canister mid-height has almost returned to the initial in-situ conditions (Figure 6.36).

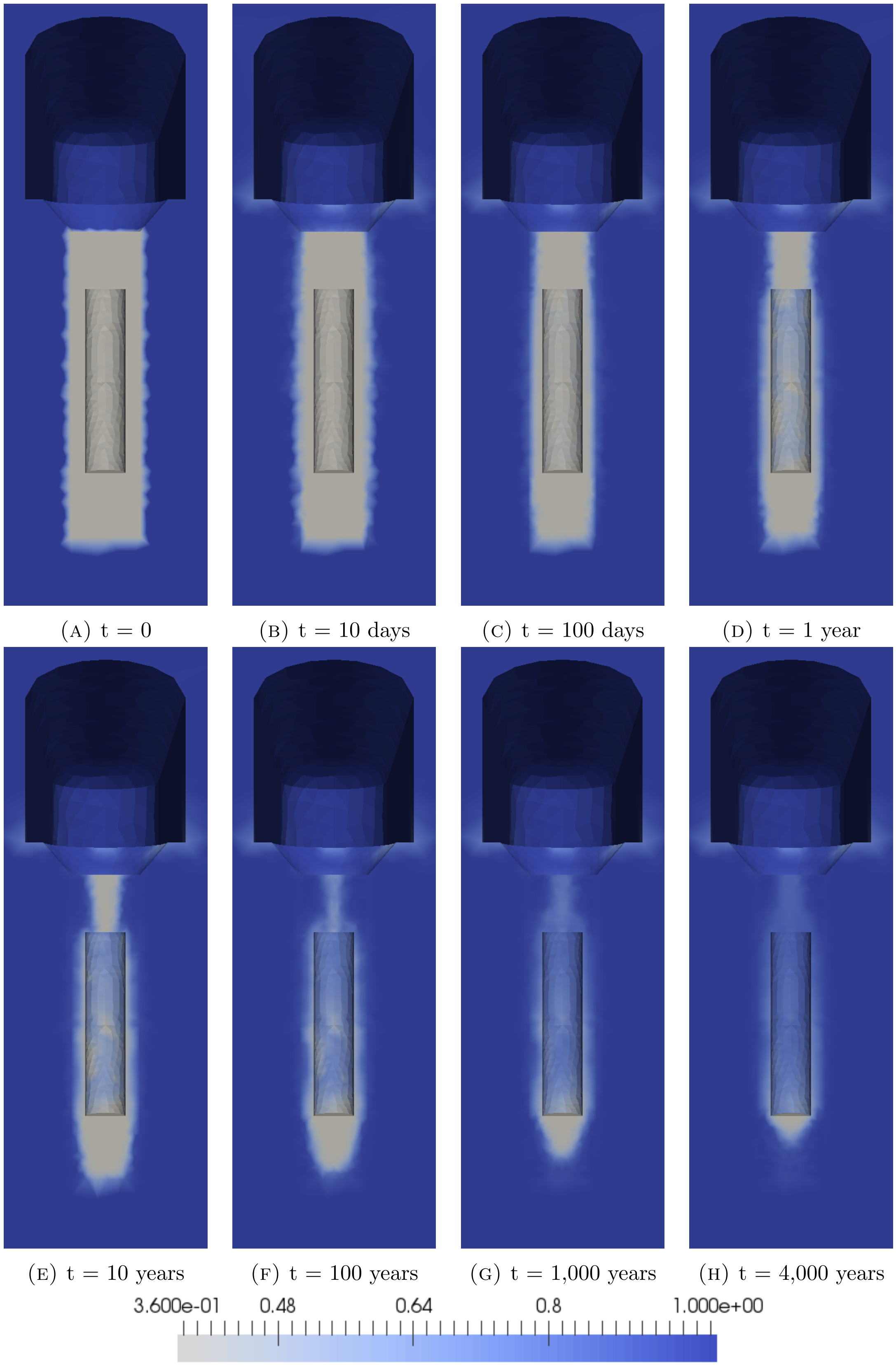

(A) t = 0

(B) t = 10 days

(C) t = 100 days

(D) t = 1 year

(E) t = 10 years

(F) t = 100 years

(G) t = 1,000 years

(H) t = 4,000 years

FIGURE 6.37: Simulation results of the evolution of saturation over time in the deposition hole and tunnel.

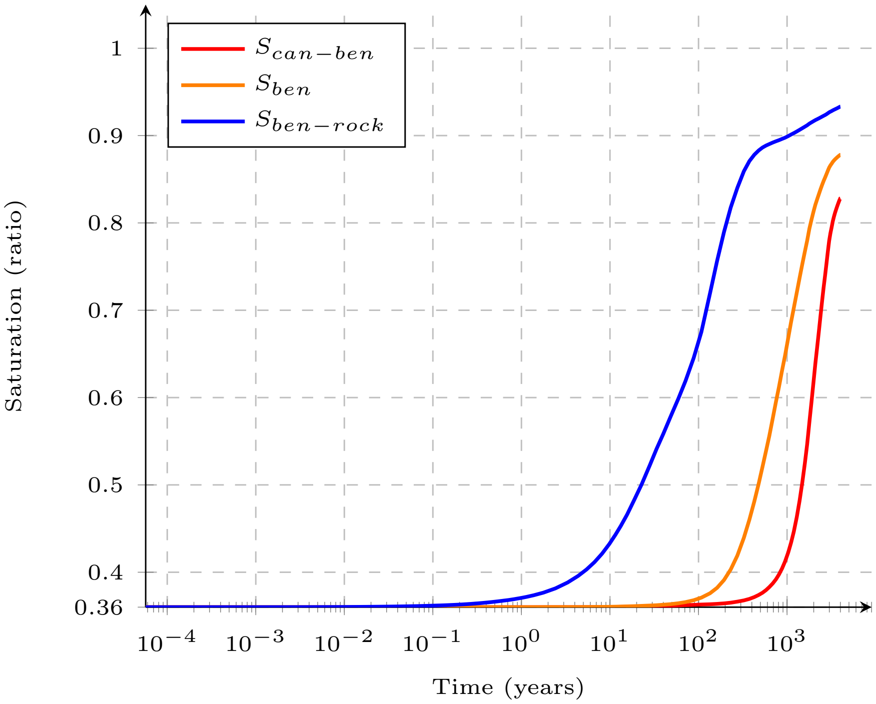

FIGURE 6.38: Temperature versus time at three different locations.

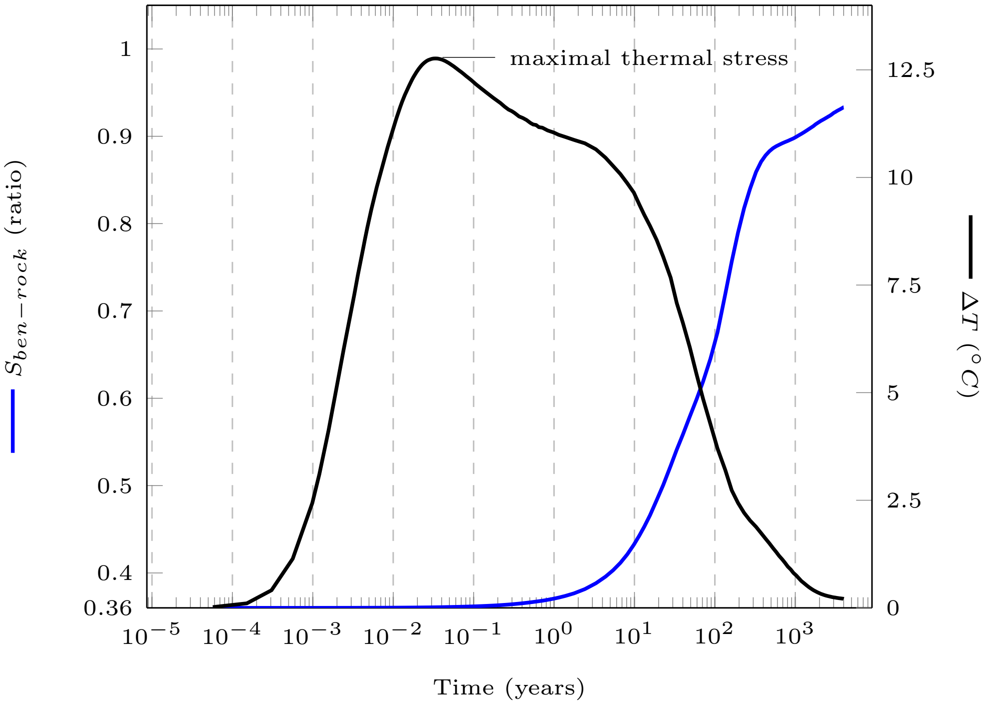

FIGURE 6.39: Saturation $S_{ben-rock}$ and temperature difference $\Delta T = T_{ben-rock} - T_{rock}$ versus time.

6.4 Concluding Remarks

In this chapter, a numerical framework for the simultaneous analysis of saturation and thermal spalling was presented. The results from the simulations showed that heating caused up to a 4% increase in compressive stress, with no spalling or thermal spalling occurring in the considered configuration. Furthermore, the findings show that changes in saturation that are driven solely by hydrostatic pressure, leads to a scenario whereby the bentonite is unable to swell in time to provide full support pressure, when maximal thermal stress occurs.

In addition, it should be noted that the initial and boundary conditions were simplified, and this may have impacted the results. In particular, the results show that the temperature is not negligible at the outer boundaries of the geomechanical model (see T_{rock} on Figure 6.31). As the stress boundary condition does not include thermal effects (Equation 6.4), it fails to represent accurately the in-situ conditions. To solve this issue, two solutions can be implemented i) introduce a temperature dependent term in the Kirsch equation (Zoback, 2007) or ii) increase the size of the model up to a few tens of meters, as the temperature variations then become negligible. Note that when considering the fracture model, only i) can be envisaged because of the element size restriction and the associated computational cost. On the contrary, when using the continuum model both solutions can be implemented.

A preliminary insight into the importance of saturation on the thermal spalling phenomena has been provided. Due to time constraints, this work has stopped short of integrating the following:

- Thermally induced fracturing (as performed in Sections 4.2.4 and 4.2.5). Modelling the initiation of cracks and their propagation due to stress changes driven by thermal effects in the deposition hole will enable to quantify the extent of failure over time. Additionally, scenarios where spalling has occurred prior to heating, as a result of the in-situ stress could be investigated.
- Multi-material configurations in Solidity (as performed in Section 4.2.5). Defining an extra material in the geomechanical model to represent the bentonite buffer will enable to emulate different support pressure conditions on the excavation walls. However, for the bentonite swelling behaviour to be represented in full, the

introduction of a constitutive model is necessary e.g. the Cam-Clay model or the Barcelona Basic Model as implemented by Rutqvist et al. (2011) in TOUGH2. It should also be noted that this implementation also implies that the saturation must be projected from Fluidity to Solidity.

- Saturation dependent rock strength. This feature can be tackled with a weak coupling of the rock mechanical properties together with the water content and therefore requires the saturation to be projected from Fluidity to Solidity.
- Hydro-mechanical coupling based on the work of Obeysekara (2018) on hydraulic fracturing within the Fluidity-Solidity framework which enables:
  - the H→M coupling with the impact of fluid pressure changes (Fluidity) on the effective stress of the rock matrix and the fracture walls (Solidity)
  - the M→H coupling with changes in fracture aperture (Solidity) influencing the hydraulic conductivity (Fluidity)

  The above technology will allow models to include the pre-existing fractures of the of the excavation damage zone. This will have a significant impact on the saturation time (Dessirier et al., 2017) and the distribution of in-situ and thermal stress (Lei et al., 2017b). Moreover, the evolution of the thermal stress over time will affect the hydraulic conductivity of fractures (Lei et al., 2017c, 2017a). In addition, it is important to highlight that when considering pre-existing fractures it is not necessary to use the fracture model. Thus, the associated mesh requirements do not apply and as a result, more effective simulations can be performed on larger domains.
- Thermal expansion of the fluids. This feature is widely tested in Fluidity and its incorporation to the thermal spalling model is trivial.
- Bentonite suction strength. In Fluidity, capillary pressure models such as the power law or the Brooks-Corey model are available. However, the most suitable option would be to implement the Van Genuchten model which has been calibrated with field data (Vidstrand et al., 2017).

It must be emphasised that all of the THM coupled features mentioned above are either already available in the dual framework or can be integrated with relatively small implementation efforts. Nevertheless, appropriate validation work will need to be conducted on the new coupling features. The development of the Fluidity-Solidity framework will be the objective of further post-doctoral research on thermal spalling in collaboration with SKB. The objective coupling scheme for this research is presented on Figure 6.40.

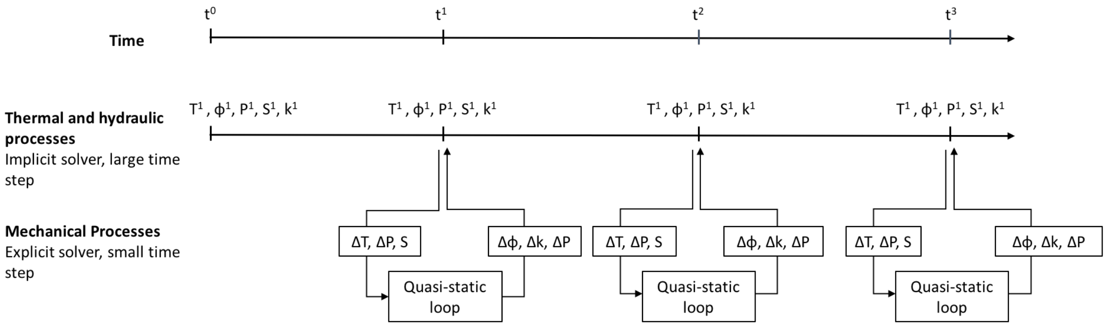

FIGURE 6.40: Illustration of the objective sequential scheme of Fluidity-Solidity. With T the temperature, ϕ the porosity, k the hydraulic conductivity, P the fluid pressure and S the saturation of the porous media.

Chapter 7

Discussion

7.1 Overall Conclusions and Limitations

This thesis successfully presented the formulation, validation and application of key numerical features incorporated into a dual code framework and resulting in a robust numerical method for the modelling of THM coupled processes. In comparison to previous methods employed for the modelling of THM coupled processes in the context of geological disposal of radioactive waste, there were a number of novel aspects that were used in the present approach. This includes the use of i) a porous media multiphase flow solver (Fluidity) with a continuum formulation and ii) a geomechanical solver (Solidity) with a discontinuum formulation capable of explicitly representing fractures and fracturing. The present configuration allows for each of the THM processes to be represented with the most appropriate formulation. As a result, the method has the potential to tackle complex THM coupled configurations involving un-saturated flow in fractured porous media. However, it should be noted that enhanced accuracy is achieved at the expense of higher computational costs compared to other continuum or discontinuum only numerical methods.

7.2 Discussion on Key Developments

The key features that contributed to the THM coupled framework are 1) the explicit and implicit solvers for heat conduction and contact heat transfer in Solidity (Chapter 3), 2) the thermo-mechanical coupling formulation for thermal stress and thermal fracturing in Solidity (Chapter 4) and 3) the novel immersed shell-body method allowing for heat transfer in the dual Fluidity-Solidity framework (Chapter 5).

It is important to note that despite having contributed to the dual framework, some of the features summarised above were found to have limited interest in the context of the thesis. As a result, the research in those areas was not carried on further than their validation. More specifically, the explicit thermal solver of Solidity is not practical when modelling GDF performance as a result of the large time scales that have to be considered for the thermal processes. Moreover, it was discussed in Section 3.7 that the contact heat transfer model is most appropriate to represent highly fractured dry rocks where closed fractures conduct heat whilst open, air-filled fractures are heat resisting. However, as thermal processes in GDF performance scenarios involve saturated and unsaturated conditions, they are best represented with a continuum which can account for heat transfer in the rock matrix and the interstitial fluid as discussed in Section 5.4. Furthermore, the immersed shell-body method applies to FSI problems with the Navier-Stokes equations and thus is not applicable in porous media.

Nonetheless, it was discussed in Section 5.4 that an immersed body type of method can be employed to capture the heat transfer between the rock matrix and the pore fluid. It can be highlighted that, once combined with the contact heat transfer, this could create a framework of interest to model the THM processes taking place at the fracture scale. In such a framework, the thermal interactions between the fracture walls, the rock matrix and the interstitial fluids would be fully resolved.

In all of the numerical studies cited in this thesis, the thermal equilibrium between the pore fluid and the rock matrix is assumed in the models (Table 2.4). It is worth highlighting that the framework used in this work has the potential to verify if this assumption is valid at all times in the vicinity of heat-generating waste canister; using thermal coupling between the thermo-hydraulic and the thermo-mechanical models. However, as discussed in Section 2.4.4, modelling thermal imbalances in the porous media is not part of the key features necessary to investigate GDF performance, and specifically thermal spalling.

As a result, there was no requirement of keeping both the thermal solver in Solidity and Fluidity. It being understood that hydrological processes are solved implicitly in

Fluidity, that mechanical process are solved explicitly in Solidity and that hydraulic and thermal processes have similar time step requirements; it is more advantageous to solve thermal processes implicitly in Fluidity rather than in Solidity. Note that this partition between thermo-hydraulic and mechanical solvers is the most popular route among other THM coupled numerical tools, as highlighted in Section 2.4.4. In this sequential configuration, the temperature only needs to be projected from the Fluidity mesh to the Solidity mesh, with the temperature variation used as an input to the thermo-mechanical model (Section 6.2.4). Further, in this approach the implicit thermal solver of Solidity (Chapter 3) is not necessary either. Nevertheless, as demonstrated in Chapter 4 this solver can be used to perform thermo-mechanical coupled analysis within Solidity alone.

7.3 Further Work Towards Fully THM Coupled Investigation of Thermal Spalling

In Chapter 6, the investigation of thermal spalling with the Fluidity-Solidity framework has made possible to render in time the evolution of concurrent factors influencing spalling. The maximal thermal stress on the excavation hole walls was found to occur several tens of years before any significant level of saturation could be observed in the bentonite buffer. Consequently, it was concluded that the bentonite swelling would have occurred too late to provide a support pressure to the excavation walls and thus would be unable to prevent eventual thermal spalling. Due to time constraints, this work has stopped short of integrating some of the features that were available in the framework, they are:

- Thermally induced fracturing
- Multi-material configurations in Solidity
- Saturation dependent rock strength
- Hydro-mechanical coupling in pre-existing fractures
- Thermal expansion of the fluids
- Capillary pressure

As discussed in Section 6.4, integrating all of the above-mentioned THM coupled features can be achieved with reasonable research efforts. These additions will be the objective of further post-doctoral research on thermal spalling in collaboration with SKB. In further work on thermal spalling, benchmarking will be conducted on fundamental THM coupled problems (Kolditz et al., 2012b, Walther et al., 2016) in order to build confidence in the models. In addition, thermo-mechanical analysis of brittle failure will be conducted. Note that in the present work, only thermally induced tensile failure has been presented. Thus the ability of Solidity's fracture model to represent spalling must be demonstrated.

With increased confidence in the thermo-hydro-mechanical results together with appropriate sensitivity analysis, the research expects to give definitive answers to the interrogations raised when reviewing previous numerical and experimental studies:

- At what points in time and under which conditions can thermal spalling initiate before the bentonite buffer provides a sufficient support pressure?
- Can the saturation levels have a significant negative impact on the spalling phenomena at a certain point in time?
- In which proportions can the changes in pore space and fracture aperture influence the saturation time?
- What is the influence of pre-existing and propagating fractures on the distribution of thermal stress and thermal spalling?

References

Abdalla, H. (2006). Concrete cover requirements for FRP reinforced members in hot climates. *Composite Structures*, 73(1):61–69.

Abhyankar, S., Brown, J., Constantinescu, E. M., Ghosh, D., Smith, B. F., and Zhang, H. (2018). PETSc/TS: A Modern Scalable ODE/DAE Solver Library. *arXiv preprint arXiv:1806.01437*.

Åkesson, M., Kristensson, O., Börgesson, L., and Dueck, A. (2010). THM modelling of buffer , backfill Critical processes and scenarios. *Time*, (March).

Alonso, E. E., Gens, A., and Josa, A. (1990). A constitutive model for partially saturated soils. *Géotechnique*, 40(3):405–430.

Andersson, C. J. (2007). Äspö Hard Rock Laboratory. Äspö Pillar Stability Experiment, Final report. Rock mass response to coupled mechanical thermal loading. SKB TR-07-01, Svensk Kärnbränslehantering AB. Technical report, SKB.

André, D., Levraut, B., Tessier-Doyen, N., and Huger, M. (2017). A discrete element thermo-mechanical modelling of diffuse damage induced by thermal expansion mismatch of two-phase materials. *Computer Methods in Applied Mechanics and Engineering*, 318:898–916.

Angot, P., Bruneau, C. H., and Fabrie, P. (1999). A penalization method to take into account obstacles in incompressible viscous flows. *Numerische Mathematik*, 81(4):497–520.

Apte, S. V., Martin, M., and Patankar, N. A. (2009). A numerical method for fully resolved simulation (FRS) of rigid particle-flow interactions in complex flows. *Journal of Computational Physics*, 228(8):2712–2738.

Bäckström, A., Antikainen, J., Backers, T., Feng, X., Jing, L., Kobayashi, A., Koyama, T., Pan, P., Rinne, M., Shen, B., and Hudson, J. A. (2008). Numerical modelling of uniaxial compressive failure of granite with and without saline porewater. *International Journal of Rock Mechanics and Mining Sciences*, 45(7):1126–1142.

Bandis, S. C., Lumsden, A. C., and Barton, N. R. (1983). Fundamentals of rock joint deformation. *International Journal of Rock Mechanics and Mining Sciences and*, 20(6):249–268.

Barton, N. and Bakhtar, K. (1985). Description and Modeling of Rock Joints for the Thermo-hydro-mechanical design of Nuclear Waste Values. TR-418. Technical report.

BEIS (2017). The Clean Growth Strategy. Technical report.

BEIS (2018a). 2017 UK Greenhouse Gas Emissions, Provisional Figures: Statistical release. Technical Report March.

BEIS (2018b). Advanced Nuclear Technologies - GOV.UK.

Bénet, L.-V., Blaud, É., and Wendling, J. (2017). Modelling of water and gas flow through an excavation damaged zone in the Callovo-Oxfordian argillites in the framework of a single porosity model. *Geological Society, London, Special Publications*, 443(1):319–332.

Benoit, P. (2007). Modélisation avec la méthode XFEM de la propagation dynamique et l'arrêt de fissure. page 188.

Biot, M. A. (1941). General theory of three-dimensional consolidation. *Journal of Applied Physics*, 12(2):155–164.

Birkholzer, J., Rutqvist, J., and Sonnenthal, E. (2005a). Lawrence Berkeley National DECOVALEX-THMC Task D : Long-Term Permeability / Porosity Changes in the EDZ and Near Field due to THM and THC Processes in Volcanic and Crystaline-Bentonite Systems , Status Report October 2005 DECOVALEX-THMC Task D : Long-Term. Technical report, DECOVALEX.

Birkholzer, J., Rutqvist, J., Sonnenthal, E., and D, B. (2005b). Lawrence Berkeley National DECOVALEX-THMC Task D : Long-Term Permeability / Porosity Changes in the EDZ and Near Field due to THM and THC Processes in Volcanic and Crystaline-Bentonite Systems , Status Report October 2005 DECOVALEX-THMC Task D : Long-Term. Technical report, DECOVALEX.

Black, J. H. (2012). Selective review of the hydrogeological aspects of SR-Site. Technical report.

Bobet, A., Fakhimi, A., Johnson, S., Morris, J., Tonon, F., and Yeung, M. R. (2009). Numerical Models in Discontinuous Media: Review of Advances for Rock Mechanics Applications. *Journal of Geotechnical and Geoenvironmental Engineering*, 135(11):1547–1561.

Bond, A. E., Benbow, S., Wilson, J., McDermott, C., and English, M. (2012). Coupled hydro-mechanical–chemical process modelling in argillaceous formations for DECOVALEX-2011. *Mineralogical Magazine*, 76(8):3131–3143.

Buchan, A. G., Farrell, P. E., Gorman, G. J., Goddard, A. J., Eaton, M. D., Nygaard, E. T., Angelo, P. L., Smedley-Stevenson, R. P., Merton, S. R., and Smith, P. N. (2014). The immersed body supermeshing method for modelling reactor physics problems with complex internal structures. *Annals of Nuclear Energy*, 63:399–408.

Byrne, G. D. and Hindmarsh, A. C. (1975). A Polyalgorithm for the Numerical Solution of Ordinary Differential Equations. *ACM Transactions on Mathematical Software*, 1(1):71–96.

Cappa, F., Guglielmi, Y., Rutqvist, J., Tsang, C.-F., and Thoraval, A. (2008). Estimation of fracture flow parameters through numerical analysis of hydromechanical pressure pulses. *Water Resources Research*, 44(11):1–48.

Chan, T., Khair, K., Jing, L., Ahola, M., Noorishad, J., and Vuillod, E. (1995). International comparison of coupled thermo-hydro-mechanical models of a multiple-fracture bench mark problem: DECOVALEX phase I, bench mark test 2. *International Journal of Rock Mechanics and Mining Sciences and*, 32(5):435–452.

Chijimatsu, M., Nguyen, T. S., Jing, L., De Jonge, J., Kohlmeier, M., Millard, A., Rejeb, A., Rutqvist, J., Souley, M., and Sugita, Y. (2005). Numerical study of the THM effects on the near-field safety of a hypothetical nuclear waste repository - BMT1 of the DECOVALEX III project. Part 1: Conceptualization and characterization of the problems and summary of results. *International Journal of Rock Mechanics and Mining Sciences*, 42(5-6 SPEC. ISS.):720–730.

Cho, N., Martin, C., and Christiansson, R. (2002). Suppressing fracture growth around underground openings. *Proc. 5th North American Rock Mechanics Symposium and 17th Tunnelling Association of Canada Conference.*

Clark, D. K., Hassan, H. A., and Salas, M. D. (1986). Euler calculations for multielement airfoils using Cartesian grids. *AIAA Journal*, 24(3):353–358.

Clay, O. (2004). *Thermo-Hydro- Mechanical and Geochemical Behaviour of the Argillite and the Thermo-Hydro- Argillite and the.*

CODE-BRIGHT (2018). Code_Bright User Guide. (May).

Coquerelle, M. and Cottet, G. H. (2008). A vortex level set method for the two-way coupling of an incompressible fluid with colliding rigid bodies. *Journal of Computational Physics*, 227(21):9121–9137.

Crouch, S. L. (1976). Solution of plane elasticity problems by the displacement discontinuity method. I. Infinite body solution. *International Journal for Numerical Methods in Engineering*, 10(2):301–343.

Cundall, P. A. and Strack, O. D. L. (1979). A discrete numerical model for granular assemblies. *Géotechnique*, 29(1):47–65.

de Vries, D. A. (1975). Heat transfer in soils, Wiley. *Heat and mass transfer in the biosphere. Part I: Transfer processes in plant environment*, (5-28):4–28.

DECC (2010). UK Strategy for the Management of Solid Low Level Radioactive Waste from the Nuclear Industry. Technical Report January.

DECC (2014). Implementing Geological Disposal 2014 White Paper. *Urn 14D/235*, (July):5–54.

Dessirier, B. (2018). Research on Resaturation of Bentonite Buffer - Coupling between Bentonite and Rock. Technical report, Uppsala University.

Dessirier, B., Frampton, A., and Jarsjö, J. (2017). Two-phase flows during re-saturation of sparsely fractured bedrock and bentonite around canisters for deep storage of spent nuclear fuel Modelling Task 8 of SKB Task Forces. Technical Report June.

DeZeeuw, D. and Powell, K. G. (1993). An Adaptively Refined Cartesian Mesh Solver for the Euler Equations.

Donea, J., Huerta, A., Ponthot, J., and Ferran, A. (2004). Chapter 14 Arbitrary Lagrangian-Eulerian Methods. *Encyclopedia of Computational ...*, pages 1–25.

Dorfman, A. and Renner, Z. (2009). Conjugate problems in convective heat transfer: Review. *Mathematical Problems in Engineering*, 2009.

DTi (2006). The Energy Challenge. Energy Review Report. Technical report.

Dueck, A. and Nilsson, U. (2010). Thermo-Hydro-Mechanical properties of MX-80 : Results from advanced laboratory tests. Technical Report December.

Duflot, M. (2008). The extended finite element method in thermoelastic fracture mechanics. *International Journal for Numerical Methods in Engineering*, 74(5):827–847.

Dunne, T. and Rannacher, R. (2006). Adaptive Finite Element Approximation of Fluid-Structure Interaction Based on an Eulerian Variational Formulation. In *Fluid-Structure Interaction*, pages 110–145. Springer Berlin Heidelberg, Berlin, Heidelberg.

Enayatpour, S., Patzek, T., and Others (2013). Thermal shock in reservoir rock enhances the hydraulic fracturing of gas shales. *Unconventional Resources Technology Conference*, pages 1–11.

Engels, T., Kolomenskiy, D., Schneider, K., and Sesterhenn, J. (2015). Numerical simulation of fluid-structure interaction with the volume penalization method. *Journal of Computational Physics*, 281:96–115.

Enssle, C. P., Croisé, J., Poller, A., Mayer, G., and Wendling, J. (2011). Full scale 3D-modelling of the coupled gas migration and heat dissipation in a planned repository for radioactive waste in the Callovo-Oxfordian clay. *Physics and Chemistry of the Earth*, 36(17-18):1754–1769.

Fadlun, E. A., Verzicco, R., Orlandi, P., and Mohd-Yusof, J. (2000). Combined Immersed-Boundary Finite-Difference Methods for Three-Dimensional Complex Flow Simulations. *Journal of Computational Physics*, 161(1):35–60.

Farhat, C., Lesoinne, M., and Le Tallec, P. (1998). Load and motion transfer algorithms for fluid/structure interaction problems with non-matching discrete interfaces:

Momentum and energy conservation, optimal discretization and application to aeroelasticity. *Computer Methods in Applied Mechanics and Engineering*, 157(1-2):95–114.

Farrell, P. and Maddison, J. (2011). Conservative interpolation between volume meshes by local Galerkin projection. *Computer Methods in Applied Mechanics and Engineering*, 200(1-4):89–100.

Feng, X. T., Chen, S., and Li, S. (2001). Effects of water chemistry on microcracking and compressive strength of granite. *International Journal of Rock Mechanics and Mining Sciences*, 38(4):557–568.

Feng, X. T., Pan, P. Z., and Zhou, H. (2006). Simulation of the rock microfracturing process under uniaxial compression using an elasto-plastic cellular automaton. *International Journal of Rock Mechanics and Mining Sciences*, 43(7):1091–1108.

Feng, Y. T., Han, K., Li, C. F., and Owen, D. R. (2008). Discrete thermal element modelling of heat conduction in particle systems: Basic formulations. *Journal of Computational Physics*, 227(10):5072–5089.

Feng, Y. T., Han, K., and Owen, D. R. (2009). Discrete thermal element modelling of heat conduction in particle systems: Pipe-network model and transient analysis. *Powder Technology*, 193(3):248–256.

Fernández, A. M., Kaufhold, S., Sánchez-ledesma, D. M., Rey, J. J., Melón, A., Robredo, L. M., Fernández, S., Labajo, M. A., and Clavero, M. A. (2018). Applied Geochemistry Evolution of the THC conditions in the FEBEX in situ test after 18 years of experiment : Smectite crystallochemical modifications after interactions of the bentonite with a C-steel heater at 100 Degree C. *Applied Geochemistry*, 98(December 2017):152–171.

Feucht, L. J. and Logan, J. M. (1990). Effects of chemically active solutions on shearing behavior of a sandstone. *Tectonophysics*, 175(1-3):159–176.

Fransson, Å., Åkesson, M., and Technology, C. (2017). R-14-11 Bentonite Rock Interaction Experiment. Technical Report April.

Fries, T.-P. and Belytschko, T. (2010). The extended/generalized finite element method: An overview of the method and its applications. *International Journal for Numerical Methods in Engineering*, 84:353–304.

García, X., Pavlidis, D., Gorman, G. J., Gomes, J. L. M. A., Piggott, M. D., Aristodemou, E., Mindel, J., Latham, J.-P., Pain, C. C., and ApSimon, H. (2011). A two-phase adaptive finite element method for solid-fluid coupling in complex geometries. *International Journal for Numerical Methods in Fluids*, 66(1):82–96.

Gauthier-Lafaye, F., Holliger, P., and Blanc, P. L. (1996). Natural fission reactors in the Franceville basin, Gabon: A review of the conditions and results of a "critical event" in a geologic system. *Geochimica et Cosmochimica Acta*, 60(23):4831–4852.

Giannopoulos, G. I. and Anifantis, N. K. (2005). Thermal fracture interference: A two-dimensional boundary element approach. *International Journal of Fracture*, 132(4):349–368.

Gibou, F. and Min, C. (2012). Efficient symmetric positive definite second-order accurate monolithic solver for fluid/solid interactions. *Journal of Computational Physics*, 231(8):3246–3263.

Glamheden, R., Fälth, B., Jacobsson, L., Harrström, J., Berglund, J., and Bergkvist, L. (2010). TR-10-37 Counterforce applied to prevent spalling. Technical Report April.

Glowinski, R., Pan, T. W., and Periaux, J. (1994). A fictitious domain method for external incompressible viscous flow modeled by Navier-Stokes equations. *Computer Methods in Applied Mechanics and Engineering*, 112(1-4):133–148.

Gomes, J. L., Pavlidis, D., Salinas, P., Xie, Z., Percival, J. R., Melnikova, Y., Pain, C. C., and Jackson, M. D. (2017). A force-balanced control volume finite element method for multi-phase porous media flow modelling. *International Journal for Numerical Methods in Fluids*, 83(5):431–445.

Griffith, B. E., Hornung, R. D., McQueen, D. M., and Peskin, C. S. (2007). An adaptive, formally second order accurate version of the immersed boundary method. *Journal of Computational Physics*, 223(1):10–49.

Guo, L. (2014). *Development of a three-dimensional fracture model for the combined finite-discrete element method.* PhD thesis.

Guo, L., Latham., J.-P., Xiang, J., and Lei, Q. (2013). A numerical investigation of fracture pattern and fracture aperture development in multi-layered rock using a combined finite-discrete element method. *47th U.S. Rock Mechanics/Geomechanics Symposium*, page 686.

Guvanasen, V. and Chan, T. (2000). A three-dimensional numerical model for thermo-hydromechanical deformation with hysteresis in a fractured rock mass. *International Journal Of Rock Mechanics And Mining Sciences*, 37(1-2):89–106.

Hökmark, H., Lönnqvist, M., and Fälth, B. (2010). Tr-10-23. Technical Report May, SKB.

Hökmark, H., Lönnqvist, M., and Kristensson, O. (2009). Strategy for Thermal Dimensioning of the Final Repository for Spent Nuclear Fuel. R-09-04. Technical report.

Holton, D. and Hoch, A. (2017). Calibrated modelling of resaturation in the Bentonite Rock Interaction Experiment (BRIE) Task 8D of SKB Task Forces EBS and GWFTS. Technical Report August.

Hübner, B., Walhorn, E., and Dinkler, D. (2004). A monolithic approach to fluid-structure interaction using space-time finite elements. *Computer Methods in Applied Mechanics and Engineering*, 193(23-26):2087–2104.

Hudson, J. A., Bäckström, A., Rutqvist, J., and Jing, L. (2008). DECOVALEX-THMC Project. Task B. Understanding and characterizing the excavation disturbed zone (EDZ). Final Report. Characterising and Modelling the Excavation Damaged Zone (EDZ) in Crystalline Rocks in the Context of Radioactive Waste Disposal.

IAEA (2017). IAEA 2017 Nuclear power reactors in the world. Technical report.

Incropera, F. P., DeWitt, D. P., Bergman, T. L., and Lavine, A. S. (2011). *Fundamentals of Heat and Mass Transfer*, volume 7th.

Itasca (2018). Fluid Flow in Joints. Date accessed:20/08/2018 url: https://www.itascacg.com/software/products/udec/features/fluid-flow-in-joints.

Itasca CG (2017). FLAC3D 6.0 Theory and Background.

Jackson, M., Percival, J., Mostaghimi, P., Tollit, B., Pavlidis, D., Pain, C., Gomes, J., Elsheikh, A. H., Salinas, P., Muggeridge, A., and Blunt, M. (2015). Reservoir Modeling for Flow Simulation by Use of Surfaces, Adaptive Unstructured Meshes, and an Overlapping-Control-Volume Finite-Element Method. *SPE Reservoir Evaluation & Engineering*, 18(02):115–132.

Jacobsson, L. and Bäckström, A. (2005). IPR-05-33 Uniaxial compression tests of intact distilled , saline and formation water. Technical report, SKB.

Jaiman, R. K., Jiao, X., Geubelle, P. H., and Loth, E. (2006). Conservative load transfer along curved fluid-solid interface with non-matching meshes. *Journal of Computational Physics*, 218(1):372–397.

Jiao, Y. Y., Zhang, X. L., Zhang, H. Q., Li, H. B., Yang, S. Q., and Li, J. C. (2015). A coupled thermo-mechanical discontinuum model for simulating rock cracking induced by temperature stresses. *Computers and Geotechnics*, 67:142–149.

Jindal, S., Khalighi, B., and Iaccarino, G. (2005). Numerical Investigation of Road Vehicle Aerodynamics Using the Immersed Boundary RANS Approach. *SAE paper*, 2005(2005-01):546.

Jing, L. (1998). Formulation of discontinuous deformation analysis (DDA) - an implicit discrete element model for block systems. *Engineering Geology*, 49(3-4):371–381.

Jing, L. (2003). A review of techniques, advances and outstanding issues in numerical modelling for rock mechanics and rock engineering. *International Journal of Rock Mechanics and Mining Sciences*, 40(3):283–353.

Jing, L., Ma, Y., and Fang, Z. (2001). Modeling of fluid flow and solid deformation for fractured rocks with discontinuous deformation analysis (DDA) method. *International Journal of Rock Mechanics and Mining Sciences*, 38(3):343–355.

Jing, L., Rutqvist, J., Stephanson, O., Tsang, C.-F., and Kautsky, F. (1993). DECOVALEX- Mathematical Models of Coupled T-H-M Processes for Nuclear Waste Repositories.

Jing, L. and Stephansson, O. (2007). *Fundamentals of Discrete Element Methods for Rock Engineering: Theory and Applications, Volume 85 (Developments in Geotechnical Engineering)*. Elsevier Science.

Joulin, C., Xiang, J., Latham, J.-p., and Pain, C. (2016). A new Finite Discrete element approach for heat transfer in complex shaped multi bodied contact problems. In *DEM7*, pages 1–10.

Kajishima, T., Takigushi, S., Hamasaki, H., and Miyake, Y. (2001). Turbulence Structure of Particle-Laden Flow in a Vertical Plane Channel Due to Vortex Shedding. *JSME International Journal Series B*, 44(4):526–535.

Karantzoulis, N. (2017). *Development and Implementation of Inelastic Material Models for Use in Femdem Numerical Methods With Applications*. PhD thesis.

Karatela, E. and Taheri, A. (2018). Three-dimensional hydro-mechanical model of borehole in fractured rock mass using discrete element method. *Journal of Natural Gas Science and Engineering*, 53(July 2017):263–275.

Kim, B. S., Lee, D. S., Ha, M. Y., and Yoon, H. S. (2008). A numerical study of natural convection in a square enclosure with a circular cylinder at different vertical locations. 51:1888–1906.

Kim, J. and Choi, H. (2004). An immersed-boundary finite-volume method for simulation of heat transfer in complex geometries. *KSME International Journal*, 18(6):1026–1035.

Kolditz, O., Bauer, S., Beinhorn, M., De Jonge, J., Kalbacher, T., McDermott, C., Wang, W., Xie, M., Kaiser, R., and Kohlmeier, M. (2003). ROCKFLOW — theory and users manual, release 3.9.

Kolditz, O., Bauer, S., Bilke, L., Böttcher, N., Delfs, J. O., Fischer, T., Görke, U. J., Kalbacher, T., Kosakowski, G., McDermott, C. I., Park, C. H., Radu, F., Rink, K., Shao, H., Shao, H. B., Sun, F., Sun, Y. Y., Singh, A. K., Taron, J., Walther, M., Wang, W., Watanabe, N., Wu, Y., Xie, M., Xu, W., and Zehner, B. (2012a). OpenGeoSys: An open-source initiative for numerical simulation of thermo-hydro-mechanical/chemical (THM/C) processes in porous media. *Environmental Earth Sciences*, 67(2):589–599.

Kolditz, O., Görke, U. J., Shao, H., and Wang, W. (2012b). Thermo-hydro-mechanical-chemical processes in fractured porous media. *Lecture Notes in Computational Science and Engineering*, 86 LNCSE.

Koyama, T., Chijimatsu, M., Shimizu, H., Nakama, S., Fujita, T., Kobayashi, A., and Ohnishi, Y. (2013). Numerical modeling for the coupled thermo-mechanical processes and spalling phenomena in äspö pillar stability experiment (APSE). *Journal of Rock Mechanics and Geotechnical Engineering*, 5(1):58–72.

Kwon, S., Lee, C., Jeon, S., and Choi, H. J. (2013). Thermo-mechanical coupling analysis of APSE using submodels and neural networks. *Journal of Rock Mechanics and Geotechnical Engineering*, 5(1):32–43.

Latham, J. P., Mindel, J., Xiang, J., Guises, R., Garcia, X., Pain, C., Gorman, G., Piggott, M., and Munjiza, A. (2009). Coupled FEMDEM/Fluids for coastal engineers with special reference to armour stability and breakage. *Geomechanics and Geoengineering*, 4(1):39–53.

Latham, J.-P., Munjiza, A., Garcia, X., Xiang, J., and Guises, R. (2008). Three-dimensional particle shape acquisition and use of shape library for DEM and FEM/-DEM simulation. *Minerals Engineering*, 21(11):797–805.

Latham, J. P., Xiang, J., Belayneh, M., Nick, H. M., Tsang, C.-F., and Blunt, M. J. (2013). Modelling stress-dependent permeability in fractured rock including effects of propagating and bending fractures. *International Journal of Rock Mechanics and Mining Sciences*, 57:100–112.

Le Fichoux, E. (2011). Presentation et Utilisation de CAST3M.

Lee, H. S. and Jing, L. (2004). An inverse stress reconstruction algorithm for modelling excavation and thermo-mechanical effects of rock structures. *Engineering Analysis with Boundary Elements*, 28(7):833–842.

Lei, Q. (2016). *Characterisation and modelling of natural fracture networks: geometry, geomechanics and fluid flow.* PhD thesis.

Lei, Q., Latham, J. P., and Tsang, C.-F. (2017a). The use of discrete fracture networks for modelling coupled geomechanical and hydrological behaviour of fractured rocks. *Computers and Geotechnics*, 85:151–176.

Lei, Q., Latham, J. P., and Xiang, J. (2016). Implementation of an Empirical Joint Constitutive Model into Finite-Discrete Element Analysis of the Geomechanical Behaviour of Fractured Rocks. *Rock Mechanics and Rock Engineering*, 49(12):4799–4816.

Lei, Q., Latham, J. P., Xiang, J., and Tsang, C.-F. (2015). Polyaxial stress-induced variable aperture model for persistent 3D fracture networks. *Geomechanics for Energy and the Environment*, 1:34–47.

Lei, Q., Latham, J. P., Xiang, J., and Tsang, C. F. (2017b). Role of natural fractures in damage evolution around tunnel excavation in fractured rocks. *Engineering Geology*, 231(August):100–113.

Lei, Q., Latham, J. P., Xiang, J., Tsang, C.-F., Lang, P., and Guo, L. (2014). Effects of geomechanical changes on the validity of a discrete fracture network representation of a realistic two-dimensional fractured rock. *International Journal of Rock Mechanics and Mining Sciences*, 70:507–523.

Lei, Q., Wang, X., Xiang, J., and Latham, J.-P. (2017c). Polyaxial stress-dependent permeability of a three-dimensional fractured rock layer. *Hydrogeology Journal*, pages 2251–2262.

Lin, W., Ramirez, A., and Wat, D. (1991). Temperature Measurements from a Horizontal Heater Test in G-Tunnel. Technical report, Lawrence Livermore National Laboratory.

Liu, P., Yu, T., Bui, T. Q., Zhang, C., Xu, Y., and Lim, C. W. (2014). Transient thermal shock fracture analysis of functionally graded piezoelectric materials by the extended finite element method. *International Journal of Solids and Structures*, 51(11-12):2167–2182.

Lloret, A. and Alonso, E. E. (1985). State surfaces for partially saturated soils. pages 557–562.

Manepally, C., Fedors, R., Basagaoglu, H., Ofoegbu, G., Pabalan, R., and Antonio, S. (2011). COUPLED PROCESSES WORKSHOP REPORT Center for Nuclear Waste Regulatory Analyses. Technical Report September, U.S. Nuclear Regulatory Commission.

Manteufel, R. D., Ahola, M. P., Turner, D. R., and Chowdhury, A. H. (1993). A literature review of coupled thermal-hydrologic-mechanical-chemical processes pertinent to the proposed high-level nuclear waste repository at Yucca Mountain. Technical report, U.S. Division of High-Level Waste Management.

Martin, D. (2005). Preliminary assessment of potential underground stability (wedge and spalling) at Forsmark, Simpevarp and Laxemar sites. R-05-71. Technical report, SKB.

Maul, P. (2010). Modelling Coupled Processes in the Evolution of Repository Engineered Barrier Systems using QPAC-EBS. Technical report, Swedish Radiation Safety Authority.

Maul, P. (2013). QPAC : Quintessa's General-Purpose Modelling Software.

Maul, P., Bond, A., Maul, P., and Maul, P. (2008). The Use of QPAC-EBS for Project THERESA Benchmarking Studies. (July).

Michler, C., Hulshoff, S. J., van Brummelen, E. H., and de Borst, R. (2004). A monolithic approach to fluid-structure interaction. *Computers and Fluids*, 33(5-6):839–848.

Mikic, B. B. and Rohsenow, W. M. (1966). Thermal contact resistance. *Technical Report DSR 74542-41*.

Millard, A., Durin, M., Stietel, A., Thoraval, A., Vuillod, E., Baroudi, H., Plas, F., Bougnoux, A., Vouille, G., Kobayashi, A., Hara, K., Fujita, T., and Ohnishi, Y. (1995). Discrete and continuum approaches to simulate the thermo-hydro-mechanical couplings in a large, fractured rock mass. *International Journal of Rock Mechanics and Mining Sciences and*, 32(5):409–434.

Miller, W. W. M. (2000). *Geological disposal of radioactive wastes and natural analogues : lessons from nature and archaeology*. Pergamon.

Min, K. B., Rutqvist, J., Tsang, C.-F., and Jing, L. (2005). Thermally induced mechanical and permeability changes around a nuclear waste repository - A far-field study based on equivalent properties determined by a discrete approach. *International Journal of Rock Mechanics and Mining Sciences*, 42(5-6 SPEC. ISS.):765–780.

Mittal, R., Dong, H., Bozkurttas, M., Najjar, F. M., Vargas, A., and von Loebbecke, A. (2008). A versatile sharp interface immersed boundary method for incompressible flows with complex boundaries. *Journal of Computational Physics*, 227(10):4825–4852.

Mittal, R. and Iaccarino, G. (2005). Immersed Boundary Methods. *Annual Review of Fluid Mechanics*, 37(1):239–261.

Morgan, W. E. and Aral, M. M. (2015). An implicitly coupled hydro-geomechanical model for hydraulic fracture simulation with the discontinuous deformation analysis. *International Journal of Rock Mechanics and Mining Sciences*, 73:82–94.

Munjiza, A. (2004). *The Combined Finite-Discrete Element Method.*

Munjiza, A. and Andrews, K. R. (2000). Penalty function method for combined finite-discrete element systems comprising large number of separate bodies. *International Journal for Numerical Methods in Engineering*, 49(11):1377–1396.

Munjiza, A., Andrews, K. R., and White, J. K. (1999). Combined single and smeared crack model in combined finite-discrete element analysis. *International Journal for Numerical Methods in Engineering*, 44(1):41–57.

Munjiza, A., Latham, J. P., and John, N. W. (2003). 3D dynamics of discrete element systems comprising irregular discrete elements-Integration solution for finite rotations in 3D. *International Journal for Numerical Methods in Engineering*, 56(1):35–55.

Munjiza, A., Owen, D. R., and Bicanic, N. (1995). *A combined finite-discrete element method in transient dynamics of fracturing solids*, volume 12.

Munjiza, A., Xiang, J., Garcia, X., Latham, J. P., D'Albano, G. G., and John, N. W. (2010). The Virtual Geoscience Workbench, VGW: Open Source tools for discontinuous systems. *Particuology*, 8(2):100–105.

NAMRC (2015). UK New Build Plans.

NAO (2017). Hinkley Point C. Technical report.

NDA (2015). NDA Higher Activity Waste Treatment Framework. Technical Report October.

NDA (2016). Geological Disposal: Generic Disposal Facility Design. Technical Report DSSC/412/01.

NDA (2017a). 2016 UK Radioactive Waste and Materials Inventory: UK Radioactive Waste Inventory Report. Technical report.

NDA (2017b). Interim Storage of Higher Activity Waste Packages – Integrated Approach. Technical Report 3.

NDA and BEIS (2017). Radioactive Wastes in the UK: A Summary of the 2016 Inventory. Technical Report March.

Neretnieks, I. (2006). R-06-91 Flow and solute transport in a zone damaged due to spalling. *Engineering and Technology.*

Nguyen, T. S. (1996). Description of the computer code FRACON. *Developments in Geotechnical Engineering*, 79(C):539–544.

Nguyen, T. S. and Selvadurai, A. P. (1995). Coupled thermal-mechanical-hydrological behaviour of sparsely fractured rock: Implications for nuclear fuel waste disposal. *International Journal of Rock Mechanics and Mining Sciences and*, 32(5):465–479.

Nguyen, T. S., Selvadurai, A. P., and Armand, G. (2005). Modelling the FEBEX THM experiment using a state surface approach. *International Journal of Rock Mechanics and Mining Sciences*, 42(5-6 SPEC. ISS.):639–651.

Nikishkov, G. (2010). Finite Element Equations for Heat Transfer. *Programming Finite Elements in Java^{TM}*, pages 13–19.

Noda, N., Hetnarski, R. B., and Tanigawa, Y. (2003). *Thermal stresses.* Taylor & Francis.

Noorishad, J. and Tsang, C.-F. (1996). ROCMAS Simulator; A Thermohydromechanical Computer Code.

Noorishad, J., Tsang, C.-F., and Witherspoon, P. A. (1984). Coupled Thermal-Hydraulic-Mechanical Phenomena in Saturated Fractured Porous Rocks: Numerical Approach. *Journal of Geophysical Research*, 89(B12):10365–10373.

Obeysekara, A. (2018). *Numerical Modelling of Fluid-Driven Fracturing in Naturally Fractured Rock.* PhD thesis, Imperial College London.

Obeysekara, A., Lei, Q., Salinas, P., Pavlidis, D., Xiang, J., Latham, J., and Pain, C. (2017). Modelling the evolution of a fracture network under excavation- induced unloading and seepage effects based on a fully coupled fluid-solid simulation. *American Rock Mechanics Association.*

Obeysekara, A., Lei, Q., Salinas, P., Pavlidis, D., Xiang, J., Latham, J. P., and Pain, C. C. (2018). Modelling stress-dependent single and multi-phase flows in fractured porous media based on an immersed-body method with mesh adaptivity. *Computers and Geotechnics*, 103(January):229–241.

Oda, M. (1986). An equivalent continuum model for coupled stress and fluid flow analysis in jointed rock masses. *Water Resources Research*, 22(13):1845–1856.

Ogden, R. W. (1997). *Non-linear elastic deformations.* Dover Publications.

Ohnishi, Y., Shibata, H., and Kobayashi, A. (1987). Development of Finite Element Code for the Analysis of Coupled Thermo-Hydro-Mechanical Behaviors of a Saturated-Unsaturated Medium. *Coupled Processes Associated with Nuclear Waste Repositories*, 92101:679–697.

Olivella, S., Carrera, J., Gens, A., and Alonso, E. E. (1994). Nonisothermal multiphase flow of brine and gas through saline media. *Transport in Porous Media*, 15(3):271–293.

Olsson, R. and Barton, N. (2001). An improved model for hydromechanical coupling during shearing of rock joints. *International Journal of Rock Mechanics and Mining Sciences*, 38(3):317–329.

Pain, C. C., Umpleby, A. P., de Oliveira, C. R., and Goddard, A. J. (2001). Tetrahedral mesh optimisation and adaptivity for steady-state and transient finite element calculations. *Computer Methods in Applied Mechanics and Engineering*, 190(29-30):3771–3796.

Pan, P. and Feng, X. (2013). Numerical study on coupled thermo-mechanical processes in Äspö Pillar Stability Experiment. *Journal of Rock Mechanics and Geotechnical Engineering*, 5(2):136–144.

Pan, P., Feng, X., and Zhou, H. (2012). Development and applications of the elasto-plastic cellular automaton. *Acta Mechanica Solida Sinica*, 25(2):126–143.

Pan, P. Z., Feng, X. T., Huang, X. H., Cui, Q., and Zhou, H. (2009). Coupled THM processes in EDZ of crystalline rocks using an elasto-plastic cellular automaton. *Environmental Geology*, 57(6):1299–1311.

Parry, A. (2017). A Stable Fluid Rigid Body Interaction Algorithm: Application to Industrial Problems. *American Society of Mechanical Engineers, Pressure Vessels and Piping Division (Publication) PVP*, 485(PART 1):1–8.

Patrick, W. C. (1986). Spent-Fuel Test — Climax : An Evaluation of the Technical Feasibility of Geologic Storage of Spent Nuclear Fuel in Granite Executive Summary of Final Results MAS1B. Technical report, Lawrence Livermore National Laboratory.

Peskin, C. S. (1972). Flow patterns around heart valves: A numerical method. *Journal of Computational Physics*, 10(2):252–271.

Philip, J. R. and De Vries, D. A. (1957). Moisture movement in porous materials under temperature gradients. *Eos, Transactions American Geophysical Union*, 38(2):222–232.

Piggott, M. D., Gorman, G. J., Pain, C. C., Allison, P. A., Candy, A. S., Martin, B. T., and Wells, M. R. (2008). A new computational framework for multi-scale ocean modelling based on adapting unstructured meshes. *International Journal for Numerical Methods in Fluids*, 56(8):1003–1015.

Potyondy, D. O. and Cundall, P. A. (2004). A bonded-particle model for rock. *International Journal of Rock Mechanics and Mining Sciences*, 41(8 SPEC.ISS.):1329–1364.

Prior, A. M. (1994). Applications of implicit and explicit finite element techniques to metal forming. *Journal of Materials Processing Tech.*, 45(1-4):649–656.

Pruess, K. (1991). TOUGH2: A general-purpose numerical simulator for multiphase fluid and heat flow. *Office*, (May):LBL–29400.

Rafiee, A. and Thiagarajan, K. P. (2009). An SPH projection method for simulating fluid-hypoelastic structure interaction. *Computer Methods in Applied Mechanics and Engineering*, 198(33-36):2785–2795.

Rickelt, S., Kruggel-Emden, H., Wirtz, S., and Scherer, V. (2009). Simulation of Heat Transfer in Moving Granular Material by the Discrete Element Method with Special Emphasis on inner Particle Heat Transfer. *Proceedings of the ASME 2009 Heat Transfer Summer Conference*, pages 1–11.

Rinne, M., Shen, B., and Backers, T. (2013). Modelling fracture propagation and failure in a rock pillar under mechanical and thermal loadings. *Journal of Rock Mechanics and Geotechnical Engineering*, 5(1):73–83.

Russell, D. and Wang, Z. J. (2003). A Cartesian grid method for modeling multiple moving objects in 2D incompressible viscous flow. *Journal of Computational Physics*, 191(1):177–205.

Rutqvist, J., Bäckström, A., Chijimatsu, M., Feng, X.-T., Pan, P. Z., Hudson, J. A., Jing, L., Kobayashi, A., Koyama, T., Lee, H. S., Huang, X. H., Rinne, M., and Shen, B. (2009a). A multiple-code simulation study of the long-term EDZ evolution of geological nuclear waste repositories. *Environmental Geology*, 57(6):1313–1324.

Rutqvist, J., Barr, D., Birkholzer, J. T., Fujisaki, K., Kolditz, O., Liu, Q. S., Fujita, T., Wang, W., and Zhang, C. Y. (2009b). A comparative simulation study of coupled THM processes and their effect on fractured rock permeability around nuclear waste repositories. *Environmental Geology*, 57(6):1347–1360.

Rutqvist, J., Börgesson, L., Chijimatsu, M., Kobayashi, A., Jing, L., Nguyen, T. S., Noorishad, J., and Tsang, C.-F. (2001a). Thermohydromechanics of partially saturated geological media: Governing equations and formulation of four finite element models. *International Journal of Rock Mechanics and Mining Sciences*, 38(1):105–127.

Rutqvist, J., Börgesson, L., Chijimatsu, M., Nguyen, T. S., Jing, L., Noorishad, J., and Tsang, C.-F. (2001b). Coupled thermo-hydro-mechanical analysis of a heater test in fractured rock and bentonite at Kamaishi Mine - comparison of field results to predictions of four finite element codes. *International Journal of Rock Mechanics and Mining Sciences*, 38(1):129–142.

Rutqvist, J., Ijiri, Y., and Yamamoto, H. (2011). Implementation of the Barcelona Basic Model into TOUGH–FLAC for simulations of the geomechanical behavior of unsaturated soils. *Computers & Geosciences*, 37(6):751–762.

Rutqvist, J. and Tsang, C.-F. (2003). Analysis of thermal-hydrologic-mechanical behavior near an emplacement drift at Yucca Mountain. *Journal of Contaminant Hydrology*, 62-63:637–652.

Rutqvist, J., Wu, Y. S., Tsang, C.-F., and Bodvarsson, G. (2002). A modeling approach for analysis of coupled multiphase fluid flow, heat transfer, and deformation in fractured porous rock. *International Journal of Rock Mechanics and Mining Sciences*, 39(4):429–442.

RWM (2016). Geological Disposal. Generic Disposal System Specification Part A: High Level Requirements. Technical report.

RWM (2019). RWM Coupled Processes Project. First Annual Report for DECOVALEX-2019. Technical Report December 2017.

Ryzhakov, P. B., Rossi, R., Idelsohn, S. R., and Oñate, E. (2010). A monolithic Lagrangian approach for fluid-structure interaction problems. *Computational Mechanics*, 46(6):883–899.

Salinas, P., Pavlidis, D., Xie, Z., Osman, H., Pain, C. C., and Jackson, M. D. (2018). A discontinuous control volume finite element method for multi-phase flow in heterogeneous porous media. *Journal of Computational Physics*, 352:602–614.

Shen, B. (2018). Modeling Rock Fracturing Processes With FRACOD. In *Hydraulic Fracture Modeling*, pages 265–321. Gulf Professional Publishing.

Shen, B., Rinne, M., and Stephansson, O. (2006). FRACOD 2D, User's Manual.

Shen, B. and Stephansson, O. (1993). Numerical analysis of mixed mode I and Mode II fracture propagation. *International Journal of Rock Mechanics and Mining Sciences and*, 30(7):861–867.

Shen, B., Stephansson, O., and Rinne, M. (2013). *Modelling Rock Fracturing Processes: A Fracture Mechanics Approach Using FRACOD.*

Shi, G. H. (1992). Discontinuous deformation analysis: A new numerical model for the statics and dynamics of deformable block structures. *Engineering Computations*, 9(2):157–168.

Silling, S. A. (2000). Reformulation of elasticity theory for discontinuities and long-range forces. *Journal of the Mechanics and Physics of Solids*, 48(1):175–209.

Simulia (2017). Abaqus 6.11 Theory Manual.

SKB (2000). Integrated account of method , site selection and programme prior to the site investigation phase. Technical report.

SKB (2010a). Design, construction and initial state of the underground openings. (December).

SKB (2010b). Design, production and initial state of the buffer. TR-10-15. Technical Report December.

SKB (2010c). TR-10-12 Design and production of the KBS-3 repository. Technical Report December.

SKB (2018). Detailed site i nvestigation programme for the construction and operation of the Repository for spent nuclear fuel. Technical Report June.

Snow, D. T. (1965). *PhD. Thesis: A Parallel Plate Model of Fractured Permeable Media.* PhD thesis.

Stephansson, O., Hudson, J. A. J. A., and Jing, L. (2004). *Coupled thermo-hydro-mechanical-chemical processes in geo-systems : fundamentals, modelling, experiments and applications*. Elsevier.

Stephansson, O., Jing, L., and Kobayashib, a. (1996). Y. Ohnishi a and A. Kobayashib aSchool of Civil Engineering, Kyoto University, Yoshida-honmachi, Sakyo-ku, Kyoto. 79:545–549.

Stietel, A., Millard, A., Reille, E., Vuillod, E., Thoraval, A., and Ababou, R. (1996). Continuum representation of coupled hydromechanic processes of fractured media: Homogenisation and parameter identification. In *Developments in Geotechnical Engineering*, volume 79, pages 135–164.

Su, K., Latham, J. P., Pavlidis, D., Xiang, J., Fang, F., Mostaghimi, P., Percival, J. R., Pain, C. C., and Jackson, M. D. (2015). Multiphase flow simulation through porous media with explicitly resolved fractures. *Geofluids*, 15(4):592–607.

Sukumar, N., Moës, N., Moran, B., and Belytschko, T. (2000). Extended finite element method for three-dimensional crack modelling. *International Journal for Numerical Methods in Engineering*, 48(11):1549–1570.

Terzaghi, C. (1925). Principles of Soil Mechanics. *Engienering News-Record*, 95(95):19–27.

Thatcher, K. E., Newson, R. K., and Benbow, S. J. (2018). Research on Resaturation of Bentonite Buffe. 2018:21. Technical report, Quintessa.

THERESA (2009). Coupled Thermal-Hydrological-Mechanical-Chemical Processes for Application in Repository Safety Assessment, Project description & Status. Technical report, Group of Engineering Geology & Geophysics. Department of land & Water Resources Engineering, Royal Institute of Technology Stockholm, Sweden.

Thomas, H., He, Y., Sansom, M., and Li, C. (1996). On the development of a model of the thermo-mechanical-hydraulic behaviour of unsaturated soils. *Engineering Geology*, 41(1-4):197–218.

Thomas, H. R., He, Y., and Onofrei, C. (1998). An examination of the validation of a model of the hydro/thermo/mechanical behaviour of engineered clay barriers. *International Journal for Numerical and Analytical Methods in Geomechanics*, 22(1):49–71.

Tsang, C.-F. (1987). *Coupled processes associated with nuclear waste repositories.* Academic Press.

Tsang, C.-F. (1991). Coupled hydromechanical-thermochemical processes in rock fractures. *Reviews of Geophysics*, 29(4):537–551.

Tsang, C.-F., Jing, L., Stephansson, O., and Kautsky, F. (2005). The DECOVALEX III project: A summary of activities and lessons learned. *International Journal of Rock Mechanics and Mining Sciences*, 42(5-6 SPEC. ISS.):593–610.

Tsang, C.-F., Orlando, E., and Berkeley, L. (1998). Flow Channelling in Heterogeneous Fractured Rocks. *Reviews of Geophysics*, (97):275–298.

Tsang, C.-F., Stephansson, O., Jing, L., and Kautsky, F. (2009). DECOVALEX Project: From 1992 to 2007. *Environmental Geology*, 57(6):1221–1237.

Tsang, C.-F., Stephansson, O., Kautsky, F., and Jing, L. (2004). *Coupled thm processes in geological systems and the decovalex project*, volume 2. Elsevier Ltd.

Udaykumar, H. S., Mittal, R., Rampunggoon, P., and Khanna, A. (2001). A sharp interface Cartesian grid method for simulating flows with complex moving boundaries. *Journal of Computational Physics*, 174(1):345–380.

Udaykumar, H. S., Mittel, R., and Shyy, W. (1999). Computation of Solid-Liquid Phase Fronts in the Sharp Interface Limit on Fixed Grids. *Journal of Computational Physics*, 153(2):535–574.

Udaykumar, H. S., Shyy, W., and Rao, M. M. (1996). ELAFINT: A Mixed Eulerian–Lagrangian Method for Fluid Flows with Complex and Moving Boundaries. *International Journal for Numerical Methods in Fluids*, 22(June 1994):691–712.

UNFCCC (2016). The Paris Agreement. Technical report.

Van Loon, R., Anderson, P. D., van de Vosse, F. N., and Sherwin, S. J. (2007). Comparison of various fluid-structure interaction methods for deformable bodies. *Computers and Structures*, 85(11-14):833–843.

Vidstrand, P., Stigsson, M., Åkesson, M., and Fransson, Å. (2017). Modelling the Interaction Between Engineered and Natural Barriers.

Viré, A., Xiang, J., Milthaler, F., Farrell, P. E., Piggott, M. D., Latham, J. P., Pavlidis, D., and Pain, C. C. (2012). Modelling of fluid-solid interactions using an adaptive mesh fluid model coupled with a combined finite-discrete element model. *Ocean Dynamics*, 62(10-12):1487–1501.

Viré, A., Xiang, J., and Pain, C. C. (2015). An immersed-shell method for modelling fluid - Structure interactions. *Philosophical Transactions of the Royal Society A: Mathematical, Physical and Engineering Sciences*, 373(2035).

Viré, A., Xiang, J., Piggott, M., Cotter, C., and Pain, C. (2013). Towards the fully-coupled numerical modelling of floating wind turbines. *Energy Procedia*, 35(0):43–51.

Vujosevic, L. and Lubarda, V. (2002). Finite-strain thermoelasticity based on multiplicative decomposition of deformation gradient. *Theoretical and Applied Mechanics*, 28(28-29):379–399.

Walther, M., Heiss, J. W., Magri, F., Delfs, J.-O., and Graf, T. (2016). Thermo-Hydro-Mechanical-Chemical Processes in Fractured Porous Media: Modelling and Benchmarking: Benchmarking Initiatives. *Terrestrial Environmental Sciences*, (November):97–105.

Wang, H. Y. (2015). Numerical modeling of non-planar hydraulic fracture propagation in brittle and ductile rocks using XFEM with cohesive zone method. *Journal of Petroleum Science and Engineering*, 135:127–140.

Wang, J. S. and Tsang, C.-F. (1980). Buoyancy Flow in Fractures Intersecting a Nuclear Waste Repository. Technical report, Lawrence Berkeley National Laboratory.

Wang, J. S., Tsang, C.-F., Cook, N. G., and Witherspoon, P. A. (1981). A study of regional temperature and thermohydrologic effects of an underground repository for nuclear wastes in hard rock. *Journal of Geophysical Research*, 86(B5):3759–3770.

Wang, Y., Zhou, X., and Kou, M. (2018). A coupled thermo-mechanical bond-based peridynamics for simulating thermal cracking in rocks. *International Journal of Fracture*, 211(1-2):13–42.

Wanne, T. S. and Young, R. P. (2008). Bonded-particle modeling of thermally fractured granite. *International Journal of Rock Mechanics and Mining Sciences*, 45(5):789–799.

Wheel, M. A. (1996). A geometrically versatile finite volume formulation for plane elastostatic stress analysis. *Journal of Strain Analysis for Engineering Design*, 31(2):111–116.

Wheeler, A. F., Myers, S., and Lever, D. (2015). Project Ankhiale : Estimating the uplift due to high-heat-generating waste in a Geological Disposal Facility. Technical Report 3, AMEC for RWM.

Wilde, A. J. and Aliabadi, M. H. (1999). Boundary element analysis of geomechanical fracture. *International Journal for Numerical and Analytical Methods in Geomechanics*, 23(12):1195–1214.

Wilder, D. G. and Ramirez, A. L. (1991). Prototype Engineered Barrier System Field Tests (PEBSFT). Technical Report May 1989, Lawrence Livermore National Laboratory.

WNA (2018). World Nuclear Performance Report. Technical report.

Xia, M. (2015). Thermo-mechanical coupled particle model for rock. *Transactions of Nonferrous Metals Society of China (English Edition)*, 25(7):2367–2379.

Xia, M., Zhao, C., and Hobbs, B. E. (2014). Particle simulation of thermally-induced rock damage with consideration of temperature-dependent elastic modulus and strength. *Computers and Geotechnics*, 55:461–473.

Xiang, J., Munjiza, A., and Latham, J.-P. (2009a). Finite strain, finite rotation quadratic tetrahedral element for the combined finite–discrete element method. *International Journal for Numerical Methods in Engineering*, 27(79):946–978.

Xiang, J., Munjiza, A., Latham, J. P., and Guises, R. (2009b). On the validation of DEM and FEM/DEM models in 2D and 3D. *Engineering Computations (Swansea, Wales)*, 26(6):673–687.

Yan, C. and Zheng, H. (2017). A coupled thermo-mechanical model based on the combined finite-discrete element method for simulating thermal cracking of rock. *International Journal of Rock Mechanics and Mining Sciences*, 91(November 2016):170–178.

Yang, P. (2018). *High fidelity fluid-structure turbulence modelling using an immersed-body method*. PhD thesis, Imperial College London.

Yang, P., Xiang, J., Chen, M., Fang, F., Pavlidis, D., Latham, J. P., and Pain, C. C. (2017). The immersed-body gas-solid interaction model for blast analysis in fractured solid media. *International Journal of Rock Mechanics and Mining Sciences*, 91(March 2016):119–132.

Yang, P., Xiang, J., Fang, F., Pavlidis, D., Latham, J. P., and Pain, C. C. (2016). Modelling of fluid-structure interaction with multiphase viscous flows using an immersed-body method. *Journal of Computational Physics*, 321:571–592.

Yaseen, M. (2004). Use of thermal heating-cooling process for rock fracturing : numerical and experimental analysis. page 150.

Yoon, H. S., Yu, D. H., Ha, M. Y., and Park, Y. G. (2010). International Journal of Heat and Mass Transfer Three-dimensional natural convection in an enclosure with a sphere at different vertical locations. *International Journal of Heat and Mass Transfer*, 53(15-16):3143–3155.

Yovanovich, M. M. (2005). Four decades of research on thermal contact, gap, and joint resistance in microelectronics. *IEEE Transactions on Components and Packaging Technologies*, 28(2):182–206.

Zamani, A. and Eslami, M. R. (2010). Implementation of the extended finite element method for dynamic thermoelastic fracture initiation. *International Journal of Solids and Structures*, 47(10):1392–1404.

Zhang, K., Wu, Y., and Pruess, K. (2008). Lawrence Berkeley National User ' s Guide for TOUGH2-MP - A Massively Parallel Version of the User ' s Guide for TOUGH2-MP - A Massively Parallel Version of the TOUGH2 Code. *Sciences-New York*, (May).

Zoback, M. D. (2007). *Reservoir geomechanics.* Cambridge University Press.

Appendix A

Description of THM Coupled Computer Codes

A.1 Finite element method

A.1.1 ABAQUS

ABAQUS (Simulia, 2017) is commercial 2D and 3D stress analysis code largely used in range of areas including rock mechanics. ABAQUS includes capabilities for two way coupled thermo-mechanical analysis and hydro-mechanical analysis of partially saturated porous media. Part of those features where implemented in a modified ABAQUS-CLAY approach (Clay technologies, Sweden) for the Kamaishi mine heater test (Rutqvist et al., 2001a,b).

A.1.2 CAST3M

CAST3M (Le Fichoux, 2011) is developed by the Commissariat à l'Énergie Atomique (CEA). CAST3M is for 2D and 3D and possess extensive THM coupled capabilities: Darcy flow for saturated porous media and fracture mechanics with extended finite elements (X-FEM) (Benoit, 2007, Sukumar et al., 2000) where a discontinuous function is introduced in the continuum to represent the crack surface. Alternatively, a wide range of damage models may be used. CASTEM solves the coupled THM equations in a sequential manner (Millard et al., 1995, Parry, 2017) with a dedicated procedure:

'PASAPAS'. Quasi-static and dynamic explicit time integration as well as fully implicit time integration may be used. Although CAST3M was principally developed for the modelling of concrete structures, it was applied to radioactive waste repository performance in the first DECOVALEX programs (Chijimatsu et al., 2005, Millard et al., 1995) and more recently the code was applied to HM coupling of two phase flow through an excavation damage zone (Bénet et al., 2017).

A.1.3 CODE-BRIGHT

CODE-BRIGTH (COupled DEformation, BRine Gas and Heat Transport. CODE-BRIGHT, 2018) is finite element THM coupled code developed at the Department of Civil and Environmental Engineering of the Polytechnic University of Catalonia (UPC). It was initially targeted for non-isothermal multiphase flow of brine and gas through saline media (Olivella et al., 1994) and the code now extends to THM coupled processes. The main specificity of the code is that the solid is considered as a phase according to Philip and De Vries (1957) theory, thus the following equations may be solved in a monolithic manner on the same mesh: equilibrium of stresses, mass balance of solid, mass balance of water, mass balance of air, energy equation (thermal equilibrium assumed). The research project contributing to this computer code is funded by several national radioactive waste management organisations: SKB (Sweden), Posiva (Finland), GRS (Germany) and the ANDRA (France); in this context, CODE-BRIGHT was employed for several laboratory and repository scale simulations (Clay, 2004, Tsang et al., 2005).

A.1.4 COMPASS

COMPASS (Thomas et al., 1996) is a two dimensional THM coupled finite element code for clay based engineered barriers, clay rock formations and buffer-rock interactions. COMPASS was part of the CNFWMP (Canadian Nuclear Fuel Waste Management Program) and was involved in verifications of the adequacy of numerical modelling to represent the behaviour of engineered barriers sytems (Thomas et al., 1998). The code is extended from a heat and two-phase moisture transfer model with non-linear elastic (Lloret and Alonso, 1985), elasto-plastic (Alonso et al., 1990) and thermo-plastic stress-strain relationships. The finite element discretisation is achieved on quadratic quadrilateral elements for pore water pressure, pore air pressure, temperature and displacement. Thermo-hydraulic on one side and mechanical equations on the other are solved separately in a sequential manner. For a given time step the procedure iterates between the two until convergence is achieved.

A.1.5 COMSOL

COMSOL is a commercial multi-purpose finite element platform able to solve for THMC coupled systems of PDEs. COMSOL possesses a geomechanics module and a subsurface flow module for Darcy flow in saturated and unsaturated porous media. The poroelastic approach adopted in the subsurface module may be coupled with non-linear geomechanics models (Cam-Clay, Drucker-Prager, Mohr-Coulomb, Matsuoka-Nakai and Lade-Duncan) of the geomechanics module. In a three-dimensional geometry, fractures may be represented by introducing planar internal boundaries onto which pressure is solved. COMSOL is currently involved in DECOVALEX-2019, task E (RWM, 2019).

A.1.6 FRACON

FRACON (FRActure medium CONsolidation, Nguyen and Selvadurai 1995 and Nguyen 1996) is developed by the Canadian Atomic Energy Control Board and McGill University for THM process of sparsely fractured porous rock. FRACON is solving three or two dimensional problems on hexahedral elements with Biot's equation of consolidation (Biot, 1941), Darcy's law and Fourier's law for heat conduction only. The mechanical equilibrium equations are solved on quadratic elements while the pore pressure and temperature are interpolated on the linear nodes of the quadratic elements. FRACON also incorporates joint elements to represent discontinuities in the rock, the mechanical behaviour of the element is controlled by a stiffness tensor for shear and dilation while the hydraulic and thermal behavior of joints are governed by specific tranverse and longitudinal permeability and heat conductivity. Orignially, FRACON solves all coupled equations in a monolothic manner, using a theta method time integration. However, similarly to ROCMAS, a sequential solution approach is implemented to handle large time spans for repository modelling (Rutqvist et al., 2001a) thus, hydro-mechanical equations are solved separately to the heat equation and with respective time steps. FRACON was part of many DECOVALEX numerical studies: DECOVALEX II - Task

2C: Kamaishi Mine heater test (Rutqvist et al., 2001a,b), DECOVALEX III - FEBEX experiment (Nguyen et al., 2005) and DECOVALEX III - BMT1: Study of the THM effects on the near field (Chijimatsu et al., 2005). However, none of the cited studies involve the modelling of discontinuities.

A.1.7 MOTIF

MOTIF (Model Of Transport In Fractured/porous media Guvanasen and Chan 2000). Developed at AECL (Atomic Energy of Canada Limited) based on the small strain theory of continuum mechanics, this 3D code has a THMC coupled approach. In MOTIF, discrete fractures are represented by insertion of special quadrilateral elements for which the hydro-mechanical equilibrium is governed by local mechanical stress and fluid pressure. Deformation of the joint elements are based on a hyperbolic normal-displacement, normal-stress relationship (Bandis et al., 1983) and the hydraulic conductivity of a fracture is calculated using an empirical relationship between mechanical and hydraulic aperture (Barton and Bakhtar, 1985). MOTIF was applied successfully in the early stages of DECOVALEX (Chan et al., 1995).

A.1.8 OpenGeoSys

OpenGeoSys (OGS, Kolditz et al., 2012a) is an open source framework for THMC processes in fractured porous media. OGS is a mature platform which has absorbed several decades of developments on different numerical codes such as RockFlow (Kolditz et al. 2003, Center for Applied Geosciences, University of Tübingen, and Institute of Fluid Mechanics, University of Hannover) for flow processes in complex geological structures and FEFLOW (Academy of Sciences, Chemnitz) for density-dependent flow processes in porous media. In OGS fully coupled thermo-hydro-mechanical equations may be solved in a monolithic manner and alternatively, a sequential approach may be used for T-H and H-M couplings (Geosys/Rockflow, Birkholzer et al. 2005b).

A.1.9 ROCMAS

ROCMAS (ROCk Mass Analysis Scheme) is developed at the Lawrence-Berkley National Laboratory (Noorishad and Tsang, 1996, Rutqvist et al., 2001a) for saturated or un-staturated porous and fractured rocks based on Biot's theory of consolidation (Biot, 1941). The formulation considers three phases: gas, liquid and solid based on Philip and De Vries (1957) theory for moisture movement in porous materials. To represent fractures, ROCMAS introduces elements with weaker mechanical properties and correlates strain with permeability changes (Hudson et al., 2008). To tackle the large time ranges of waste repository simulations, equations are solved in a sequential manner because the time step requirements of the hydrological equations are much smaller compared to the thermal equation (Rutqvist et al., 2009b). ROCMAS greatly contributed to the DECOVALEX project (Birkholzer et al., 2005a, Chan et al., 1995, Chijimatsu et al., 2005, Min et al., 2005, Rutqvist et al., 2009a,b, 2001a,b).

A.1.10 THAMES

THAMES (Thermal, Hydraulic And MEchanical System analysis). This 2D and 3D code is developed at Kyoto University, Japan (Ohnishi et al., 1987, Stephansson et al., 1996) particularly for THM coupled processes in fully or partially saturated porous medium applications. Its thermal, hydraulic and mechanical governing equations are fully coupled and solved simultaneously with any type of finite difference scheme. In THAMES, major discontinuities such as faults may be represented explicitly with the insertion of joint elements whereas minor fractures and fracture networks are represented with a crack tensor equivalent continuum approach (Oda, 1986). This code was used extensively within the DECOVALEX project: Kamaishi mine heater test (Rutqvist et al., 2001a,b), DECOVALEX III - BMT1 (Chijimatsu et al., 2005), DECOVALEX-THMC Task B (Hudson et al., 2008, Rutqvist et al., 2009a) and Task D Birkholzer et al. (2005a,b).

A.2 Finite difference and Finite Volume method

A.2.1 Cellular Automata: EPCA

EPCA (Elasto-Plastic Cellular Automaton) is a 2D and 3D code combining, cellular automata, fluid flow, thermo-elasto-plastic theory and fracture mechanics (Pan et al., 2012). Fractures are represented with a damage model and by introducing weak elements upon failure. For THM analysis, poro-elasticity, Darcy flow and heat conduction are solved sequentially.

Fluid-fracture interaction is possible as permeability and incidentally heat conduction may be a function of damage, plasticity, mean stress or volumetric strain. With this approach, a mechanical only analysis was performed to assess the permeability changes in the EDZ of a waste repository (Hudson et al., 2008, Pan et al., 2009, Rutqvist et al., 2009a). EPCA 3D has also been employed in the ASPE (Pan and Feng, 2013) in a coupled thermo-mechanical approach.

A.2.2 QPAC

QPAC (Maul, 2013) is a 3D FVM code developed by the company Quintessa to tackle strongly coupled THMC non-linear processes. QPAC was part of DECOVALEX 2011 (Bond et al., 2012) and is part of DECOVALEX 2019 task E (RWM, 2019). This code was also employed in the European THERESA project (Maul et al., 2008) for which a specific QPAC-EBS (Maul, 2010) was developed with the following coupled technologies: heat conduction and convection, multiphase Darcy flow, Visco-poro-elastic model with swelling, thermal expansion and grain deformation effects. All coupled equations are solved with an implicit time marching procedure (Byrne and Hindmarsh, 1975).

A.2.3 FLAC3D

FLAC3D (Fast Lagrangian Analysis of Continua in 3 Dimensions), Itasca CG (2017), is a 3D explicit FDM and FVM geomechanical solver with a wide range of elastic and plastic models. FLAC3D can solve for heat conduction, heat convection and the Darcy equation for flow in porous media under saturated and unsaturated conditions.

For coupled THM processes FLAC3D adopts a quasi-static approach that can be applied to saturated porous media problems with heat conduction only. One-way T→M and T→H couplings are still possible due to thermal expansion in the fluid and the solid. Starting from a state of mechanical equilibrium, a coupled hydro-mechanical quasi-static simulation in FLAC3D involves a series of steps. Each step includes one or more flow steps (flow loop) followed by enough mechanical steps (mechanical loop) to maintain quasi-static equilibrium.

The hydraulic and thermal equations may be solved explicitly or implicitly and the coupling process is sequential: starting from a mechanical equilibrium each coupling iteration involves one or more flow or thermal steps followed by a sufficient number of mechanical steps to achieve quasi-static equilibrium.

In the context of geological waste disposal, the thermo-mechanical coupling capabilities of FLAC3D were demonstrated in the Äspö Pillar Stability Experiment (APSE, Kwon et al. 2013), where mechanical and thermal spalling were studied.

A.2.4 TOUGH2

TOUGH2 (Transport Of Unsaturated Groundwater and Heat) is developed at the Lawrence Berkeley National Laboratory (Pruess, 1991), this code solves for non-isothermal multiphase flow in one, two, and three-dimensional porous and fractured media. TOUGH2 also includes reactive transport and is thus thermo-hydro-chemically coupled (THC). A parallel version, TOUGH-MP (Zhang et al., 2008) was employed by Enssle et al. (2011) for the study of long-term hydraulic perturbations induced by gas and heat generation at the repository scale.

A.2.5 TOUGH-FLAC

TOUGH-FLAC is a simulator of coupled THM processes under multiphase fluid flow conditions developed at the Lawrence Berkeley National Laboratory (Rutqvist et al., 2002). It is based on two existing FDM codes, TOUGH2 for multiphase flow and FLAC3D for geomechanical analysis, both codes have already been introduced in this section. TOUGH-FLAC solves only one mesh, however, an interpolation is still required because TOUGH2 mesh has one nodal point in each element and FLAC3D has 4 nodes in each corner, see Figure A.1. The local fluid-solid thermal equilibrium is assumed and thus heat transfer is only calculated in TOUGH2, the variation of temperature within one iteration being passed to FLAC3D as a coupling parameter.

In TOUGH-FLAC, the main discontinuities can be defined within the rock matrix by inserting weak elements but essentially the code treats the porous rock mass as a continuum. To represent fractured media an empirical model is applied to correct permeability as a function of the three-dimensional stress field (Rutqvist et al., 2009b, 2002). This permeability model has been employed for THM coupled process analysis with the Yucca Mountain project (Rutqvist and Tsang, 2003), where anisotropic permeability changes were accounted for by assuming three sets of orthogonal fractures.

With TOUGH2-FLAC3D, Rutqvist et al. (2009a) modelled the thermo-hydro-mechanical behavior of a pre-existing discrete fracture network in the EDZ of a deposition hole. This was achieved with a fine mesh by softening and weakening the grid elements at the fracture's positions with a Mohr-Coulomb law to capture their mechanical behaviour. Another approach by Rutqvist et al. (2002) and Kwon et al. (2013) consisted in using a crack tensor (Oda, 1986).

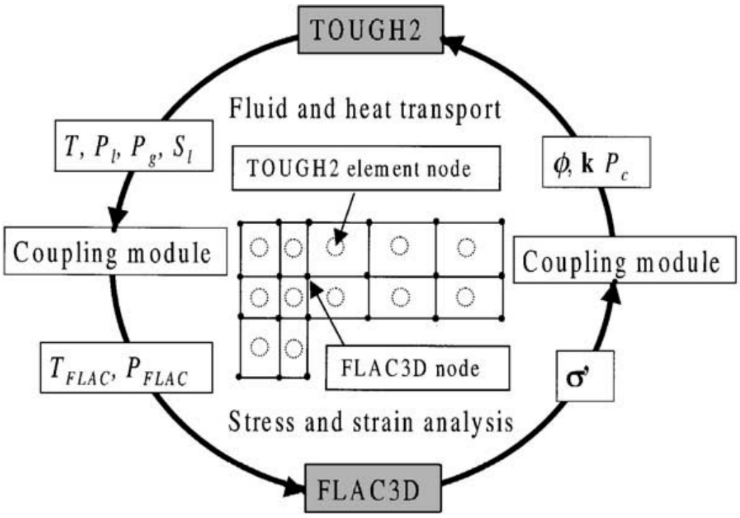

FIGURE A.1: Interpolation and exchange of coupling information between TOUGH2 and FLAC3D, Rutqvist et al. (2002).

In TOUGH-FLAC, the real time transient TH analysis is performed by TOUGH2 and a quasi-static mechanical analysis is conducted by FLAC3D. The code has two possible time marching procedures as shown on Figure A.2): (1) 'explicit sequential' where after each fluid time step, a quasi-static analysis is performed until the solid has reached mechanical equilibrium; and (2) 'implicit sequential' where the quasi-static analysis may be performed within a fluid iteration, enabling the permeability and porosity to be updated to correct the fluid solution, rather than only evaluating them once per time step.

As compensation for less accuracy, the explicit procedure is less computationally expensive because quasi static analysis and interpolation need only to be executed once per time step. Moreover, Rutqvist et al. (2002) highlights that the explicit procedure should be accurate if the porosity and permeability changes are relatively small within one time step.

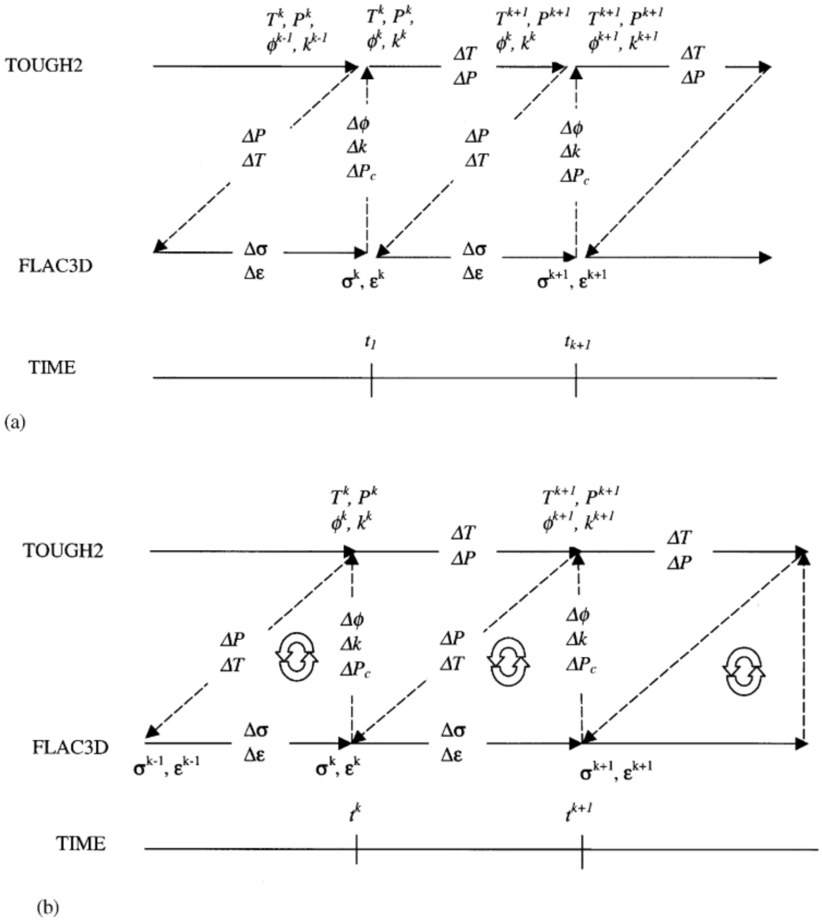

FIGURE A.2: (a) Explicit sequential and (b) implicit sequential coupling procedures in TOUGH2-FLAC3D, Rutqvist et al. (2002)

A.3 Boundary Element Method: FRACOD

FRACOD 2D (Shen et al., 2013) is developed by FRACOM Ltd, Finland, based on the displacement discontinuity method (DDM, Crouch 1976 and Shen et al. 2006) which solves for the displacements of discontinuities such as fractures or domain boundaries. In the DDM the two walls of a crack are represented with one fracture element. Initiation, propagation and interaction of fractures in an elastic rock medium are calculated based on the F-criterion which accounts for tensile and shear failure (Shen and Stephansson, 1993). Like other boundary element methods, the DDM relies on an implicit time marching procedure. However, in the case of a fracturing event, an explicit scheme is recruited. Additionally, a sub-critical crack growth model (implicit time integration) is implemented for time-dependent creep. It is worth mentioning that this model was employed in the context of repository modelling and that the research "showed only insignificant sub-critical crack growth, which occurred during the first 100 years of thermal loading" (Rutqvist et al., 2009a).

FRACOD can perform thermo-mechanical and hydro-mechanical couplings. No THM coupling is available although the authors of the code communicate that this feature is under development (Shen et al., 2013). Coupled equations are solved sequentially and a different type step may be used for each process.

The thermo-mechanical coupling is based on the thermo-elastic theory with linear thermal expansion which allows FRACOD to perform thermally induced fracturing. This feature was demonstrated in the Äspö Pillar Stability Experiment (APSE) where thermal stresses led to minor spalling (Rinne et al., 2013).

The hydro-mechanical coupling is achieved by discretisation of the fracture into a number of connected hydraulic elements upon which the pressure is solved (Figure A.3). Leak-off to the porous matrix is also considered by introducing a variable of the domain pore pressure. The HM coupling iteration scheme is as follows:

1. Fluid flow between domains and leakage into rock
2. Domain fluid pressure change
3. Fracture deformation
4. Domain geometry change
5. Domain fluid pressure change

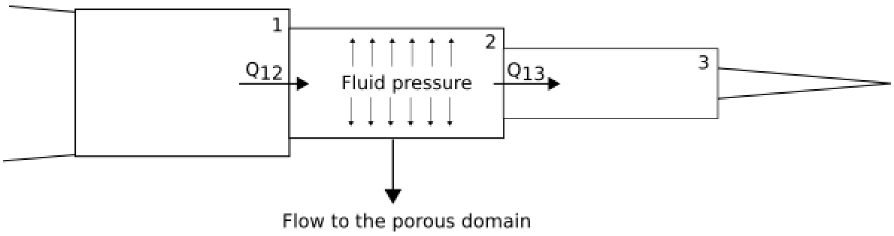

FIGURE A.3: Subdivision of the fracture into flow elements in FRACOD, after Shen et al. (2013)

A.4 Explicit DEM

A.4.1 3DEC and UDEC

3DEC (3D Distinct Element Code) and UDEC (Universal Distinct Element Code, the two-dimensional version) are specifically developed for discontinuous media such as fractured rock masses. The rock mass is represented as an assembly of blocks which may be considered deformable with a finite difference method.

In 3DEC the domain may be discretised with polyhedral elements and a bonded block model (BBM) approach ensures that elements are mechanically bonded at their interface, enabling crack initiation and crack propagation.

In UDEC (itasca.com: fluid flow in joints) and in 3DEC (Cappa et al., 2008), fluid flow in fractures is achieved with a network of fluid domains placed where there is contact between grid points or between an edge and a grid point (Figure A.4). Domains are considered of uniform pressure and fluid may flow from one domain to its neighbours, creating a discrete network of interconnected pressure points. The flow is governed by pressure differential between neighbouring domains and is controlled by the aperture of the rock joint according to the cubic law of flow between parallel plates Snow (1965).

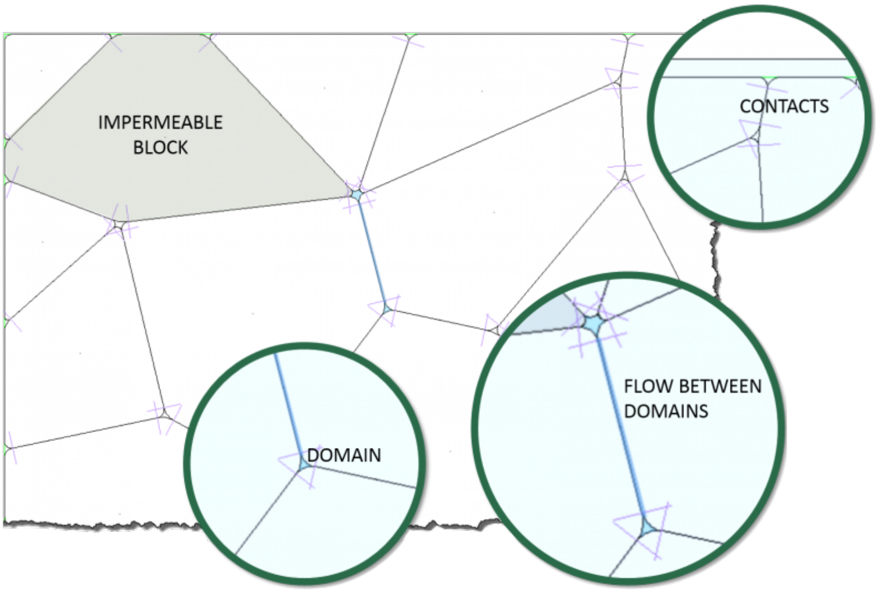

Figure A.4: Fluid flow in-between discrete elements (Itasca, 2018)

Blocks are considered impermeable in UDEC but a steady-state pore pressure may be applied as a boundary condition, in 3DEC saturated porous media flow is considered within the rock blocks. In both codes, the fluid flow model may be coupled with the hydraulic model (Cappa et al., 2008, Karatela and Taheri, 2018) and thermal model with the compressibility and the thermal expansion of the saturated material taken into account. Although the finite difference formulation of the distinct element method may employ an implicit scheme, the contact detection algorithm and the computation of the contact forces can only be resolved explicitly, therefore the thermo-mechanical and hydro-mechanical couplings are achieved sequentially.

This enables the fluid and thermal solver to be independent to the mechanical solver and in the case of modelling THM processes over large time spans, there is no limitation in using the most adapted time marching procedure which is the implicit scheme. For DECOVALEX II BMT2, a 'balloon scheme' was employed to achieve the sequential coupling of THM processes with UDEC (Chan et al., 1995). The scheme runs first a thermal cycle on a thermal time scale, then the temperature is held constant and a hydro-mechanical cycle is run on a different time step (see Figure A.5). In the hydro-mechanical cycle, a hydraulic calculation is first performed, then the mechanical solver iterates until an equilibrium is reached and finally, pressure in the domain is modified proportionally to the fluid domain change due to mechanical deformation and displacements.

3DEC was employed by SKB (Svensk Kärnbränslehantering Aktiebolag, the Swedish nuclear fuel and waste management company) for the modelling of far, medium and near field THM coupled processes (Hökmark et al., 2010). The coupled processes considered in this study are the thermal stresses (T➞M), the effective pore pressure (H➞M) and the change of fracture hydraulic properties due to fracture opening and closing based on different permeability models (M➞H). The hydraulic behaviour is not explicitly modelled and the approach may not be referred to as fully coupled, only fully TM coupled. Moreover, in this work no new fracturing was considered and only a few fractures were represented as simplified planes intersecting the rock model. 3DEC was also part of DECOVALEX III for simpler configurations (Tsang et al., 2005). UDEC has been widely used in DECOVALEX (Chan et al., 1995, Millard et al., 1995, Tsang et al., 2005, 2004) for THM coupled simulations also with the omission of HM and TH fully coupled behaviours.

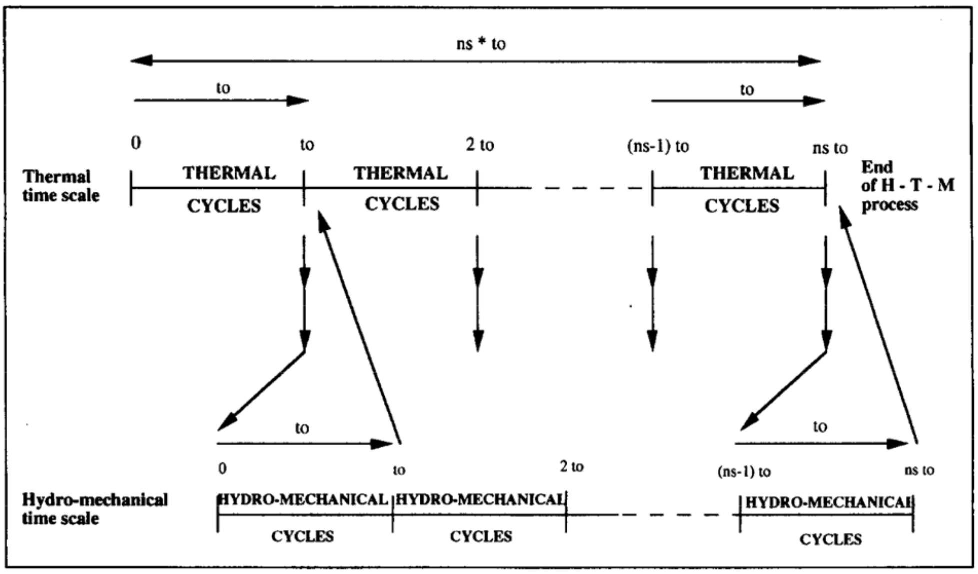

to = NTHER * THDT = NMECH * DTFLOW

Where NTHER = number of thermal steps
THDT = value of a thermal step (s)
NMECH = number of hydro-mechanical steps
DTFLOW = value of a hydro-mechanical step (s)

Fig. A1. Transient thermo-hydro-mechanical process in UDEC.

Figure A.5: ‘Balloon scheme’ for the sequential coupling of THM processes with UDEC (Chan et al., 1995)

This approach suggests that fluid pressure may be exerted on the fracture walls. However, if there is no representation of the effective stress on the rock matrix, there is no poro-elastic behaviour.